

Innovative Concepts for the Electronic Interface of Massively Parallel MRI Phased Imaging Arrays

Zur Erlangung des akademischen Grades

Doktor der Ingenieurwissenschaften

der Fakultät für Maschinenbau
Karlsruher Institut für Technologie (KIT)
genehmigte

Dissertation

von

M.Sc. Mazin Jouda

Tag der mündlichen Prüfung: 6. Juni 2016

Hauptreferent:

Prof. Dr. Jan G. Korvink

Korreferent:

Jun.-Prof. Dr. Jens Anders

Karlsruher Institut für Technologie
Institut für Mikrostrukturtechnik
H.-v.-Helmholtz Platz 1
76344 Eggenstein-Leopoldshafen

Abstract

In its very primitive structure, the magnetic resonance imaging (MRI) or magnetic resonance spectroscopy (MRS) hardware consists of a magnet where the sample is placed, a radio frequency (RF) transmission coil that excites the magnetization of the sample, an RF reception coil to detect the magnetic resonance (MR) signals, and an RF transceiver. During the last two decades, the concept of MR phased arrays, where multiple decoupled coils are employed to simultaneously acquire the MR signals, was extensively applied. These phased arrays led to significant improvements in performance, especially in MRI, by increasing the resolution, decreasing the imaging time, and enlarging the field of view (FoV). Moreover, they showed great potential for further enhancements by increasing the number of reception coils. However, employing the phased arrays resulted in a number of drawbacks such as the increased size, cost, and complexity of the MR system since each coil is an independent channel and, therefore, requires a separate cable and a separate RF receiver. With increasing the number of coils within the array, these drawbacks become more challenging and ultimately prevent having arrays with large numbers (>128) of coils.

This thesis introduces a novel solution that allows having MR phased arrays with many coils with no penalty of increased size, cost, or complexity. This new solution is based on the design and fabrication of a CMOS frequency division multiplexer (FDM) that is capable of merging up to eight channels and transmitting them over a single coaxial cable to a single RF receiver. The size-efficient (chip area $\approx 3 \times 4 \text{ mm}^2$) and power-efficient (56 mA/ch) integrated FDM is designed in XH035 CMOS technology, and comprises, for each channel, a low-noise amplifier (LNA), a frequency mixer, and a bandpass filter (BPF). The chip was fabricated, and the performance of its various blocks was characterized. Moreover, the influence of the magnetic field on the chip's performance was verified, and the results showed a normal operation in magnetic fields up to 11.7 T. Finally, the CMOS chip was tested in spectroscopy and imaging experiments in an 11.7 T and 9.4 T Bruker scanners respectively. These experiments revealed a number of technical issues and challenges to be considered when interfacing custom hardware to commercial scanners. However, in all experiments, the results obtained from the chip exhibited a high degree of resemblance to

their counterparts provided by the commercial systems.

Furthermore, the thesis presents a novel simulation method with which to design, characterize, and optimize hardware (electronic interfaces) for MRI receivers. The Matlab-based toolbox generates idealized MR signals for the RF reception coil from real MR images, thus allows the user to carry out a virtual MRI experiment by running a transistor-level simulation of the desired MR receiver's hardware. The simulation outputs are read back into the toolbox, which thereafter reconstructs the MR image. By comparing the reconstructed image with the original one, many important circuit characteristics, such as noise figure, linearity, and inter-channel coupling can be investigated. The new simulation tool was validated by conducting an imaging experiment through the aforementioned 8-channel FDM, and through a proposed 16-channel frequency-division and time-division (FDTD) multiplexer. All the images were successfully reconstructed from the simulations. Moreover, the noise and linearity results obtained from this new method showed good propinquity to the conventional simulation results.

Finally, a new fully-integrated MRI receiver architecture was proposed. Besides the low-noise amplification, frequency mixing, and filtering, the new architecture employs a third-order $\Sigma\Delta$ modulator to digitize the signals. Having these signals in digital form allows to perform time multiplexing on the digital data streams, and to replace the coaxial cables with optical fibers. Therefore, the new receiver is conceived to be a serious competitor to the FDM, and can show superiority especially in the case of MR arrays with large number of coils, where the FDM capabilities become limited. The new receiver was realized and verified at both the system-level and the transistor-level using the above-mentioned Matlab toolbox.

Zusammenfassung

Grundlegend besteht Hardware für Messgeräte der Magnetresonanztomografie oder der Magnetresonanzspektroskopie aus einem Magneten in dem die Messprobe platziert ist, einer Sendespule betrieben im Radiofrequenzbereich zur Anregung der Magnetisierung der Probe, einer Empfangsspule zur Detektion des (MR) Signales und einem RF Transceiver. Während der letzten zwei Jahrzehnten wurde das Konzept der phasengesteuerten Gruppenantennen umfangreich angewandt. Hierbei werden mehrere voneinander entkoppelte Spulen zur Detektion des MR Signals eingesetzt. Speziell in der MRT führten diese phasengesteuerten Antennen zu einem signifikanten Anstieg der Leistungsfähigkeit. Der Grund liegt in der Erhöhung der Auflösung, der Reduktion der Aufnahmezeit und der Vergrößerung des Sichtfeldes (FoV). Darüber hinaus zeigten diese Antennen großes Potential für weitere Fortschritte durch die Erhöhung der Anzahl der Empfangsspulen. Jedoch zeigten sich in der Anwendung etliche Nachteile wie beispielsweise eine Erhöhung der Baugröße, der Kosten und der Komplexität des MRT Systems, da jede Spule einen eigenen unabhängigen Kanal darstellt und daher eine separate Verkabelung und Empfangstechnik erfordert. Diese Nachteile werden mit steigender Anzahl an Spulen innerhalb der Antenne schwieriger zu bewältigen und verhindern letztendlich die Herstellung von Antennen mit einer großen Anzahl (>128) an Spulen.

Im Rahmen dieser Thesis wird eine neue Lösung präsentiert die es erlaubt phasengesteuerte MR Antennen zu herzustellen, ohne Einbußen hinsichtlich der Baugröße, Kosten oder Komplexität erleiden zu müssen. Die Lösung basiert auf dem Design und der Herstellung eines CMOS Frequenzmultiplexers (FDM) welcher in der Lage ist Signale von bis zu acht Kanälen zu überlagern und diese über eine einzelne Koaxialverbindung zu einem Empfänger zu übertragen. Der kompakte (Chip-Fläche $\approx 3 \times 4 \text{ mm}^2$) und leistungsstarke (56 mA/ch) integrierte Multiplexer wurde in XH035 CMOS Technologie konzipiert und beinhaltet für jeden Kanal einen rauscharmen Verstärker (LNA), einen Frequenzmischer sowie einen Bandpassfilter (BPF). Der Chip wurde hergestellt, sowie die Leistungsfähigkeit der verschiedenen Einheiten charakterisiert. Darüber hinaus wurde der Einfluss des magnetischen Feldes auf die Leistungsfähigkeit des Bausteins geprüft, wobei die Resultate zeigen, dass die Funktionalität bis zu Magnetfeldstärken von 11,7 T gewährleistet ist.

Abschließend wurde der Chip in Spektroskopie- und Bildgebungsexperimenten sowohl an einem 9,4 T als auch an einem 11,7 T Bruker MRT-System getestet. Die Experimente zeigten eine Reihe an technischen Fragestellungen und Herausforderungen die es zu beachten gibt, wenn benutzerdefinierte Hardware an kommerzielle Systeme angeschlossen wird. Die erhaltenen Resultate aller Experimente zeigten jedoch Ähnlichkeiten in hohem Maße im Hinblick auf die kommerziell erhältlichen Ausfertigungen.

Zusätzlich wird im Rahmen dieser Thesis eine neue Simulationsmethode vorgestellt, die es erlaubt Hardware (elektronische Schnittstellen) für MRT Empfänger zu entwerfen, zu charakterisieren sowie zu optimieren. Ausgehend von realen MRT Bildern erzeugt die MATLAB-basierte Toolbox idealisierte MRT-Signale für RF Empfangsspulen. Basierend auf einer Transistor-Level-Simulation, erlaubt dies dem Benutzer, virtuelle MRT Experimente gewünschter Empfänger Hardware durchzuführen. Die Ergebnisse der Simulation werden wiederum in der Toolbox eingelesen und ein MRT Bild kann rekonstruiert werden. Der Vergleich des rekonstruierten Bildes mit dem Original erlaubt die Untersuchung wichtiger Schaltungscharakteristiken wie beispielsweise der Rauschzahl, Linearität und der Kanalkopplung. Das neue Simulationswerkzeug wurde evaluiert mit der Durchführung von MRT Experimenten anhand des zuvor genannten 8-Kanal Multiplexers sowie eines geplanten 16-Kanal Frequenz-Zeit-Multiplexers (FDTD). Aufbauend auf den Simulationsergebnissen konnten alle Bilder wieder erfolgreich rekonstruiert werden. Darüber hinaus zeigten die erhaltenen Resultate der Simulationen eine gute Übereinstimmung mit den konventionellen Simulationsergebnissen hinsichtlich des Rauschens und der Linearität.

Abschließend wurde eine vollintegrierte MRT Empfangsarchitektur geplant. Neben der rauscharmen Verstärkung, einem Frequenzmischer und Frequenzfilterung, ist in der neuen Architektur ein $\Sigma\Delta$ Modulator zur Digitalisierung der Signale integriert. Das Vorliegen der Signale in digitaler Form erlaubt die Durchführung von Zeitmultiplexing an digitalen Datenströmen sowie die Einführung von optischen Glasfaserkabel anstelle von Koaxialkabel. Der neue Empfänger ist geplant als ernsthafte Konkurrenz zur FDM und wird eine deutliche Überlegenheit zeigen im Hinblick auf phasengesteuerte Gruppenantennen mit einer großen Anzahl an Einzelspulen, bei denen die FDM Kapazitäten limitiert sind. Der neue Empfänger wurde realisiert und verifiziert, beiderseits, auf System- und Transistor-Level anhand der erwähnten MATLAB-Toolbox.

Nomenclature

Abbreviations

Abbreviation	Meaning
MR	Magnetic Resonance
MRI	Magnetic Resonance Imaging
MRS	Magnetic Resonance Spectroscopy
RF	Radio Frequency
LO	Local oscillator
IF	Intermediate frequency
FoV	Field of View
NMR	Nuclear Magnetic Resonance
CT	Computed Tomography
FID	Free Induction Decay
ppm	Part per million
ppb	Part per billion
FEG	Frequency Encoding Gradient
PEG	Phase Encoding Gradient
SSG	Slice-Select Gradient
ADC	Analog-to-digital converter
DAC	Digital-to-analog converter
AC	Alternating current
LNA	Low-noise amplifier
SNR	Signal-to-noise ratio
VGA	Variable Gain Amplifier
DC	Direct Current
SAW	Surface Acoustic Wave
FFT	Fast Fourier Transform
GE	Gradient echo
TE	Echo time
TR	Repetition time

Abbreviation	Meaning
SE	Spin echo
TDM	Time Division Multiplexing
FDM	Frequency Division Multiplexing
DDS	Direct Digital Synthesizer
FPGA	Field Programmable Logic Array
MUX	Multiplexer
DEMUX	Demultiplexer
CS LNA	Common-source LNA
CG-CS LNA	Common-Gate common-source LNA
PVT	Process-Voltage-Temperature
CCC	Capacitive cross coupling
BPF	Bandpass filter
Opamp	Operational amplifier
SR	Slew rate
GBW	Gain-bandwidth product
EMI	Electromagnetic Interference
GUI	Graphical User Interface
OSR	Oversampling ratio
ENOB	Effective number of bits
$\Sigma\Delta$ M	Sigma-delta modulator
SQNR	Signal-to-quantization noise ratio
STF	Signal transfer function
NTF	Noise transfer function
IBN	In-band noise
PSD	Power spectral density
UHFLI	Ultrahigh frequency lock-in amplifier

Symbols

Symbol	Meaning	Unit
I	Spin number	-
$\hat{\mu}$	Magnetic moment	A m ²
\hat{S}	Spin angular momentum	kg m ² s ⁻¹ rad ⁻¹
γ	Gyromagnetic ratio	Hz/T
B_0	Static magnetic field in z-direction	T

Symbol	Meaning	Unit
ω_0	Larmor frequency	rad/s
\hbar	Reduced Max Planck's constant	J s
k_B	Boltzmann constant	J/K
T	Temperature	K
M_0	Net magnetization	A/m
M_z	Longitudinal magnetization	A/m
M_{xy}	Transverse magnetization	A/m
B_1	Time-varying sample-exciting magnetic field	T
α	Flip angle	°
τ	Pulse duration	s
T_1	Spin-lattice relaxation time	s
T_2	Spin-spin relaxation time	s
μ_0	Permeability of free space	H/m
Z_c	Coil impedance	Ω
r_c	Internal resistance of the coil	Ω
L_c	Coil inductance	H
C_t	Tuning capacitor	F
C_m	Matching capacitor	F
K	Scalar inhomogeneity factor of B_0	-
K	Stern stability factor	-
Δf	MR receiver's bandwidth	Hz
F	Noise factor	-
G	Gain	dB
g_m	Transistor transconductance	S
C_{gs}	gate-source capacitance	F
ω_T	Transition frequency of the transistor	rad/s
NF	Noise figure	dB
γ	Channel's thermal noise coefficient	-
μ_n	Charge carrier effective mobility	$\text{m}^2 \text{V}^{-1} \text{s}^{-1}$
C_{ox}	Gate oxide capacitance per unit area	F

Contents

Abstract	i
Zusammenfassung	iii
Nomenclature	v
1. Introduction	1
1.1. Motivation	1
1.2. Thesis Scope and Organization	3
1.3. Main contributions	4
2. Magnetic Resonance System	7
2.1. Introduction	7
2.2. Fundamentals of Magnetic Resonance	7
2.3. The MRI Scanner	11
2.3.1. The magnet	11
2.3.2. The gradient coils	13
2.3.3. The RF transmitter	13
2.3.4. The RF receiver	14
2.4. Magnetic Resonance Imaging (MRI)	22
2.4.1. Spatial Encoding	22
2.4.2. Imaging Sequences	23
2.4.3. Image Construction	26
2.5. MR Phased Arrays	28
2.5.1. Overview	28
2.5.2. Pros and Cons	31
2.5.3. State of The Art	32
2.6. Summary	35
3. Frequency Division Multiplexer	39
3.1. Introduction	39

3.2.	The low-noise amplifier	42
3.2.1.	Common-Source LNA	43
3.2.2.	Common-Gate Common-Source LNA	45
3.3.	The Frequency Mixer	50
3.3.1.	Double-balanced Gilbert Mixer	51
3.4.	The Bandpass Filter	55
3.5.	The Operational Amplifier	58
3.6.	Additional Elements	61
3.6.1.	Inter-stage Buffers	62
3.6.2.	Biasing Circuits	62
3.7.	Layout	63
3.8.	Summary	65
4.	Simulation of The MR Receiver	67
4.1.	Introduction	67
4.2.	Generating Coil FID Signals from MR Images	68
4.3.	Image Reconstruction from Coil Signals	70
4.4.	Simulation of 8-Channel FDM	75
4.4.1.	Effect of LO Phase Noise	79
4.4.2.	Channel Linearity	79
4.5.	New Receiver Architecture	80
4.5.1.	Circuit Diagram	80
4.5.2.	Simulation Results	81
4.6.	Summary	83
5.	Fabrication and Measurements	89
5.1.	Measurements at $B_0 \approx 0$	90
5.1.1.	LNA	90
5.1.2.	The Mixer	90
5.1.3.	The Bandpass Filter	91
5.1.4.	Entire Channel Measurement	92
5.1.5.	Chip Heating	95
5.2.	Measurements at $B_0 = 11.7$ T	95
5.3.	Experiment in 11.7 T Spectrometer	98
5.3.1.	MRS of Water	98
5.3.2.	MRS of Sugar	101
5.4.	Experiment in 9.4 T Spectrometer	101
5.4.1.	Single Pulse Experiment	103

5.4.2. Imaging Experiment	104
6. New Fully Integrated Receiver Architecture	113
6.1. Introduction	113
6.2. Sigma-Delta ADC	115
6.2.1. Working Principle	115
6.2.2. First-order $\Sigma\Delta$ ADC	117
6.2.3. Higher-order $\Sigma\Delta$ ADCs	118
6.3. System-Level Verification of the Proposed MRI Receiver	120
6.3.1. Sigma-Delta ADC	122
6.3.2. Simulation Results	122
6.4. Circuit-Level Implementation of the Proposed MRI Receiver	125
6.4.1. Simulation Results	128
6.5. Summary	129
7. Conclusion and Outlook	131
7.1. CMOS Frequency Division Multiplexer	131
7.2. New Simulation Method for MR Circuits Characterization	132
7.3. New Fully Integrated MR Receiver	133
A. Appendix	135
A.1. Ocean Script Example	135
B. Appendix	139
B.1. UHFLI Run Script	139
B.2. Image Reconstruction Script	141
Bibliography	143
Acknowledgments	165

1. Introduction

1.1. Motivation

Since the time they were first introduced, the concepts of magnetic resonance imaging (MRI) and magnetic resonance spectroscopy (MRS) have found their way in a wide variety of applications. Such applications comprise, in case of MRI, the medical diagnosis and investigation of tumors [66, 75], bleeding, and infection. While, in the case of MRS, the major applications are found in chemistry to study the various properties of atoms and molecules, and in structural biology to study the proteins and the nucleic acids [15, 20, 95, 99]. As a result, there has always been a non stopping demand for developments and enhancements in all relevant aspects including theory, methodology, hardware, and software.

Generally speaking, an MRI or MRS system is built up from a number of major parts that include:

- The magnet in which the sample under investigation is placed.
- An RF transmission coil that generates RF power so as to excite the magnetization within the sample.
- An RF reception coil that detects the energy released from the sample as MR signals.
- An RF transceiver that provides the RF exciting signals and receives the MR signals.
- A software that controls the MR experiment and processes the resulting MR signals.

An example for the development of the hardware for MRI or MRS systems is the use of phased arrays of reception coils [89]. According to this concept, multiple reception coils are employed to simultaneously detect the MR signals. The coils within the array are typically decoupled, i.e., they have no mutual interaction, therefore each can pick different MR signals from the sample. By processing the signals from all the coils, considerable advances in performance can be achieved. Such advances include an increased SNR and resolution [62, 107], a larger field of view, or a decreased scan time [92, 108]. These great advantages of phased arrays made them a fundamental concept applied in almost all commercial scanners. On the other hand however, utilizing phased arrays of reception coils necessitates more cables to carry the MR signals and more RF receivers to process

these signals simultaneously. Thus leading to increased cost, size, and complexity of the MR system, which scale with the number of coils in the array, and hence make receive arrays with massive number (>256 for example) of coils virtually impossible (commercial scanners have a maximum of 108 channels, while the research ones have up to 128 channels with 128 separate receivers).

With this prefatory introduction, the need to develop innovative solutions and ideas with which to overcome the stumbling blocks that prevent having phased arrays with large numbers of coils has become obvious. Figure 1.1 epitomizes the goal this thesis aims to achieve. The image on the left side displays a head imaging 96-coil array with 96 preamplifiers. What is not shown in the image, are the 96 cables that carry the MR signals to the RF receivers (normally the receivers are few meters away from the array), and the 96 RF receivers that process the MR signals. The reader can therefore imagine how complex, costly, and bulky such a system is. As such, the required solution has to

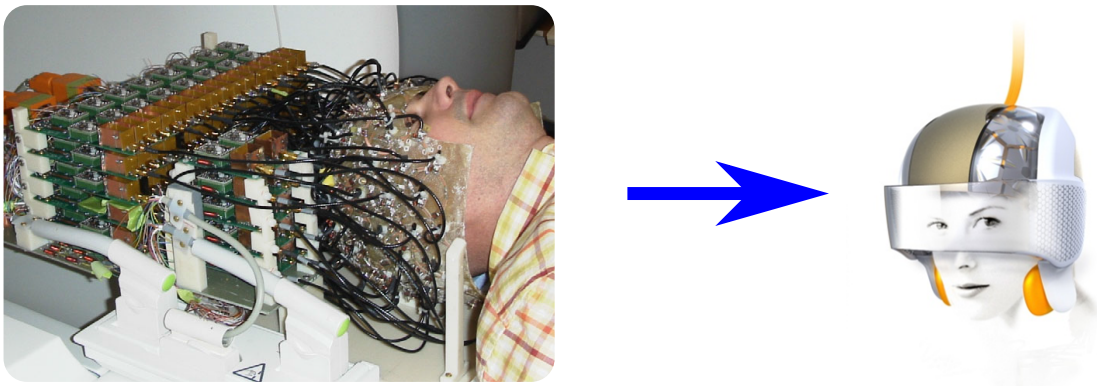


Figure 1.1.: Description of the main target of the thesis which is to find a remedy to the cost, size, and complexity issues associated with MR phased arrays. (left) 96-coils array with preamplifiers for head imaging [106]. The RF receivers are not shown in the image. (Right) Figurative plot of the imagined solution intended to replace the array in the left image.

address two main hypotheses which are:

1. Replacing the bulky electronics interfaces of commercial systems with CMOS integrated circuits. In fact the CMOS integrated electronics provided amazing solutions which found their way in many different applications, especially the ones where the space is extremely limited. However, in magnetic resonance imaging CMOS is still in its infancy, which means that MRI is a very attractive new field in which the power of CMOS technology can be applied.

2. Reducing the number of coaxial cables by applying signal multiplexing. The same argument of the previous hypothesis applies here. The signals multiplexing techniques (frequency or time multiplexing) have been extensively applied in all kinds of today's communications systems. However, in MRI, which is basically a kind of communications system, such techniques are rarely found. Again, this shows that MRI is also a new attractive field for signals multiplexing techniques.

According to these hypotheses, the solution intended to interface MR phased arrays should consider a number of issues of which the following points are the most important:

- Compatibility with commercial MR systems.
- Operation in high magnetic fields.

This means that the desired MR interface has to be compatible with the commercial MR systems with no or minor hardware and the software changes. Moreover, it has to be applicable to different MR imaging and spectroscopy systems available with various magnetic field strengths. Besides, it must exhibit a robust and stable operation in high magnetic fields. Previous reports on integrated CMOS electronics in a 7 T magnetic field showed normal operation and recorded no remarkable influence of the field on the performance [6, 7, 17]. Moreover, an elaborate study of the effects of high magnetic fields on CMOS transistors, introduced by Höfflin et al. [47], showed very slight influence of the magnetic field (up to 11.7 T) on the drain-source current I_{DS} as well as the channel resistance R_{DS} when the transistor operates in the saturation region irrespective of the orientation with respect to the direction of the magnetic field.

1.2. Thesis Scope and Organization

This thesis is organized as follows:

- Chapter 2 establishes a theoretical background that explains a number of concepts which are continuously referred to by subsequent chapters. First, it gives a glance at the fundamentals of magnetic resonance (MR) and the physics behind the MR signals. Then, it briefly introduces the various hardware components of a standard MR system. The overview of the MR system is followed by a detailed description of the MR receiver whose development is the main target of the thesis. After that, the concept of MR phased receive-only arrays is discussed, and the advantages and drawbacks of these arrays are highlighted. Finally, glimpses on the state of art solutions to the challenges associated with these arrays are given.

- Chapter 3 introduces an 8-channel CMOS FDM as a novel solution to the size, cost, and complexity issues related to the MR phased arrays. It describes in detail the design of every component of the multiplexer, and shows its simulation results including gain, s-parameters, noise, and linearity.
- Chapter 4 presents a novel simulation toolbox that allows testing and characterizing the MR receiver's hardware via performing virtual MR imaging experiments. The chapter describes how the MR reception coil's signals are reconstructed, and used as inputs to simulate various MR circuits so as to verify their functionality.
- Chapter 5 discusses the fabrication of the CMOS FDM introduced in chapter 3. It shows the measurements results of the various parts of the FDM. Moreover, it investigates the influence of the high magnetic field (11.7 T) on the performance of the chip. Finally, it exhibits the results of using the chip in spectroscopy and imaging experiments in 11.7 T and 9.4 T scanners respectively, and compares them with the corresponding results obtained from the commercial systems.
- A new fully integrated MR receiver is described in chapter 6. First, the chapter explores the technical limitations of the CMOS FDM introduced in chapter 3. With this preliminary done, the chapter highlights the advantages of the new proposed receiver which can make it superior to the CMOS FDM. After that, a system-level implementation of the new receiver is described, and the simulation results are depicted. Finally, a circuit-level implementation with ample description of the circuit components and simulation results is introduced.
- Finally, chapter 7 provides a brief summary of the entire thesis. It also gives a future outlook.

1.3. Main contributions

The main contributions of this thesis to the field, which led to three (two published and one submitted) journal papers, can be summarized as:

- Design, implementation, and test of an eight-channel CMOS frequency division multiplexer as an optimum solution to the size and complexity issues associated with MRI arrays. This FDM is intended mainly for systems operating at 400 MHz [56, 58].
- Development of a novel Matlab-Cadence software toolbox that enables the test and characterization of the MRI electronic circuitry via a transistor-level simulation of

the MRI experiment [59]. Although this new simulation method is not expected to replace the conventional characterization methods, it is strongly believed that it will be a significant addition which will facilitate testing and debugging MRI electronics before fabrication, thus reducing the cost of iterations.

- Design of a fully integrated CMOS MRI receiver that incorporates the signal conditioning analog blocks as well as the analog-to-digital conversion (ADC) [57]. This new receiver is designed to avoid all of the technical limitations that might restrict the CMOS FDM. Therefore, it is expected to provide a paradigm shift to the field of parallel imaging, resulting in an incredibly compact MRI system, with substantially higher resolution, less imaging time, higher throughput, and fewer components.

2. Magnetic Resonance System

2.1. Introduction

The concept of Nuclear Magnetic Resonance (NMR) was first described and measured in 1938 by Isidor Radi [85], who was later awarded the Nobel prize. Since then, NMR has found its way into a very wide range of applications. These applications can be divided into two main categories, namely, the NMR spectroscopy (also known as magnetic resonance spectroscopy MRS) and the Magnetic Resonance Imaging (MRI) which was introduced for the first time by Paul Lauterbur [67] in 1973. NMR spectroscopy is extensively used in biology, chemistry, and biochemistry to investigate molecular physics, crystals, and non-crystalline materials. Typical samples of NMR spectroscopy range from simple compounds that can be analyzed via 1-dimensional spectroscopy [29] to complex proteins that need 3-dimensional [60] spectroscopy. On the other hand, MRI is an imaging technique that has been very widely exploited in medicine for diagnoses because of its ability to image soft and hard tissues. It is a non-invasive imaging technique that is based on exciting the sample using Radio Frequency (RF) signals. Moreover, it is a non-ionizing technique which makes it superior to Computed Tomography (CT) that utilizes x-ray radiation, leading to increased risk of cancer [1, 96].

2.2. Fundamentals of Magnetic Resonance

The literature is rich in books that explain the theory and fundamentals of magnetic resonance. Examples of these books are found in [27, 61, 70]. In principle, the NMR is based on the intrinsic quantum property of the atomic nuclei that is called the *spin*. The spin can be thought of as a form of the angular momentum. However, it is not generated by the rotation of the particle, but it is an intrinsic property that does not vanish even at the absolute zero temperature. The spin of a nucleus is formed by the spins of its constituting protons and neutrons (nucleons). It has a quantum number called the spin quantum number and usually denoted by I . This number is of great importance in NMR, since the nuclei with $I \neq 0$ (e.g. ^1H and ^{13}C) are detectable by NMR, while the ones with $I = 0$ are invisible to NMR. Due to the spin property, the nucleus has a magnetic moment

$\hat{\mu}$ and a spin angular momentum \hat{S} [70]. The ratio $\hat{\mu}/\hat{S}$ is called the *gyromagnetic ratio* γ which is, in turn, an intrinsic property of the nucleus. The gyromagnetic ratio can have either sign (positive or negative) depending on the alignment of $\hat{\mu}$ with respect to \hat{S} . Thus when $\hat{\mu}$ is parallel to \hat{S} , then γ is positive, while it has a negative value when the magnetic moment and the angular momentum are anti-parallel as shown in figure 2.1.

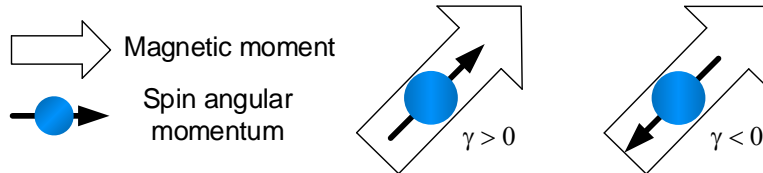


Figure 2.1.: Dependence of the sign of the gyromagnetic ratio *gamma* on the alignment of $\hat{\mu}$ with respect to \hat{S} .

The direction of the spin angular momentum \hat{S} is referred to as the *spin polarization axis* and it may point in all possible directions. Once the nucleus is placed in a magnetic field \mathbf{B}_0 , that is conventionally pointing in the z-direction, then the net magnetic moment starts rotating around \mathbf{B}_0 and wandering towards a parallel alignment with \mathbf{B}_0 as illustrated in figure 2.2. This rotation is called *precessing* and the frequency with which the magnetic moments precess around \mathbf{B}_0 is called the *Larmor frequency* ω_0 . This frequency is directly proportional to the strength of \mathbf{B}_0 as described by the following equation

$$\omega_0 = -\gamma B_0 \quad (2.1)$$

Considering an ensemble of nuclei as in figure 2.3a; in the absence of a magnetic field, the magnetic moments of the nuclei are distributed randomly, thus they cancel each other and hence there will be no net magnetization of the sample in any direction. If a magnetic field B_0 is applied in the z-direction, then a portion of the magnetic moments (N_{up}) tends to achieve a parallel alignment to B_0 , while another portion of the magnetic moments (N_{down}) achieves an anti-parallel alignment with B_0 as depicted in figure 2.3b. In thermal equilibrium condition, the number of parallel and anti-parallel

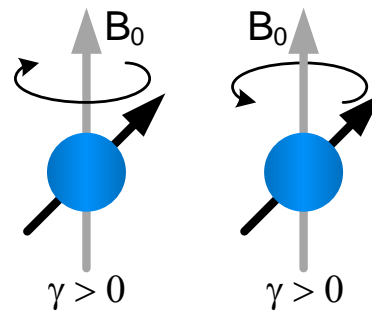


Figure 2.2.: Precessing of spin polarization axis around \mathbf{B}_0 . The direction of the precessing depends on the sign of γ .

magnetic moments is determined by a *Boltzmann distribution*

$$\frac{N_{up}}{N_{down}} = e^{-\left(\frac{\hbar\omega_0}{k_B T}\right)} \quad (2.2)$$

The difference between N_{up} and N_{down} results in a net magnetization M_0 in the z-direction called the *longitudinal magnetization*, while the magnetization in the xy-plane M_{xy} (transverse magnetization) remains zero in this case. The net magnetization M_0 is of great significance in NMR since it is the portion of the magnetic moments which can generate the magnetic resonance (MR) signals. Therefore, in order to increase the amplitude of the MR signals, one can either utilize a stronger magnetic field or decrease the temperature of the sample as it is stated in equation 2.2. Considering the case of figure 2.3b, where a net

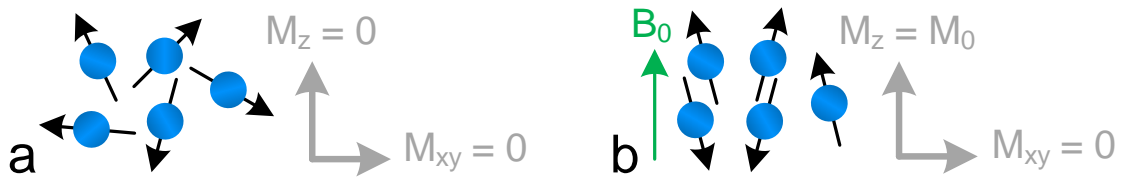


Figure 2.3.: Effect of applying an external magnetic field B_0 on the magnetic moments of an ensemble of nuclei. (a) No field is applied. The randomly distributed magnetic moments cancel each other and hence the net magnetization (longitudinal and transverse) is zero. (b) A magnetic field B_0 is applied in the z-direction. A net longitudinal magnetization M_0 is formed due to the difference between the parallel and antiparallel magnetic moments. The transverse magnetization M_{xy} is zero.

magnetization M_0 is formed due to B_0 . If a Radio Frequency (RF) pulse that generates an oscillating magnetic field B_1 with frequency ω_0 is applied to the sample, the magnetization M_0 will be flipped with an angle α towards the xy-plane. The value of the flip-angle α is directly proportional to both B_1 and the duration of the RF pulse τ according to the following equation

$$\alpha = \gamma B_1 \tau \quad (2.3)$$

During the application of the RF pulse and over the passage of time, the longitudinal magnetization M_z decreases while the transverse magnetization M_{xy} increases. If a flip-angle of 90° is reached, then M_z reaches zero and M_{xy} achieves its maximum (M_0). This effect of exciting the sample with an RF pulse is illustrated in figure 2.4.

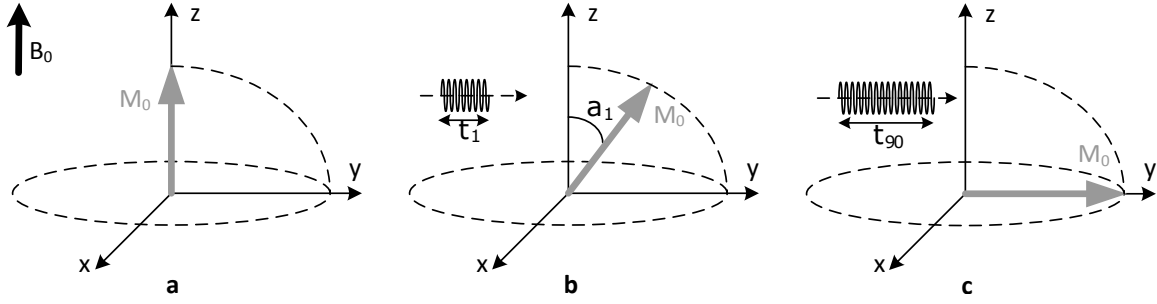


Figure 2.4.: Effect of applying an RF excitation pulse on the magnetization of a sample. (a) No RF pulse is applied. In this case $M_z = M_0$ and $M_{xy} = 0$. (b) Applying an RF pulse with duration τ_1 results in a tilt of the magnetization by a flip angle α_1 . In this case $M_z = M_0 \cos \alpha$ and $M_{xy} = M_0 \sin \alpha$. (c) A 90° pulse is utilized resulting in $M_z = 0$ and $M_{xy} = M_0$.

If the RF pulse is turned off, the magnetic moments of the nuclei and the corresponding net magnetization M_0 continue precessing around B_0 with the Larmor frequency ω_0 . Simultaneously, M_0 starts tilting back towards parallel alignment with B_0 towards the thermal equilibrium condition it had before the RF excitation. This effect is shown in figure 2.5a. In this case the longitudinal magnetization M_z increases while the transverse magnetization M_{xy} decays as illustrated in figure 2.5b. The time it takes M_z to recover 63 % of M_0 is called T_1 (*spin-lattice relaxation time*). During the precession of the magnetic moments around B_0 , they accumulate very slight frequency differences which are mainly due to the inhomogeneities of the magnetic field. These differences in frequency cause phase incoherence between the magnetic moments which, in turn, leads to the transverse magnetization decay. This decay is characterized by T_2 (*spin-spin relaxation time*) that represent the time over which M_{xy} decays to 37 % of M_0 . The following equations describe M_z and M_{xy} after the RF pulse is turned off.

$$M_z = M_0 \cdot \left(1 - \exp\left(-\frac{t}{T_1}\right)\right) \quad (2.4)$$

$$M_{xy} = M_{xy}(0) \cdot \exp\left(-\frac{t}{T_2}\right) \quad (2.5)$$

If a coil, with a magnetic field perpendicular to the B_0 , is placed close enough to the sample as it is depicted figure 2.5c, then the precessing net magnetization of the sample generates an induced voltage in the coil according to **Faraday's law**. This voltage will be a sinusoid with a frequency ω_0 and it will be decaying according to the decay of M_{xy} . This is the MR signal and it is conventionally referred to as the Free Induction Decay (FID).

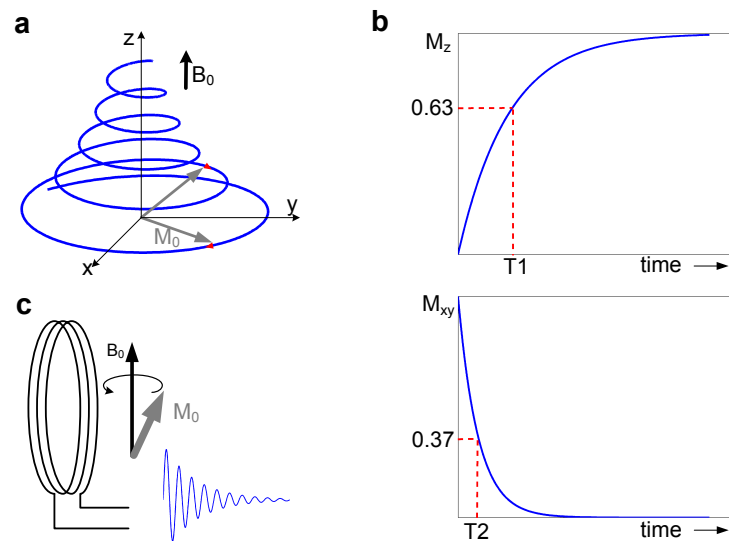


Figure 2.5.: Behavior of the magnetization after being excited with 90° pulse. (a) After turning off the RF pulse, M_0 starts tilting towards B_0 while precessing with the Larmor frequency ω_0 . (b) Recovery of M_z and decay of M_{xy} over time. (c) The precessing magnetic moments induce an electrical current in a coil that is close enough to the sample. The signal generated in the coil is the MR FID which is basically a decaying sinusoid with frequency ω_0 .

2.3. The MRI Scanner

Figure 2.6 shows the block diagram of a typical MRI scanner. The block diagram of a spectrometer is more or less the same as the one in figure 2.6 except for the gradient coils which are generally not needed in the MRS experiments. However, the gradient coils may be employed in voxel-based MRS experiments. Therefore, the MRI scanner can, in principle, be used to conduct NMR spectroscopy experiments. The different blocks and components of the MRI scanner can be briefly described as follows:

2.3.1. The magnet

This is responsible for generating the static magnetic field B_0 so as to align the magnetic moments of the nuclei of the sample, thus produce a net magnetization in it. For high resolution NMR experiments, the B_0 has to be extremely homogeneous with 1 ppb (part per billion) variation. Furthermore, the magnet must maintain the homogeneity over the entire sample volume. Within the homogeneous field, all the magnetic moments of the desired nuclei precess with approximately identical phases and Larmor frequencies. Thus their MR signals add up and produce a total MR signal with high amplitude. Nowadays, most of

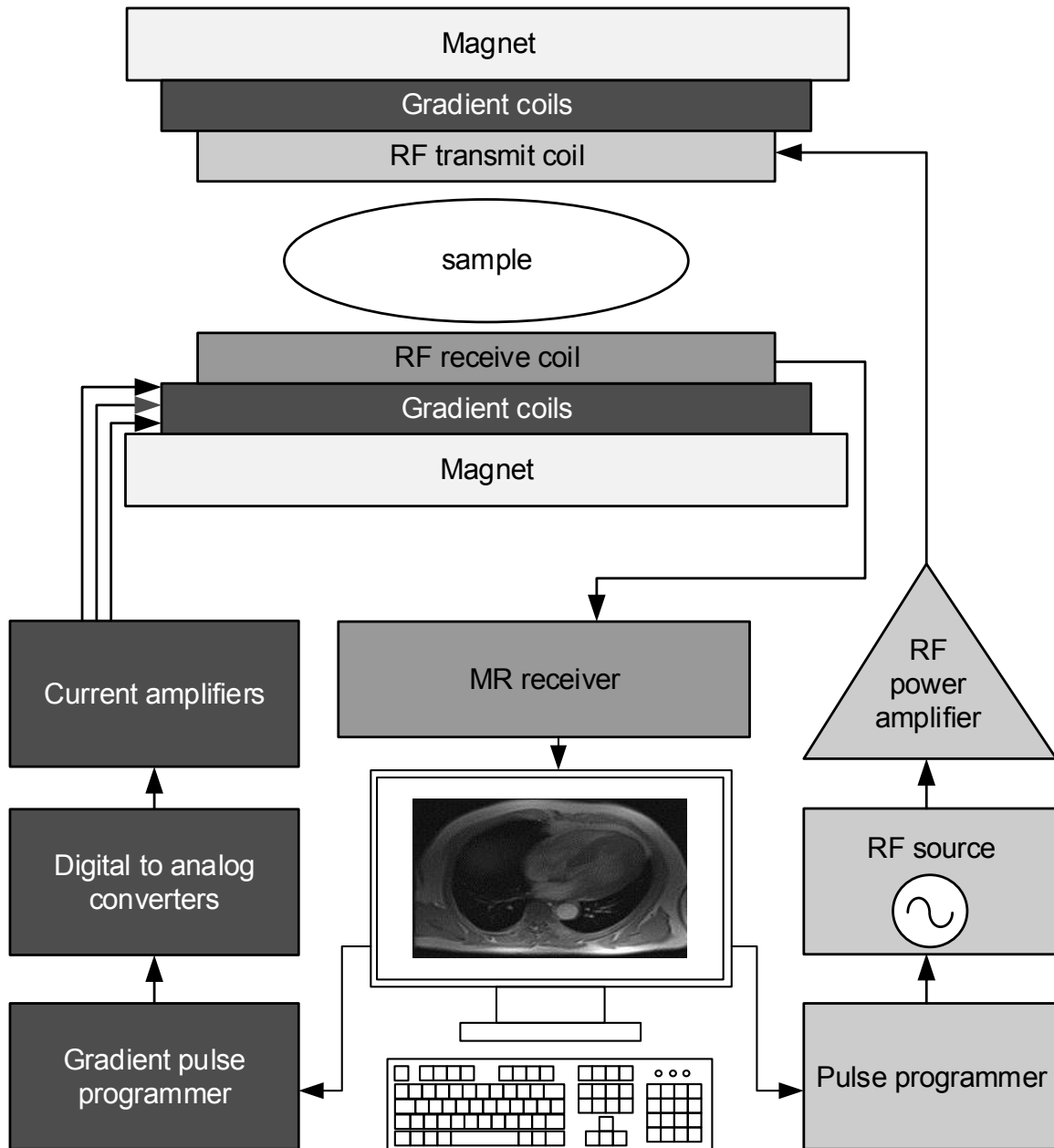


Figure 2.6.: Block diagram of a typical magnetic resonance imaging scanner.

the scanners employ superconducting magnets which can achieve very homogeneous and high (today's commercially-available spectrometers can have up to 22.3 T) magnetic fields.

2.3.2. The gradient coils

These coils are particularly used to produce an MR image by *spatially-encoding* the MR signals. They introduce slight and well-controlled magnetic field gradients to B_0 in all axes. Therefore, there are typically three gradient coils that generate gradient magnetic fields along x, y, and z-axes. They comprise the Frequency Encoding Gradient (FEG), the Phase Encoding Gradient (PEG), and the Slice-Select Gradient (SSG). The driving circuit of the gradient coils is illustrated in figure 2.6. It consists of a pulse programmer, a digital-to-analog converter (DAC), and a current amplifier. With all gradients applied, the MR signals from each voxel of the sample will possess a unique frequency-phase combination.

2.3.3. The RF transmitter

As the name suggests, this part of the scanner is responsible for flipping the net magnetization M_0 of the sample by irradiating it with RF waves. Therefore, the transmitter section consists of an RF coil (*transmit coil*) that is tuned to resonate at the desired frequency. RF synthesizers are usually employed to generate the excitation signals. They can provide extremely precise and low phase-noise signals. The angle α , by which M_0 is flipped, is controlled by varying the duration τ of the applied RF signal which is, in turn, controlled by a very fast switch called the *pulse gate*. This switch as well as the phase shift of the synthesizer's output are controlled by the pulse programmer as depicted in figure 2.6. Finally, the gated signals, plotted in figure 2.7, is amplified so as to excite all the magnetic moments in the sample. This amplification is accomplished by means of a power amplifier which, in typical scanners, can provide up to 1 kW of power.

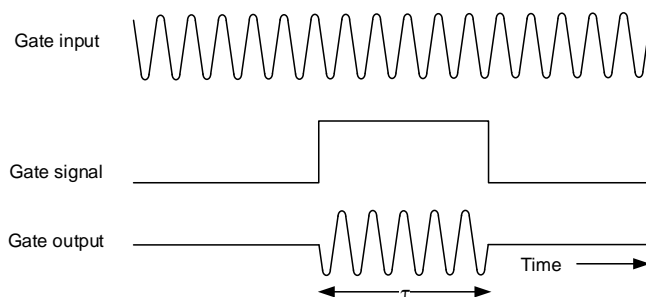


Figure 2.7: Controlling the RF pulse duration τ and inherently the flip angle α by a gating signal.

2.3.4. The RF receiver

After switching off the RF excitation pulse, the sample releases the absorbed energy. An RF receive coil, close to the sample, collects this energy and produces an electrical signal representing the MR signal. The detection of the MR signals can be accomplished by a separate receive-only RF coil, or by using the RF transmit coil as a transmit/receive coil. In this case, the use of an RF switch is mandatory to switch between the transmit phase and the receive phase, otherwise the high power of the RF transmit signals can cause severe damage to the electronic circuitry of the receive chain. Figure 2.8 shows the block diagram of a typical receive chain of the magnetic resonance scanner [18, 48]. A detailed description of the individual elements of this chain can be found in the next subsections.

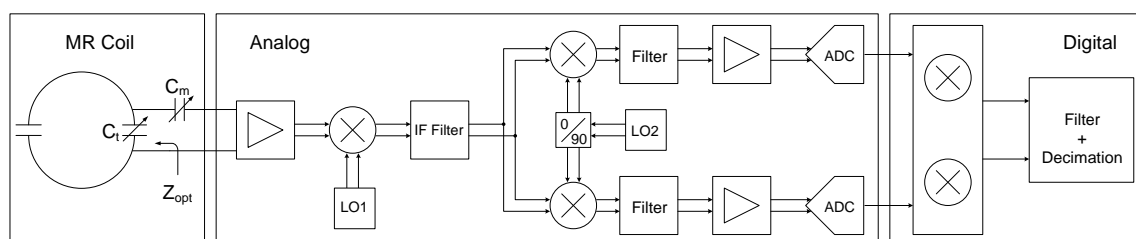


Figure 2.8.: Block diagram of a typical receive chain in the magnetic resonance scanner.

2.3.4.1. The Receiving Coil

The receive coil is the first fundamental element in the MR receiver. The design and optimization of the receive coils requires a great attention since they have to detect the weak MR signal which is being emitted from the sample. Numerous papers were published to investigate the design and optimization of these coils for numerous applications [26, 74, 103]. Therefore, there is a broad variety of coil types (brain coils [107], cardiac coils [92]) and sizes ranging from macro to micro coils [9, 31, 79, 80]. However, the MR receive coils are generally categorized as either surface coils or volume coils. Examples for a surface and a volume coils are shown in figure 2.9. As it can be seen from this figure, the MR

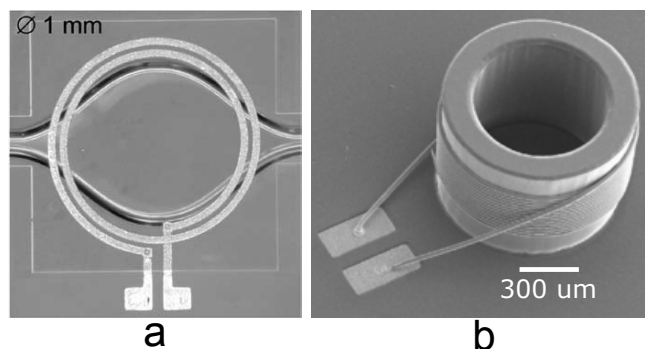


Figure 2.9: Different types of MR coils. (a) Example of an MR surface coil [72]. (b) MR volume coil example [65].

coil is typically an inductor whose magnetic field B_1 can be calculated at any point, with position vector \mathbf{r} , using the Biot-Savart law demonstrated by equation 2.6:

$$\mathbf{B}(\mathbf{r}) = \frac{\mu_0}{4\pi} \int_C \frac{I d\mathbf{l} \times \mathbf{r}}{|\mathbf{r}|^3} \quad (2.6)$$

where μ_0 is the permeability and I is the current. Nevertheless, the MR coil is a non-ideal inductor with impedance $Z_c = r_c + jX_c$, where r_c is the intrinsic resistance of the coil which is usually a fraction of Ohm up to few Ohms. In order to achieve maximum power transfer from the coil to the preamplifier, the coil impedance has to match the input impedance of the preamplifier (50 Ω standard in MRI spectrometers) [48]. Moreover, this impedance match allows to minimize the noise figure of the preamplifier [87]. A parallel resonance configuration, as illustrated in figure 2.10a, can readily achieve the 50 Ω match [74]. This circuit employs two capacitors C_t (tuning) and C_m (matching) so as to tune and match the coil impedance to 50 Ω . To understand how the tuning and match is performed, let us assume that the coil inductance is $L_c = 40$ nH and its parasitic resistance $r_c = 1.5$ Ω , and the coil is planned to operate in a 9.4 T scanner that corresponds to $\omega_0 = 400$ MHz for the ^1H protons. When the tuning capacitor C_t is added then the circuit will have a resonance frequency ω_r that can be determined from the following equation:

$$\omega_r = \sqrt{\frac{1}{L_c C_t} - \frac{r_c^2}{L_c^2}} \quad (2.7)$$

Figure 2.10b plots the real and imaginary parts of the circuit impedance Z_{s1} with only C_t added. It can be seen from this figure that the real part of Z_{s1} touches the 50 Ω at two frequencies. These are ω_1 which is less than ω_r and the circuit in this case is inductive, while the second frequency is ω_2 which is greater than ω_r and the circuit at this frequency is capacitive. Therefore, in order to tune the coil, the value of C_t is chosen such that $\omega_0 = \omega_1$ or $\omega_0 = \omega_2$. In this case, it is more favorable to choose C_t such that $\omega_0 = \omega_1$ because the circuit at this frequency is inductive and, therefore, Z_{s1} can be easily matched to 50 Ω by using a trimmer capacitor C_m which is easier to secure than a trimmer inductor. Figure 2.10c depicts the real and imaginary parts of source impedance of the coil Z_s when both the tuning and matching capacitors are included and adjusted. In this case $\Re(Z_s) = 50$ Ω and $\Im(Z_s) = 0$ Ω at $\omega_0 = 400$ MHz. The input reflection coefficient S_{11} , defined as the reflected power divided by the incident power, of the tuned and matched circuit is plotted in figure 2.10d, from which it can be seen that the 50 Ω match condition achieves maximum power transfer from the MR coil to the preamplifier, since the power reflected from the preamplifier back to the coil is extremely minimized.

Another important parameter relevant to the MR coil is the voltage level of the induced

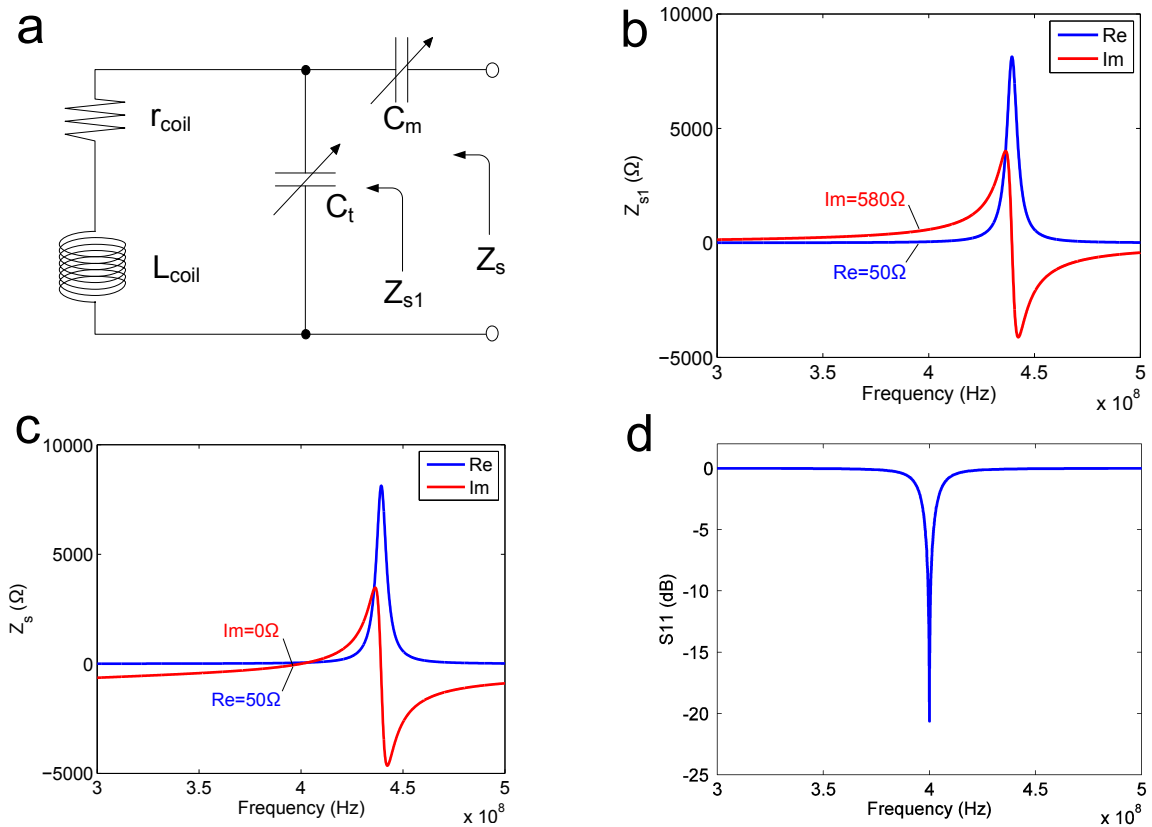


Figure 2.10.: Tuning and matching the MR coil to $50\ \Omega$ at 400 MHz. (a) Circuit schematic showing the coil in parallel with the tuning capacitor C_t and in series with the matching capacitor C_m . (b) Real and imaginary part of the circuit impedance Z_{s1} with only C_t . (c) Real and imaginary parts of Z_s when both C_t and C_m are connected. (d) The input reflection coefficient S_{11} of the circuit.

MR signal in the RF receive coil. This voltage is determined by equation 2.8 [49].

$$V_{signal} = K\omega_0(B_1)_{xy}M_0V_s \cos(\omega_0 t) \quad (2.8)$$

In this equation, K is a scalar inhomogeneity factor, B_1 is the magnitude of the transverse magnetic field for a unit current in the receive coil, M_0 is the net magnetization of the sample, and V_s is the sample volume. The magnetization of a homogeneous sample can be calculated by the following equation:

$$M_0 = \frac{N\gamma^2\hbar^2 I(I+1)B_0}{3kT_s} \quad (2.9)$$

where N is the number of spins per unit volume, γ is the gyromagnetic ratio ($42.576 \text{ MHz T}^{-1}$ for ^1H protons), \hbar is the reduced Planck's constant, I is the spin quantum number, k is the Boltzmann constant, T_s is the sample temperature in Kelvin. The MR coil noise is described by the following equation:

$$V_{noise} = \sqrt{4kT_c\Delta f R} \quad (2.10)$$

where T_c is the coil temperature in Kelvin, Δf is the bandwidth of the receiver in Hz, and R is the AC electrical resistance of the coil including the skin and proximity effects. This noise is commonly called *Johnson noise* [54, 78]. From the previous equations it can be noticed that the voltage level of the MR signal, and thus the signal-to-noise ratio (SNR), can be boosted by:

- Utilizing a higher static magnetic field B_0 , where the signal voltage increases quadratically with B_0 . In this case the increase in SNR will be at the expense of increased cost of the scanner.
- Using more efficient receive coils with higher and more homogeneous B_1 field.
- Increasing, if possible, the sample volume V_s which inherently augments the number of spins.
- Decreasing the temperature of the sample, however in many cases, especially the living samples, this will not be a feasible solution.

Moreover, the SNR of the detected MR signals can be further enhanced by lowering the noise level in the coil through decreasing its resistance. Therefore, the optimized MR coil is the one which can provide high and more homogeneous time varying magnetic field B_1 with extremely low AC resistance.

2.3.4.2. The Low-Noise Amplifier (LNA)

The low-noise amplifier (LNA) is the first element in the electronics chain of the MR receiver. It has a very essential role in the performance of the receiver, since it is the first

element to handle the low-level MR signals coming from the receive coil. It mainly has to prepare the MR signals so that they can drive the succeeding blocks in the receiver chain such as the mixer, the filter, and the analog-to-digital convert (ADC). Therefore, the LNA is usually designed and optimized so as to boost the voltage level of the MR signals while maintaining the SNR by adding as little noise as possible. Many considerations need to be addressed during the design of the LNA. Nonetheless, the following points require great attention:

- The Noise Figure:

Just like any other active signal processing circuit, the LNA adds undesired noise to the MR signals. This noise exhibits a constant spectral power (white noise) over the frequency range of the vast majority of RF circuits. However, at low frequencies (from 0 Hz to few kilo Hz) the noise shows inverse proportionality with the frequency f . Figure 2.11 shows a block diagram of an RF receiver that comprises several elements with the i -th element having F_i noise factor and G_i gain. The total noise factor for this receiver can be determined by Friis' formula as follows [30]:

$$F_{total} = F_1 + \frac{F_2 - 1}{G_1} + \frac{F_3 - 1}{G_1 G_2} + \frac{F_4 - 1}{G_1 G_2 G_3} + \dots \quad (2.11)$$

According to this formula if the LNA has a high gain, then the noise performance of the entire receiver chain is dominated by the noise contribution from the LNA. Therefore, for a high quality MR receiver, it is necessary to design a LNA with high gain and low noise figure. However, one has to be careful when increasing the gain of the LNA because the higher the LNA gain the more pronounced is the nonlinearity of the subsequent stages of the receiver. Nevertheless, a fair compromise between high gain and high linearity is usually feasible.

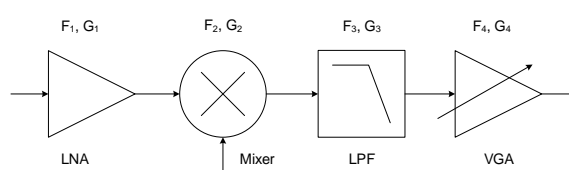


Figure 2.11.: The total noise figure of a receiver chain consisting of a LNA followed by different signal processing blocks.

- The Input Matching:

The interface between the LNA and the antenna (the receive coil in our case) has always been a critical issue that needs a lot of consideration from the RF and microwave engineers. The reason for that is the fact that the interface differs

according to the intended objective of the amplifier. For example, in case the LNA is expected to operate as a voltage amplifier, then it should be designed in a way such that its input impedance is ideally infinite. On the other hand, if it is required to amplify the power of the signal, then conjugate matching between the LNA and the antenna is needed. In the case of MR systems, the detection coil is usually connected to the LNA via a coaxial cable, therefore it is common to match the input impedance of the amplifier to the characteristic impedance of the cable Z_0 which is in most of the cases 50Ω .

2.3.4.3. The Frequency Mixer

After the MR signals have been amplified by the LNA, they are introduced to a frequency conversion (mixing). This frequency conversion is performed by a device called the frequency mixer, which typically has three ports. These are namely: the **RF** (radio frequency) port to which the MR signals coming from the LNA are applied, the **LO** port to which the local oscillator frequency is introduced, and the **IF** (intermediate frequency) port from which the mixing output is obtained. Basically the frequency mixers perform a multiplication of the RF and the LO signals. Thus if the RF is centered at frequency f_{RF} and the LO signal is a sinusoid with frequency f_{LO} , then the IF output will contain two frequency-shifted versions (sidebands) of the RF signal at frequencies $(f_{LO} - f_{RF})$ and $(f_{LO} + f_{RF})$ as illustrated in figure 2.12. As such, mixers can be used either to up-convert the signals (as it is the case in RF and MR transmitters) or to down-convert the signals (as it is the case in RF and MR receivers). In MR receivers the frequency mixers are employed to down-convert the MR signals from the high Larmor frequency ω_0 (for example, 400 MHz for ^1H in a 9.4 T magnetic field) to a baseband frequency. This frequency conversion is essential because processing the MR signals at high frequency is extremely difficult and costly, while at the baseband frequency it is much easier and less costly. For example, at the baseband frequency, the variable gain amplifiers (VGA), which are much easier to realize at lower frequencies [48], can be employed. Moreover, at low frequencies the MR signals can be digitized with high resolution ($\geq 16 \text{ bits}$) and adequate oversampling ADCs, which are not easy to achieve at higher frequencies. There are three architectures which are common for frequency conversion:

- Direct Conversion:

This is also called homodyne or zero-IF architecture. In this frequency conversion scheme the LO signal employed has exactly the same frequency as the carrier (ω_0 in the MR receivers), thus the resulting IF signal will be centered at zero frequency and hence the name. The main advantages of this architecture comprise simplicity and integrability. Besides, the needed bandwidth of the signal is half compared

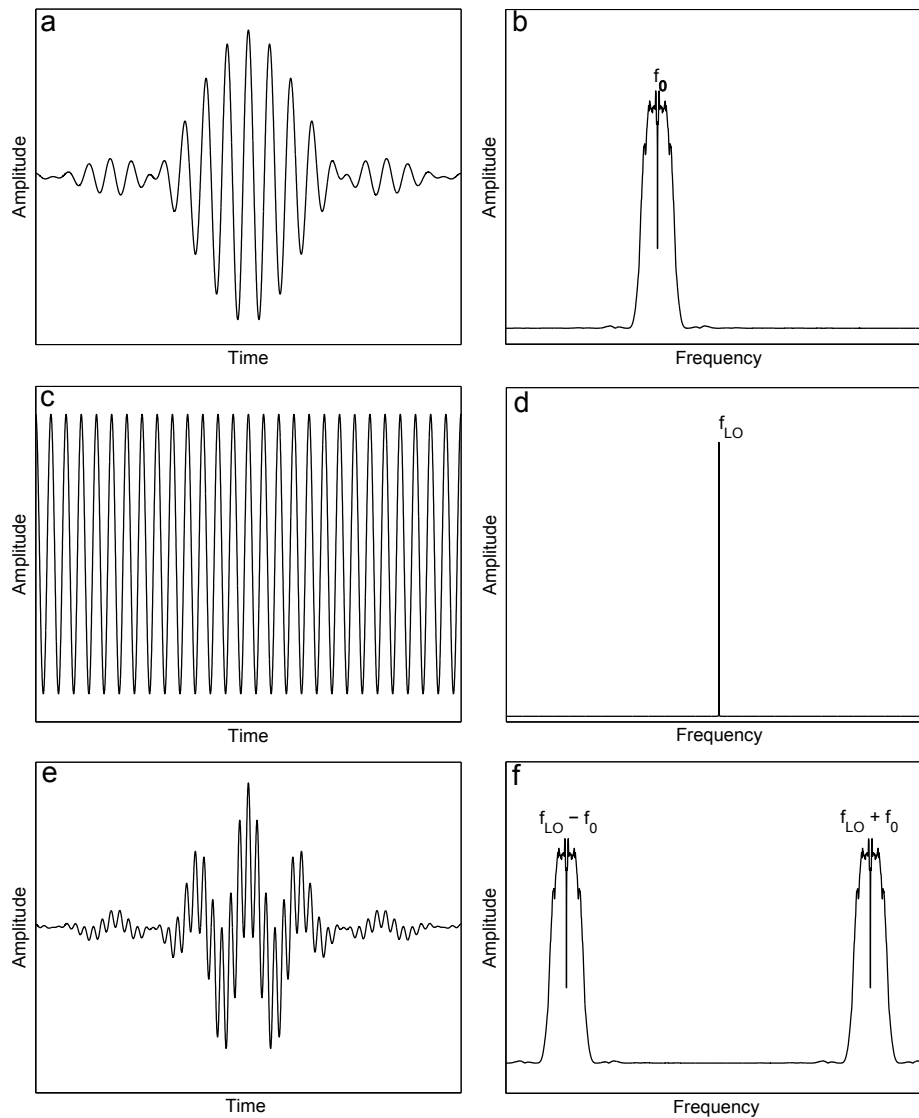


Figure 2.12.: Demonstration of the frequency mixing operation. (a) The RF signal in the time domain. (b) Fourier transform of the signal in (a). The RF signal is centered at f_0 . (c) The LO signal in the time domain. (d) Fourier transform of LO. (e) The IF signal (IF = RF x LO) in time domain. (f) Fourier transform of IF where the RF signal now is shifted to $(f_{LO} - f_0)$ and $(f_{LO} + f_0)$.

to the other conversion architectures. Furthermore, the homodyne scheme has a great benefit that it does not suffer from the frequency image problems [87], thus no image rejection filters are required. In spite of the aforementioned advantages, the homodyne architecture, however, encounters drawbacks such as the DC offsets and the flicker noise. The flicker noise can be tackled by increasing the area of the transistor, while the DC offsets can be compensated for via techniques such as AC coupling and DC cancellation [86, 87]. Unfortunately, these techniques necessitate increased cost.

- The Low-IF Conversion:

In this architecture, the desired RF signal is down-shifted to a low non-zero frequency (usually one or two orders of the channel's bandwidth). Therefore, it will not be vulnerable to the DC offsets and the flicker noise as it is the case in the homodyne receivers. However, this low-IF architecture suffers from the problem of RF image which, nevertheless, is not as severe as in the heterodyne architecture. Techniques such as the high-Q image-rejection and the quadrature demodulation with polyphase filtering can provide a remedy to the problem of signal image [13, 22]. However, in MRI applications the image rejection is not very crucial since there are usually no interferers at the image frequency of the desired MR signal, and hence it can be skipped. Unfortunately, the thermal noise at the image frequency is unavoidably added to the MR signal leading to a degradation in the noise figure by approximately 3 dB. This reveals a trade-off between better noise performance of the receiver circuit and the complexity of the system.

- Heterodyne Architecture:

Figure 2.8 shows an example of this architecture which is the most widely used in today's communications systems. In this scheme the desired RF signal is down-converted to a fixed intermediate frequency IF1, which is subsequently filtered and further shifted to another intermediate frequency IF2. The quadrature demodulation can be employed in the second mixing stage in order to obtain the in-phase I and quadrature Q components of the signal. The heterodyne receivers feature the same advantages that pertain the low-IF receiver such as avoiding the DC offsets and the flicker noise. However, this architecture suffers heavily from the image problem which makes the use of high-Q surface acoustic waves (SAW) filters irreplaceable. Nonetheless, using these filters makes the heterodyne receivers highly selective.

2.3.4.4. The Analog-to-Digital Convert (ADC)

After the received FID signals have been shifted to a low frequency band, they will be low-pass filtered so as to reject the higher sidebands and the out-of-band noise. Then they will be converted to the digital domain by means of high resolution (>12 bits) ADC. At this stage the digital MR signals are largely immune to noise and, in addition, the excellent computational power and speed of the digital signal processing [83] can be employed. For example, the signals can be further down-shifted to zero frequency and filtered using high quality digital filters. Moreover, the SNR of these signals can be enhanced by averaging the extra samples. Finally, the samples of the MR signals are used to fill a discrete k-space matrix, which is, in turn, transformed afterwards via a discrete Fast Fourier Transform (FFT) into the MR image. A detailed description on the k-space filling follows in the next section.

2.4. Magnetic Resonance Imaging (MRI)

2.4.1. Spatial Encoding

The imaging in magnetic resonance was first introduced by Paul Lauterbur in 1973 [67], and the principal idea was to superimpose gradient magnetic fields to B_0 . These gradient fields cause a well-defined variation in the homogeneity of the static magnetic field B_0 resulting in what is usually referred to as *spatial encoding* of the MR signals within the sample. The magnetic field of a scanner when linear gradient fields are applied can be described by one or combination of the following equations:

$$\mathbf{B} = (B_0 + G_x x)\mathbf{e}_z \quad (2.12)$$

$$\mathbf{B} = (B_0 + G_y y)\mathbf{e}_z \quad (2.13)$$

$$\mathbf{B} = (B_0 + G_z z)\mathbf{e}_z \quad (2.14)$$

where G_x , G_y , and G_z are the magnitude of the gradient with respect to x, y, and z-axes respectively. As mentioned in the previous section, there are typically three gradient fields. Namely, the slice select gradient *SSG*, the phase encoding gradient *PEG*, and the last one is the frequency encoding gradient *FEG*. They typically act along three different orthogonal axes and their concept can be explained as follows:

2.4.1.1. SSG

When this gradient is applied, the magnetic moments within the sample will be subjected to different magnetic field strengths and thus precess at different Larmor frequencies

according to their position on the axis of the gradient. Therefore, if an RF pulse, that contains a certain range of frequencies, is applied simultaneously with the SSG, then only the spins within a specific region of the sample will be excited as illustrated in figure 2.13b. This region is referred to as the *slice*. The RF excitation is usually a pulse-shaped sinc function whose FFT shows a range of frequencies and whose time-domain width, in conjunction with the strength of the SSG, defines the thickness of the slice.

2.4.1.2. PEG

After the SSG and the RF excitation pulse are switched off, the spins within the desired slice precess with approximately the same phase and frequency. Thereafter, the PEG is applied along an axis perpendicular to that of the SSG. During the application of the PEG, the excited spins in the selected slice will precess with different frequencies according to their position on the axis of the PEG. After this PEG gradient is turned off, the spins will precess (neglecting the field inhomogeneities) with approximately the same frequency but with different phases as displayed in figure 2.13c. The phase differences between the spins can be controlled by either adjusting the magnitude of the PEG or the duration over which it is applied. However, it is common to fix the time duration and change the magnitude of the PEG.

2.4.1.3. FEG

We have seen that after applying the PEG the spins will precess with approximately the same frequency but different phases. Now the FEG is applied along the third axis which is mutually perpendicular to the axes of the SSG and the PEG. In this case the spins, which are already precessing with different phases, precess with different frequencies according to their position on the axis of the FEG, and thus the MR signal can be recorded during the application of the FEG. This is why this gradient is also called *readout gradient*. Now this recorded signal, generated from the whole slice, contains the phase and frequency information of the spins from each pixel of the desired image.

2.4.2. Imaging Sequences

There are various combinations of the gradient fields with the RF excitation pulses that can be used to produce the MR image. These combinations are called the *imaging sequences*. In this section we will introduce two standard sequences that will be referenced in the next chapters. These sequences are: the spin-echo and the gradient-echo sequence [16, 41].

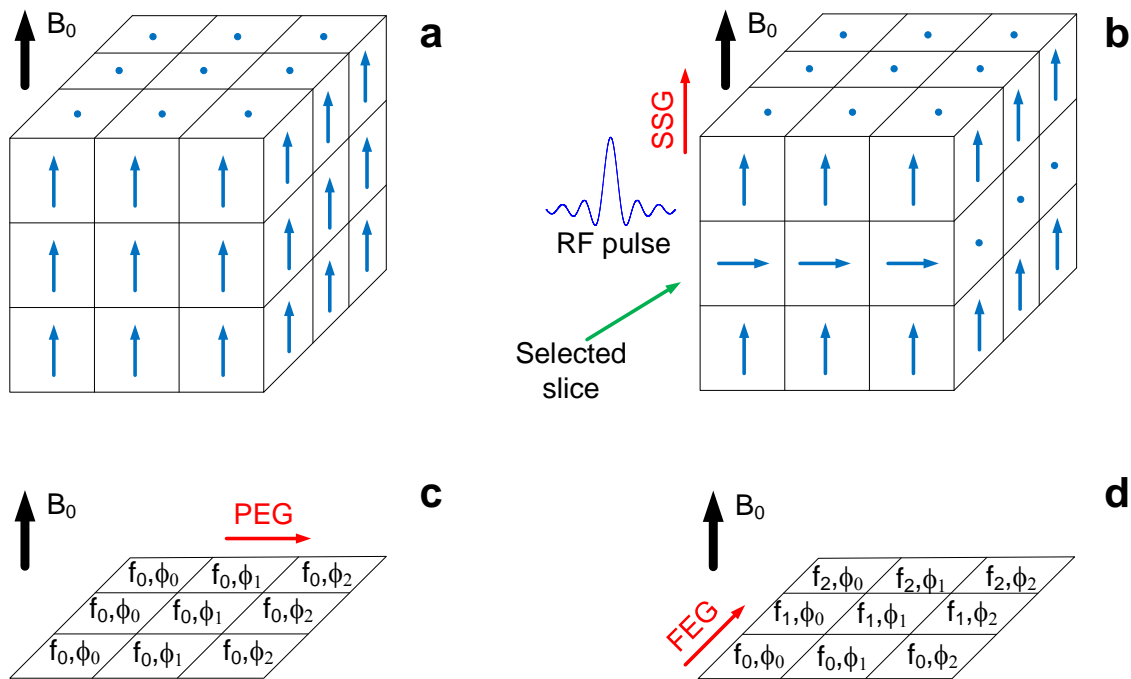


Figure 2.13.: The effect of applying the gradient fields on the magnetic moments within the sample. (a) Due to B_0 a net magnetic moment, that aligns parallel to it, will be generated in each voxel of the sample. (b) An SSG is applied simultaneously with an RF pulse. In this case the magnetic moments within a single slice of the sample will respond to the RF pulse and will accordingly tilt by a certain angle. (c) The application of the PEG results in a change in the phase of the precessing magnetic moments that is proportional to their position on the axis of the gradient. (d) During the FEG gradient the magnetic moments will exhibit different frequencies beside the different phases due to PEG. The MR signal can therefore be recorded during the FEG.

2.4.2.1. Spin-echo sequence (SE)

Figure 2.14 shows the timing diagram of a typical spin-echo imaging sequence. This sequence starts with the SSG that is simultaneously applied with a 90° RF pulse to excite the spins within a certain slice. After tilting the magnetic moments in the slice by a flip angle $\alpha = 90$, the SSG and the RF pulse are switched off. Then the PEG is applied with a certain magnitude step in order to achieve a phase gradient between the magnetic moments within the selected slice according to their position on the gradient axis. After that the SSG is turned on simultaneously with a 180° RF re-phasing pulse so as to compensate the dephasing of the magnetic moments due to the inhomogeneities of B_0 within the slice. This refocusing of the magnetic moments increases the net magnetization, and thus the amplitude of the MR signal, until it reaches a maximum before it starts decreasing again due to magnetic moments dephasing. This mountain-like shape of the MR signal is called the MR *echo*. Finally, the FEG is applied to introduce a gradient in the precessing frequency of the magnetic moments according to their position on the gradient axis. The MR echo is recorded during the application of the FEG. The sequence is repeated by changing the magnitude of the PEG one step higher or lower. The time at which the echo is obtained is called the echo time TE , while the time after which the sequence is repeated is referred to as the repetition time TR . One drawback of this sequence is that it requires high RF power to produce the 180° pulse.

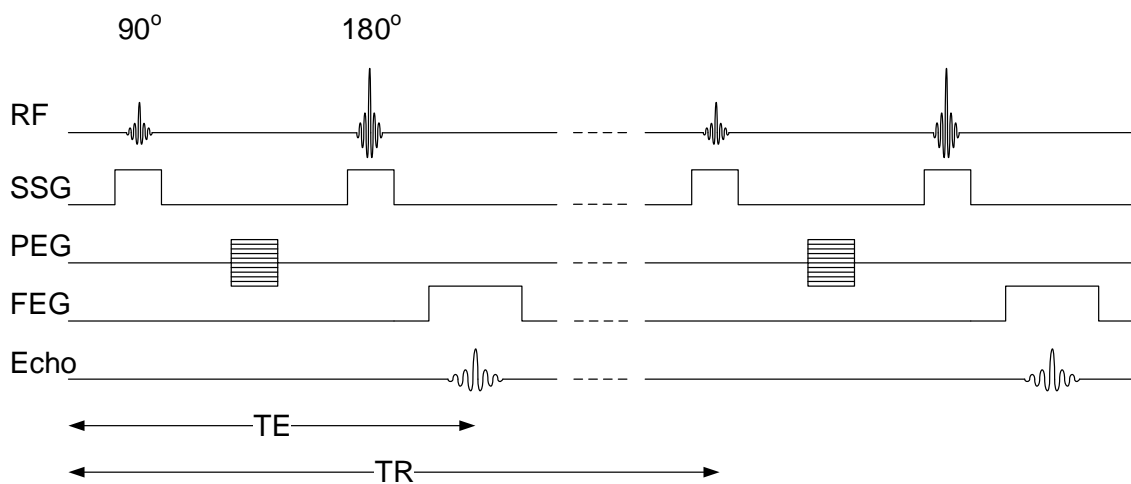


Figure 2.14.: The timing diagram of a typical spin-echo imaging sequence.

2.4.2.2. Gradient-echo sequence (GE)

The timing diagram of a typical gradient-echo sequence is depicted in figure 2.15. It starts with an RF excitation pulse simultaneously applied with the SSG gradient applied. Then, the PEG gradient is applied with a certain magnitude step to achieve phase encoding. A

negative FEG is simultaneously applied with the PEG so as to compensate the expected dephasing of the magnetic moments during the readout gradient. After that a positive FEG (readout) gradient is applied. During this gradient the already out-of-phase magnetic moments (due to the negative FEG) start refocusing and inherently the MR signal starts increasing until it reaches the maximum when a maximum of the magnetic moments are in-phase. Then, with the passage of time, the magnetic moments start dephasing again causing a decay in the amplitude of the MR signal. Now it is obvious that the main difference between the two sequences is that the SE employs a 180° high-power RF pulse to generate the MR echo, while the GE uses a negative FEG to refocus the magnetic moments and generate the echo.

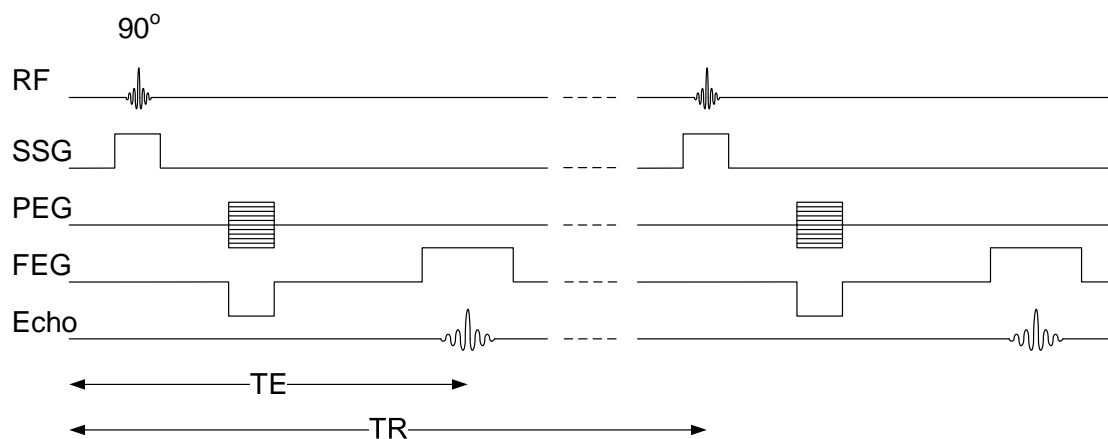


Figure 2.15.: The timing diagram of a typical gradient-echo imaging sequence.

2.4.3. Image Construction

For the image formation, we first need to fill the k-space matrix (N_x, N_y) which is a representation of the sampled MR signals that already contain spatial encoding information about the sample. Having the k-space matrix filled, the MR image can then be obtained by applying a two dimensional Fourier transformation to the k-space. Figure 2.16 explains how the k-space matrix is filled with the samples of the MR signals (echos). From this figure it can be seen that the pixels of a single row of the k-space are filled with the samples of the MR echo taken at a sampling time Δt . Therefore the number of pixels within the k-space row N_x is determined by the sampling time Δt and the readout duration (sampling duration) T_s . Figure 2.16 demonstrates also that each row of the k-space corresponds to a single acquisition of the MR echo. Therefore in order to fill the whole k-space, the MR sequence should be repeated N_y times with the PEG magnitude changed every time. Thus the number of PEG steps is equal to the number of rows in the k-space N_y , and therefore

the acquisition time of a single MR image is:

$$t_{acq} = TR \cdot N_y \quad (2.15)$$

The peripheral rows of the k-space features PEG with higher steepness, therefore the dephasing between the magnetic moments is higher, and thus the signal amplitudes are lower. On the other hand, the rows near the center of the k-space have higher amplitudes since the steepness of the PEG is smaller. This can be obviously observed in the gray map of the k-space matrix depicted in figure 2.16. Eventually, the figure illustrates how the final MR image can be obtained by applying a two-dimensional Fourier transform to the k-space matrix.

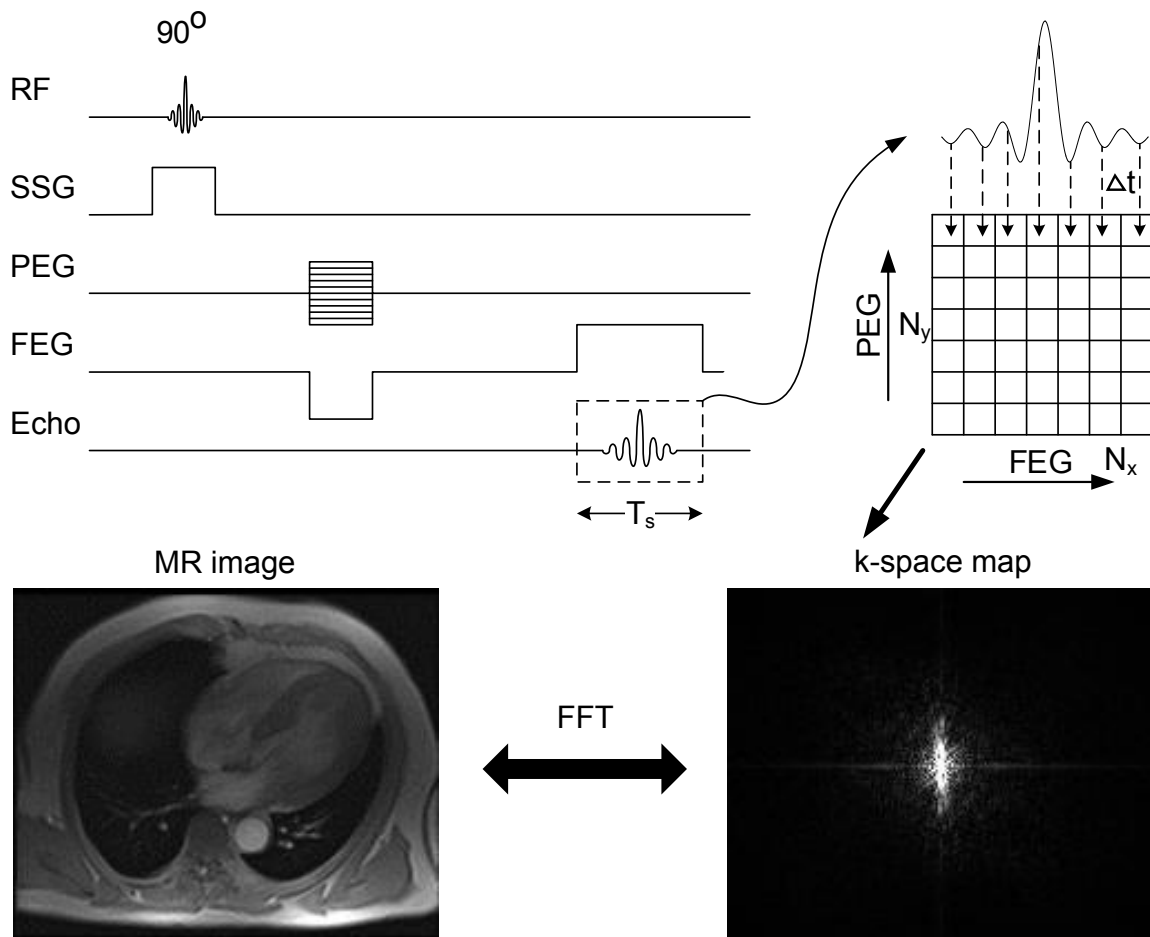


Figure 2.16.: Sampling the MR signal (echo) and filling the k-space matrix. Obtaining the MR image from the k-space matrix via two dimensional Fourier transform.

2.5. MR Phased Arrays

2.5.1. Overview

We have seen throughout the former sections that the MR signals are detected and received by an RF coil, which is essentially the first element in the receiver chain. The detected MR signals are then processed by the different electronic blocks of the receiver, and finally they are digitized and processed by a computer to produce the MR image. In 1986 Hyde et al. introduced the concept of coil arrays where two or more local coils are employed to detect the MR signals instead of a single coil [52]. In his paper, Hyde proved the potential of this concept to decrease the scan time provided that the receive coils are perfectly decoupled, i.e., the mutual inductances of the coils are negligible and therefore they do not interact with each other. The effect of decoupling can be thought of as having two or more independent sources of the MR signals that provide different information on the sample at the same time. In 1990 Roemer et al. reported the first practical NMR phased array of coils [89]. He introduced a method to eliminate the interaction between the coils by physically overlapping them and by employing low input-impedance preamplifiers as illustrated in figure 2.17. As such, the coils can operate simultaneously and collect different information from the sample. After processing the signals from these coils, the results showed that one can obtain the high SNR of the smaller coils for the same field-of-view (FoV) imaged with a larger coil with no penalty of scan time. After Roemer's paper, which focused mainly on the imaging of the spine, the concept of MR phased arrays was rapidly extended to imaging of different body parts [21, 28, 43–45] as well as spectroscopy applications [38, 104]. Since then, this concept became a standard in commercial scanners [63] and therefore it has dramatically evolved and numerous papers have been published to investigate the potential of these MR arrays. Furthermore, the trend toward MR arrays with higher number of coils has increased over the years; from elementary arrays with 4 coils, to 16-32 coil arrays found in most new scanners, to research investigations with 64-128 coil

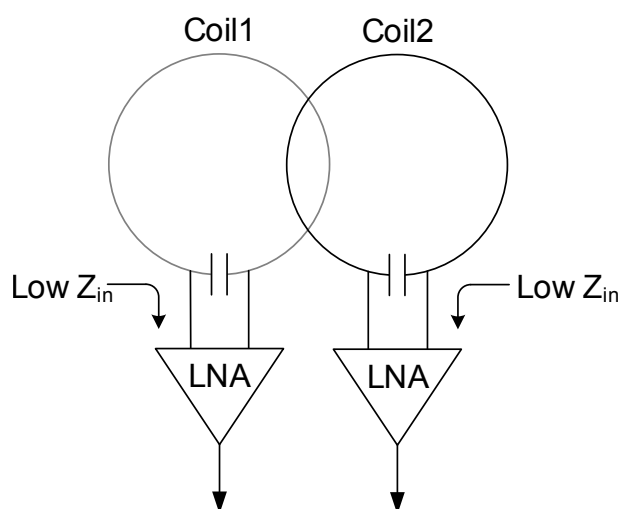


Figure 2.17.: Reducing the coupling and mutual inductances between the coils via geometrical overlapping and low input-impedance preamplifiers.

arrays. Aside from the development of the MR receive arrays, elegant algorithms have been introduced to optimally combine the MR signals from the array coils in order to generate the image allowing to decrease the scan time drastically. Examples of these algorithms include generalized auto-calibrating partially parallel acquisition (GRAPPA) [35], Sensitivity encoding for fast MRI (SENSE) [84], and simultaneous acquisition of spatial harmonics (SMASH) [97].

In order to explore the potential and advantages of the MRI phased arrays, we will introduce some examples of these arrays with brief explanation and highlighting of the most important advancements. These are:

2.5.1.1. 32-Coil Array

In 2006 Wiggins et al. [107] presented a 32-channel receive-only MR phased array. The array targeted head imaging in 3 T scanners and was built of circular elements arranged in hexagonal and pentagonal shapes. The decoupling between the array elements was achieved by geometrically overlapping the coils and by transforming the input impedance of the preamplifier to high impedance at the coil side. Compared to commercial eight channel head array, the 32-channel array showed improved SNR of about 1.4-fold to 3.5-fold according to where it is measured in the brain. Moreover, the noise amplification (g-factor) was significantly enhanced by 59% for 4-fold imaging acceleration and 26% for 5-fold acceleration compared to the 8-channel array. Another 32-channel array was introduced by Hardy and colleagues [39] in 2004. This body-survey array was designed to operate in a 1.5 T scanner. An imaging acceleration factor of 4 was achieved with this array. Furthermore, the FoV was doubled in two dimensions during accelerated imaging with no degradation in resolution.

2.5.1.2. 64-Coil Array

In 2013 Keil et al. [62] introduced a 64-channel array for brain imaging in a 3 T scanner. The coil array was designed to be compared with 32-channel array, thus allowing to distinguish the effect of doubling the number of coils within the receive array. The new design featured a 1.3-fold SNR in the brain cortex compared to the 32-channel array. Furthermore, the 64-channel array showed one unit enhancement in the imaging acceleration for the same noise amplification (g-factor) of the 32-channel array.

2.5.1.3. 96-Coil Array

In 2009 Wiggins et al. [108] reported a 96-coil array for head imaging in 3 T scanners. The receive-only array was a continuation of the development of the previous 32-channel array introduced in [107]. The results of brain imaging showed a significant improvement in the SNR as well as a remarkable enhancement in the g-factor compared to the former 32-channel array. In numbers, the 96-coil array showed a 35% enhancement in the maximum g-factor compared to the 32-channel array for an imaging acceleration rate of 4.

2.5.1.4. 128-Coil Array

In what has become the largest system, Schmitt et al. [92] presented in 2008 a 128-coil array for highly accelerated cardiac imaging in a 3 T scanner. This arrays showed a considerable increase in the SNR (up to 2.2 fold) compared to the commercial 24-channel array. Furthermore, this array offered seven-times improved g-factor for a seven-fold imaging acceleration factor which reflects a great convenience for highly accelerated imaging.

2.5.1.5. 7-coil Micro Phased Coil Array

Unlike the aforementioned phased arrays that are based on the macro (centimeter range) coils, Gruschke et al. [36] introduced in 2012 a micro phased array of seven coils designed specifically for the investigation of sub-millimeter samples. The coil array depicted in figure 2.18 combines the advantages of high resolution imaging at micro scale due to the use of micro coils and large field of view. The results of testing this coil array showed high



Figure 2.18.: Phased array of several hexagonally wire bonded micro coils [36]. The phased array of micro coils with tuning and matching electronics is mounted on a PCB. Seven low-noise preamplifiers are connected to the phased array.

resolution ($30 \times 30 \mu\text{m}^2$) imaging of biological samples, as well as high resolution (2.9 Hz spectral line width) spectroscopy.

2.5.2. Pros and Cons

From the aforementioned discussion we can summarize the benefits of the MR coil-arrays compared to single receive coils as follows; by increasing the coils within the MR arrays, it is possible to achieve one or a combination of the following advantages:

- Increasing the SNR of the acquired image.
- Decreasing the scan time via down-sampling the k-space (using less phase encoding steps) and compensating for the missing samples from the sensitivity maps of the coils within the array [24, 84]. In this case the phase encoding of the MR signals will be accomplished by the gradient coils and the locations of the array coils.
In certain cases, for example the imaging of the lungs where the patient has to hold the breath during imaging, fast imaging becomes an indispensable solution.
- Increasing the FoV with no time penalty.

As it has just been discussed, the MR coil arrays offer many valuable advantages, however they, on the other hand, encounter a number of challenges and disadvantages that one has to trade off. The main drawbacks associated with MR arrays comprise size, cost, and complexity of the MR system which all increase with the number of coils within the array and become ultimately the limiting factor to having arrays with massive (>128) number of coils. In order to understand these drawbacks, we can simply have a look at the 96-coil array

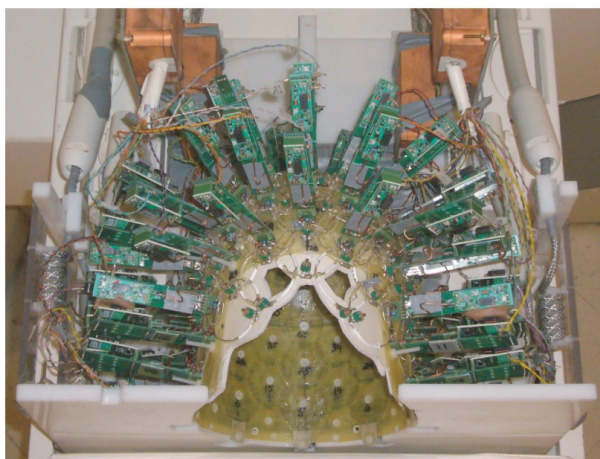


Figure 2.19: 96-coil array for brain imaging implemented by Graham C. Wiggins and colleagues in 2009 [108]. The picture shows the RF coils placed on a helmet form and their respective preamplifiers. What is not illustrated in the figure are the bulky bundles of coaxial cables used to carry the MR signals to the 96 receivers.

in figure 2.19 and the block diagram of the MR receiver in figure 2.8. In order to achieve an optimum performance of the arrays, the coils have to be perfectly decoupled. Moreover, the MR signals from these coils have to be simultaneously acquired and processed. Therefore, each coil of the MR array necessitates a complete and separate receive chain such as the one in figure 2.8. Thus adding more coils in the MR array means more receivers and inherently increased cost and size. Another issue, that becomes more critical with larger number of coils within the array, is the decoupling between the coils. As previously mentioned, one

way to decouple the coils is to geometrically overlap them such that the mutual inductance is approximately zero. However, this method is applicable only to the adjacent coils. For the nonadjacent ones, the decoupling can be implemented by connecting the coils to low input-impedance preamplifiers as illustrated in figure 2.17 [89]. Therefore, and in order to avoid signal attenuation, low input-impedance preamplifiers have to be mounted as close as possible to the coils and connected to them. This necessarily entails bulkiness and increased complexity of the MR system. Furthermore, the number of coaxial cables carrying the MR signals from the array to the receive electronics increases linearly with the number of coils. These drawbacks of size and complexity become particularly challenging in the case of micro-coil MR arrays such as, for example, the micro phased coil array in figure 2.18. Besides the coil array, this figure also shows the respective preamplifiers that are connected in a close proximity to the micro-coils.

As it is seen in the figure, the preamplifiers occupy several orders the volume occupied by the micro-coil array and, therefore, adding more coils to the array will drastically increase the size of the system which is usually limited by the diameter of the bore of the MR scanner.

The discussion so far about the pros and cons of the MR coil arrays raises an urgent need to find innovative solutions and ideas so as to overcome the problems and difficulties that arise with adding more coils to the array.

2.5.3. State of The Art

In this subsection we will see a brief overview on the contributions that have been so far published to introduce solutions to the aforementioned challenges associated with MR arrays.

2.5.3.1. Four-channel Time Domain Multiplexer

Time division multiplexing (TDM) is an old technique that returns to the late 1800s, and is used to transmit and receive multiple independent channels on a single common transmission medium. The basic idea of this multiplexing scheme, as illustrated in figure 2.20, is to pass a sample from each channel at a time through the transmission medium, ensuring that the time interval Δt between the samples of each channel fulfills the Nyquist rate. At the other side of the transmission line, the receiver separates the samples and allocates them to various groups. As such, the signals from all the channels are transmitted simultaneously over the same single path.

Based on this multiplexing scheme, in 1994 Porter et al. [82] presented a four-channel multiplexer to be a cost-effective alternative for the multiple receivers MRI system. The

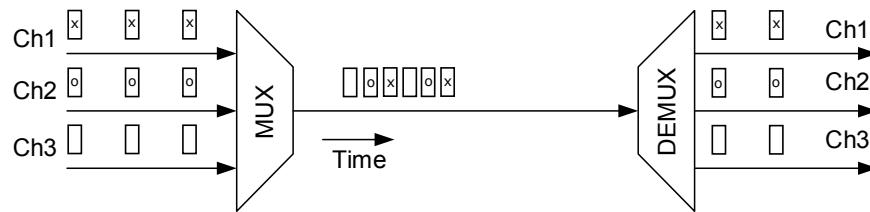


Figure 2.20.: Demonstration of the principle of time division multiplexing.

multiplexer that is designed to operate in a 1 T MR scanner (approximately 41 MHz Larmor frequency for the ^1H protons) allows the simultaneous acquisition of four MR images. The block diagram of this multiplexer is illustrated in figure 2.21. As it can be seen in the figure,

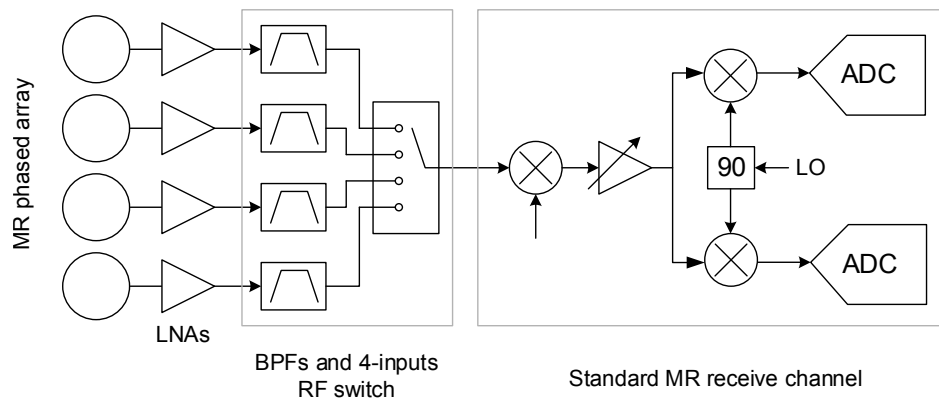


Figure 2.21.: Block diagram of a four-channel time division multiplexer (TDM) introduced in [82].

the MR signals from four independent coils are first preamplified, then introduced to four crystal-based bandpass filters with narrow bands and rapid roll-off in order to prevent noise aliasing and cross-talk between the channels. The time-multiplexing of the signals, which follows the bandpass filtering stage, is performed by means of a 4-to-1 RF switch that passes a sample from each channel at a time. After that the multiplexed signals are transferred over a single cable to the conventional scanner's receiver where they will be demodulated and digitized. Finally, the recorded samples are separated and allocated to their corresponding k-spaces and then the images are reconstructed. Assuming that the Nyquist rate sampling is sufficient to reconstruct the images and the RF switch is ideal, the maximum bandwidth of the images acquired by a single coil will be $1/4$ of the receiver's bandwidth. Therefore, this reveals a major drawback of this approach which is the limited number of channels that can be multiplexed, since the receiver's bandwidth is limited. Furthermore, this approach still suffers from the size and complexity problems since the

preamplifiers, the bandpass filters, the RF switch, and the control circuitry need to be mounted close enough to the coil array.

2.5.3.2. Four-channel Frequency Division Multiplexer

Unlike the TDM, the frequency division multiplexing (FDM) divides the total available bandwidth of the transmission medium into a number of series non-overlapping sub-bands, each of which is dedicated to carry the signals from a separate channel as depicted in figure 2.22. Having non-overlapping sub-bands allows retrieving the different channels by simply introducing the multiplexed signal to as many demodulators as the number of channels and applying lowpass filtering afterwards. A four-channel solution that is based

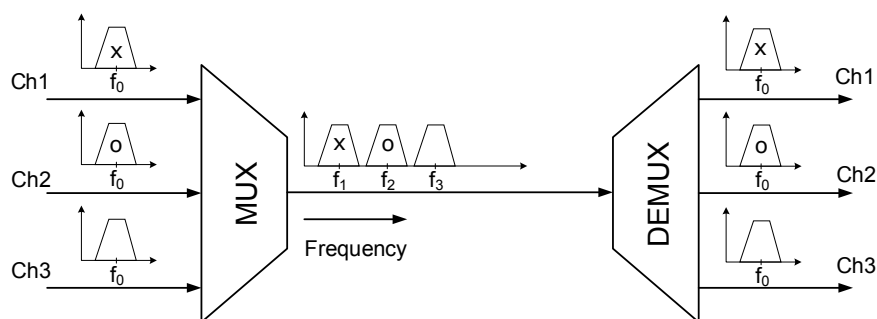


Figure 2.22.: Demonstration of the principle of the frequency division multiplexing.

on the principle of multiplexing the MR signals in the frequency domain was introduced in 2007 by He et al. [46]. The multiplexer illustrated in figure 2.23 is designed to interface MR receive array of four coils to a 0.3 T scanner. From the displayed figure, one can visualize

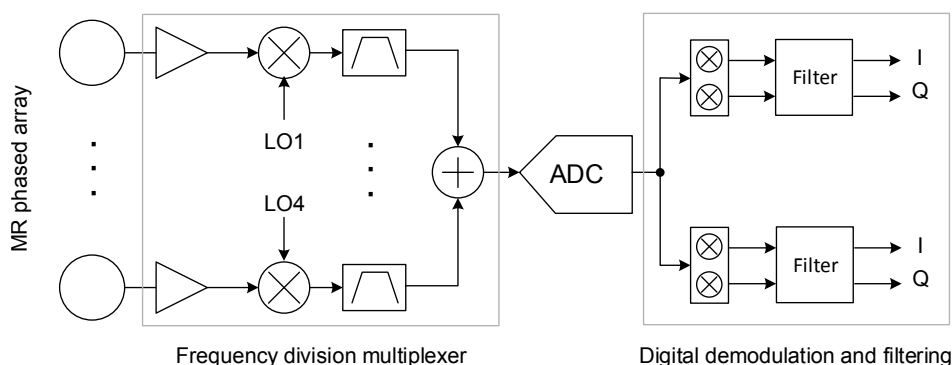


Figure 2.23.: Block diagram of a four-channel frequency division multiplexer designed for a 0.3 T MR scanner [46].

how this multiplexer works. Firstly, the MR signals are preamplified by means of four separate low-noise amplifiers. Then, another four variable gain amplifiers are employed

to further boost the amplitude of the signals. After that the signals are introduced to separate frequency mixers that convert them into four different intermediate frequencies (sub-bands). These are 10.7, 4.5, 5.5, and 6.5 MHz. The frequency domain multiplexer employs a direct digital synthesizer (DDS) to generate the respective local oscillators. After the mixing stage the signals are introduced to four distinct bandpass filters with center frequencies corresponding to the desired intermediate frequencies. The purpose of these filters is to eliminate the higher sideband and the out-of-band noise. Finally, the MR signals are combined together and transmitted over a single cable. One ADC is utilized to digitize the combined MR signals, and a field programmable logic array (FPGA) is exploited so as to perform a direct demodulation of the digitized signals. Although the FDM solution showed superior performance regarding the cross-talk between the channels compared to the TDM, it still suffers from the size problem since it is based on the use of discrete components which makes it inflexible to operate in different MR scanners especially with higher Larmor frequencies and larger number of channels.

2.6. Summary

In this chapter an elaborate introduction, that establishes a theoretical background of magnetic resonance, has been given. Many concepts, that explain the fundamentals of MR and from where the MR signals originate, were introduced. This was followed by a detailed description of the MR hardware, especially the MR receiver whose development is the major goal of the thesis. After that, the concept of MR phased reception arrays was introduced with examples showing the advantages of using such arrays as well as the resulting technical challenges, such as size, cost, and complexity. The advantages and disadvantages of a phased array can be better understood by considering the head imaging as an example. In this case the head is surrounded by the array coils. The head surface area can be approximated by the surface of a sphere with a radius of 10 cm. Figure 2.24a shows the decrease in the area enclosed by a single coil as the number of detectors with the array increases. In the same figure it is noted that the number of cables and RF receivers increases linearly with the number of coils. Figure 2.24b shows, on the other hand, a theoretical prediction, based on the formulas given in [10, 49], for the SNR in the head areas close to the coils for different acceleration factors. In this figure, R1 refers to the lowest acceleration, while R5 represents the highest. The figure demonstrates that the MRI phased arrays of receive coils are capable of providing significant enhancements in the signal-to-noise ratio of the MR signals as well as the imaging speed. These advantages make them very attractive for the commercial systems. However since each coil is an independent channel, the number of cables and RF receivers scales linearly with the number of coils. Thus,

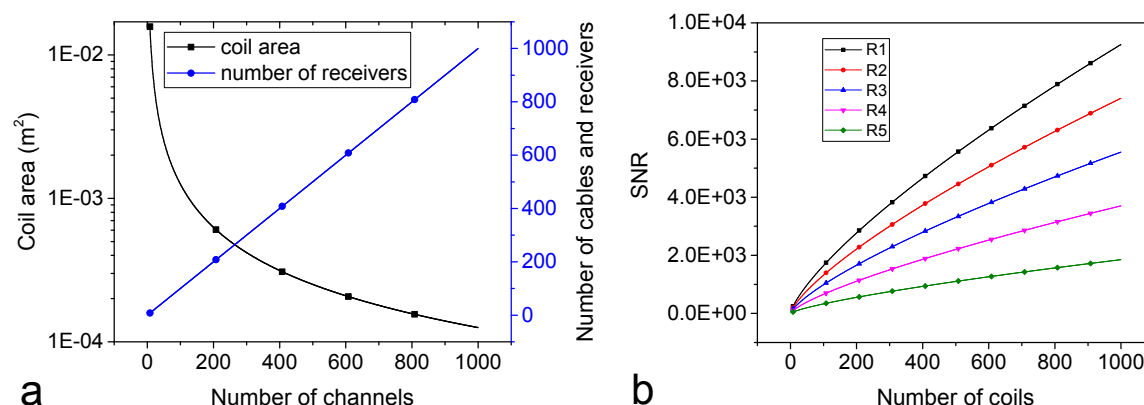
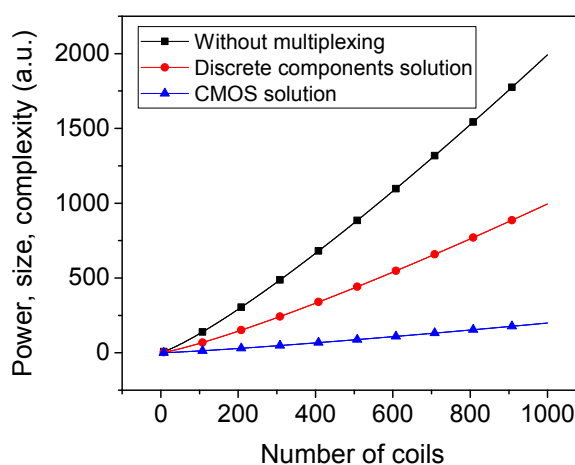


Figure 2.24.: Effects of increasing the number of receive coils of an MRI array. (a) The coil area decreases inherently as the number of coils increases, while the number of cables and RF receivers scales linearly. (b) Calculation of the enhancement of the SNR in the head areas close to the coils for different acceleration factors.

the power consumption, the size of the system, and its complexity scale, in the best case, linearly as a result. In fact, the increase in power consumption, size, and complexity can be better described by a higher order polynomial as shown in figure 2.25. This is due to the fact that the more coils are incorporated, the more components and electronics are required to remedy the accompanying challenges, such as the coil coupling, cable crosstalk, etc. In addition, the increased number of coils necessitates more complex back-ends for the signal processing, data storage, and image reconstruction. Solutions based on discrete

Figure 2.25: Effect of increasing the number of coils in an MRI array on the overall power consumption, size, and complexity of the system. Discrete-components multiplexers can reduce the demands of power, size, and complexity. However, they fail to be an optimum solution, especially for massive number of coils. Therefore, CMOS integrated solutions are very promising in this case.



electronics, such as time and frequency multiplexers, can reduce the number of cables and receivers used. Yet such solutions still suffer from the size, complexity, and lack of design flexibility issues, and become more impractical as the number of coils increases further. For example, they might be helpful for arrays with 32 coils but surely not for arrays with a thousand coils. Therefore, there is still a persistent need for novel and more appropriate

solutions that make MR arrays of large and even increasing numbers of coils possible, with no penalties of power consumption, size, or complexity. The use of CMOS integrated electronics seems to be the optimum candidate in this case. The robust well-characterized commercial CMOS technologies allow integrating massive numbers of transistors in a single tiny chip, resulting in extremely high computational and signal processing capabilities. Furthermore, the CMOS integrated electronics offer a tremendous reduction in power consumption. As such, the CMOS integrated chip can be employed in designing both the front-end and the back-end of MR receivers where, in this case, the front-end chips (low-noise amplifiers, mixers, filters, multiplexers, and possibly ADC's) can be placed directly at the coils in order to eliminate the need for an excessive number of coaxial cables.

Thus, the task that will be presented in the following chapters is the design and implementation of a prototype CMOS multiplexer as a promising future size- and power-efficient solution for magnetic resonance receive arrays with a massive number of detectors.

3. Frequency Division Multiplexer

3.1. Introduction

In this chapter a novel solution to overcome the challenges associated with MR phased receive arrays is introduced. This solution comprises a complementary metal oxide (CMOS) [4, 68, 105] frequency division multiplexer (FDM) that targets a 9.4 T (400 MHz ^1H Larmor frequency) MRI system [58], and is based on a high quality 0.35 μm CMOS technology from XFab [2]. As depicted in figure 3.1, the FDM supports an MRI phased arrays of up to

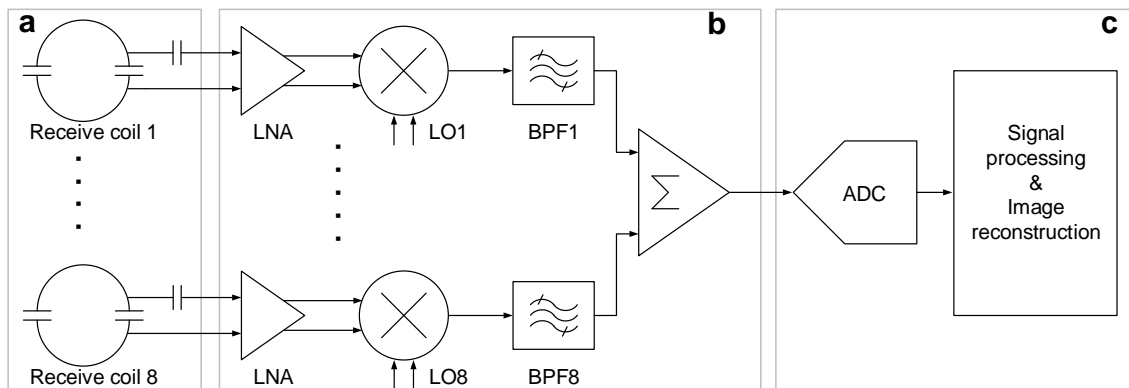


Figure 3.1.: Block diagram of the magnetic resonance system employing the CMOS frequency multiplexer as a novel solution for MR phased arrays. (a) Eight-coils MRI phased array. (b) Block diagram of the CMOS FDM consisting of eight channels, where each comprises a low-noise amplifier (LNA), a frequency mixer, and a bandpass filter. (c) Analog-to-digital converter to digitize the multiplexed signal and a signal processing unit to reconstruct the MR images.

eight receive coils. Then these signals are introduced to the CMOS FDM which consists of eight channels, where each includes a low-noise amplifier (LNA), a frequency mixer, and a bandpass filter. The MR signals in the FDM are down-converted from the Larmor frequency ω_0 to eight different intermediate frequencies $IF_j, j \in \{10, 15, 20, 25, 30, 35, 40, 45\}$ MHz. Then they are added using a high speed operational amplifier (op-amp) in order to be transmitted over a single coaxial cable. Finally, the multiplexed output of the FDM can be

3. Frequency Division Multiplexer

digitized and digitally processed to extract the data of the individual coils. The multiplexer is designed to interface coils with diameters in the range of millimeters to few centimeters, thus the maximum amplitude of the MR signals induced in such coils can be determined from equations 2.8 and 2.9 as follows:

$$V_{MR,max} = K\omega_0(B_1)_{max}M_0V_s \quad (3.1)$$

by substituting the magnetization formula and replacing ω_0 with γB_0 , equation 3.1 becomes:

$$V_{MR,max} = \frac{K(B_1)_{max}N_T\gamma^3\hbar^2I(I+1)B_0^2}{3kT_s} \quad (3.2)$$

where N_T is the total number of spins in the sample. It can be estimated using the following formula:

$$N_T = \frac{0.001 * V_s * \rho}{N_A \cdot (Molar\ mass)} \quad (3.3)$$

where V_s is the sample volume, ρ is the density, and N_A is Avogadro's number. The B_1 field, for a surface coil of radius R_c , can be calculated at the center of the coil by:

$$B_1 = \frac{\mu_0 I_c}{2R_c} \quad (3.4)$$

where μ_0 is the permeability of free space and I_c is the current in the coil. According to these equations, the maximum amplitude of the MR signal, induced in a 3 cm diameter coil for a water sample, can be estimated by applying the values in table 3.1. In this case $V_{MR,max}$ is found to be approximately 1 mV. The noise in this case can be estimated according to equation 2.10 as follows:

$$V_{noise} = \sqrt{4kT_c\Delta fR} \quad (3.5)$$

In this equation R represents the conductive losses in the coil itself as well as the magnetic and dielectric losses in the sample [81]. The AC resistance of the 3 cm diameter surface coil was found from simulation (using Advanced Design System ADS) to be 1.5 Ω . Assuming the effective resistance, after including the skin effect and proximity effect, is $R = 3 \Omega$, then the root-mean square (RMS) value of the coil noise is calculated over a 50 kHz bandwidth (which is the typical bandwidth of the gradient-echo sequence in the 9.4 T Bruker BioSpec 94/20 scanner) as $V_{noise} = 49.6 \text{ nV}$. The SNR is then determined as [81]:

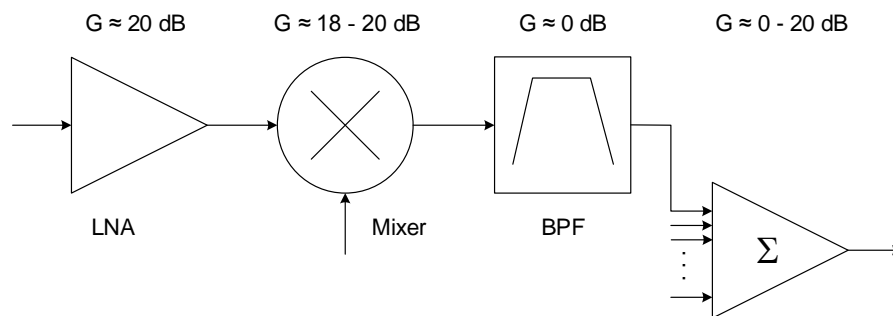
$$SNR = \frac{V_{MR,P}}{V_{noise,RMS}} = 2 \cdot 10^4 \quad (3.6)$$

Having these preliminary calculations of the MR signal amplitude and noise helps in defining the design constraints and requirements of the different components of the CMOS FDM. Figure 3.2 shows the proposed gain distribution of the different blocks of the CMOS

Table 3.1.: Parameters used to calculate the maximum amplitude of the MR signal.

Parameter	Value	Unit
K	1	-
B_0	9.4	T
γ	42.576	MHz/T
\hbar	$62607004 \cdot 10^{-34}/(2\pi)$	J.s
I	0.5	-
I_c	1	A
R_c	1.5	cm
k	$1.38064852 \cdot 10^{-23}$	J/K
T_s	298	K
V_s	80	mL
ρ	999.97	kg/m ³
μ_0	$4\pi \cdot 10^{-7}$	H/m
N_A	$6.022 \cdot 10^{23}$	mol ⁻¹
<i>Molar mass</i>	18.01528	g/mol

FDM. The proposed gain of the LNA is approximately 20 dB. This gain, according to Friis' formula (equation 2.11), minimizes the influence of the noise contribution of the blocks that follow the LNA. Moreover, this gain is not too high to make the MR signals perturb the linearity of the mixer. The proposed gain of the frequency mixer is approximately between 18 dB and 20 dB. In this case, the MR signals at the end of each channel (after the bandpass filter) will have a maximum amplitude of approximately 80 mV to 100 mV. The adding stage is supposed to have a variable gain in the range from 0 dB to 20 dB in order to adjust the amplitude of the multiplexed MR signal to achieve maximum resolution of the ADC.

**Figure 3.2.:** Proposed gain distribution of the different blocks of the CMOS FDM.

In the following sections, the individual blocks of the CMOS FDM will be explored in detail.

3.2. The low-noise amplifier

In chapter 2 we saw that the amplitude of the MR signal depends amongst other parameters on the sample's volume which is implicitly limited by the geometry of the reception coil. Therefore, when we talk about MR phased arrays of coils in the range of few centimeters or millimeters, e.g. the coil array in [36], we expect relatively low amplitudes of the MR signals (tens to hundreds of micro volts). This fact makes the use of low noise preamplifiers extremely necessary. In fact the LNA is the most critical part of the RF front end, since it prepares the RF signal to be able to drive the subsequent components in the receiver chain. Furthermore, when the LNA has a high gain, then according to equation 2.11 the noise contribution of the succeeding receiver blocks is negligible, and the receiver's overall noise performance is thus dominated by the LNA. Matlab simulations showed that a gain greater than 20 dB reduces the effect of noise of the blocks succeeding the LNA considerably. As such, the LNA not only should boost the strength of the MR signals, but also should maintain the SNR of MR signals by adding as less noise as possible. Apart from that, the LNA also provides input impedance matching (50Ω as a standard) to the input source [69]. The need for the 50Ω impedance matching is necessary to verify and characterize the performance of the circuit in real MRI experiments, and can be explained as follows; in order to adjust the MRI experiment settings and parameters, the receive coil is first connected to the commercial scanner. Therefore, the coil has to be matched to 50Ω . After setting the experiment parameters, the coil is disconnected from the scanner and connected to the custom circuit and the MRI experiment is repeated with exactly the same settings. For this reason, the circuit should have 50Ω input impedance. Thus the goal that we want to achieve in this section is to design a LNA with high gain, high linearity, and as minimum noise as possible. However, how far one can optimize these parameters depends very much on the topology.

There are various topologies used to realize LNA's in CMOS technology, among which two very common topologies will be investigated in this section, namely the inductively-degenerated common-source (CS) LNA and the common-gate common-source (CG-CS) LNA.

3.2.1. Common-Source LNA

Figure 3.3 shows the schematic of a typical common-source LNA that employs inductive source degeneration (L_s) to achieve 50Ω input matching [94]. This technique makes the CS-LNA's conventionally appropriate for narrow-band applications [19]. However special feedback or matching networks may be used to allow using the CS-LNA's in wide-band circuits [19].

The LNA in figure 3.3 also employs, in what can be considered as a current reuse, the common-gate transistor M2 in a cascode configuration to increase the power gain and achieve better reverse isolation [3, 34, 98]. The input impedance of the CS-LNA with inductive source degeneration can be expressed as [88]

$$Z_{in} \approx j\omega(L_g + L_s) + \left(\frac{1}{j\omega C_{gs}} + \frac{g_m L_s}{C_{gs}} \right) \quad (3.7)$$

where g_m and C_{gs} are the transconductance and the gate-to-source capacitance of M1 respectively. The 50Ω input matching can be achieved, at the input resonance frequency ω_0 , by setting the real part of equation 3.7 to 50Ω while setting the imaginary part to zero. In this case the matching conditions will be described by

$$R_s = \frac{g_m L_s}{C_{gs}}, \quad \omega_0^2 C_{gs} (L_g + L_s) = 1 \quad (3.8)$$

with R_s being the input resistance of the source (50Ω in this case). This equation shows that the matching condition of the CS-LNA can easily be achieved by adjusting the values of the inductors L_g and L_s which is considered to be a good advantage of this topology. Assuming the input matching condition and neglecting the gate-drain capacitance, the voltage gain of the CS-LNA can be calculated as [88]

$$A_v = \frac{V_{out}}{V_{in}} = \frac{\omega_T}{2\omega_0} \frac{R_L}{R_s} \quad (3.9)$$

where ω_T is a process parameter called the transition frequency of the transistor, and R_L is the real part of the load impedance. This equation shows that if the LNA is operated at a

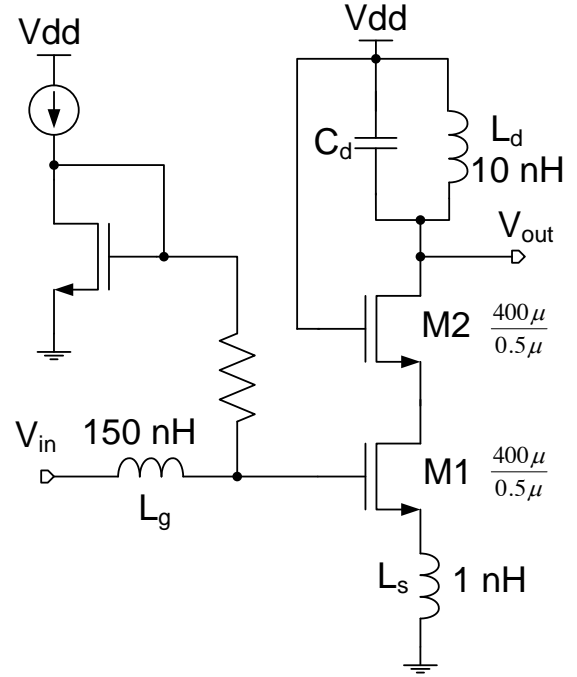


Figure 3.3.: Schematic of a typical common-source (CS) LNA.

3. Frequency Division Multiplexer

frequency below ω_T then the voltage gain will be independent of the transconductance g_{m1} . The noise figure, which is a very important parameter that should be considered with a lot of attention during the design of the LNA, is given by

$$NF = 1 + g_m R_s \gamma \left(\frac{\omega_0}{\omega_T} \right)^2 \quad (3.10)$$

where γ is the bias-dependent coefficient of the channel's thermal noise. The LNA depicted in figure 3.3 was designed using $0.35 \mu\text{m}$ CMOS technology from XFab [2]. It operates at 400 MHz and features a 50Ω input impedance while consuming 3 mA from a 1.5 V source. Figure 3.4 summarizes the simulation results of the CS-LNA.

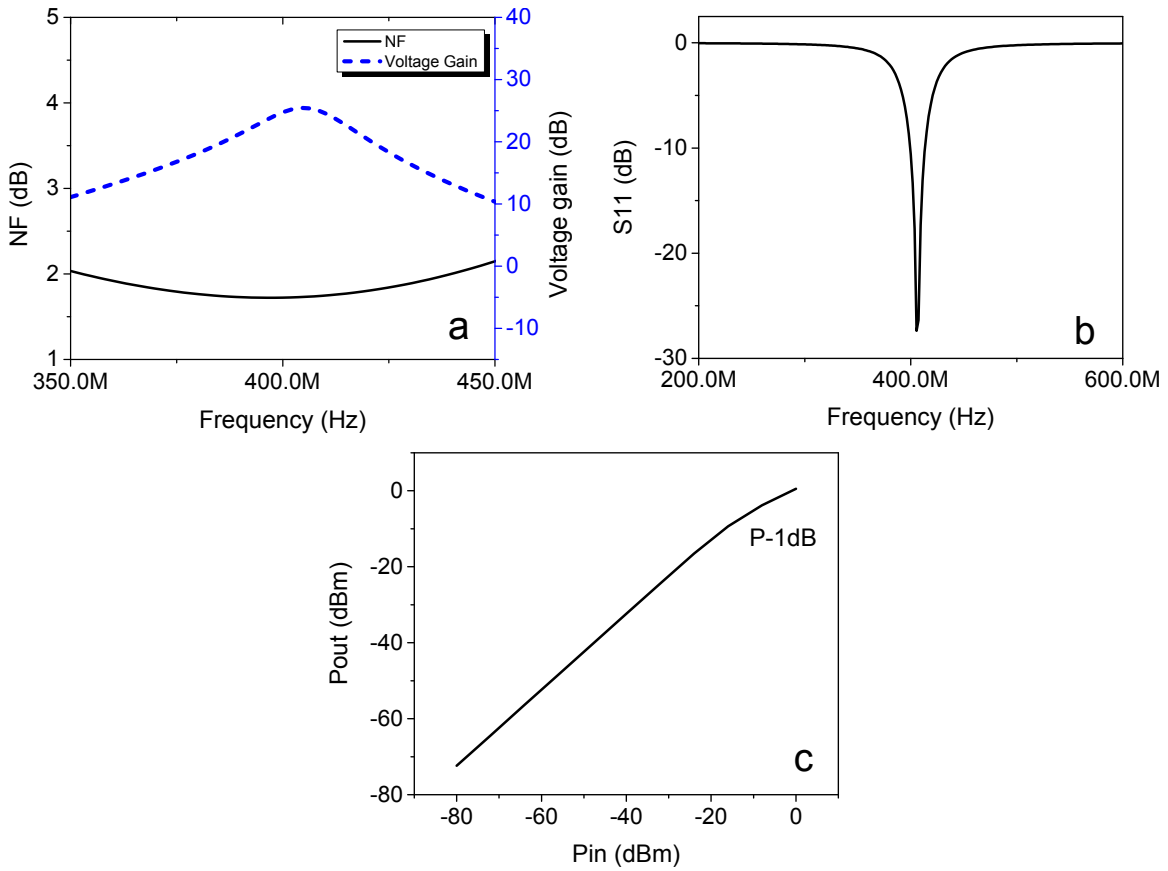


Figure 3.4.: Simulation results of the CS-LNA. (a) Voltage gain and noise figure. (b) Input power reflection for 50Ω source impedance. (c) 1-dB gain compression.

It shows superior performance of the CS-LNA in the aspects of voltage gain, noise figure, and source impedance matching. However, this performance is normally achieved at the expense of larger die area due to the spiral on-chip inductors, which is considered to be a main drawback of this topology especially when we talk about differential CS-LNA architecture. Another issue that prohibits the use of this LNA topology in the proposed

FDM is the possible eddy currents which can be induced in the on-chip inductors due to the switching of the gradient fields. These currents can be severely high and cause damage to the circuit.

Table 3.2 summarizes the simulation results of the common-source LNA.

Table 3.2.: Summary of the common-source LNA simulation parameters.

Parameter	Value	Unit
Voltage gain (max)	25.1	dB
Noise figure (min)	1.7	dB
IIP1 (linearity)	-16	dBm
$S_{11,\min}$	-27.36	dB
Vdd	1.5	V
Current consumption	3	mA

3.2.2. Common-Gate Common-Source LNA

An alternative LNA topology, that dispenses with the use of on-chip inductors, was employed in the design of the MRI FDM. This topology, depicted in figure 3.5, is a differential common-gate common-source (CG-CS) low-noise amplifier (LNA). This CG-CS LNA has

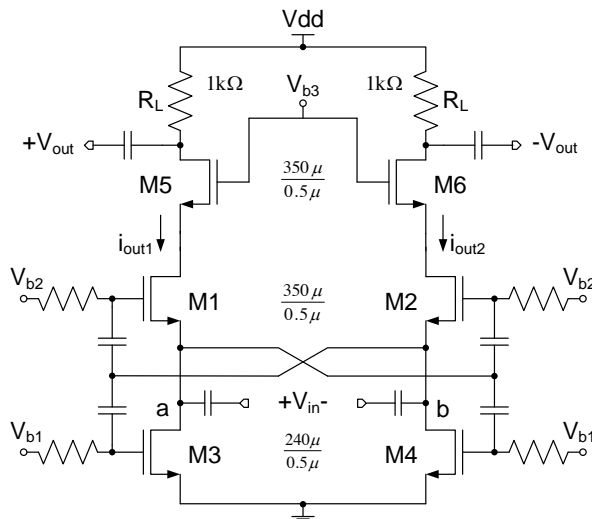


Figure 3.5: Schematic of the differential common-gate common-source (CG-CS) low-noise amplifier (LNA) employed in the frequency division multiplexer.

the advantage of low power operation. Furthermore, it has superior linearity, stability, and robustness to process-voltage-temperature (PVT) variations compared to the CS-LNA [23]. It also exhibits higher effective trans-conductance g_m than that of a conventional CG-LNA that uses inductors to provide the DC current path for the transistors M1 and M2. This

higher g_m offers additional advantages to the CG-CS LNA [109]. First, the noise figure (NF) is improved, and second, there is no trade off between the power consumed and the achievable voltage gain, since g_m has been increased without increasing the current. The CG-CS LNA also employs a capacitive cross-coupling (CCC) negative feedback configuration. This configuration guarantees a differential operation of the LNA and boosts the trans-conductance g_m , and thus increasing the voltage gain of the amplifier [110]. The g_m boosting can be explained as follows: the differential input voltage v_{in} is applied to the sources of the transistors M1 and M2. Thus the voltages at nodes a and b are $+v_{in}/2$ and $-v_{in}/2$ respectively. The output current $i_{out,1}$ at the drain of M1 is the superposition of two currents $i'_{out,1}$ and $i''_{out,1}$. The current $i'_{out,1}$ is proportional to $(g_{m1}(+v_{in}/2))$ where M1 operates as a common-gate (CG) amplifier, while the current $i''_{out,1}$ is proportional to $(-g_{m2}(-v_{in}/2))$ where M2 operates as a common-source (CS) amplifier. As a result, the total current $i_{out,1}$ is proportional to $(2g_{m1,2}(+v_{in}/2))$.

Noise Analysis

By neglecting the noise contribution of the amplifiers' load, the CG-LNA has a minimum noise factor given by [5]

$$F = 1 + \gamma, \quad (3.11)$$

where γ is the excess channel thermal noise coefficient. In general, a CG-LNA that uses inductors to provide a current path to the transistors M1 and M2 shows a worse noise performance compared to the inductively degenerated CS-LNA. This degradation is due to the fact that the noise performance is influenced by the matching condition, which is directly related to g_m in the case of a CG-LNA. Replacing the inductors in the CG-LNA with transistors M3 and M4 adds a degree of freedom to the choice of the input trans-conductance, and thus renders the improvement of the noise performance possible. The refinement of the noise performance in this case will be at the expense of the power consumption as demonstrated in figure 3.6a. This figure shows the simulation results for the noise figure and the power consumption of the CG-CS LNA when the channel widths of M3 and M4 vary. The following formula describes the input-power matching condition for the CG-CS LNA

$$R_s = \frac{R_{in}}{2} = \frac{1}{2g_{m,1} - g_{m,3}} \quad (3.12)$$

Figure 3.6b depicts a simplified noise model of the CG-CS LNA, in which the transistors' thermal noise is assumed to be dominant. The coupling capacitors C_c are presumed to be much larger than the capacitance of the input transistors C_{gs} , thus they are replaced by short circuits in the noise model. This noise model shows the noise sources of only one half of the LNA circuit, and these sources include v_{ns} (the noise due to the source resistance),

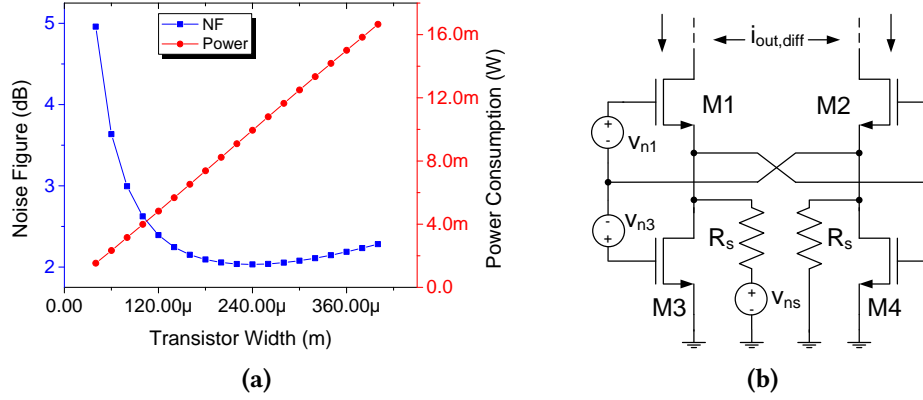


Figure 3.6.: (a) The trade-off between the noise performance and the power consumption of the CG-LNA when the channel widths of M3 and M4 change. The simulation involved in this figure is periodic-steady state (pss) and a periodic s-parameters (psp) with a parametric sweep of the channel width. (b) Simplified noise model of the common-gate common-source low noise amplifier. This model shows the noise sources associated with one half of the amplifier circuit.

v_{n1} (the noise due to M1), and v_{n3} (the noise due to M3). The squared differential output current values of these noise sources are given by

$$i_{ns}^2 = g_{m1}^2 v_{ns}^2 = 4KT R_s g_{m1}^2 \quad (3.13)$$

$$i_{n1}^2 = 4KT \gamma_1 g_{m1} (g_{m1} R_s - 1)^2 \quad (3.14)$$

$$i_{n3}^2 = 4KT \gamma_3 g_{m1}^2 g_{m3} R_s^2 \quad (3.15)$$

Assuming, for simplicity, that $\gamma_1 = \gamma_3 = \gamma$, the noise factor F of the CG-CS LNA is then given by

$$F = 1 + \gamma \left[\frac{(g_{m1} R_s - 1)^2}{g_{m1} R_s} + 2g_{m1} R_s - 1 \right] \quad (3.16)$$

According to the last equation, figure 3.7 shows the effect of the source impedance R_s on the noise figure of the LNA for $g_{m1} = 12 \text{ mS}$, and for different values of the excess channel noise factor γ [33, 53]. It is observed from this figure that the 50Ω matching condition not only achieves maximum power transfer from the receive coil, but also provides best noise performance.

Simulation Results

The voltage gain of the CG-CS LNA is given by [5]

$$\frac{v_o}{v_{in}} \cong \frac{2g_{m1} R_L}{1 + sC_{d5} R_L} \quad (3.17)$$

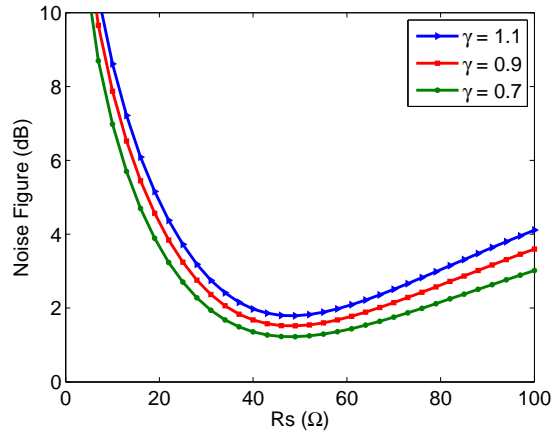


Figure 3.7: Effect of the source impedance on the noise figure of the LNA.

where C_{d5} is the total capacitance at the drain of M5. The voltage gain of the LNA, according to this equation, is mainly dependent on the transconductance of M1 and the load resistance R_L . Therefore, increasing g_{m1} boosts the voltage gain of the LNA but, on the other hand, it deteriorates the matching condition, resulting in increased power consumption. Figure 3.8a shows the simulated voltage gain of the post layout of the LNA

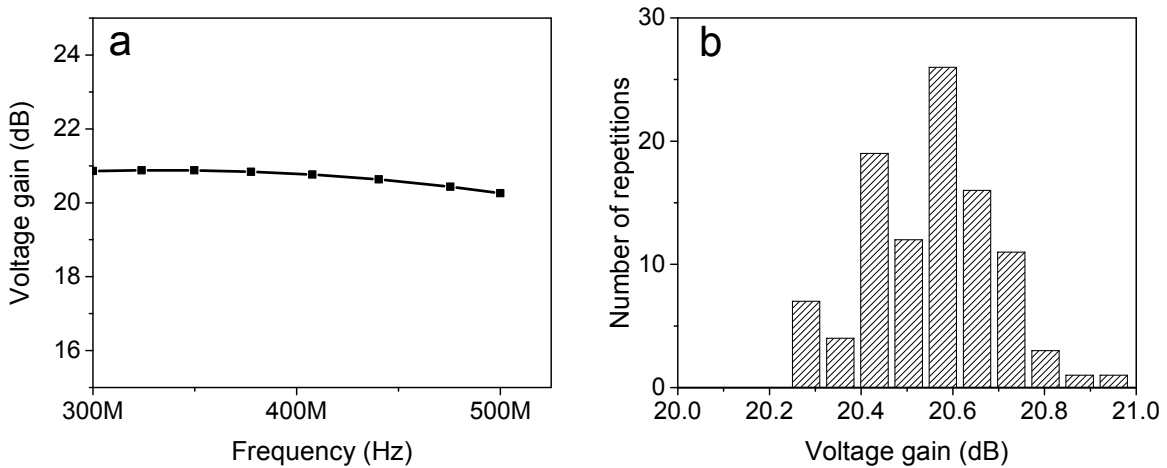


Figure 3.8.: Voltage gain simulation of the CG-CS-LNA. (a) Gain over frequency. (b) 80-runs MonteCarlo simulation of the maxim gain of the LNA.

versus frequency. In this figure it can be seen that the amplifier has a nearly constant voltage gain (approximately 20.6 dB) over a wide frequency range. Figure 3.8b demonstrates the histogram of 80-runs Monte-Carlo simulation of the voltage gain of the LNA. In this figure, it can be seen that the average gain is approximately 20.6 dB. Moreover, the figure shows the robustness of this LNA topology against the process errors and tolerances.

The input power reflection is depicted in figure 3.9a. This figure shows that the LNA has an input power reflection less than 15 dB over wide frequency range which, in conjunction

with figure 3.8a, confirms the superiority of the CG-CS-LNA in wide-band applications compared to the CS-LNA. The plot of the output power of the CG-CS-LNA versus the

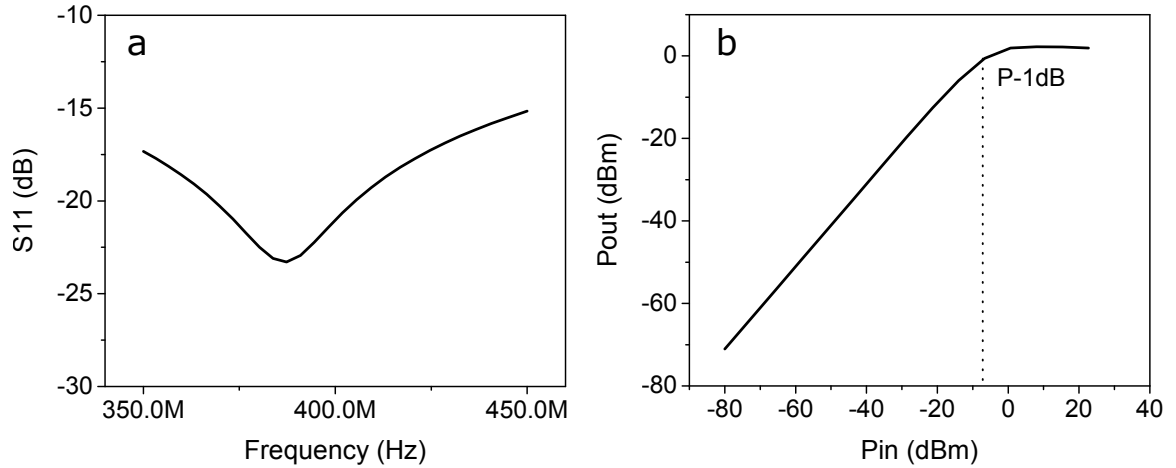


Figure 3.9.: Characteristics of the common-gate common-source LNA. (a) S11. (b) 1-dB gain compression.

input power is shown in figure 3.9b. This figure proves that the CG-CS-LNA exhibits better linearity performance compared to the CS-LNA.

For LNA's the stability is a very important issue that should be considered with great attention. This is because the LNA interfaces off-chip sources with arbitrary impedances especially at frequencies outside the desired operation band. Therefore, the LNA must preserve stability for all source impedances at all frequencies. The so-called "Stern stability factor" is a common parameter used to express the stability of the amplifier. It is calculated from the scattering parameters as follows

$$K = \frac{1 + |\Delta|^2 - |S_{11}|^2 - |S_{22}|^2}{2|S_{21}||S_{12}|} \quad (3.18)$$

with $\Delta = S_{11}S_{22} - S_{12}S_{21}$. If $K > 1$ and $|\Delta| < 1$, the amplifier is unconditionally stable. Figure 3.10a shows the Stern stability factor (K-factor) of the LNA while the value of Δ is plotted in figure 3.10b. From these figures it can be seen that the CG-CS-LNA has a robust stability over a very wide frequency range which again proves the appropriateness of this topology in the design of the FDM. Table 3.3 summarizes the simulation results of the main parameters of the CG-CS-LNA.

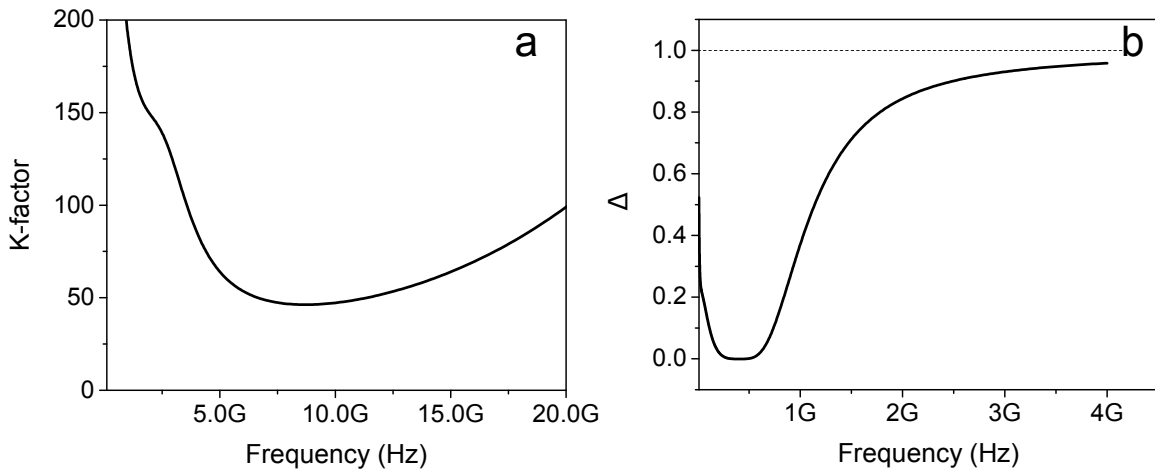


Figure 3.10.: Plot of the Stern stability factor of the CG-CS-LNA. (a) K-factor. (b) Δ .

Table 3.3.: Summary of the common-gate common-source LNA simulation parameters.

Parameter	Value	Unit
Voltage gain (max)	20.8	dB
Noise figure (min)	2.1	dB
IIP1 (linearity)	-6.6	dBm
$S_{11,min}$	-23.3	dB
Vdd	3.3	V
Current consumption	6.15	mA

3.3. The Frequency Mixer

The frequency mixer is the next element in the MR FDM. The function of this mixer is to multiply the amplified RF signal, coming from the LNA and centered at the Larmor frequency (400 MHz), with a local oscillator signal generated from an external direct digital synthesizer (DDS) [48]. This multiplication causes a frequency shift or translation of the RF signal into two new frequency bands, namely, $(f_L - f_{LO})$ and $(f_L + f_{LO})$ as shown in figure 3.11. There is a variety of mixer topologies used in the design of CMOS integrated receivers. They differ according to the specifications and constraints introduced by the receiver architecture in which they are employed. Nevertheless, the frequency mixers can be divided, according to the need of DC biasing, into two main categories. These are: the active mixers, and the passive mixers [88]. The most important feature of the passive mixers is their zero static-power dissipation which makes them very suitable for low-power applications. Furthermore, they exhibit higher linearity and low flicker noise

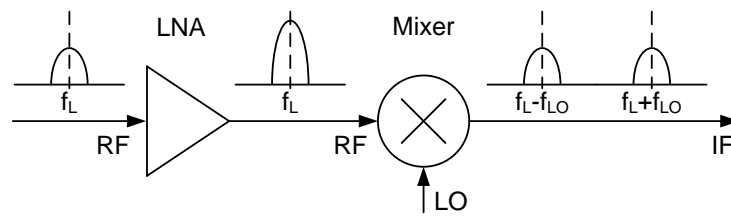


Figure 3.11.: Block diagram of the LNA-mixer interface. The local oscillator (LO) is generated using an external digital synthesizer (DDS). Commercially available DDS's (for example the LMK03806 from Texas Instruments) can provide sufficiently high precision and low jitter noise requirements as needed for the successful reception of the MR signals

which makes them attractive, especially in direct-conversion receivers. However, the passive mixers suffer from the conversion loss (typically 4~6 dB) compared to the active mixers which can achieve decent conversion gain.

3.3.1. Double-balanced Gilbert Mixer

The Gilbert mixer [32] is a very commonly used active mixer in CMOS systems. Figure 3.12 displays a double-balanced Gilbert cell that is exploited in the design of the CMOS FDM. Basically, it is a combination of two single-balanced Gilbert cells, and consists of a differential input trans-conductance stage (M1 and M2) to amplify the RF signal, a switching core (M3 - M6) to perform the multiplication of the RF with the local oscillator (LO), and a current mirror load (M7 and M8) to perform a differential-ended to single-ended signal transformation. The differential topology is used particularly because of its ability to suppress the even-order distortions at the output of the mixer [86], which improves the linearity performance. Furthermore, the double-balanced topology exhibits low feed-through of the LO frequency to the output port [101] and to the RF port as well.

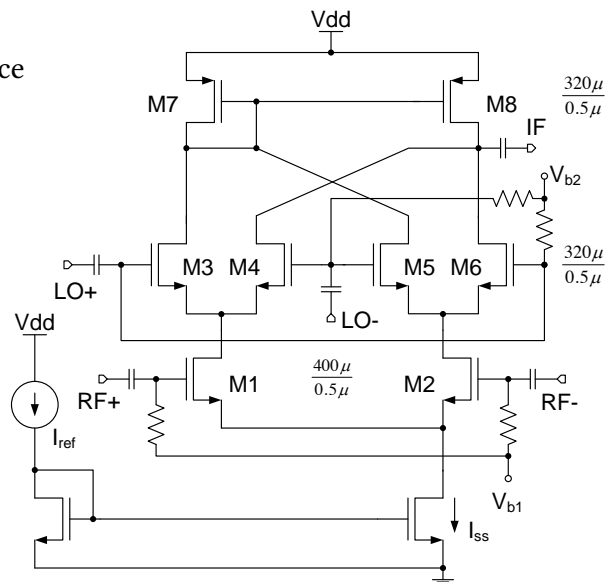


Figure 3.12.: CMOS 0.35 μm double-balanced Gilbert mixer used in the MR FDM.

The operation of the Gilbert mixer is based on the principle of a switched current [88]; i.e., at any time during the mixer operation, two LO transistors are on, while the other two are ideally off. Therefore, a large enough amplitude of the LO signals is required to ensure complete switching of the LO transistors. The switching process of the LO transistors is typically modeled by an ideal ± 1 square wave which, in turn, is described in a Fourier series as a sum of sinusoids. Thus, the output of the mixer is given by

$$V_{IF} = AV_{RF} \cos(\omega_{RF}t) \frac{4}{\pi} \left[\sin(\omega_{LO}t) + \frac{1}{3} \sin(3\omega_{LO}t) + \frac{1}{5} \sin(5\omega_{LO}t) + \dots \right] \quad (3.19)$$

where A is the gain of the amplification stage of the mixer. After filtering out the higher order side-bands at intervals of $2\omega_{LO}$ that result from the mixer, the IF signal will be

$$V_{IF} = \frac{2}{\pi} AV_{RF} \sin[(\omega_{RF} - \omega_{LO})t] \quad (3.20)$$

The conversion gain of the mixer is given by

$$\frac{V_{IF}}{V_{RF}} = \frac{2}{\pi} g_{m1} R_L \quad (3.21)$$

This equation shows that the gain is mainly dependent on the transconductance of the RF transistors (M1, M2), and on the load impedance R_L . Neglecting the loss in the LO switching transistors, and assuming that they act as perfect switches, the remaining contribution to the distortion in the mixer is from the RF transistors [77].

The input-referred third-order intercept point, IIP3, which is a measure of the linearity is given by

$$IIP3 \approx \sqrt{\frac{32I_{ss}}{3\mu_n C_{ox}}} \quad (3.22)$$

where μ_n is the charge carrier effective mobility and C_{ox} is the gate oxide capacitance per unit area. According to the last equation, the linearity of the mixer is proportional to the square root of the biasing current I_{ss} , thus the linearity of the mixer can be enhanced at the expense of more power consumption.

Flicker noise

All three stages of the Gilbert mixer contribute to the overall flicker noise. However, the contribution of transistors (M7, M8) can be minimized by the good sizing (increasing the transistors area) of these transistors, whereas the flicker noise contribution of the amplifying transistors (M1, M2) at the IF output is quite negligible since it is mixed with the LO signals and consequently shifted to high frequency. Therefore, the main contribution to the flicker noise is due to the switching transistors (M3-M6). In systems that employ

direct conversion schemes, the flicker noise becomes more challenging, since it is inversely proportional to the frequency. Nonetheless, in the proposed CMOS FDM, the RF (MR signals) are shifted to intermediate frequency bands that are far from the DC-band (in the proposed FDM the minimum IF is 10 MHz) which makes the effect of the mixer's flicker noise negligible.

Simulation Results

The double-balanced Gilbert mixer in figure 3.12 was designed in $0.35\ \mu\text{m}$ CMOS technology. The biasing voltage of the RF amplifying stage (V_{b1}) and the LO switching stage (V_{b2}) are provided by Beta multiplier circuits (such as the circuit in figure 3.25) which have good robustness against process and temperature variations. The following figures summarize the simulation results of the frequency mixer. Figure 3.13 depicts the transient output of the mixer for sinusoidal input signals. The RF and the LO signals are

$$RF = 250 \cdot 10^{-6} \sin(2\pi \cdot 400 \cdot 10^6 t), \quad LO = 0.5 \sin(2\pi \cdot 390 \cdot 10^6 t)$$

From this figure it can be seen that the mixer successfully multiplies the RF and LO signals generating the upper and lower sidebands. Although the two sidebands seem to be amplified versions of the input RF signal, the upper one shows lower amplitude which expresses a desirable low-pass filtering behavior of the mixer. The scattering parameters (s-

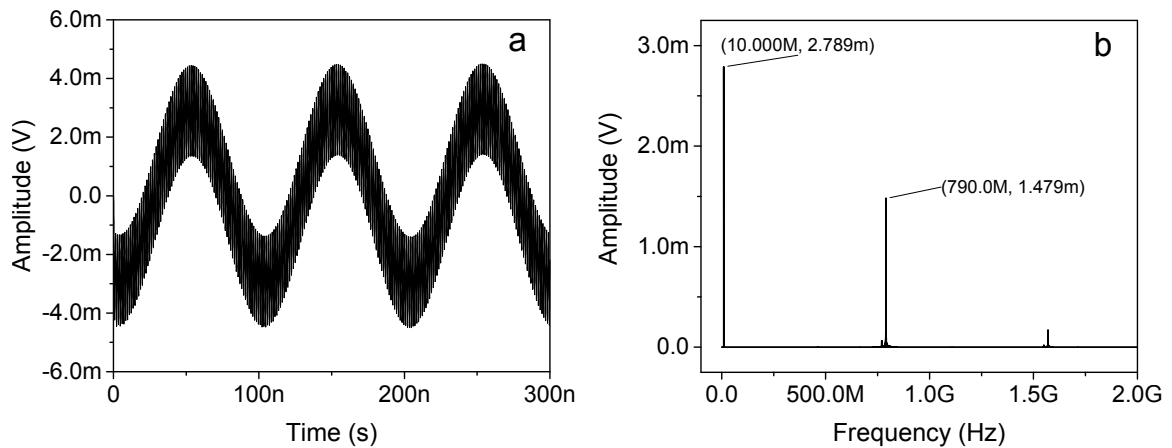


Figure 3.13.: Transient simulation of the double-balanced Gilbert mixer in figure 3.12 for a sinusoidal input. RF = 400 MHz while LO = 390 MHz. (a) Time domain. (b) Frequency domain.

parameters) of the frequency mixer are depicted in figure 3.14, from which one can see that the mixer exhibits a high (approximately 11 dB) forward conversion power gain, $S_{(IF-RF)}$. The mixer also shows a low feed-through of the LO into the RF port, $S_{(RF-LO)} < -80\ \text{dB}$,

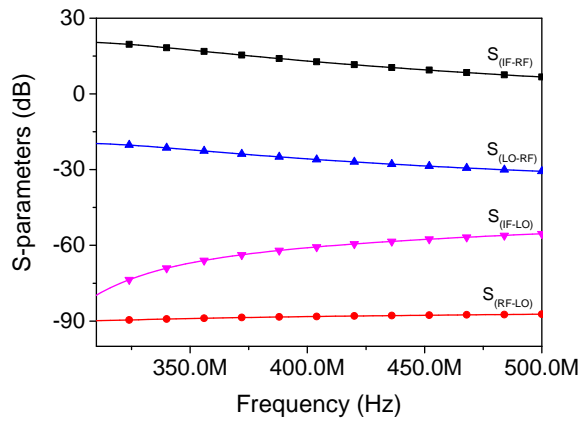


Figure 3.14: Plot of the S-parameters of the double-balanced Gilbert mixer.

which prevents the self mixing of the local oscillator and thus lowers the risk of having DC offset in the mixer’s output. Moreover, the mixer features a good suppression of the LO at the output port IF, $S_{(IF-LO)} < -50 \text{ dB}$. The noise figure of the mixer is an important parameter that affects the overall performance of the receiver. Usually the noise figure of the mixer is larger than that of the LNA. However, if the LAN has a large gain ($\geq 20 \text{ dB}$ for example), then the effect of the mixer noise is less severe. Figure 3.15a shows the noise figure of the mixer over a frequency range of 200 MHz with the RF and the LO being swept from 300 MHz to 500 MHz. The noise figure in this case ranges from 5.5 dB to 7 dB. Another important parameter of the mixer is the amount of LO power needed to achieve optimum operation of the mixer. In figure 3.15b the conversion power gain is plotted versus the power of the LO showing that the mixer can achieve maximum gain when the LO is -10 dBm.

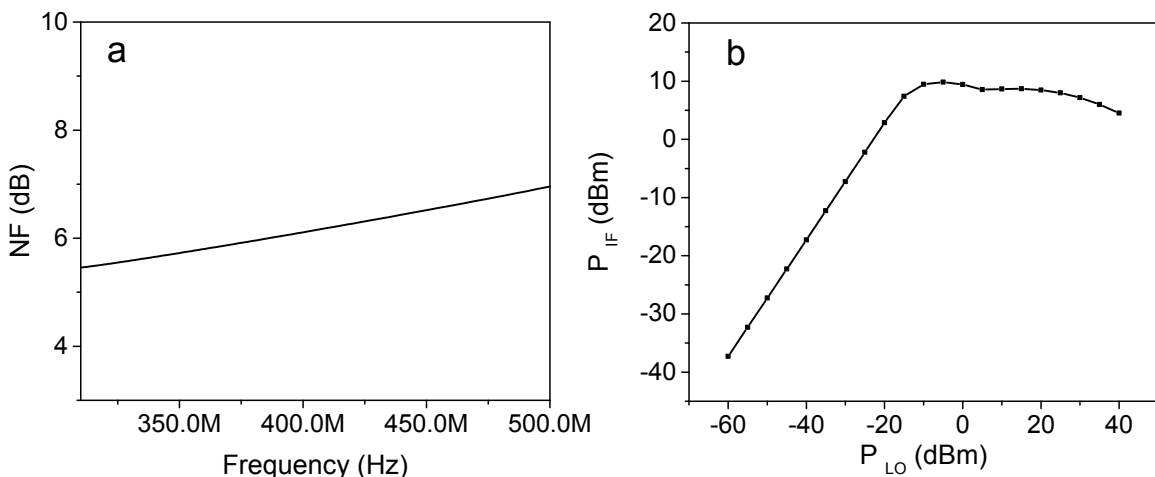


Figure 3.15.: Characteristics of the double-balanced Gilbert mixer. (a) Noise figure. (b) Conversion gain of the mixer versus the power of the local oscillator.

Table 3.4.: Summary of the frequency mixer's simulation parameters.

Parameter	Value	Unit
Voltage conversion gain (max)	20	dB
Noise figure (@ 400 MHz)	6.07	dB
S_{IF-LO}	<-50	dB
S_{RF-LO}	<-80	dB
Vdd	3.3	V
Current consumption	6.5	mA

3.4. The Bandpass Filter

The next component in the chain of a single channel of the MR FDM in figure 3.1 is the bandpass filter. It is particularly used to reject the up conversion sidebands that result from the mixing of the RF signal and the LO signal. Moreover, it cancels out any out-of-band noise and DC offsets. The main requirements the bandpass filter is supposed to fulfill can be summarized as follows

- The filter should have a center frequency $f_{c,j} \in \{10, 15, 20, 25, 30, 35, 40, 45\}$ MHz, since the MR signals are shifted to these intermediate frequencies.
- The flat bandwidth of the bandpass filter should be sufficient to handle a wide variety of MR signals from different samples, fields of view (FoV), and imaging configurations.
- The filter has to achieve adequate (at least - 50 dB) suppression of the undesired sidebands.
- The gain of the filter has to be flat in the pass band in order for the MR signals to be evenly amplified.

A passive bandpass filter such as the one shown in figure 3.16 can achieve the above requirements. However, and in spite of their advantages, the passive filters are not a thinkable solution in this case because they require large inductances (in the range of μH), which is impossible in CMOS technology due to the large area required. Therefore, the only conceivable solution is to employ active filters.

Amongst many different topologies and architectures used to realize active filters in CMOS technology, the multi-feedback RC topology, depicted in figure 3.17 [76, 90, 91], was chosen. This opamp-based topology was preferred to the Gm-C, mainly because of its higher linearity and input dynamic range. Furthermore, it offers more flexibility in

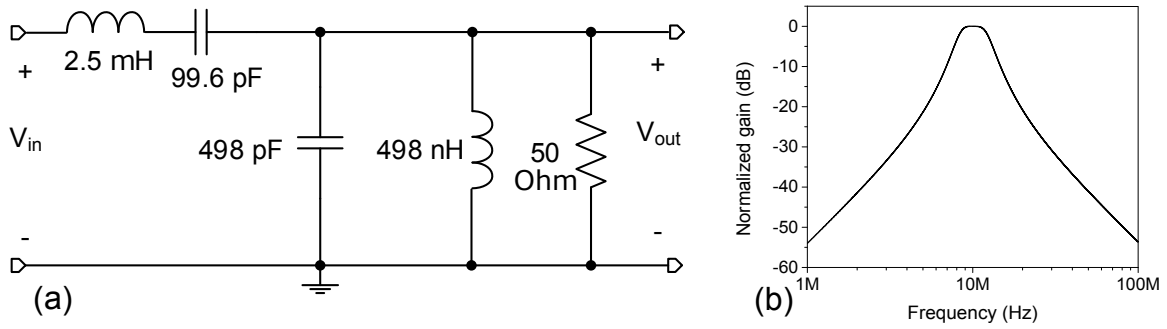
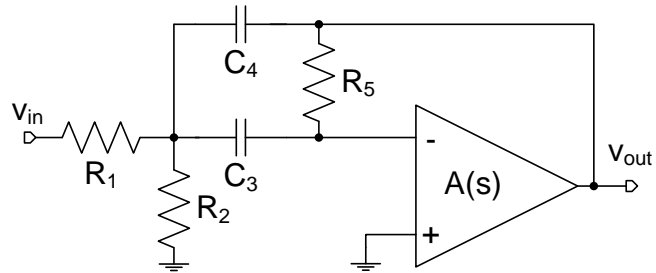


Figure 3.16.: A 4-th order Butterworth passive bandpass filter. (a) Schematic. (b) Frequency response.

designing the filter (especially defining the center frequency f_c), since it can be set by adjusting the values of R and C without modifying the opamp. The single-ended operation of the filter was chosen in order to save area and power. In figure 3.17, if $A(s)$ is the open

Figure 3.17: Schematic of a second-order bandpass filter realized using a multi-feedback RC active topology.



loop transfer function of the operational amplifier, then the transfer function, $H(s)$, of the circuit in figure 3.17 can be calculated by applying straightforward circuit theory as shown in equation 3.23.

$$H(s) = \frac{-G_1}{\alpha(G_1 + G_2 + sC_3 + sC_4) + sC_4 - sC_3/A(s)} \quad (3.23)$$

Here G_1 , G_2 , and G_5 are the reciprocals of R_1 , R_2 , and R_5 respectively, and α is given by

$$\alpha = \frac{G_5 + sC_3 + A(s)G_5}{A(s)sC_3} \quad (3.24)$$

If the open-loop gain, A , is much larger than 1 ($A \gg 1$) and $sG_5(C_3 + C_4)/A \cdot sC_3G_1$ is approximately zero, then $H(s)$ can be approximated by

$$H(s) = \frac{-sG_1C_3}{s^2C_3C_4 + sG_5(C_3 + C_4) + G_5(G_1 + G_2)} \quad (3.25)$$

which expresses the transfer function of a second-order Butterworth bandpass filter with center frequency f_c given by

$$f_c = \frac{1}{2\pi\sqrt{R_2R_5C_3C_4}} \quad (3.26)$$

Assuming $C_3 = C_4 = C$ (which is the usual case for the bandpass filter with this topology), the gain A_v , quality factor Q , and bandwidth BW of the filter are determined by the following equations

$$A_v = -\frac{R_5}{2R_1} \quad (3.27)$$

$$Q = \pi f_c R_5 C \quad (3.28)$$

$$BW = \frac{1}{\pi R_5 C} \quad (3.29)$$

The order of the bandpass filter can be increased to fourth order by cascading two second-order filters with center frequencies ($f_{c,1}$ and $f_{c,2}$) symmetrically around the desired center frequency f_c as shown in figure 3.18a. Figure 3.18b shows the results of a Monte-Carlo

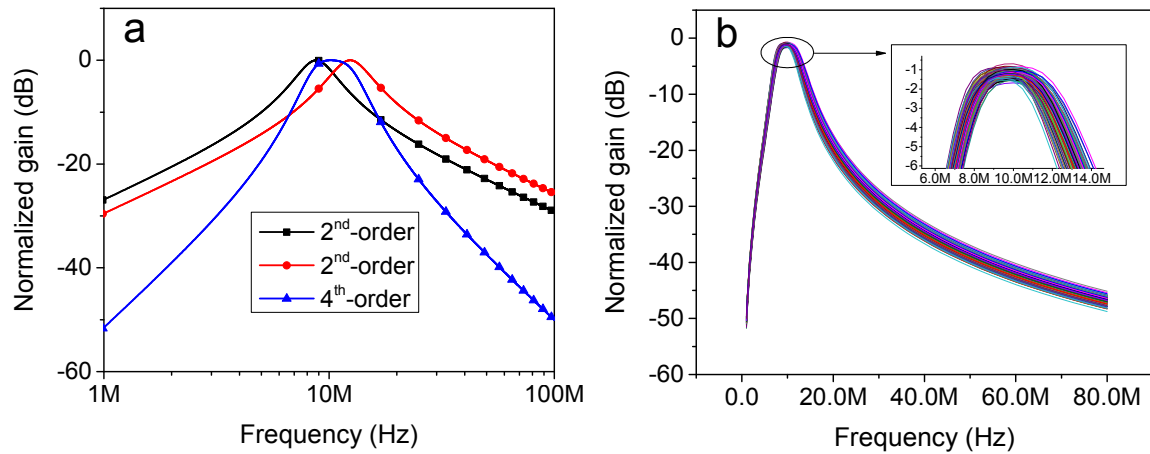


Figure 3.18.: (a) Frequency response of the bandpass filter depicted in figure 3.17. The lines marked with small circles and squares show the response of two second-order filters while the line marked with small triangles shows the response of a fourth-order filter realized by cascading the two second-order filters. (b) Result of 100 Monte-Carlo simulation runs for the extracted layout of a 10 MHz fourth-order BPF.

simulation for the extracted layout of a 10 MHz fourth-order BPF design over 100 runs. The simulation results demonstrate that the bandpass filter design described above is, to a good extent, robust against process variations and errors. The filter is likely to have a small drift in the center frequency of the filter due to process tolerances but since the bandwidth of a filter is at least a factor of two larger than that of its associated MR signal, this shift will not be a crucial problem. Another method to overcome the drift is through the fine adjustment of the local oscillator frequencies which will be generated externally using digital synthesizers.

Figure 3.19 shows the frequency response of the extracted layout of eight fourth-order bandpass filters realized by cascading two active filters, such as the one in figure 3.17, and

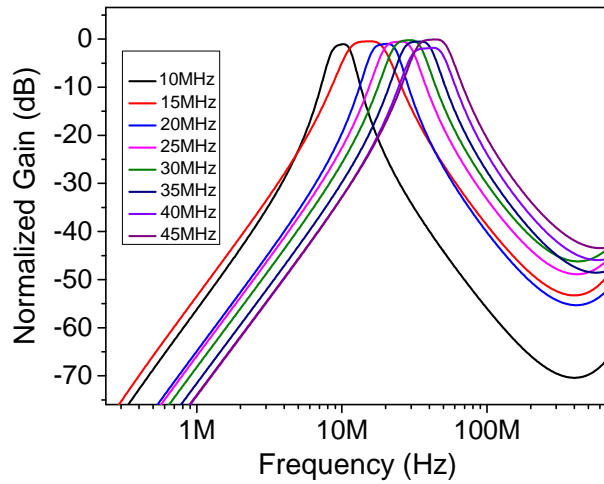


Figure 3.19: Frequency response of the extracted layouts of eight fourth-order bandpass filters employed in the MR FDM. The filters have center frequencies $f_{c,j}, j \in \{10, 15, 20, 25, 30, 35, 40, 45\}$ MHz.

adjusting the values of the feedback resistors and capacitors to obtain the desired center frequency. The opamp topology employed in the design of the eight filters is the same, and it will be discussed in the following section.

3.5. The Operational Amplifier

As discussed in the previous section, there exists a number of requirements the operational amplifier must fulfill in order to be successfully employed in the design of a BPF.

A major issue amongst these requirements is to exhibit a high open-loop gain in the frequency band of interest. In the proposed MR FDM the IF signals occupy the frequency range from 10 MHz to 45 MHz. Therefore, the design of the opamp should take into account that $(A(s) \gg 1)$ over this frequency

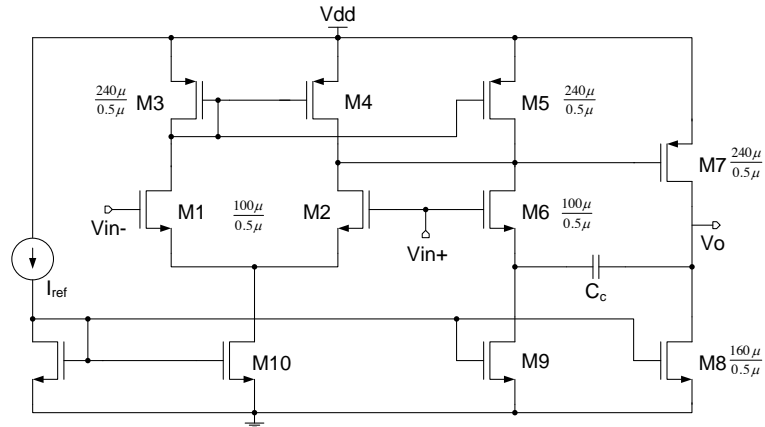


Figure 3.20.: High speed two-stage operational amplifier with indirect compensation.

be considered with great care

while designing the opamp. Therefore, the rate of change of the opamp's output has to satisfy the following equation in order to avoid distortion.

$$SR \geq 2\pi f A \quad (3.30)$$

Here f is the signal's frequency and A is its amplitude. While the last equation can calculate the minimum slew rate of the opamp, its gain bandwidth product (GBW) was determined using a Matlab script. This script assumes a single pole transfer function of the opamp as an approximation then iterates until the minimum GBW, that achieves the desired operation of the BPF, is obtained. Taking the BPF with 45 MHz center frequency as a worst case, it was found that a minimum open-loop gain of 46 dB and a minimum GBW of 1 GHz are required.

In order to achieve these requirements, the opamp's topology displayed in figure 3.20 [11] was utilized. This two-stage topology achieves a good compromise between high gain and high speed needed for a proper operation of the BPF. The first stage comprises an NMOS differential amplifier (M1 and M2), whereas the second stage consists of a PMOS CS amplifier (M7). The topology also employs a Miller compensation network (C_c). The compensation current i_c is fed indirectly through the CG transistor (M6) to the output of the first stage. This indirect compensation renders pole-splitting and ensures that the opamp does not have any zero in the right half plane. Moving the zero of the opamp to the left half plane adds its phase response to the overall phase response and thus increases the phase margin of the opamp. This increase inherently increases the stability and the speed of the operational amplifier. The opamp's unity-gain frequency f_{un} , zero f_z , and slew rate SR are described by the following equations

$$f_{un} = \frac{g_{m1}}{2\pi C_c} \quad (3.31)$$

$$f_z = \frac{g_{m6}}{2\pi C_c} \quad (3.32)$$

$$SR \propto \frac{I_{ss}}{C_L} \quad (3.33)$$

where C_L is the load capacitance.

Simulation Results

In this subsection the extracted layout simulations for the most important parameters of the opamp, shown in figure 3.20, are demonstrated. This opamp, designed in 0.35 μm CMOS technology, draws 15 mV from a 3.3 V source. Figure 3.21 depicts the open-loop gain and phase response of the opamp versus the frequency. According to this figure the opamp exhibits a GBW of 1.2 GHz which ensures that the opamp can be employed in the BPF design as explained in the previous section. Furthermore, the opamp achieves a phase margin of 65 which expresses a high-stability performance. The noise performance is another important aspect that should be carefully considered while designing the opamp. This aspect is demonstrated in figure 3.22a where it can be seen that the opamp features a

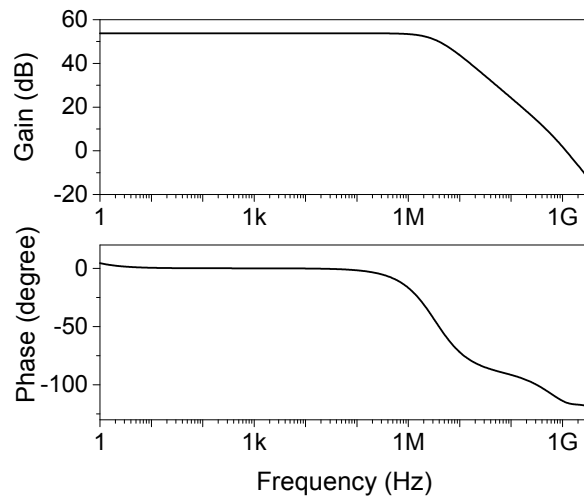


Figure 3.21: Open-loop frequency response of the operational amplifier.

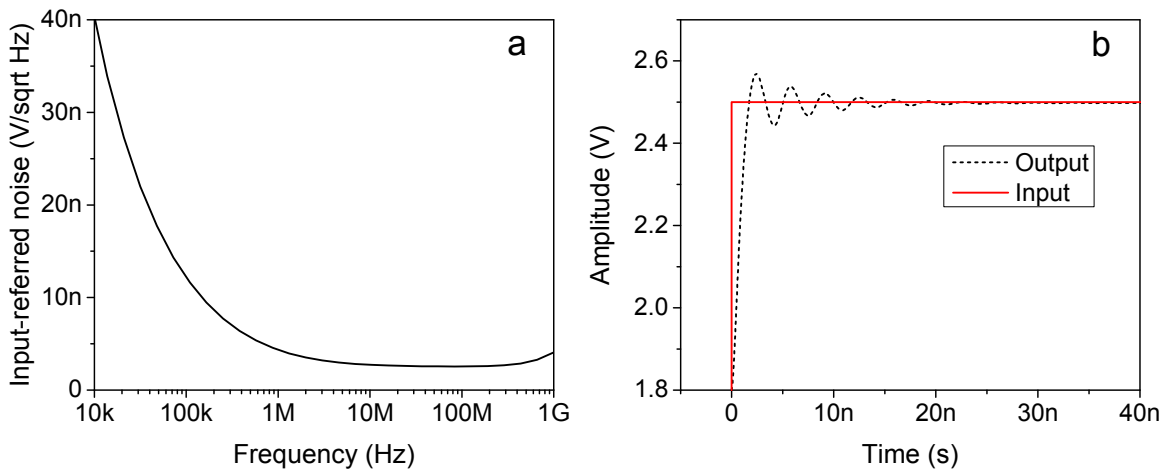


Figure 3.22.: (a) The input-referred noise of the operational amplifier. (b) The opamp's output for a transient simulation of the opamp with a pulse excitation.

relatively low ($\sim 2.7 \text{ nV}/\sqrt{\text{Hz}}$) input-referred noise over the frequency range required for the BPFs and the adder (10 MHz - 45 MHz). Figure 3.22b depicts the step response of the opamp. The dashed curve shows the time-domain output while the continuous red curve shows the input signal. In this simulation the opamp was connected as a buffer with a 20 pF capacitive load. The slew rate of the opamp can be directly estimated from this figure to be approximately $400 \text{ V}/\mu\text{s}$ which ensures that equation 3.30 is fulfilled for all possible values of signal amplitudes. After the bandpass filtering stage, the MR signals are added using the same opamp topology as in figure 3.20. Therefore, it is of high importance to characterize the performance of the opamp in a closed-loop adding operation such as the one displayed in figure 3.23a. In this figure the opamp sums and amplifies the input signals ($V_{in1}, V_{in2}, V_{in3}, \dots$). Part (b) of the figure shows the frequency response of the circuit. It can be seen from this figure that the opamp can achieve a maximum gain of 20 dB over

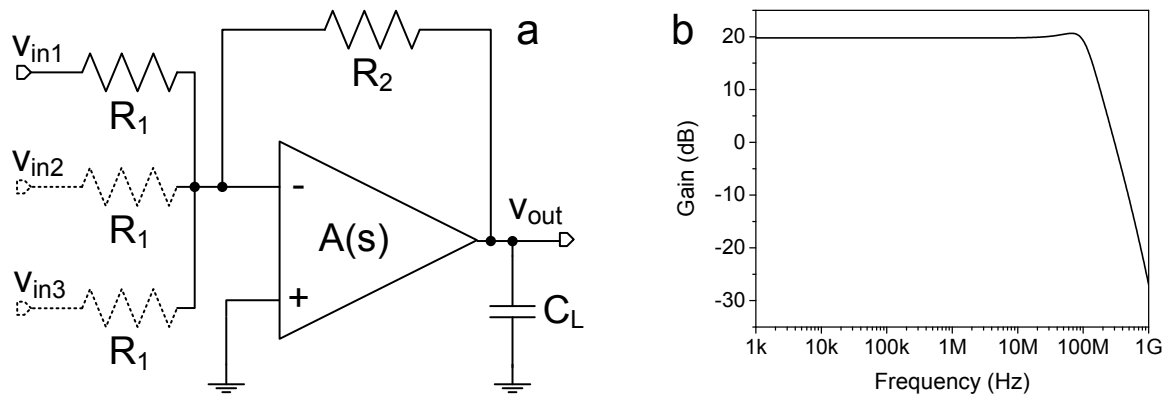


Figure 3.23.: Closed-loop operation of the operational amplifier. (a) Circuit topology of adder. The output voltage is an amplified sum of the input voltages $V_{in1}, V_{in2}, V_{in3}, \dots$. (b) The frequency response of the circuit in (a) showing a maximum achievable gain of 20 dB over a wide frequency range up to 200 MHz.

a wide frequency range up to 200 MHz which again makes it very appropriate for the MR FDM. A summary of the main specifications of the operational amplifier is found in table 3.5.

Table 3.5.: Summary of the operational amplifier parameters.

Parameter	Value	Unit
Open-loop gain	54	dB
Closed-loop gain (max)	20	dB
Gain-bandwidth product (GBW)	1.2	GHz
Slew rate	400	V/ μ s
Phase margin	65	$^\circ$
Input noise	2.7	nV/Hz ^{1/2}
Vdd	3.3	V
Current consumption	15	mA

3.6. Additional Elements

Besides the MR FDM elements that have been so far discussed, additional circuits are necessary for the complete successful functioning of the system as a whole. Such circuits comprise buffers and biasing circuits and are discussed in detail in the following subsections.

3.6.1. Inter-stage Buffers

The voltage gain of the LNA is highly dependent on the its output impedance. Therefore, it is directly influenced by the input impedance of the succeeding circuit element (the frequency mixer in this case). The simulation results of the LNA and the mixer showed that the later exhibits an input impedance that is one fourth of the output impedance of the LNA which means that the mixer will degrade the LNA's gain by approximately a factor of four. In order to avoid this decrease in the gain a buffer circuit as depicted in figure 3.24a is employed. This buffer is a differential input differential output circuit that provides relatively high input and low output impedances. Figure 3.24b shows a single-ended version of the circuit in figure 3.24a which is used as a buffer between the mixer and the BPF. This buffer is also important because it prevents the input impedance of the BPF, which varies according to the RC configuration, from affecting the mixer's gain.

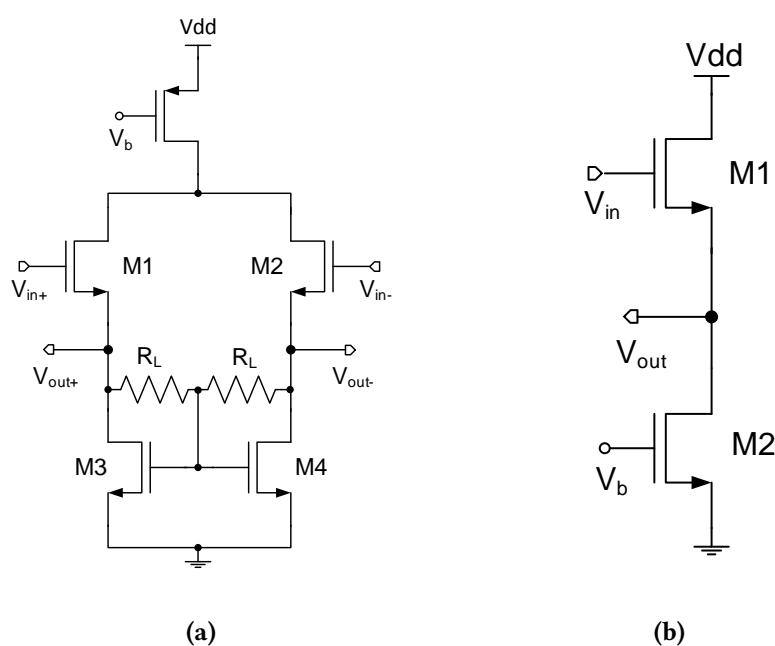


Figure 3.24.: (a) A differential buffer stage between the LNA and the mixer. (b) Single-ended buffer used after the mixer.

3.6.2. Biasing Circuits

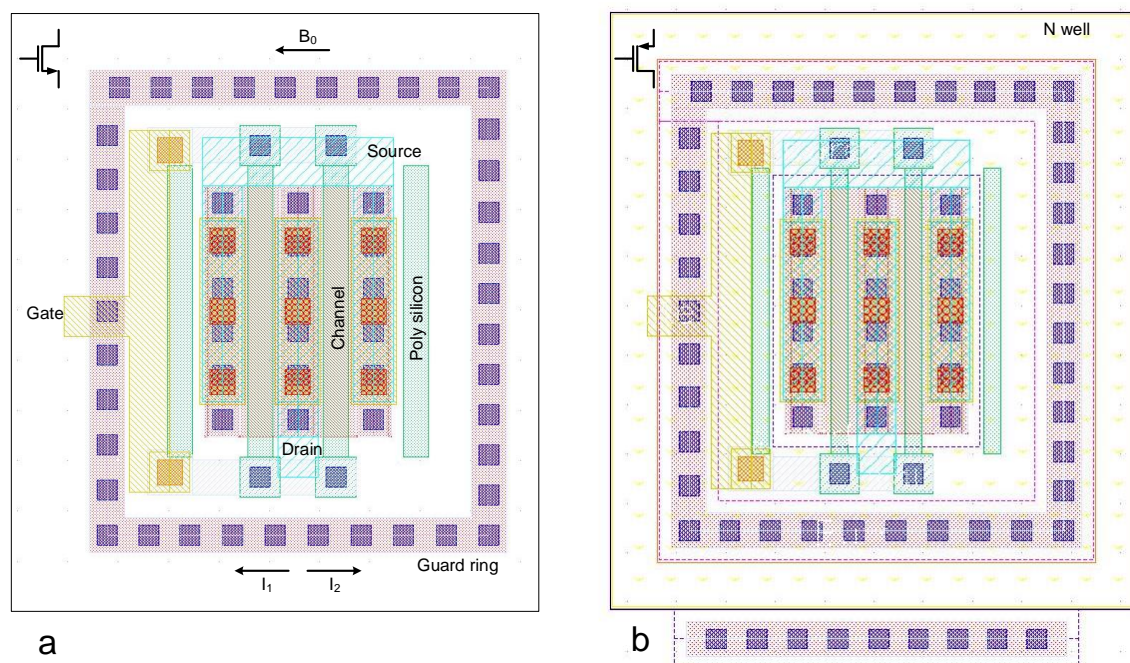


Figure 3.26.: The layout of the RF transistors employed in the design of the CMOS FDM. (a) NMOS. (b) PMOS.

between the high frequency signals. Moreover, they prevent current leakage from the diffusion layers through the substrate which can result in unwanted operation modes of the transistors. Since the CMOS FDM is designed to operate in high (up to 11.7 T) magnetic fields, great care was taken during the design of the layout to ensure that the transistors are placed in a way such that the current flow is parallel to the B_0 . In this case, the Lorentz forces and the Hall effects inside the transistors are avoided and thus the overall effect of the field on the chip performance is minimized. Various techniques were applied in order to optimize the layout design. One of these techniques is the common-centroid technique which was employed in all the differential pairs of transistors that need a very high degree of matching such as the pairs in the LNA, the buffer, the frequency mixer, and the differential pair of the opamp. This technique is applied to the transistor pair A and B by dividing each of them into a number of parallel elements. These elements are then configured such that A and B have a common centroid. By doing so, we guarantee that A and B are evenly subjected to the process errors and variations, thus preserve their matching through all the fabrication steps. This technique was also applied to the cross-coupling capacitors and the load resistors as well. Another technique that was extensively applied is the use of dummy structures, as in figure 3.27, to ensure that each active element has a symmetric interaction with the adjacent elements. Figure 3.28 shows the complete layout of the CMOS FDM with all individual elements highlighted. The total

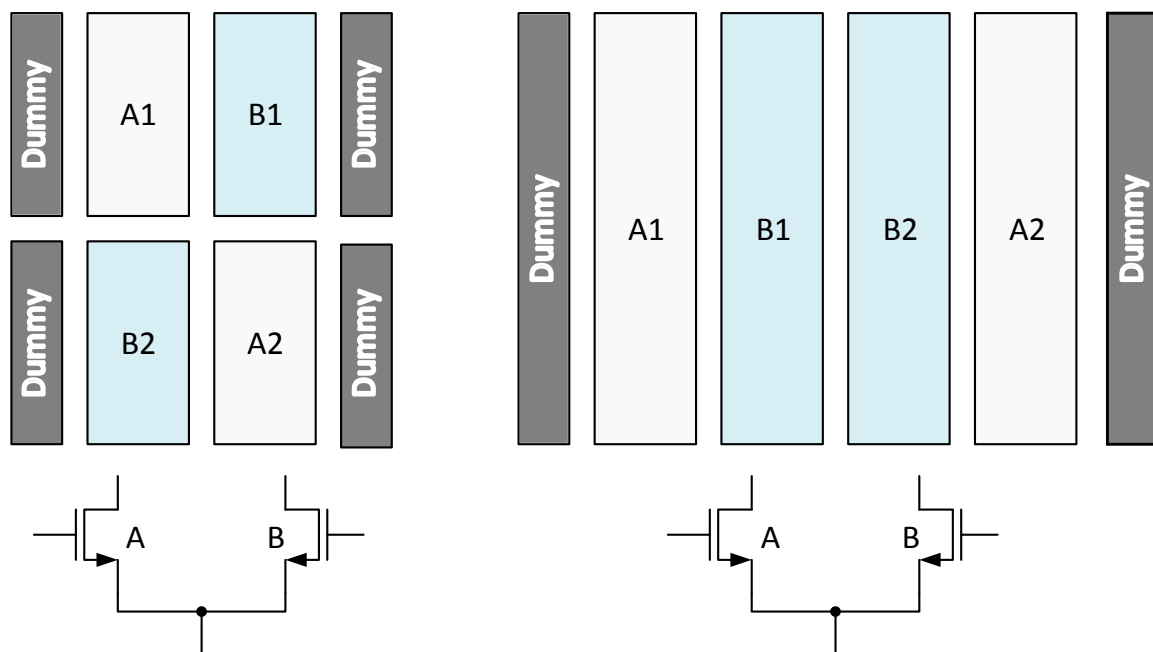


Figure 3.27.: Examples of common-centroid configurations that were employed in the design of the layout.

area of the chip is $3.4 \times 4.6 \text{ mm}^2$. Each channel is bounded by a Vdd and GND connection lines that have the same length as the channel layout and composed of all metal layers. This allows to switch each channel ON and OFF individually. Moreover, using the four metal layers in the power lines is necessary to bear the current (56 mA/Channel) of the channel.

3.8. Summary

In this chapter the design of an 8-channel magnetic resonance frequency division multiplexer (MR FDM) in CMOS technology was presented. The different components of the FDM were explained in detail including aspects such as the work principle and the advantages and disadvantages. The simulation results of the different components were depicted and discussed. Table 3.6 summarizes the post-layout simulation results of the CMOS FDM. According to this table, the channels exhibit an average voltage gain of 37 dB and an average noise figure of 6 dB. The average of the maximum allowed input signal is 9 mV. These values are very consistent with the MR signal constraints discussed in section 3.1.

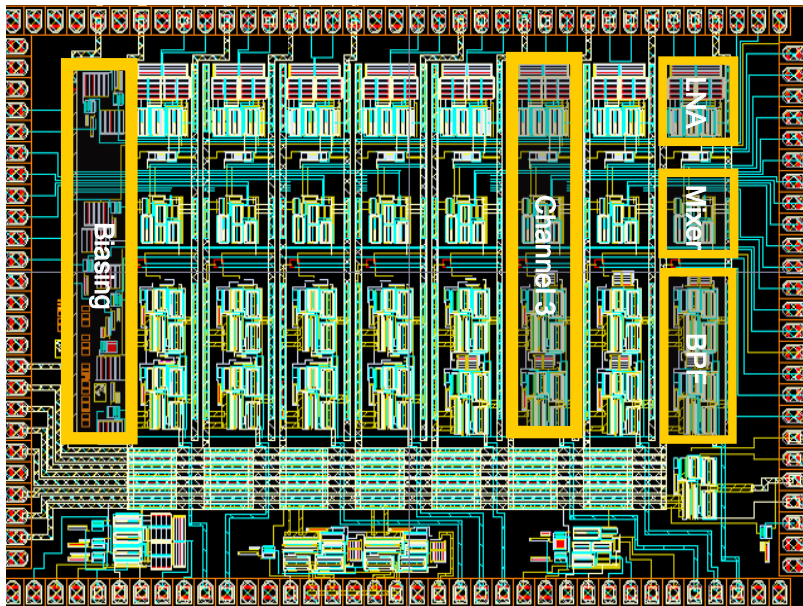


Figure 3.28.: Chip layout.

Table 3.6.: Post-layout simulation results of the CMOS FDM channels.

Parameter	Value	Unit
Channel gain (max)	37 ± 2	dB
Channel NF (min)	6.8 ± 0.2	dB
Channel linearity ($IIP1_{max}$)	6 ± 1	mV
Channel coupling (max)	-15.4 ± 0.6	dB
Power consumption/channel	184.8	mW

4. Simulation of The MR Receiver

4.1. Introduction

Predominantly, reports on the testing and characterization of MRI hardware topologies are either based on realizations of built circuits [7, 17, 42, 46, 82, 102], undergoing real tests in an MRI scanner, or based on conventional circuit simulations of gain, frequency response, linearity, noise figure, etc. Therefore, extensive practical experience is required to understand the relation between circuit design decisions and their impact on actual MRI imaging procedure. Indeed, when debugging MRI hardware, it is highly desirable to consider separately the effects of the electronic design decisions, differentiated from other components within the signal processing chain, on the MR imaging performance. As MRI systems become more complex, as for example upon moving to a large number of parallel channels [40], or employing sophisticated theoretical building blocks [48, 50, 51], effective debugging becomes a key to productive systems design work. What is therefore lacking, as surmised from the literature, is a virtual environment with which to directly evaluate the electronic signal path in the context of MR-imaging.

This chapter aims to fill this gap by introducing a novel simulation method which enables the circuit level characterization of MRI hardware whilst an MR image is being formed [59]. It involves performing a virtual MR imaging experiment using actual FID data as input to a circuit simulation program (Cadence in this case). The methodology is particularly beneficial in the design of integrated circuit (IC) hardware, which is expensive to realize (let alone to iterate designs), yet potentially offers significant gains in performance once robust solutions are obtained. The approach exclusively employs industry-standard commercial software (Matlab, Cadence) which makes it readily accessible. The block diagram in figure 4.1 describes how the method works. In brief, the user starts the simulation flow via a matlab GUI using data from an MR image file, or a commercial scanner's FID file. Then, the coil signals, corresponding to the uploaded image, are generated in a format compatible with the circuit simulator (in this case the IC design environment Cadence with Spectre simulator). After that, these signals are fed into Cadence to run a transient simulation of the transistor-level or extracted-layout of the desired hardware. Finally, the simulation outputs are fed into another Matlab GUI that reconstructs the MR image. The performance

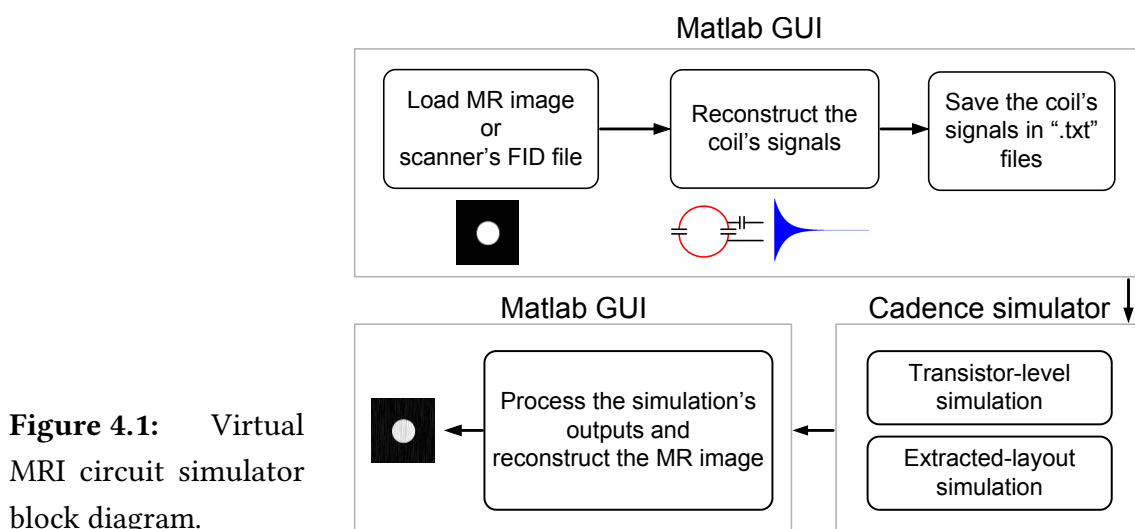


Figure 4.1: Virtual MRI circuit simulator block diagram.

of the desired hardware is evaluated by conducting a comparison between the original and the reconstructed image.

4.2. Generating Coil FID Signals from MR Images

In order to perform a realistic test and precise characterization of a custom MR receiver circuit through a virtual imaging experiment, we first need to obtain representative MR echo signals as they are induced in the reception coils. Such signals are normally not accessible to the user or the circuit designer. However in most MR scanners, samples of these signals are stored as k-space data or can be directly generated via inverse Fourier transform of real or surrogate MR images. Practically, these k-space samples are taken at the end of the receiver chain illustrated in figure 2.8. Therefore, our task, in order to regenerate the coil signals, is to propagate the k-space samples in the reverse direction along that receiver chain path.

Figure 4.2 depicts the graphical user interface of the Matlab script "Reconstruct_Echo" that performs this reversed process. The program assumes a rectilinear filling of the k-space via a Spin-Echo or gradient-echo sequence [16, 41], therefore, each row is handled independently. The process is started by uploading an MR image to the program. Then, Fourier transformation is applied to obtain the Cartesian k-space of the respective image. Each row within the k-space consists of a real part, that represent the samples of the in-phase component of the MR echo, and an imaginary part that stands for the quadrature component of the echo. The two parts of the individual row are separated and then zero-padding is applied by adding extra dummy points. This zero-padding is essential in order to avoid the unwanted effects of the transient response of the circuit. The sampling time

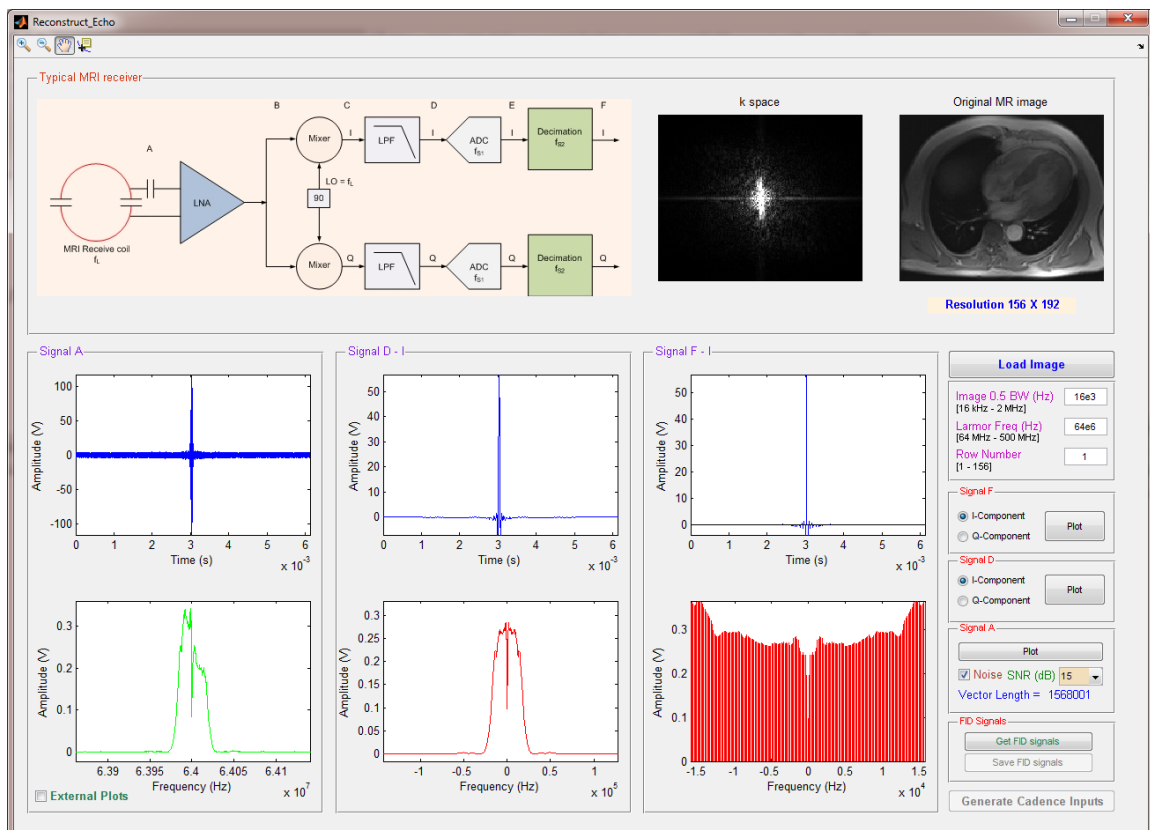


Figure 4.2.: GUI of Matlab program to reconstruct MR coil echo signals from MR image.

ts at which the samples are originally taken is mainly determined by the bandwidth of the MR signals which is, in turn, defined by various parameters including the specifications of the MR scanner, the strength of the gradient fields used, and the sample's geometry. According to these parameters, the user may specify the bandwidth of the MR signal, from which the program calculates afterwards the sampling time ts . Since the MR signals induced in the reception coil have a high frequency content (MR signals are centered at the Larmor frequency f_0), and in order to resolve them at this frequency, it is necessary to define a new sampling time ts_a that fulfills the Nyquist criteria for the signals at the desired frequency. From simulations it was found that $ts_a = 0.05/f_0$ is a fair choice. Furthermore, it was found that specifying a smaller ts_a has no noticeable influence on the quality of the simulations, but leads to a significant increase in the simulation time. Hence, this choice of ts_a achieves a good compromise for efficient simulation time. Moreover, with this sampling time it is possible to investigate the effects of high order harmonics and sidebands that result during the frequency conversion in the circuit. The samples at the intermediate time steps $n \cdot ts_a$ are determined by means of a high order interpolation scheme. Subsequently, the in-phase and quadrature components are multiplied by carriers that have the desired Larmor frequency and have 90° phase difference as illustrated in the following equation

$$x_{coil} = x_I \cdot \cos(\omega_0 t) + x_Q \cdot \sin(\omega_0 t) \quad (4.1)$$

The signal's amplitude is estimated according to equation 2.8, while equation 2.10 is referenced in determining the noise level in the signal. After adjusting the signal's amplitude, and adding white Gaussian noise (the noise is added only to images that originally do not contain noise), the signals are saved in a format compatible with the circuit simulation environment. This process is repeated for all rows of the k-space, and once it is completed, the MR signals are ready to be used as test inputs for custom receiver circuits. Figure 4.3 summarizes the steps of reproducing a single coil echo corresponding to a single row of the k-space.

4.3. Image Reconstruction from Coil Signals

In order to verify the procedure explained in the previous section, another Matlab program "Image_Reconstruct" was written. The program, with the graphical user interface depicted in figure 4.4, emulates a typical MR receiver chain that employs a direct (homodyne) frequency conversion. It consists of a low-noise amplifier, a quadrature frequency conversion, a low-pass filter, an ADC, and a decimation stage. The program allows the user to read the MR coil signal generated by the program in figure 4.2 and process them to obtain an image.

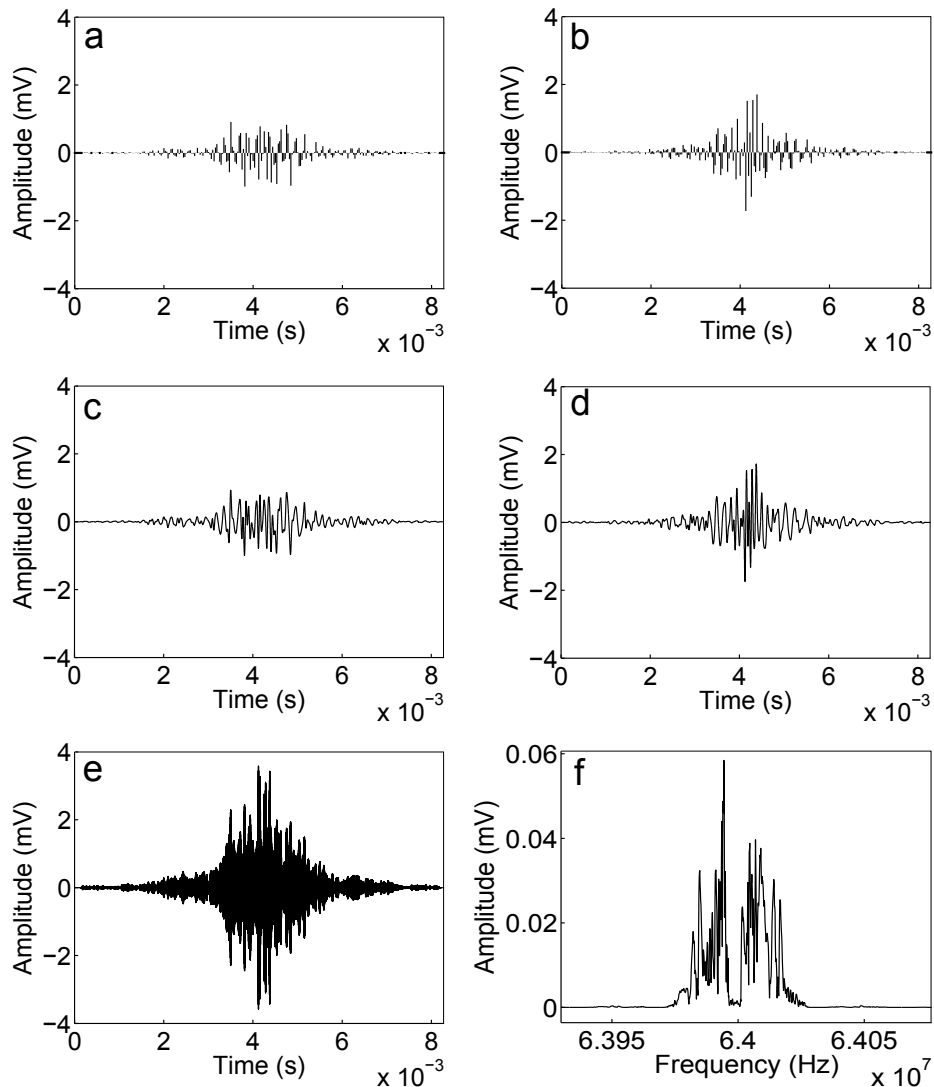


Figure 4.3.: Steps to reconstruct the MR echo for a single k-space image row. (a), (b) Samples of the In-phase and quadrature demodulated components of the MR signal. t_s is determined by the bandwidth of the signal. Zero padding is employed to avoid the effects caused by the transient response of the circuit. (c),(d) Defining the interpolation time step $t_{sa} < t_s$ and applying high order interpolation for the in-phase and quadrature signals respectively. (e) Combining the I and Q components and shifting the signal to the desired Larmor frequency (64 MHz in this case). (f) FFT of the MR echo.

4. Simulation of The MR Receiver

Moreover, the program enables the circuit designer to investigate the effects of many parameters of the circuit elements on the image quality as demonstrated in figure 4.5.

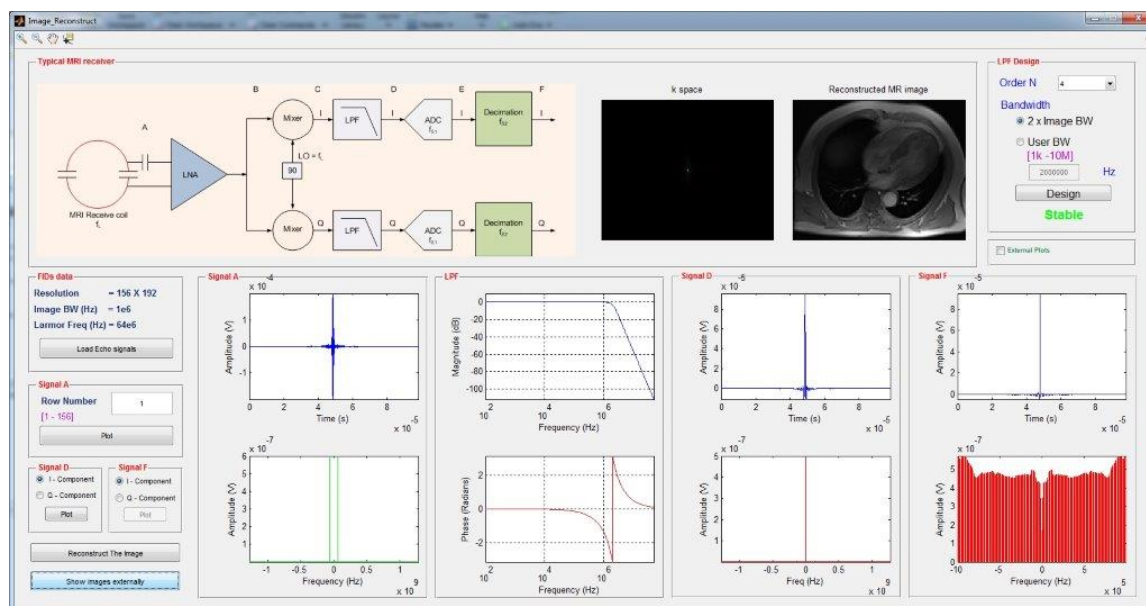


Figure 4.4.: GUI of a Matlab script that reconstructs the MR image from the coil signals generated by the program in figure 4.2.

As such, the circuit designer can employ this program to precisely determine the specifications of each component in the receiver chain. By means of the tool displayed in

Figure 4.5: Spanned GUI from the program in figure 4.4 that allows the user to set the gain and noise figure of the different elements of the MR receiver.

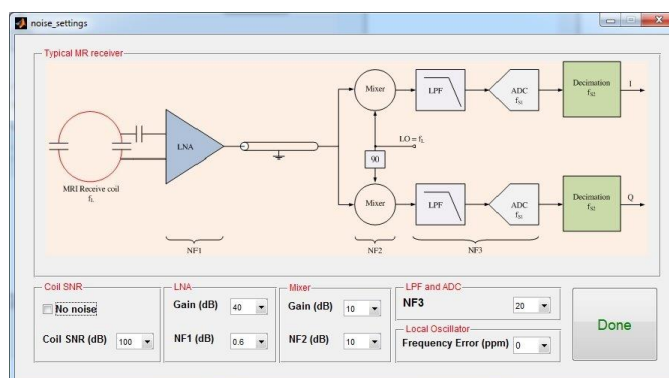


figure 4.5, the "Image_Reconstruct" program allows the user to set the gain and the noise figure of the various elements of the MR receiver. It also enables the user to set the jitter noise of the local oscillator in order to examine the effects of its phase noise on the image. Furthermore, the program exhibits another important feature with which the user can set the number of bits of the ADC to test the effect of its resolution on the image. Finally, the bandwidth and the order of the low-pass filter can be adjusted so as to investigate the

filtering effects in terms of image quality. Thus by changing these parameters, the user can see their effects as image artifacts or as a degradation in the SNR using the program in figure 4.6. This program calculates the SNR of two identical user-selectable regions



Figure 4.6: GUI of a Matlab program used to compare the original and the reconstructed MR image. It also determines the SNR of identical user-selectable regions of interest in both images, indicated here by yellow (signal region) and red (noise region) rectangles via equation 4.2.

of interest in both the original and the reconstructed images according to the following equation [25, 82]

$$SNR = \sqrt{\frac{4 - \pi}{2}} \frac{\text{Mean}(\text{Tissue})}{\text{StdDev}(\text{Air})} \quad (4.2)$$

Simulation Results

So as to verify the functionality of the programs in figures 4.2 and 4.4 a simulation of an MR image of fish oocytes, acquired with a seven-channel receive micro-array [36], was conducted. The simulation was started by uploading the original fish oocytes MR image, depicted in figure 4.7(a), to the "Reconstruct_Echo" program in figure 4.2. After setting the Larmor frequency and the bandwidth of the image, the program generates the coil signals and saves them in a ".mat" file. The program also generates another ".mat" file that contains imaging parameters necessary for the image reconstruction. These comprise image size, ts , ts_a , Larmor frequency, bandwidth, etc. After that, the generated ".mat" files that contain the coil signals are read by the "Image_Reconstruct" program in figure 4.4. After the user sets the gain and noise figure of the different elements of the MR receiver as in figure 4.5, the program first amplifies the signals, then it directly demodulates them from the high Larmor frequency to the baseband in a quadrature form in order to extract the I and Q components of the signals. After that, the signals are low-pass filtered to reject the out-of-band noise as well as the higher sidebands resulting from the frequency conversion. Finally, analog-to-digital conversion is exploited by sampling the MR signals and quantizing them into a number of levels defined by the user. The final samples are used to fill the k-space which is, in turn, converted to an MR image via a two-dimensional Fourier transform. Figure 4.7 displays the simulation results for the fish oocytes MR image.

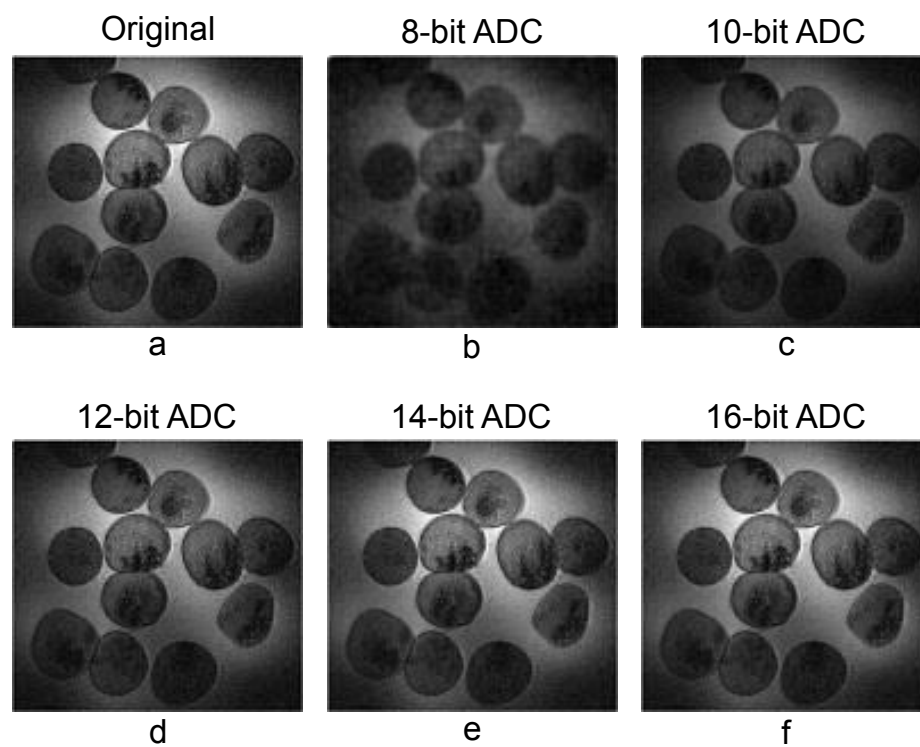


Figure 4.7.: Effect of resolution of the ADC on the quality of the reconstructed image. (a) The original image. (b,c,d,e,f) The reconstructed images using an 8, 10, 12, 14, and 16-bit ADC respectively.

It demonstrates the effect of the number of bits of the ADC on the quality of the image. Figure 4.7(a) shows the original MR image which initially drove the simulation, while figures 4.7 parts (b, c, d, e, f) show the reconstructed MR image with 8, 10, 12, 14, and 16 bit ADC resolution respectively. From this figure it is obvious that the coil signals can be successfully obtained by means of the program in figure 4.2 and the image can be swimmingly reconstructed from these signals by means of the program in figure 4.4. Moreover, it can be noticed from figure 4.7 that increasing the number of bits of the ADC significantly enhances the quality of the image. However, 14-bits seem to be a sufficient resolution of the ADC for MR receivers after which increasing the number of bits will not show a remarkable enhancement in the SNR of the image.

4.4. Simulation of 8-Channel FDM

The Matlab program in figure 4.2 also generates text files that contain time-amplitude data pairs of the signals generated in the MR coils. These files are imported as "vpwlf" sources for the integrated circuit simulator "Spectre" so as to drive a transient simulation of the custom receiver circuit. A so-called "Ocean" script [12] (see appendix A) was written to automatically import the coils MR signals from Matlab to Cadence, run the simulation, and export the simulation outputs as a ".matlab" files.

In order to process the simulation results from the 8-channel MR FDM described in chapter 3, a further Matlab program "Image_reconstruct_from_cadence" with graphical interface, as illustrated in figure 4.8, was written. This program is designed to process the simulation outputs of the 8-channel MR FDM as well as the 16-channel MR FDTD multiplexer that will be introduced later in this chapter. In the case of the 8-channel MR FDM, the image reconstruction will be performed as follows: first, the multiplexed output, which comprises eight MR signals occupying the frequency band from 10 Hz to 45 MHz, will be sampled and quantized with a number of bits of the ADC defined by the user. Then the digitized signal is introduced to eight quadrature homodyne demodulators running simultaneously. These demodulators feature the frequencies $f_i \in \{10, 15, 20, 25, 30, 35, 40, 45\}$ MHz. After the demodulation, the signals are low-pass filtered to reject the noise and the undesired sidebands. This process will be repeated for all rows in the image. Finally, the digitized and demodulated MR signals are decimated and used to fill the k-space maps which are then converted to MR images by means of Fourier transform. This process of processing the multiplexer output is summarized in figure 4.9.

To test and characterize the 8-channel MR FDM presented in chapter 3, eight unique images were created using a bitmap editor, so as to emulate the simulation of acquisition from eight perfectly decoupled coils. The image bitmaps $I_j, j \in \{1, \dots, 8\}$ graphically

4. Simulation of The MR Receiver

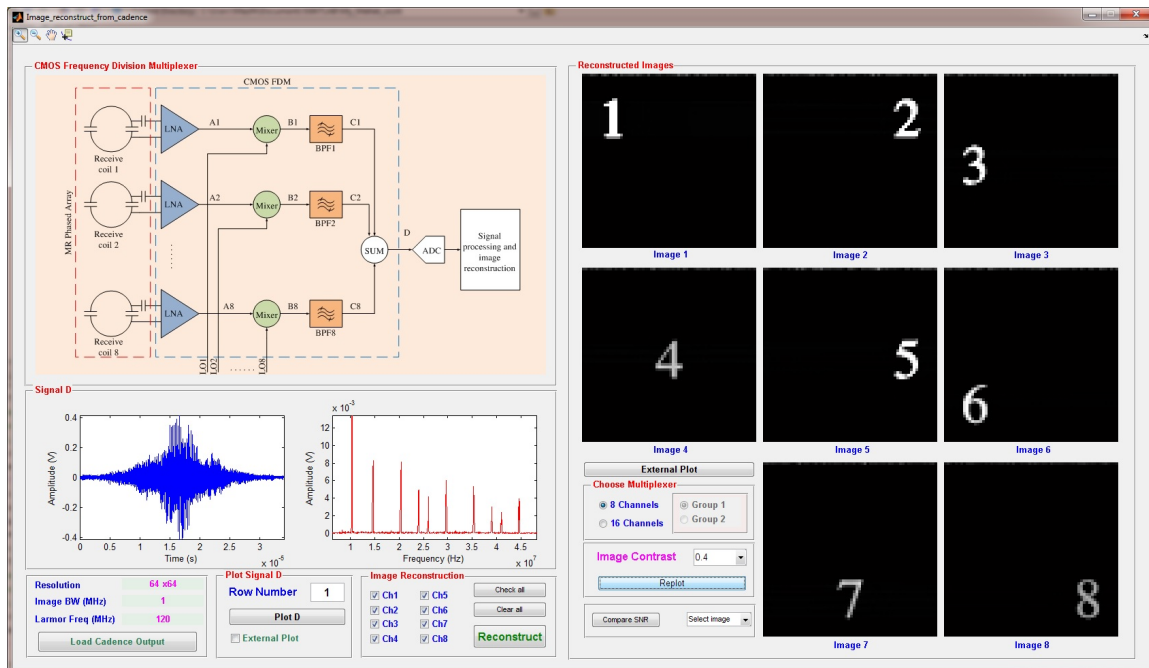


Figure 4.8.: GUI of a Matlab program that processes the outputs of the circuit simulation and reconstructs the MR images from these outputs. The program can process the simulation results from the 8-channel MR FDM in figure 3.1 as well as the 16-channel MR FDTD multiplexer depicted in figure 4.14.

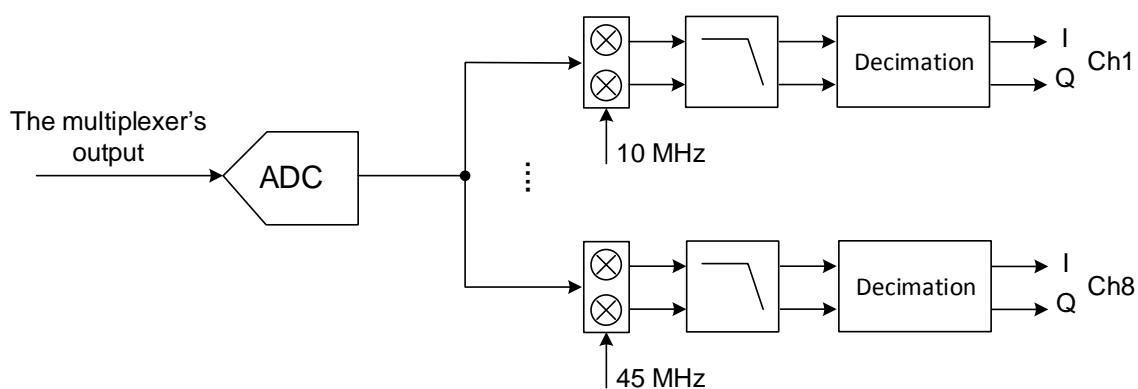


Figure 4.9.: A block diagram that describes the signal flow in the Matlab program in figure 4.8 when it is used to process the output of the 8-channels FDM.

display the number from 1 to 8, with each number occupying a unique position in the Field of View (FoV) so that merging all the images (i.e., $\cup_j I_j$) shows all the numbers without overlap. This is done to facilitate the measurement of each channel's noise figure and to determine the coupling between the channels. The coil data for these images was

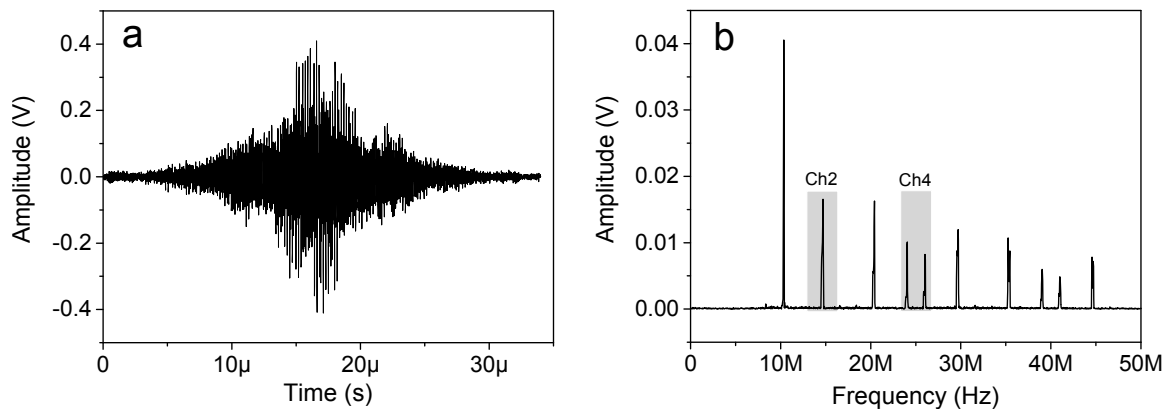


Figure 4.10.: The output of the 8-channel MR FDM for a single row data from eight decoupled images. (a) The time domain output. (b) The FFT.

obtained using the program illustrated in figure 4.2 and was then introduced to the Cadence simulator "Spectre" to drive a transient simulation of the MR FDM circuit. Figure 4.10a shows displays the time-domain output of the 8-channel multiplexer for a single row of data, while figure 4.10b shows its Fourier transform. It also demonstrates the eight frequency bands occupied by the row data from eight images. A slight difference in the gain between the channels can be observed. This difference is particularly due to the limited gain-bandwidth product (GBW) of the operational amplifier employed in the design of the band-pass filters, which leads to a decrease in the filter's gain as its center frequency increases.

Figure 4.11a shows the eight images created using a bitmap editor. They, by means of the program in figure 4.2, provided the input for a transient simulation of the 8-channel FDM in chapter 3. Figure 4.11b demonstrates the eight images reconstructed from the output of the FDM via the program in figure 4.8. It can be observed by inspection that the eight images are successfully reconstructed with all the numbers being highly recognizable. Moreover, no noticeable coupling between the channels can be seen in the images. The average degradation in the SNR of the images was determined, by means of the program in figure 4.6, to be approximately 2 dB, whereas the maximum coupling between the channels was found to be less than -14 dB.

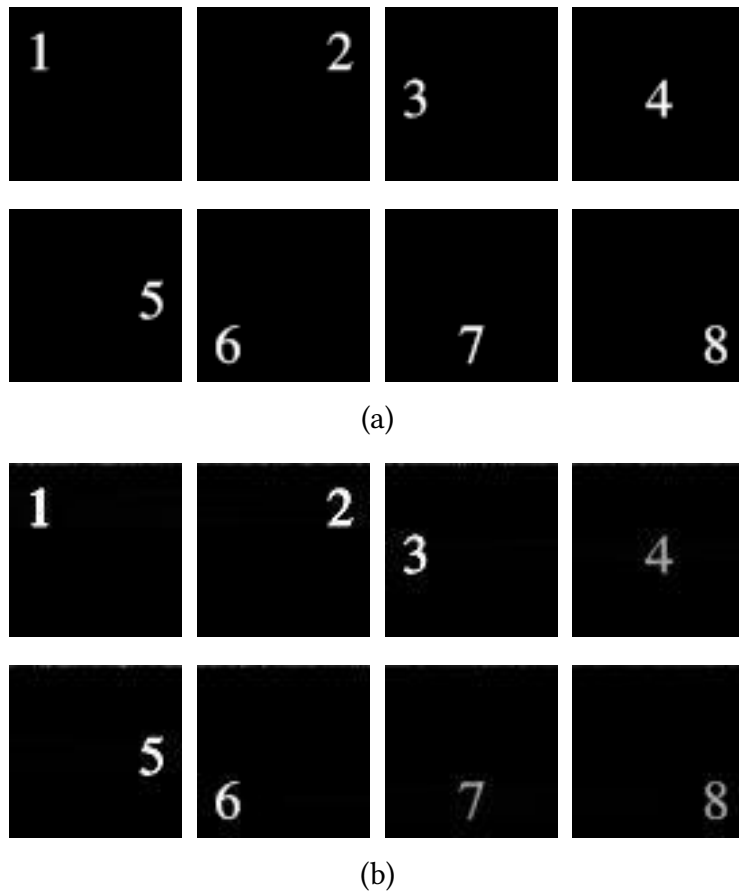


Figure 4.11.: Simulation of the 8-channel frequency division multiplexer presented in chapter 3. (a) Original images that were created using a bitmap editor so as to provide the simulation input as detailed in the text. (b) The eight reconstructed images from the multiplexed output.

4.4.1. Effect of LO Phase Noise

The stability of the local oscillator signals employed in the MR receivers plays a very important role during the image reconstruction. This is because the information of the MR image is encoded in both the frequency and the phase of the MR signals as it was explained in chapter 2. Therefore, it is of great importance to investigate the effect of the phase noise of the local oscillator that is to be used in the FDM circuit. This effect is illustrated in figure 4.12. In figure 4.12a the original image of fish oocytes [36] is depicted.

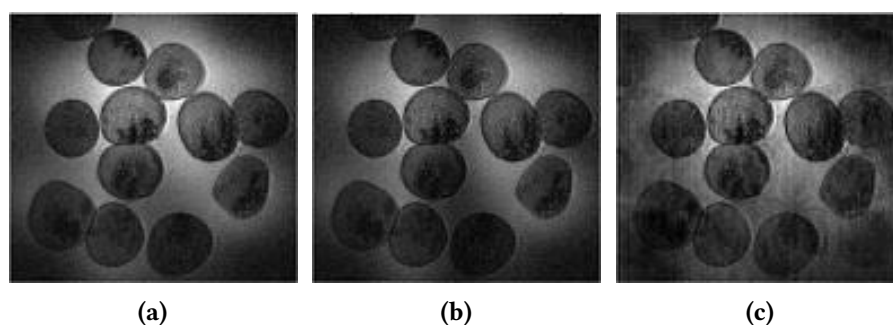


Figure 4.12.: Simulation of an MR image of fish-oocytes using a single channel of the MR FDM in chapter 3. (a) The original image. (b) Reconstructed image from the CMOS circuit including the circuit's noise. (c) Reconstructed image from the circuit with additionally added 80 ppm jitter noise to the local oscillator.

The coil signals of this image were generated by the program in figure 4.2 and introduced to cadence to run a transient simulation of a single channel of the MR FDM. Figure 4.12b demonstrates the reconstructed image from the CMOS circuit driven by an ideal local oscillator. The degradation in the SNR in this case is approximately 2 dB and is particularly due to the circuit's noise. The effect of utilizing a local oscillator with 80 ppm jitter noise is shown in figure 4.12c. From this figure, it can be observed that a LO with large phase noise can result in a severe distortion and deformation in the reconstructed image.

4.4.2. Channel Linearity

Another important aspect of the MR receiver is the linearity of its channels. Therefore, in order to have proper operation of the receiver, the maximum amplitude of the MR signals should not exceed the maximum linearity point of the MR receiver. Failing to do so results in distorted signals which, in turn, leads to a decrease in the SNR of the image. The linearity of a single channel of the MR FDM is probed in figure 4.13. Figure 4.13a shows the original MR image that provided the coil signals which were used as a simulation input, while figure 4.13b displays the reconstructed image when the maximum peak amplitude

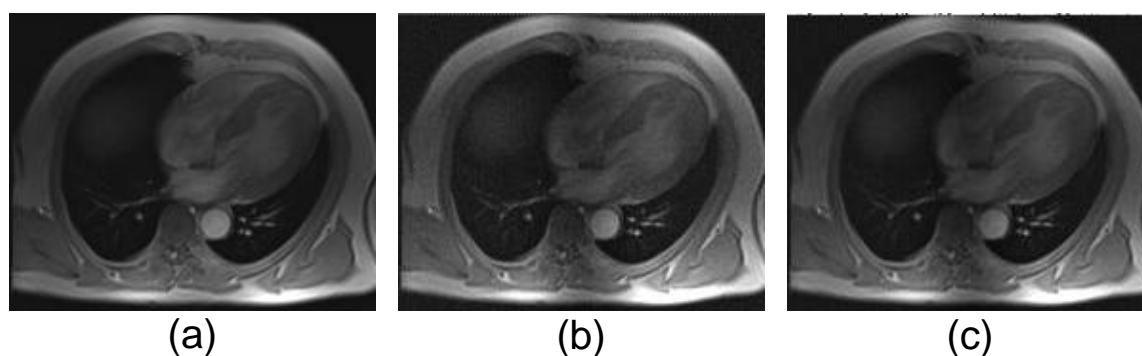


Figure 4.13.: Simulation of a chest MR image to test the effect of the multiplexer’s linearity on the MR image. (a) Original image. (b) Reconstructed image when the maximum peak amplitude of the coils signals is set to 100 μV . SNR degradation in this case is 2 dB. (c) Reconstructed image when the maximum peak amplitude of the coils signals is 20 mV. SNR degradation in this case is 3 dB.

of the coils signals is set to a level of 100 μV . This value ensures a linear operation of the circuit. The degradation in the SNR in this case is approximately 2 dB, which is merely due to the circuit’s noise. Figure 4.13c shows the reconstructed image from the output of the circuit when the maximum peak amplitude of the coils signals reaches 20 mV. In this case the SNR has decreased with respect to the linear region operation by approximately 1 dB, thus 20 mV is the maximum allowed input peak amplitude, above which the circuit saturates and the signals get distorted.

4.5. New Receiver Architecture

The results presented so far showed that the MR FDM, introduced in chapter 3, achieves the desired performance in terms of imaging. These results also validate the new simulation method, and show that it is a promising and efficient procedure to test and characterize the performance of the MR circuits. In this section a new MR receiver architecture is proposed to overcome the size, cost, and complexity drawbacks associated with MR phased arrays. This new receiver is a sixteen channel CMOS system that employs both the frequency and time division multiplexing, and conceived to be a superior solution capable of multiplexing more channels.

4.5.1. Circuit Diagram

Figure 4.14 demonstrates a typical future application of this new receiver where it will be exploited in the design of MR arrays with large number of receiving coils. The block

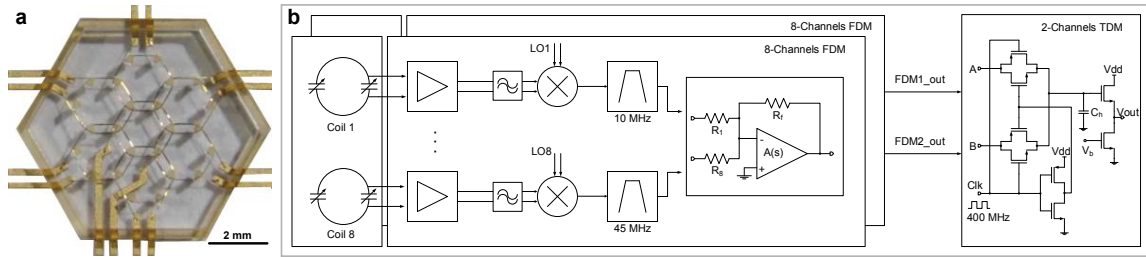


Figure 4.14.: Compact and integrated multi-channel MRI system. (a) MRI phased array of micro coils [36]. (b) Block diagram of the proposed 16-channel frequency-division and time-division multiplexer.

diagram of the two-stage architecture is plotted in figure 4.14b. The first stage implements two identical 8-channel frequency multiplexers, such as the one presented in chapter 3, while the second stage consists of a 2-to-1 time multiplexer. The two FDMs are parallel and utilize the same eight external oscillators to shift their input MR signals to the desired frequencies $f_j \in \{10, 15, 20, 25, 30, 35, 40, 45\}$ MHz. During the second stage, the frequency-multiplexed signals, each having an identical spectrum that spreads from 5 MHz to 45 MHz, are multiplexed in the time domain by switching them in alteration at a frequency of 400 MHz. The final output of the multiplexer therefore combines the NMR signals from 16 different channels, with a minimum oversampling ratio (OSR) of 4.44 for the two highest frequency down-converted NMR signals (at nominally 45 MHz), and a maximum OSR of 20 for the two lowest frequency down-converted NMR signals (nominally at 10 MHz).

4.5.2. Simulation Results

In order to test the performance of the 16-channel MR receiver proposed in section 4.5, sixteen images were created by a bitmap editor to emulate the acquisition from sixteen decoupled MR receiving coils. The images have a 64×64 resolution and they graphically display the numbers from 1 to 16 with each occupying a unique position in the FoV as shown in figure 4.17. This, as it was formerly explained, facilitates the comparison between the reconstructed images, especially estimating the coupling between the channels. The coil FID signals were generated using the program in figure 4.2 and then introduced to Cadence via an Ocean script to start a transient simulation. The Ocean script also records the simulation outputs as ".matlab" files. The sixteen images were reconstructed using the program in figure 4.8 as follows: first, the program loads the ".matlab" file that contains the multiplexed output from sixteen channels for a single row of the k-space. Then, it samples the multiplexed signal at 400 MSPS and separates the samples that correspond to the first and second 8-channel multiplexer. Practically, this can be

4. Simulation of The MR Receiver

implemented by introducing the multiplexed MR signal to two identical ADC's that are operated at 400 MHz but have a 180 phase difference. The samples are then queued into two groups A and B, where each group contains the samples that correspond to a single row acquisition from eight channels. Subsequently, the samples are quantized with a number of levels defined by the user, then quadrature demodulation is exploited. The demodulation is performed by multiplying the samples by local oscillators at each of the intermediate carrier frequencies $f_i \in \{10, 15, 20, 25, 30, 35, 40, 45\}$ MHz. In the end, demodulated signals are further processed to fill the k-space map. The digital processing of the signals comprises low-pass filtering, decimation, and phase compensation. This process is eventually repeated for all the rows of the k-space, and once it is complete, the MR images are straightforwardly obtained via Fourier transform. Figure 4.15 summarizes the signal flow in the Matlab program of figure 4.8 when it is used to process the output of the 16-channel frequency-division time-division multiplexer.

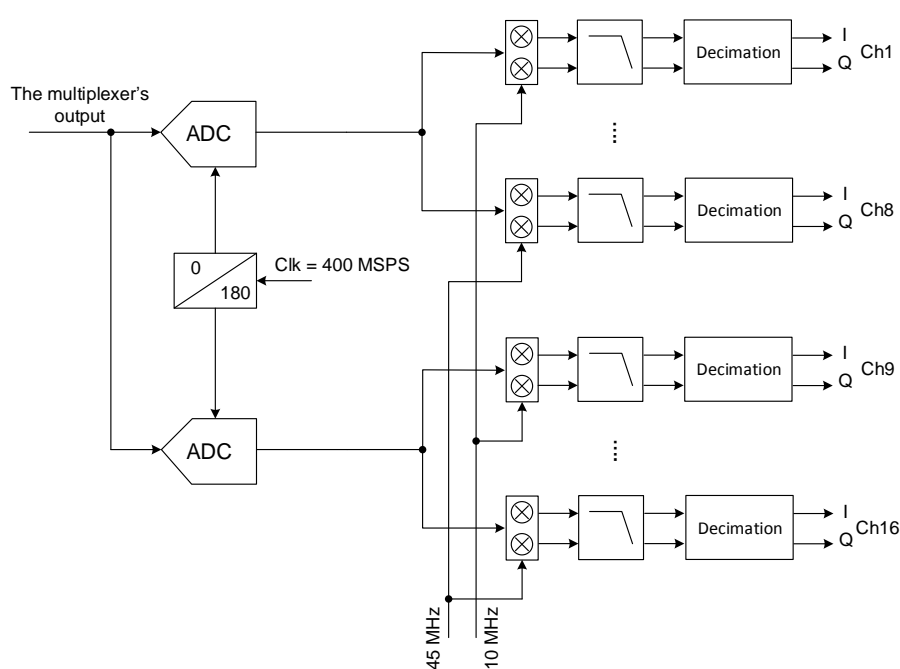


Figure 4.15.: A block diagram that describes the signal flow in the Matlab program in figure 4.8 when it is used to process the output of the 16-channels FDTD multiplexer.

The multiplexed output of the 16-channel frequency-division and time-division multiplexer is depicted in figure 4.16. Part (a) of the figure shows the time domain output, while part (b) displays the Fourier transform of the output. From this figure, the eight different frequency bands are clearly distinguished, but in this case each band contains the data from two channels compared to figure 4.10b. The sixteen images are successfully reconstructed from the multiplexed output as plotted in figure 4.17a which also shows that there is no

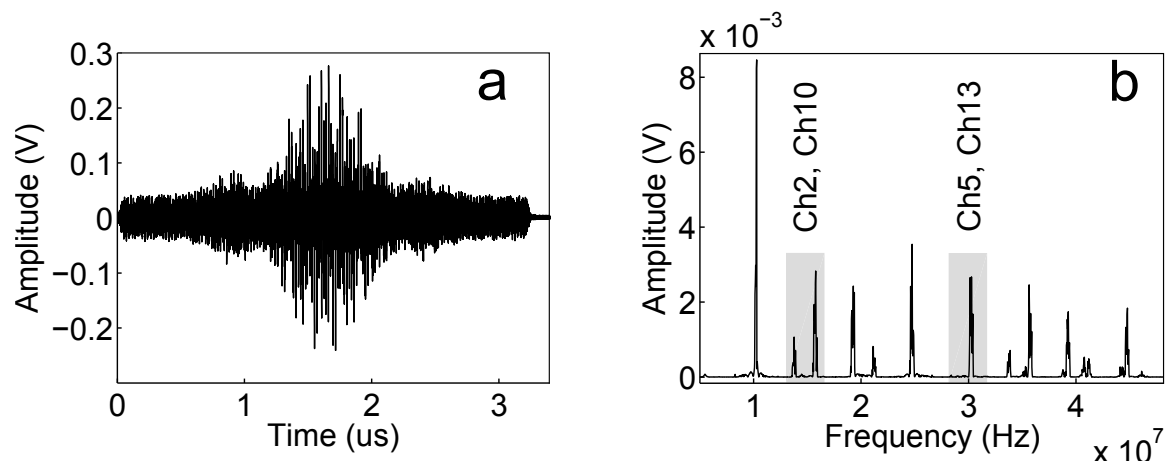


Figure 4.16.: Output of the multiplexer for a single k-space row from 16 different "channel" images. (a) Time domain signal. (b) FFT of (a).

significant coupling between the channels due to multiplexing. The corresponding k-space plots for each of the sixteen reconstructed images are depicted in figure 4.17b, while figure 4.17c plots the normalized difference between the reconstructed and the original images, highlighting the degradation, which would otherwise not be visible.

Table 4.1 provides the key performance characteristics of the multiplexer, including each channel's SNR degradation, and the minimum and maximum coupling between the channels.

4.6. Summary

Table 4.2 shows a list with a brief summary of the Matlab programs that were introduced in this chapter. The novel contributions of the approach presented in this chapter are:

1. Real or artificial MR images are utilized to generate realistic input voltages that represent the MR signal in the detection coils. These signals, in turn, are supplied to a circuit simulator to run virtual MR imaging experiments through which the performance of a custom hardware is evaluated.
2. The effects of each individual section of the custom hardware can be separately characterized by probing the time-resolved voltages and currents at any branch or node of the circuit during the simulation.
3. Furthermore, the technique can be very useful in finding the specifications (e.g., gain, noise figure, and linearity) of the different blocks in MR receivers that are implemented via hardware description languages such as Verilog or VHDL. Such

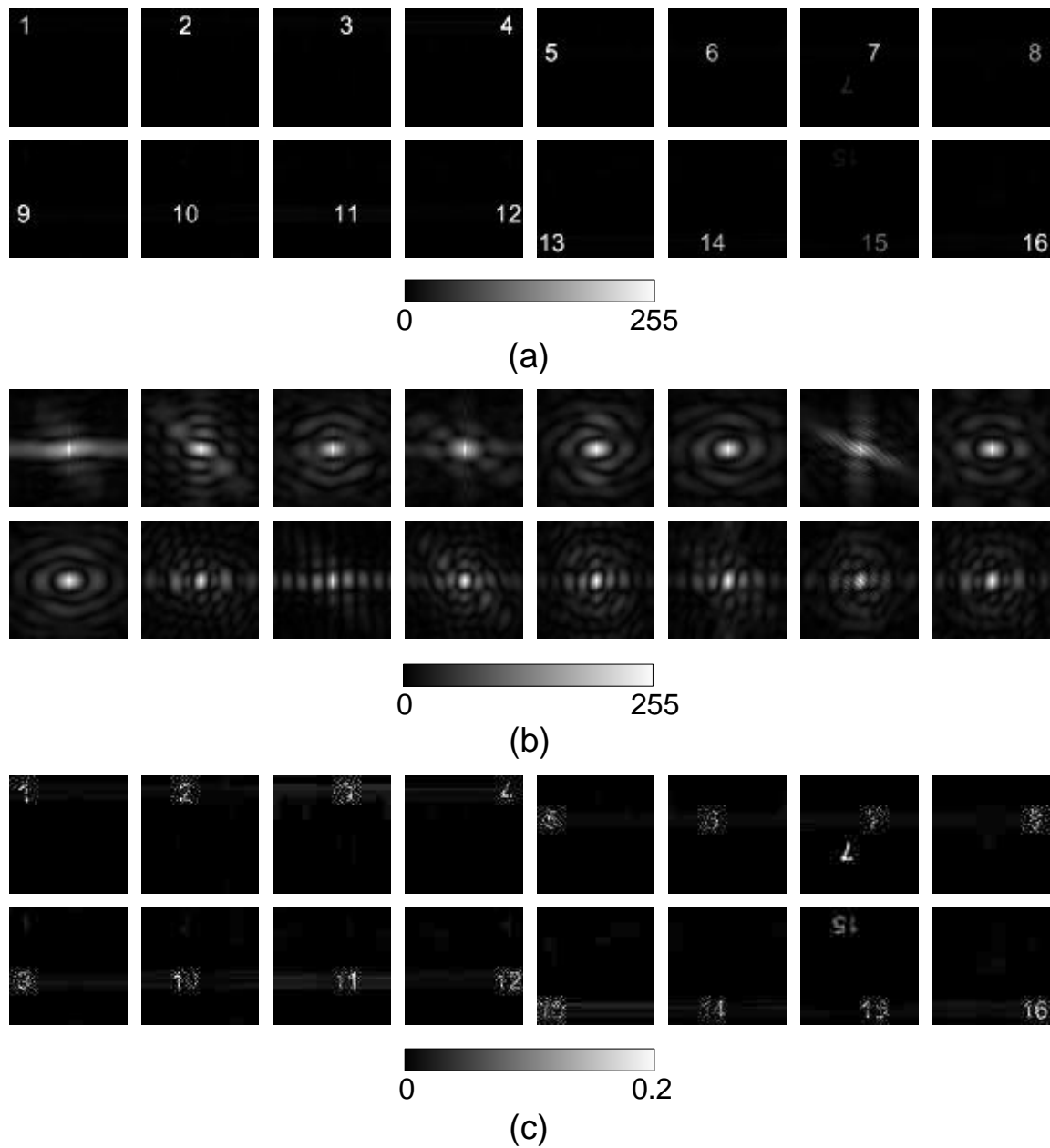


Figure 4.17.: Simulation of a 16-channel MRI experiment using the two CMOS multiplexers. The specially prepared channel images I_j were used to create the simulation input, as detailed in the text. (a) Reconstructed channel images R_j . (b) Corresponding k-space plots. (c) Corresponding difference images $E_j = (I_j - R_j)/I_j$ for each channel j .

Table 4.1.: Computed performance of the 16-channel multiplexer.

Channel	SNR Degradation [dB]	Maximum Coupling [dB]	(Ch)	Minimum Coupling [dB]	(Ch)
1	1.3	-15	2	-33	15
2	1.5	-15.5	1,3	-29	12
3	1.2	-14	1,4	-30	6
4	1.1	-14.5	2,3	-30.6	15
5	0.8	-16	6	-30.4	16
6	2.5	-19	5	-30.9	15
7	1.6	-16.3	8	-30.6	16
8	2.2	-20	7	-31.2	1
9	1	-16.4	10	-30.2	16
10	1	-15	11	-30	1
11	1.5	-14	10	-30.7	16
12	0.5	-16.5	11	-29.3	14
13	3	-17	15	-33	10
14	3	-15	13	-27	10
15	2	-15	16	-30	4
16	1.5	-16	15	-30.3	1
Mean	1.6063	-15.95	-	-30.3875	-
StdDev	0.7461	1.6525	-	1.41	-

simulations can account for many circuit non-idealities and, at the same time, ensure significant improvements in the speed of simulation.

4. Besides, the tool is perfectly appropriate for determining the required effective number of bits (ENOB) of the ADC for a specific MR receiver.

One of the remaining challenges is the simulation speed, which is mainly due to the fact that the transistor-level simulations are time consuming. Typical computations involved the simulation run for the 16-channel frequency-division and time-division multiplexer. In this simulation only the frequency mixers were replaced with their extracted layout models, while the rest of the circuit was modeled at the transistor level to speed the simulation up. The simulation required transient time steps that were much smaller than the Nyquist criterion of $1/2\Delta f = 1.25 \text{ ns}$, therefore a time step $\Delta t = 62.5 \text{ ps}$ was chosen. In order to achieve sufficient image resolution, the FID were run for at least $3.4 \mu\text{s}$, requiring 54,400 time steps. At 0.44 wall clock seconds per time step Δt , I obtained a 1.536×10^6 seconds per full image, or 2.54 weeks. Of course, typical acceleration techniques, such as the ones in [35, 84, 97], could be employed in the simulation as well, and for some quality assessment measures, a much smaller subset of FIDs could probably be used.

The simulations showed good agreement with results obtained from conventional circuit simulations such as the noise figure and the linearity. Previously, such comparisons would only be made between conventional simulations and physical measurements. As such, this method to characterizing MRI electronics hardware is expected to contribute towards more realistic evaluations of MRI hardware with realistic circuit details provided down to the transistor-level and extracted layout.

Table 4.2.: Summary of the Matlab programs that were presented in this chapter.

Reconstruct_Echo

- Reconstructs the coil's signals from an MR image or a commercial scanner's FID file.
 - Allows the user to set the bandwidth of the image, the Larmor frequency, and the noise level.
-

Image_reconstruct

- Performs a system-level simulation of the MRI experiment using the coil's signals generated from the "Reconstruct_Echo" program.
 - Allows the user to set the gain and noise figure of the different blocks of the MR receiver in order to test their effects on the image quality.
 - Allows the user to set the ADC's number of bits.
-

Ocean_script

- Introduces the MR coil's signals generated from the "Reconstruct_Echo" program to the CMOS circuit.
 - Runs a transistor-level or extracted-layout transient simulation.
 - Saves the simulation outputs.
-

Image_reconstruct_from_cadence

- Processes the simulation outputs from an eight channel FDM and reconstructs the MR images.
 - Processes the simulation outputs from sixteen channel FDTD multiplexer and reconstructs the MR images.
-

5. Fabrication and Measurements

The CMOS FDM presented in chapter 3 was fabricated in a high quality 0.35 μm process from XFab that features four metal layers. A micro-photograph of the final silicon die with all individual components highlighted is depicted in figure 5.1. The CMOS chip is

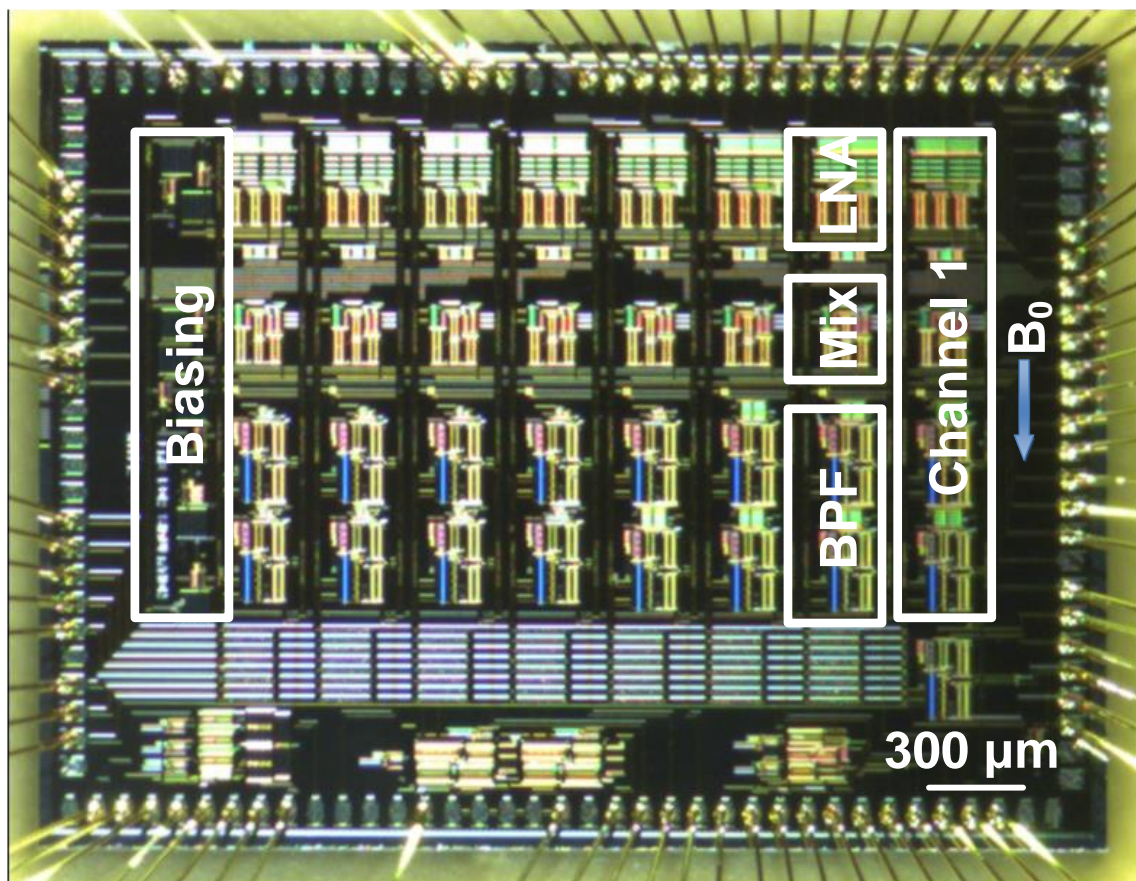


Figure 5.1.: Chip micro-photograph.

designed to operate in high (up to 11.7 T) magnetic fields. Therefore, great care was taken to ensure that the current flow in all the active elements in the circuit remains parallel to the B_0 field. This alignment minimizes the Lorentz force on the charge carriers and subsequently diminishes the Hall effect. The die was mounted on a 84-LDCC-J package, and thereafter, the bonding of the chip pads to the package was accomplished using

an ESEC 3100^{plus} automatic wire bonder. A printed circuit board (PCB), displayed in figure 5.2, was developed to conduct the measurements which were performed by means of a UHFLI lock-in amplifier from Zurich Instruments, Agilent E5071C Network Analyzers, and MSO7104B high frequency oscilloscope.

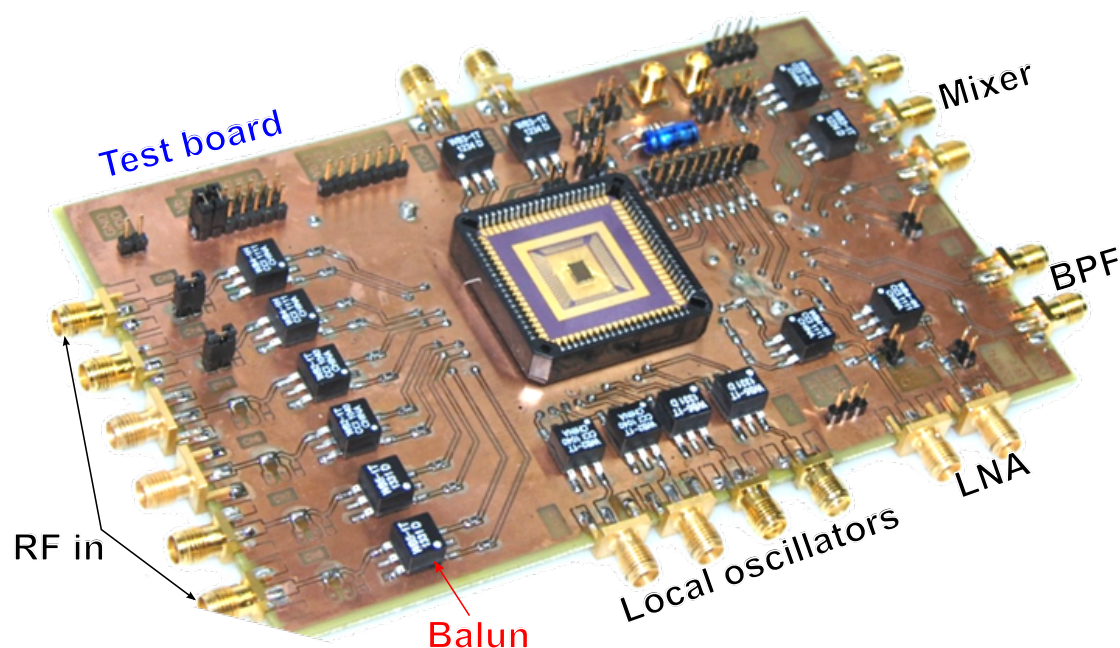


Figure 5.2.: Measurements PCB.

5.1. Measurements at $B_0 \approx 0$

5.1.1. LNA

Figure 5.3a displays the voltage gain, $G = V_{out}/V_{in}$, of the LNA for a 1 mV input excitation over the frequency range from 300 MHz to 500 MHz. The LNA exhibits a gain of approximately 18 dB at 400 MHz. The first-order input-referred intercept point is illustrated in figure 5.3b, which shows that the LNA exhibits a linear behavior for input voltages up to -42 dBV (8 mV single-ended voltage).

5.1.2. The Mixer

The measurement results of the double-balanced frequency mixer are plotted in figure 5.4. Part (a) of this figure depicts the conversion gain, $G_c = V_{IF}/V_{RF}$, of the mixer over LO frequency range from 310 MHz to 400 MHz while the RF is kept at 400 MHz. It can be

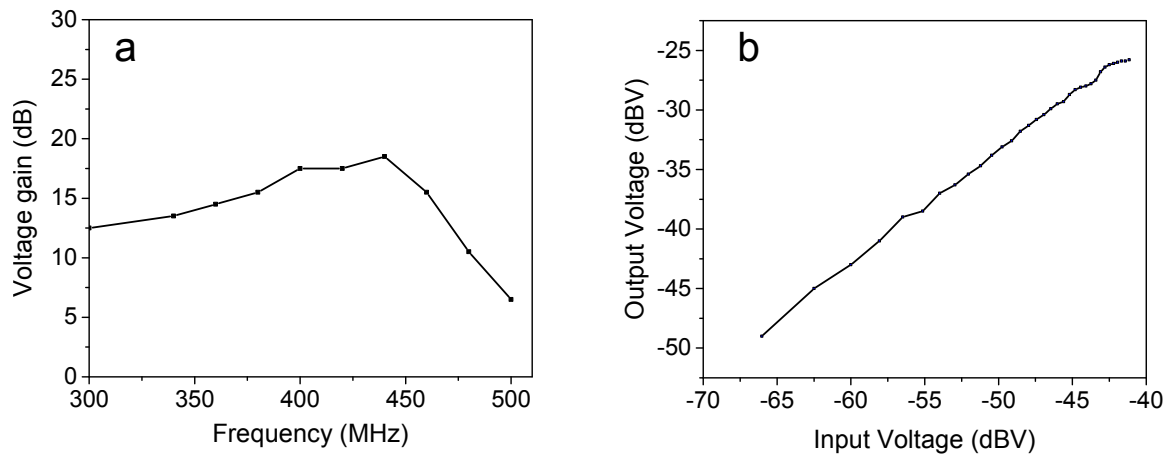


Figure 5.3.: Measurements of the low noise amplifier. (a) Voltage gain. (b) First-order input-referred intercept point IIP1.

seen from this figure that the mixer has a nearly flat gain profile (~ 18 dB) over the band of interest. Figure 5.4b plots the IF voltage versus the RF voltage for a fixed LO amplitude (800 mV). It shows that the mixer exhibits a linear operation for RF amplitudes up to -27 dBV.

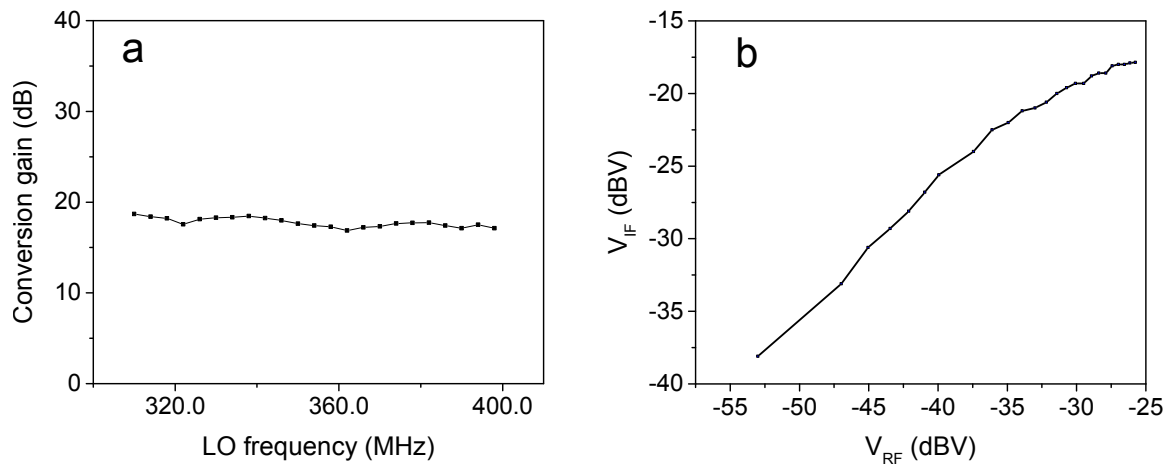


Figure 5.4.: Measurements of the frequency mixer. (a) The voltage gain. (b) The IIP1.

5.1.3. The Bandpass Filter

The bandpass filter of channel 3 was designed to have accessible pads, therefore it was chosen for the characterization of the filters performance. This BPF, as presented in chapter 3, is a fourth-order (two cascaded second-order filters) topology that has a center frequency of 20 MHz. The simulation and the measurement results of the frequency response of the filter are plotted in figure 5.5. According to this figure, it can be observed

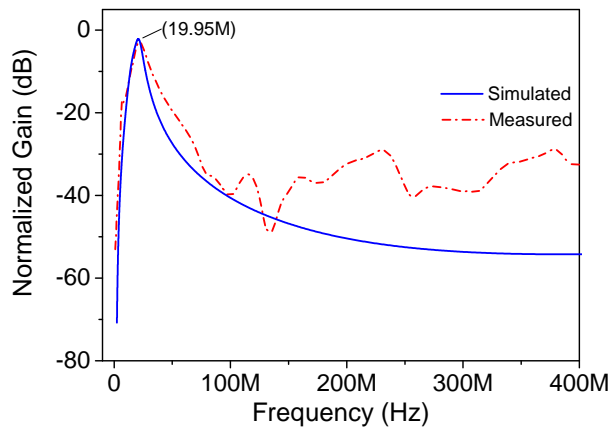


Figure 5.5: Normalized S_{21} of the BPF of channel 3 with center frequency $f_0 = 20$ MHz.

that there is a good resemblance between the simulated and the measured curves up to 100 MHz. However, an increase in the measured S_{21} can be noticed for frequencies above 100 MHz. This increase is most likely due to the parasitics of the PCB board.

5.1.4. Entire Channel Measurement

5.1.4.1. Gain

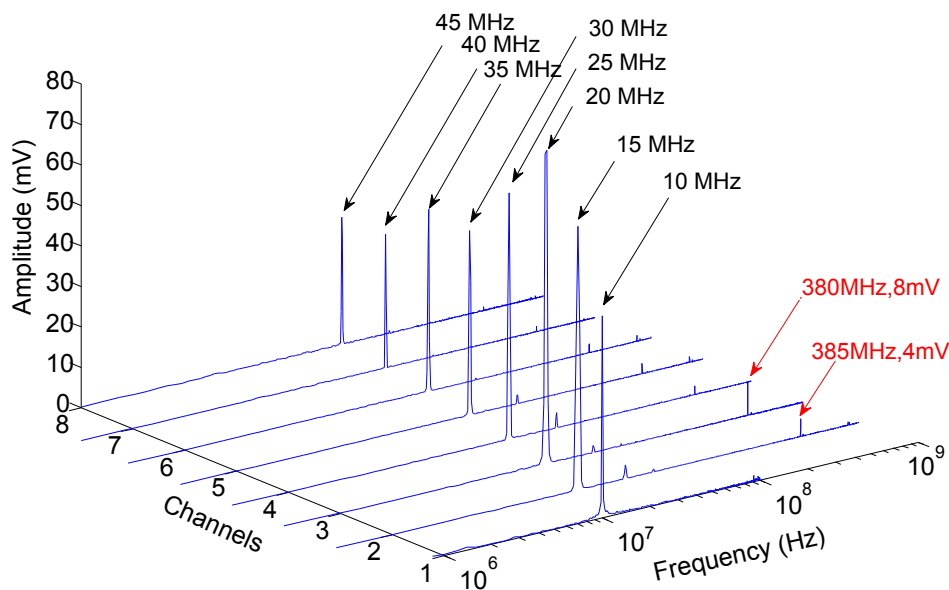


Figure 5.6.: Measured output of the eight channels for an AC input excitation. The RF inputs have 400 MHz frequency and 1 mV amplitude, while the amplitude of the LO is 800 mV.

Figure 5.6 displays the Fourier transform of the eight channels outputs for an AC input excitation. The RF input for all the channels is a constant 400 MHz sinusoid with a peak

amplitude of 1 mV, while the LO frequencies are 390, 385, 380, 375, 370, 365, 360, and 355 MHz respectively. The LO amplitude in this case is 800 mV. It can be seen from the figure that the RF signals are successfully shifted to the desired frequency bands. Moreover, the figure shows a good suppression of the LO signals. This LO suppression was found from the measured outputs to be in the range from -40 dB to -51 dB. The average gain of the channels is 33.8 dB with a standard deviation of 2.74 dB. The variations in the channels gain are mainly attributed to the gain of the BPFs, which decreases with increased frequency due to the limited 3-dB bandwidth of the operational amplifiers on which the filters are based. Nevertheless, these gain variations are not crucial since each channel is a separate receiver which is independent of the other channels. Therefore, gain compensation can be applied during the digital processing of the signals.

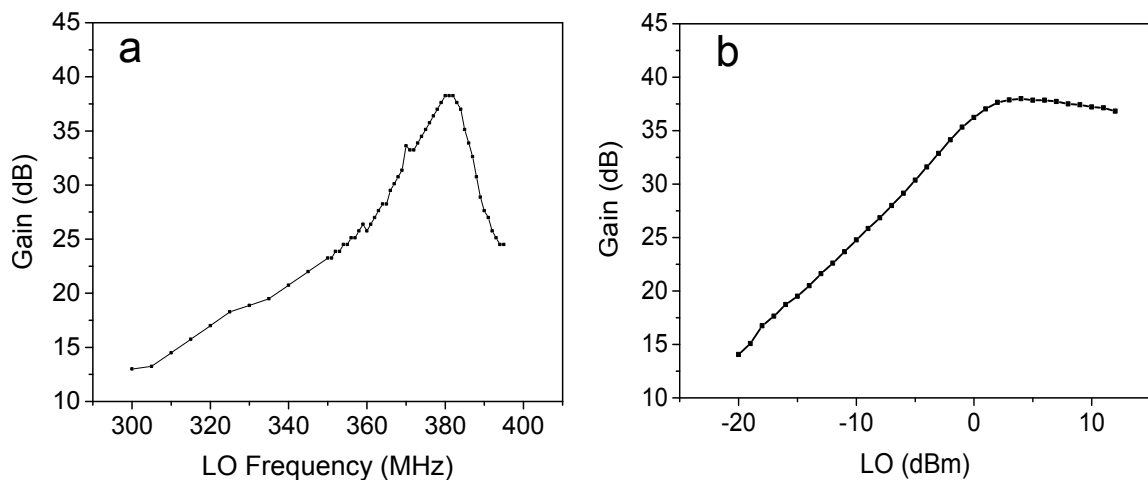


Figure 5.7.: Measured gain of channel 3. (a) Gain versus LO frequency for a fixed LO power. (b) Gain versus LO power when the LO frequency is fixed.

Figure 5.7a demonstrates the effect of sweeping the LO frequency on the voltage gain of a single channel (channel 3 in this case) for a fixed LO power. In this figure, the LO power is set to 2 dBm and the RF frequency is set to 400 MHz, while the LO frequency is swept from 300 MHz to approximately 400 MHz. The figure shows a gain profile of the channel similar to the response of the bandpass filter in figure 5.5 and , as expected, the maximum gain is achieved when the LO frequency is 380 MHz which corresponds to an IF frequency of 20 MHz. The influence of varying the LO power on the voltage gain of a single channel is investigated in figure 5.7b. In this case, the LO frequency is fixed at 380 MHz, while the LO power is varied -20 dBm to approximately 12 dBm. According to this figure, the maximum gain of the channel is achieved when the LO power is around 2 dBm.

5.1.4.2. Phase

As it was demonstrated in chapter 2, the phase of the MR signals plays a very important role in the spatial encoding and consequently the image formation. Therefore, a highly accurate and well defined phase response is a major requirement for the systems designed for MR applications. The phase responses for the eight channels of the multiplexer are plotted in figure 5.8. It is observed from this figure that the channels of the multiplexer exhibit approximately linear phase dependences over a 4 MHz band centered at the corresponding IF frequencies. These linear phase profiles make it possible to derive formulas that describe the phase of the channels at any frequency within the band of interest, and thus allows to compensate the phase shifts in the MR signals during the image formation.

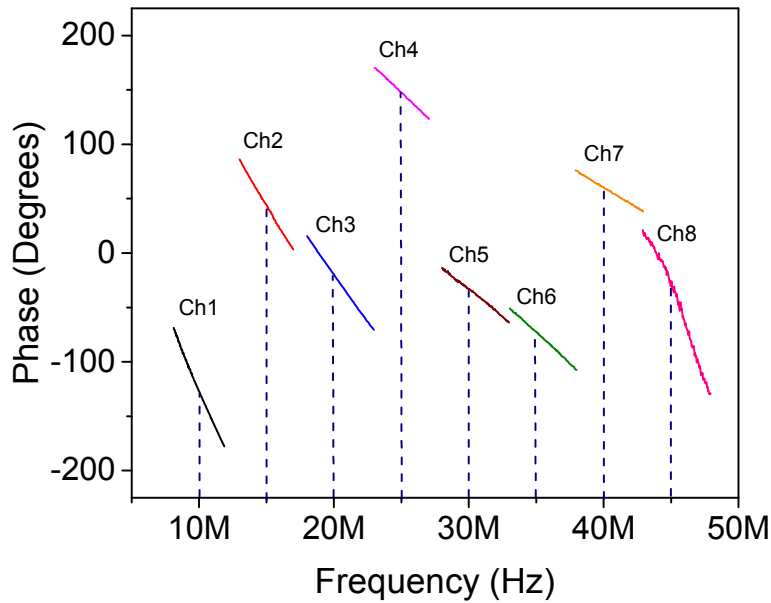


Figure 5.8.: Measured phase of each of the eight channels over a 4 MHz band centered at the IF frequency corresponding to the respective channel.

5.1.4.3. Noise Figure

The noise figure is determined according to the following equation [88]:

$$NF = 10 \cdot \log \left(\frac{S_i/N_i}{S_o/N_o} \right) \quad (5.1)$$

where $(S/N)_i$ is the signal-to-noise ratio at the input of the device, while $(S/N)_o$ is the SNR at its output. This equation can be rewritten as:

$$NF = 10 \cdot \log \left(\frac{1}{G} \frac{N_o}{N_i} \right) \quad (5.2)$$

where G is the gain of the device. According to the last equation, the noise figure was measured as follows; first, a $50\ \Omega$ termination was connected to one of the input channels of the UHFLLI lock-in amplifier. Then, the PSD of the noise was measured by means of the spectrum analyzer tool of the UHFLLI over a bandwidth Δf of 20 kHz centered at 400 MHz. After that, the $50\ \Omega$ termination was connected to the input of one of the FDM channels (channel 8 in this case with $G = 30.1$ dB), and the PSD of the output noise was measured over the same bandwidth. By applying equation 5.2, the noise figure of the corresponding channel was calculated to be approximately 7.4 dB.

5.1.5. Chip Heating

The unwanted heating of the sample is another important concern in MRI since the magnetization of the sample M_0 , according to equation 2.9, is inversely proportional to its temperature T_s . Therefore, increasing the sample's temperature results in a decrease in the amplitudes of the MR signals, and inherently reduced signals SNR. For this reason, it is significant to investigate the heating of the chip, especially if it is to be mounted in close proximity to the detection coil and the sample. Figure 5.9 illustrates the heat distribution in the CMOS chip and the holding package when six channels are simultaneously active. Each channel when activated increases the overall temperature by 5°C . The surface temperature of the chip in this figure is approximately 60°C which is tolerable, and can be further enhanced by employing thermally-efficient packaging.

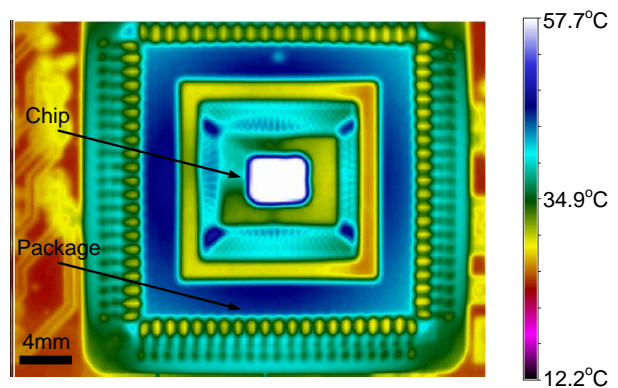
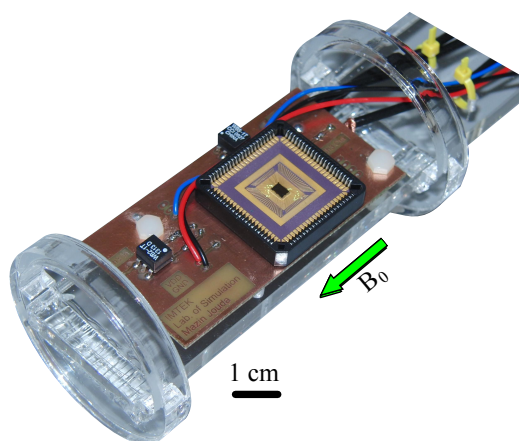


Figure 5.9.: Heat distribution in the CMOS chip and the holding package due to approximately 1.07 W power consumption.

5.2. Measurements at $B_0 = 11.7$ T

As previously mentioned, the FDM chip will be operated in a high magnetic field (9.4 T) environment. Therefore, it is necessary to characterize the influence of the field on its performance. For this reason, a new PCB was developed to fit inside the bore of an 11.7 T scanner from Bruker as demonstrated in figure 5.10. The PCB also ensures that the chip is oriented in a way such that the current flowing in all the active elements of the circuit is

Figure 5.10: PCB to test the chip inside the MR scanner. The direction of the current in all the transistors in this case is parallel to the direction of \mathbf{B}_0 .



parallel to \mathbf{B}_0 , so as to minimize its effects on the overall performance.

Figure 5.11a shows the measured gain of channel 3 outside and inside the magnet. The two curves exhibit a high degree of resemblance. However, a slight (1 ~ 2 dB) difference in the gain can be observed, which is most probably caused by the slight change in the drain current of the transistors due to the magnetic field [47]. Nonetheless, the figure proves that the \mathbf{B}_0 has a negligible influence on the chip's performance. The linearity measurement

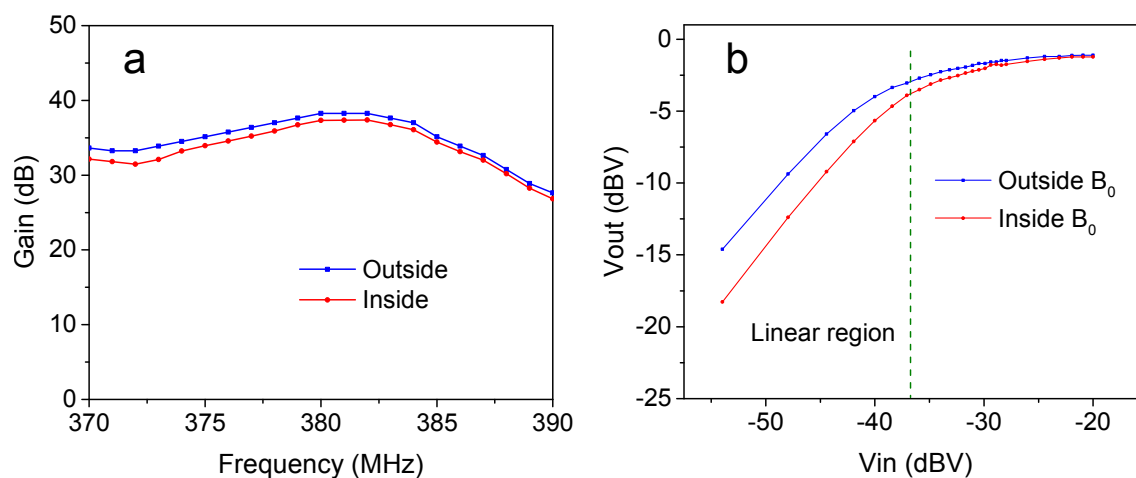


Figure 5.11.: Characterizing the chip's performance inside and outside the 11.7 T magnetic field. (a) Channel's gain. (b) Channel's linearity.

of a single channel inside and outside the magnetic field is plotted in figure 5.11b which shows that the maximum allowable input voltage level, at which the circuit becomes non-linear, is minimally altered.

Table 5.1.: Comparison between this work and other works.

Ref.	[82]	[46]	[17]	[102]	[42]	[7]	This work
Technology (μm)	-	-	0.5 CMOS	0.18 CMOS	0.12 CMOS BiCMOS	SiGe 0.35 CMOS	0.35 CMOS
Magnetic field B_0 (T)	1	0.3	7	0.5	0.9	7	9.4
Frequency (MHz)	41	12.77	300	21.3	37	300	400
Channel bandwidth (kHz)	7.2	3	- 20	1.1	250	30 - 120	4500
Integrated components	-	-	Pre-amp	LNA	LNA	LNA	LNA/Buffer
	-	-	Mixer	VGA	Mixer	Buffer	Mixer
	-	-	Amp	Mixer	LPF	-	Buffer/BPF
Gain (dB)	50	55	73	65-93	50	30	38 (After BPF)
Multiplexing	TDM	FDM	-	-	-	-	FDM
Supply voltage (V)	-	-	3.3	1.8	1.3	3.3	3.3
Power Consumption (mW)	-	-	-	-	243.7	264	178.2/channel
Number of Channels	4	4	1	1	1	8	8

Table 5.1 conducts a comparison between the CMOS FDM, which, to the author's knowledge, is the first implementation of an integrated multiplexer designed specifically to interface MR receive arrays in high magnetic fields, and the previous relevant reports [7, 17, 42, 46, 82, 102]. According to this table, the CMOS FDM offers up to 4.5 times higher bandwidth of the channel (~ 4.5 MHz), which means that the system has the flexibility to interface a wide variety of coils with different sizes, geometries, and imaging requirements. Moreover, with this large bandwidth, the multiplexer is capable of carrying without distortion the MR signals generated by a large variety of imaging sequences.

5.3. Experiment in 11.7 T Spectrometer

This section presents the results of employing the CMOS FDM in a spectroscopy application in an 11.7 T (that corresponds to 500 MHz Larmor frequency of ^1H) spectrometer. The setup of the experiment is demonstrated in figure 5.12. In this setup, the Bruker micro5 saddle coil was used to detect the MR signals. These signals were carried over a coaxial cable and introduced to one of the CMOS FDM channels (channel 3 in this case). The PCB on which the CMOS chip is mounted was placed outside the bore of the magnet due the limited space within the probe head. Since the chip performs frequency shifting of the MR signals, it was not possible to use the Bruker standard receiver whose local oscillator is set to 500 MHz. Therefore, the output of the chip was connected to one of the input channels of the UHFLI lock-in amplifier, where it is digitized, quadratically demodulated with a user-defined carrier frequency, lowpass filtered, and finally recorded as Matlab structures. The UHFLI does not only receive the chip's output, but it also acts as a local oscillator to provide the desired carrier frequency to the FDM.

5.3.1. MRS of Water

A single pulse spectroscopy experiment of a pure water sample was carried out. The sample volume in this case was 5 mL, while the flip angle was 20° . In this experiment the reception coil was first connected to the scanner's receiver to tune the coil and match it to 50Ω while it is inside the bore of the magnet. Furthermore, having the coil connected to the scanner makes it possible to apply the optimized shimming algorithms of the Bruker software, and allows adjusting the transmitted power so as to achieve the desired flip angle. After that, the coil was connected through a Bruker preamplifier to the UHFLI lock-in amplifier whose demodulator frequency was set to 500 MHz. In this experiment the sample excitation was accomplished with the Bruker system, while the signal reception was carried out with the UHFLI. In order to start the acquisition of the MR signals, the

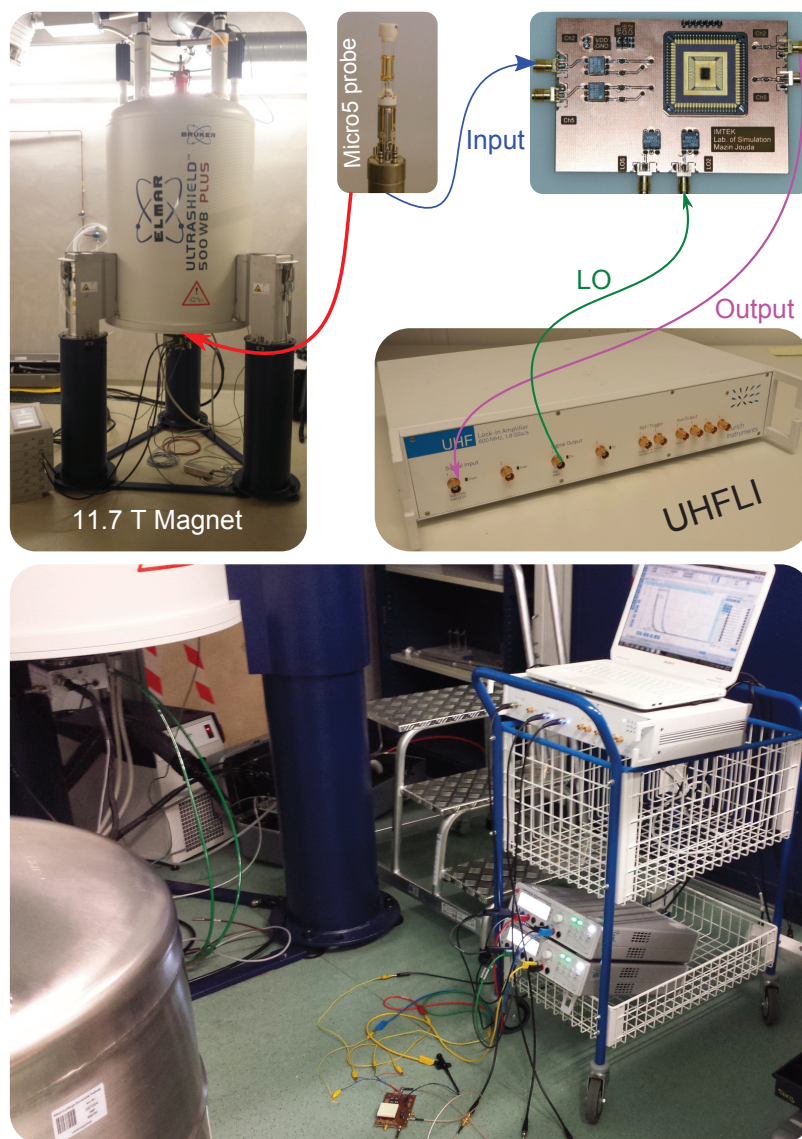


Figure 5.12.: Experiment setup in an 11.7 T spectrometer.

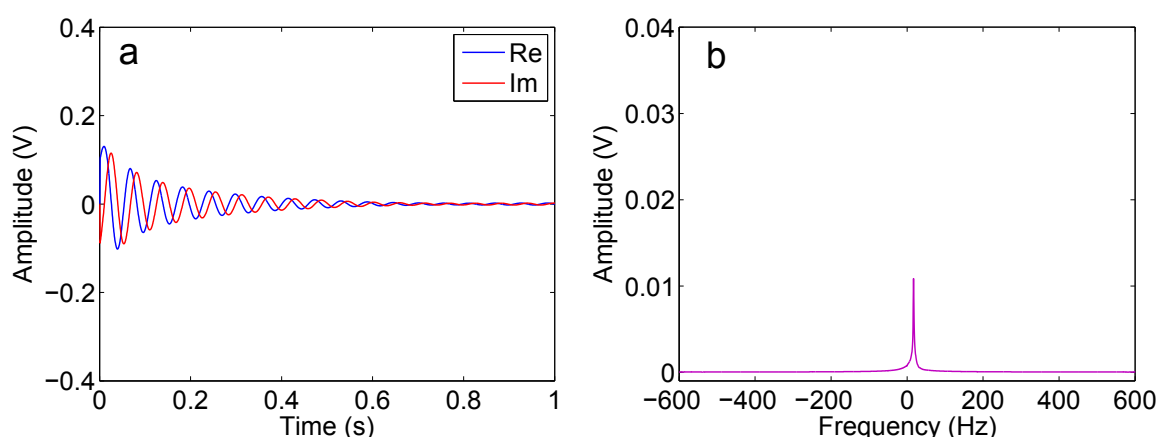


Figure 5.13.: Acquired FID of the water sample without the CMOS chip. (a) Time. (b) FFT.

UHFLI lock-in amplifier was set to be triggered by the amplitude of the demodulated input exceeding a certain threshold value. This method of triggering is not optimum since the small portion of the FID that precedes the trigger is lost, which may cause unrecoverable phase error. Nevertheless, in a single pulse experiment, this trigger suffices.

Figure 5.13a shows the real and imaginary (in-phase and quadrature) parts of the acquired FID of the water sample over a 1 s time frame. The FFT of the recorded signal is illustrated in figure 5.13b from which the spectral line width was found to be 3 Hz. The acquired FID

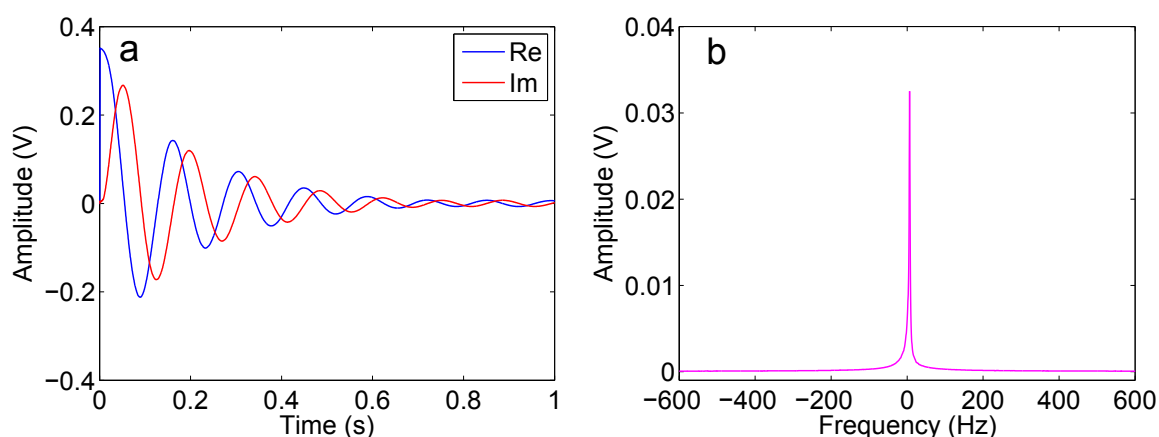


Figure 5.14.: Acquired FID of the water sample through the CMOS chip. (a) Time. (b) FFT.

of the water sample through the CMOS chip is depicted in figure 5.14. In this case, the reception coil was directly (bypassing the Bruker preamplifier) connected to one of the CMOS FDM channels (channel 2) and the output was fed to the UHFLI lock-in amplifier where the LO frequency was set to 485 MHz, the demodulation frequency to 15 MHz (corresponding to the 15 MHz output of channel 2), and the same triggering mechanism

was employed. The results obtained in this figure exhibit a high degree of resemblance to the results in figure 5.13. Moreover, the spectral line width according to figure 5.14b is exactly 3 Hz as previously found in figure 5.13b.

5.3.2. MRS of Sugar

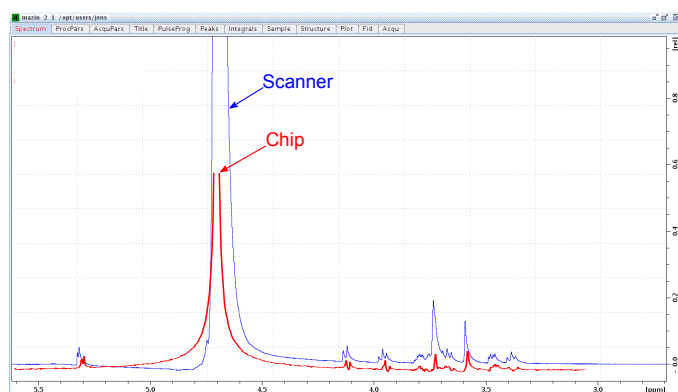


Figure 5.15: Spectroscopy of a 5 mL water sample with 100 mmol sugar in 11.7 T NMR scanner. The blue curve is from the scanner, while the red is from the chip.

The next experiment carried out in the 11.7 T scanner is the spectroscopy of a water sample with dissolved sugar. The sample volume is 5 mL and the concentration is 100 mmol. After inserting the sample, the reception coil was connected to the scanner and shimming was applied. Then the transmitted power was adjusted to achieve a flip angle of 30° , and finally, the spectrum was recorded. After that, the same experiment was repeated but this time the coil was connected to the chip and the spectrum was recorded via the UHFLI. Figure 5.15 displays the spectrum of the sugar sample plotted on top of a screen shot of the spectrum recorded by the Bruker spectrometer. According to this figure, the results obtained from the CMOS chip match, to a very good extent, those obtained by the Bruker spectrometer. However, a slight phase difference can be observed. This phase shift is mainly due to two factors; first, the RF transmitter and receiver use different frequency references, therefore, they are not synchronized, second, due to the aforementioned triggering method which results in losing a part of the signal. The effects of these two factors are more pronounced in the imaging experiment which is discussed in the next section.

5.4. Experiment in 9.4 T Spectrometer

In this section, the results of employing the CMOS FDM in spectroscopy and imaging experiments are presented. Figure 5.16 displays the respective experiment setup in which a 9.4 T Bruker scanner is used. The bore of the transmission coil in this scanner is approximately 7.5 cm, which offers enough space to test various reception coils as well as their associate electronics inside the high field. Unlike the setup in figure 5.12, the setup

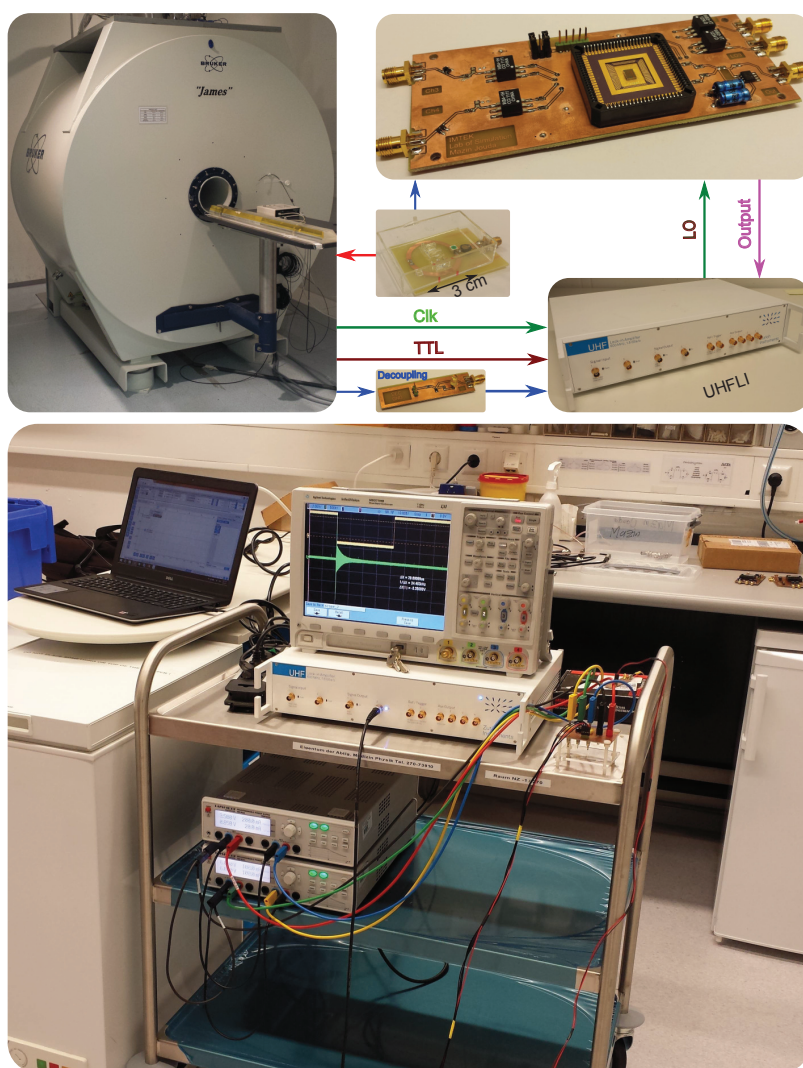


Figure 5.16.: Experiment setup in a 9.4 T scanner.

in figure 5.16 employs custom reception coils to detect the MR signals. Moreover, this setup uses two extra signals compared to the previous one. Namely, these signals are a TTL programmable pulse and an active decoupling signal, and both are used as trigger signals to process and record the MR signals in a precise manner.

5.4.1. Single Pulse Experiment

Using the aforementioned setup, a single pulse experiment was carried out. The detection coil used was a surface coil with a 1.5 cm diameter, and the sample is 30 mL pure water. To start the signal acquisition and in order to tackle the problem of losing samples, as mentioned in the previous section, an external decoupling signal was employed as a triggering signal. This signal, plotted in (yellow) in figure 5.17, is originally used to decouple the reception coil from the transmission coil during the sample excitation phase where it is high in this case. After the sample excitation, the decoupling signal goes low and hence, the falling edge of this signal can optimally trigger the FID acquisition. Figure 5.17 shows also the MR FID (in green) which starts exactly with the falling edge of the decoupling signal.

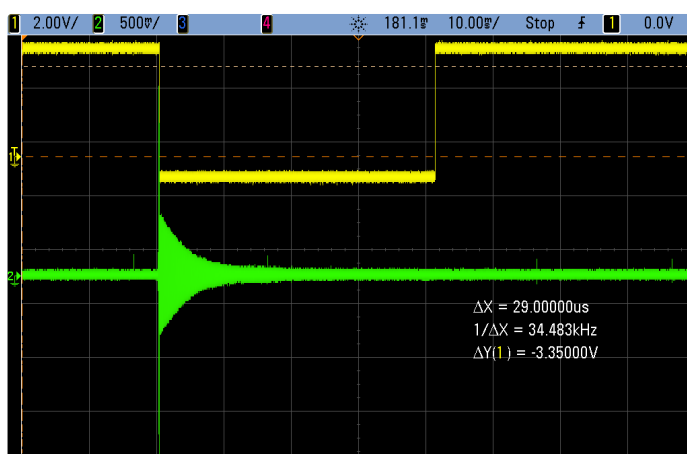


Figure 5.17: Employing an external decoupling signal to trigger the MR signal acquisition. (Yellow) decoupling signal used as a triggering signal. (Green) FID.

5.4.1.1. Chip Outside The Scanner

Figure 5.18 depicts the recorded FID of the water sample in the time domain as well as the frequency domain. In this case the PCB carrying the chip was mounted just outside the magnet in order to investigate its effect on the homogeneity of B_0 . The chip was connected to the reception coil after all the experiment parameters had been adjusted and calibrated through the Bruker transceiver. The flip angle with which the sample was excited is 30° , and the spectral line width according to figure 5.18b was approximately 66 Hz which is not

as good as the one obtained in the previous section mainly due to the custom reception coil.

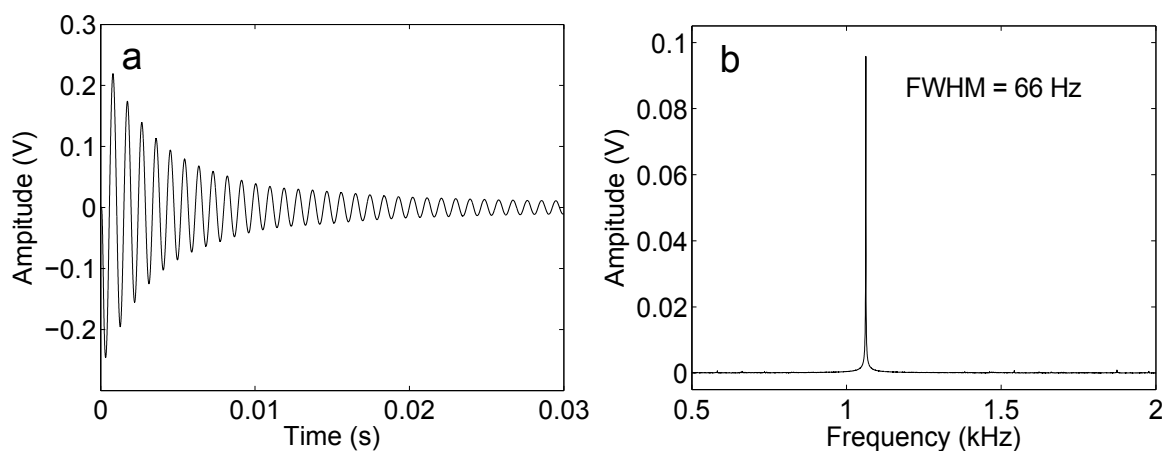


Figure 5.18.: FID of a water sample in a 9.4 T scanner when the chip is mounted outside the magnet. The flip angle α is 30° . (a) Time domain. (b) FFT.

5.4.1.2. Chip Inside The Scanner

Figure 5.19 displays the acquired FID of the water sample when the chip is inserted inside the magnet. The flip angle α in this experiment was set to 10° in order to reduce the amount of transmitted power thus avoiding any probable damage to the chip. From this figure, one can apparently observe that inserting the chip (in conjunction with the PCB baluns) inside the magnet perturbs the homogeneity of B_0 due to the differences in the materials susceptibilities, and this is why the FID spectrum exhibited multiple peaks as illustrated in figure 5.19b. To compensate for the B_0 inhomogeneity, a manual shim was employed. This was carried out by running a continuous single pulse experiment, adjusting the shimming parameters in the Bruker system, and then processing and recording the FID. This process of manual shimming is quite tedious and time-consuming, since the UHFLI inherently requires adequate time to process, record, and display the results. However, by applying this manual shimming, it is most likely to enhance the field homogeneity, at least for imaging experiments, within a reasonable amount of iterations as demonstrated in figure 5.20.

5.4.2. Imaging Experiment

After showing successful operation in spectroscopy experiments, the CMOS chip was tested in an imaging experiment in which a sample container, that contains PMMA structured letters (KIT) submerged in 20 mL of water, is placed on a 3 cm planar coil as illustrated

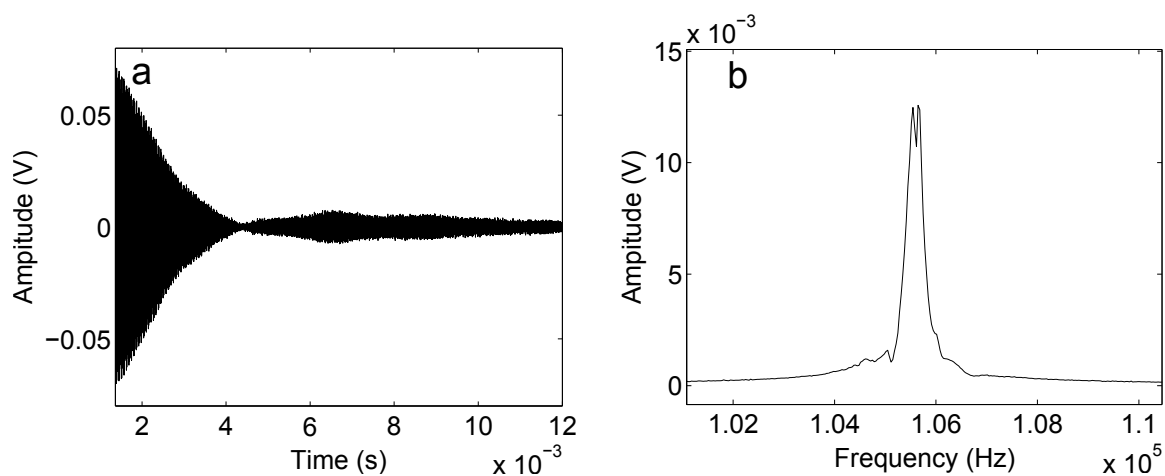


Figure 5.19.: FID of the water sample when the chip is placed inside the magnet. The flip angle α in this case is 10° . (a) Time domain. (b) FFT which shows multiple peaks due the B_0 field inhomogeneities caused by the PCB.

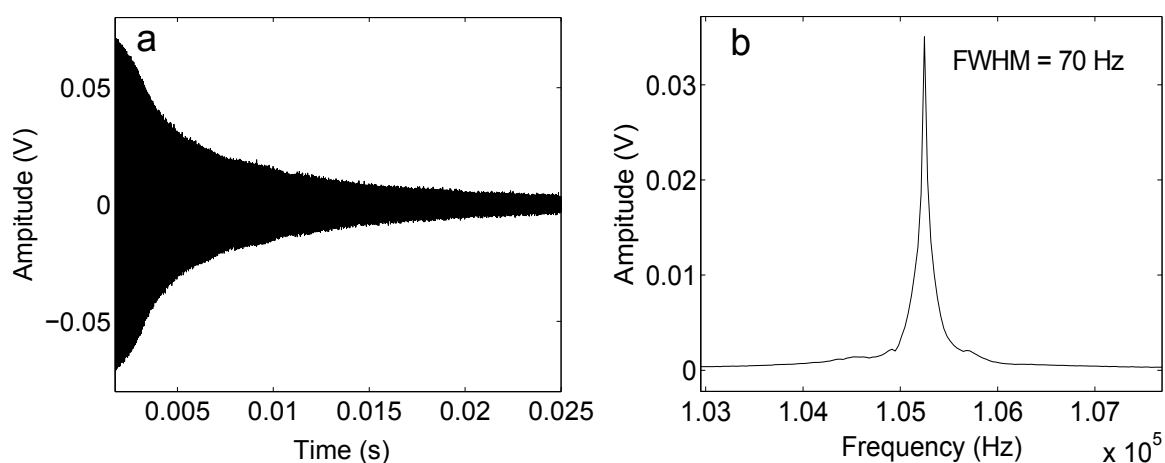


Figure 5.20.: FID of the water sample when the chip is placed inside the magnet. (a) Time domain. (b) FFT which shows a single peak after applying manual shimming.

in figure 5.16. Figure 5.21a shows the layout of the receive coil which is made of a PCB with 35 μm copper thickness and 1.5 mm substrate thickness. Figure 5.21b illustrates the measured S11 of the coil when the tuning and matching capacitors are adjusted to achieve 50 Ω input impedance at 400 MHz. After that, the coil and the sample were inserted in

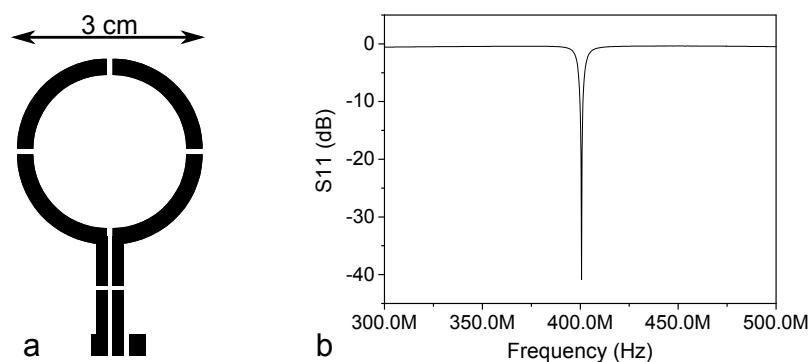


Figure 5.21.: (a) Layout of the reception coil. (b) Measured S11 of the coil.

the homogeneous region of the field in the magnet, and connected to the scanner so as to adjust and calibrate the imaging parameters. This adjustment includes:

- Automatic shimming to achieve optimum field homogeneity.
- Defining the 90° and 180° RF pulses.
- Running a three-pilot sequence that allows to define the position of the sample and to select a specific slice.
- Defining the image size and resolution.

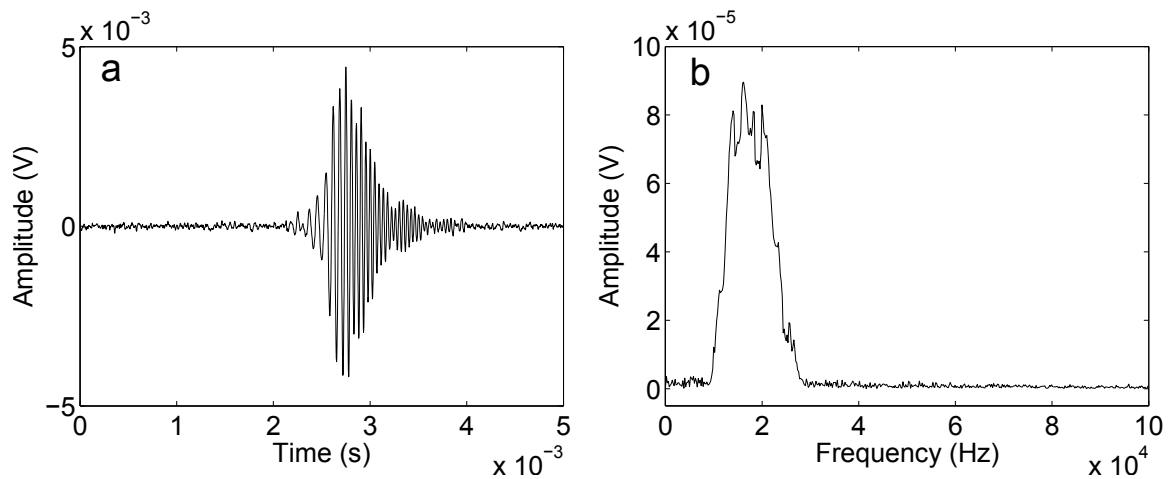
After that, the coil was connected to one of the FDM channels (channel 3 in this case) and the output was supplied to the UHFLI for digitizing and processing the MR signals. Table 5.2 summarizes the main parameter of the imaging experiment. As it can be seen in this table, the Gradient-Echo sequence was employed in order to avoid the high power 180° pulse that can possibly damage the chip. The repetition time TR was set to 1000 ms to ensure that the data is buffered from the UHFLI to the computer with no loss. Table 5.2 shows also that the image has a matrix size of 256 x 256 which means that 256 echo signals, which correspond to 256 phase encoding steps, are required to construct the image.

Unlike the FID, the MR echo does not start at the falling edge of the decoupling signal, but it starts rather sometime after it falls. Therefore, for a precise acquisition of the MR echo, the decoupling signal is no longer an optimum triggering signal. For this reason, a new TTL signal, that can be obtained from one of the TTL output ports of the scanner,

Table 5.2.: The main parameters of the imaging experiment in a 9.4 T MR scanner employing the CMOS FDM.

Parameter	Value	Parameter	Value
Coil diameter	3 cm	Flip angle	30°
Sample volume	20 mL	Slice thickness	4 mm
Imaging sequence	gradient echo	Image size	256 x 256
Echo time TE	6 ms	Field of view FoV	8 cm x 8 cm
Repetition time TR	1000 ms	-	-

was exploited to accurately trigger the signal acquisition. The position and duration of the triggering pulses in this TTL signal are precisely controlled by editing the script that describes the pulse diagram. Figure 5.22a depicts the acquisition of a single MR echo

**Figure 5.22.:** The center echo acquired from a complete slice when no phase encoding gradient is applied. (a) Time domain. (b) FFT.

in the time domain. The echo, in this case, is the center echo that is produced by the complete slice when the phase encoding gradient is zero, and therefore it exhibits the maximum amplitude. Figure 5.22b shows its FFT from which the signal's bandwidth can thereafter be determined, and subsequently the sampling time δt , at which the k-space map is filled, can be calculated. The echo acquisition was repeated 256 times which correspond to the number of phase encoding steps of the image. Within each acquisition the coming signal is shifted from the respective intermediate frequency to near DC band in a quadrature fashion. Then the demodulated signal is lowpass filtered with a 50 kHz bandwidth LPF, and finally it is sampled at 320 kS/s and transferred over a USB cable to the host computer. The reason for choosing this sampling rate is to avoid any possible

loss in the data while it is being buffered to the computer. The entire acquisition process can be initiated and fully controlled either by using the web-based graphical interface of the UHFLI, or by running the Matlab script in appendix B.1. After the samples of all the rows of the image were transferred to the computer, the Matlab script in appendix B.2 was employed to process them off-line and reconstruct the image. Figure 5.23 displays

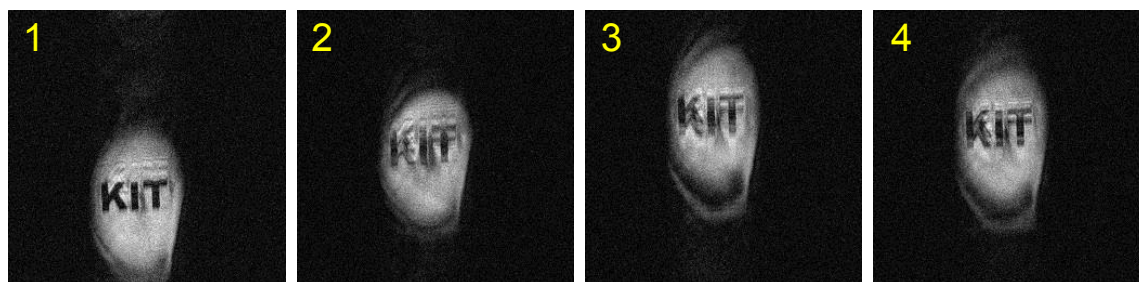


Figure 5.23.: Reconstructed images from different scans from a single channel of the CMOS FDM.

the MR images reconstructed from four scans of the same slice through one of the CMOS FDM channels. Unexpectedly, the figure shows a different reconstructed image for each scan. Furthermore, each image within the figure exhibits both distortion and displacement dilemmas which are apparently attributed to phase problems. In fact, the reconstructed image in this case experiences different phase shifts for each scan, and even the signals within a single scan experience different phase shifts. This is virtually due to the fact that the transmission path (Bruker system) and the reception path (CMOS chip + UHFLI) use separate reference clock signals, which thereby results in asynchronous phase between the excitation and the readout. Therefore in order to address this phase problem, the sample

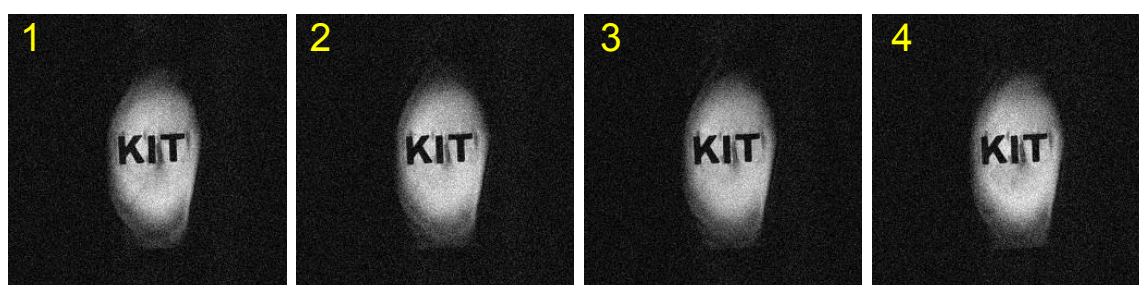


Figure 5.24.: Reconstructed images from different scans when the scanner's reference clock signal is exploited as external reference to UHFLI.

excitation and the signal readout must use the same reference clock signal. Fortunately, the 5, 10, and 20 MHz reference clock signals of the Bruker system are readily accessible at the scanner's console, and hence can be directly connected to the UHFLI, which luckily

allows the external reference. Figure 5.24 depicts the reconstructed images from four scans of the same slice when the UHFFLI is referenced by the 10 MHz Bruker reference signal. This figure shows obviously the significance of phase synchronization between transmission and reception in the MR experiment to reproduce the same results at each scan. Figure 5.25 demonstrates the SNR comparison of a four-averages reconstructed

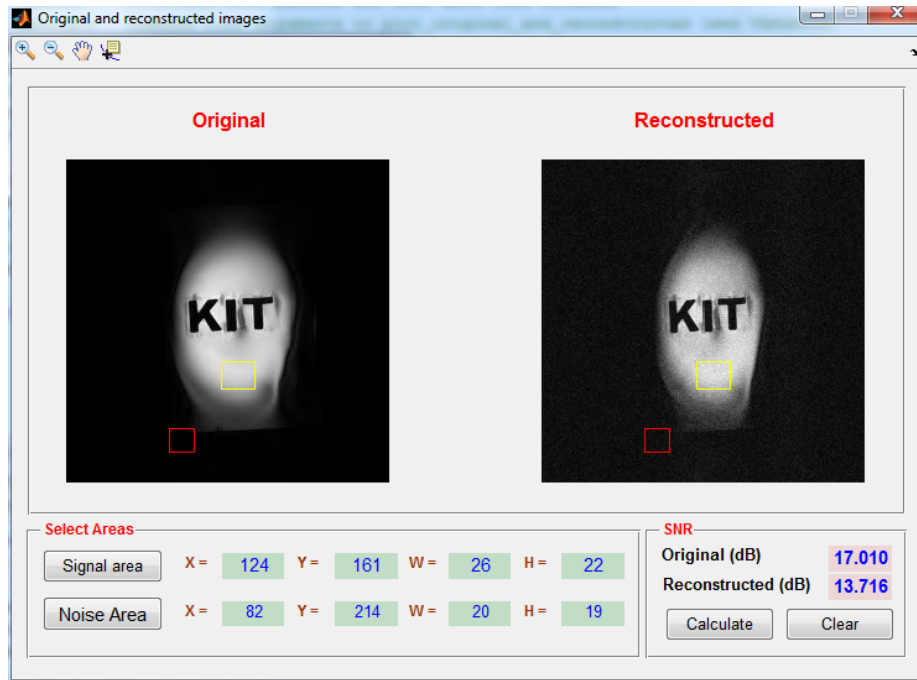


Figure 5.25.: SNR comparison between the original image obtained by the Bruker system and the image reconstructed through the CMOS chip.

image from the chip with no image processing and its original counterpart from the scanner, while figure 5.26 shows the SNR comparison between the original image obtained from the Bruker scanner and the image reconstructed via the simulation method described in chapter 4. The Matlab program presented in chapter 4 was used to calculate the SNR according to equation 4.2 by defining identical signal areas (yellow boxes) and noise areas (red boxes) in both figures. Accordingly, the SNR degradation in the image reconstructed from the simulation was approximately 0.9 dB, while the degradation in the image obtained from the real MR experiment through the CMOS chip was approximately 3.3 dB, resulting in a 2.4 dB difference between the simulation and the measurements. This difference is mainly due to the fact that the simulation does not consider the non-idealities and parasitics introduced by the chip package, socket, PCB, and cables. Ideally, the 3.3 dB SNR degradation is due to the noise contribution of the chip. However, the SNR comparison in this way is not completely fair due to the following reasons:

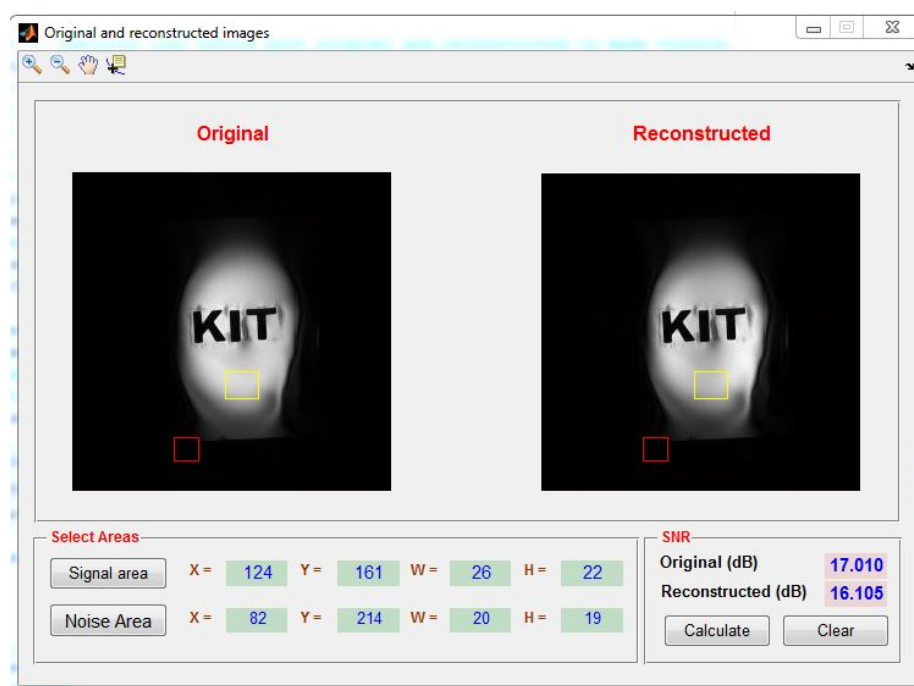


Figure 5.26.: SNR comparison between the original image obtained from the Bruker system and the image reconstructed from the simulation method described in chapter 4.

- The UHFLI employs ADCs with 12-bits resolution, which are not as high as the 16-bit ADCs used in the Bruker system [18], to digitize the input signals.
- The UHFLI was operated slightly above the Nyquist rate so as to avoid sample loss due to the limited buffer speed between the device and the computer, whereas the Bruker system's ADCs run at 20 MS/s [18] resulting in a high oversampling ratio.
- Characterization of the chip by simply comparing the two images is not possible. This is due to the fact that once the receive coil is disconnected from the scanner, many feedback-based optimization routines and image processing algorithms are not applicable anymore.

Nevertheless, the reconstructed image in figure 5.25 shows high resemblance to the original image, and therefore affirms the successful operation of the chip.

The previous imaging experiment was repeated, but in this case with a 2-channel array. The array, depicted in figure 5.27, comprises two surface coils of 1.5 cm diameter. The coils are placed apart three times their diameter in order to achieve a low coupling. Table 5.3 summarizes the main parameters of the imaging experiment. In this experiment and after having all setting and adjustments done, the coils were disconnected from the Bruker scanner and connected to channels 3 and 4 of the chip. These channels were chosen

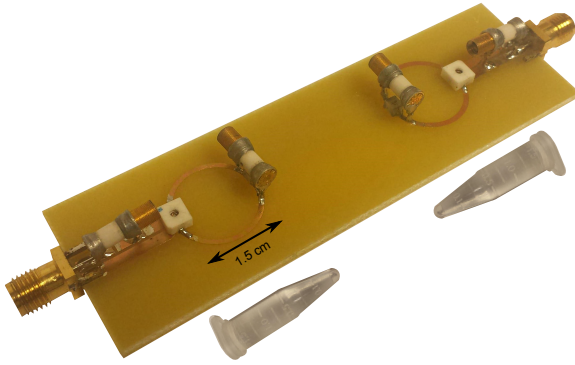


Figure 5.27: MRI receive array of two surface coils. The distance between the coils is three times the coil diameter in order to minimize coupling. The sample for each coil is Gadolinium-doped water of 1.5 mL volume.

because they have the longest adjacent traces of the local oscillator signals, which makes them most susceptible to channel coupling. The local oscillator signals were provided

Table 5.3.: The main parameters of the imaging experiment using a two-channel MRI array.

Parameter	Value	Parameter	Value
Coil diameter	1.5 cm	Flip angle	30°
Imaging sequence	gradient echo	Image size	48 x 256
Echo time TE	6 ms	Slice thickness	2 mm
Repetition time TR	1000 ms	-	-

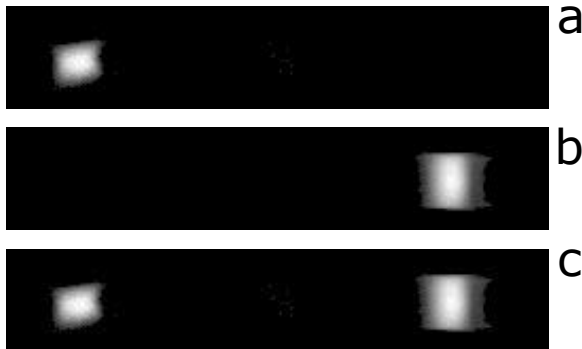


Figure 5.28: Results of the MRI experiment using two-coil array. (a) Image reconstructed from coil 1. (b) Image reconstructed from coil 2. (c) Image obtained from a sum of squares of (a) and (b).

by the UHFLI, while the output of the FDM was introduced to one of the UHFLI's inputs. Inside the lock-in amplifier, the incoming signal was first digitized, and then introduced to two quadrature digital demodulators operating simultaneously. The demodulation frequencies were 20 MHz and 25 MHz for channels 3 and 4 respectively. Figure 5.28 displays the experimental results. In this case, figure 5.28a shows the image acquired from the first coil through channel 3 of the FDM, and figure 5.28b shows the image of the second coil acquired through channel 4 of the FDM. The root sum of squares (rSoS) of the two images is displayed in figure 5.28c. The results depicted in this figure show a

successful reconstruction of two images from a multiplexed signal with no remarkable coupling between the FDM channels. The channel coupling was quantified by means of the Matlab program in figure 4.6, and was found to be less than -14 dB.

6. New Fully Integrated Receiver Architecture

6.1. Introduction

The frequency division multiplexer FDM, presented in chapter 3, shows a promising solution to overcome the size, cost, and complexity issues associated with the MR phased arrays. However, it still suffers from a number of technical limiting factors that may prevent it from being the optimum solution, especially when considering MR phased arrays with massive numbers (>120) of coils. These limiting factors can be summarized as follows:

- The bandwidth within which the MR signals are multiplexed is specifically limited by the maximum bandwidth of the commercially available ADCs that offer the desired resolution of 14 effective number of bits (ENOB) as illustrated in figure 4.7. This makes the number of channels limited.
- The FDM requires, for each channel, a dedicated local oscillator in order to shift the MR signal to a unique intermediate frequency. The fact that the channels are shifted to adjacent intermediate frequencies, in the range of 10 MHz to 45 MHz (using LOs in the range of 355 MHz to 390 MHz), makes the realization of such LOs, using a single voltage controlled oscillator, extremely difficult.
- For each additional channel, a bandpass filter with a unique center frequency is required. As the intermediate frequency IF becomes higher, the bandpass filter topology in figure 3.17 can no longer be used due to the limited GBW of the operational amplifier, and therefore new topologies have to be employed, which necessarily increases the complexity of the FDM.
- The more channels added to the multiplexer, the more noise is accumulated, and thus the SNR is more degraded.
- The maximum number of FDM channels is also limited by the input dynamic range of the intended ADC, since the amplitude of the FDM output increases with adding

more channels. This increase in the amplitude of the multiplexed signal results in decreased conversion resolution of the individual channels.

As a conclusion of this preliminary discussion, the CMOS FDM is a perfect replacement to the commercial systems used in clinics (with up to 32-coils array), but it becomes less attractive when we talk about MR arrays with more than a hundred coils, and this invites us to think about different solutions that can overcome the aforementioned limitations. Therefore, a new MR receiver architecture is proposed in this chapter. In contrary to the conventional MRI receiver and the receiver presented in chapter 3, the new architecture, illustrated in figure 6.1, suggests a CMOS integrated solution that comprises a low-noise amplifier, a quadrature frequency conversion, low-pass filters, and analog-to-digital converters. The chip is conceived to be mounted in close proximity to the detection coil so as

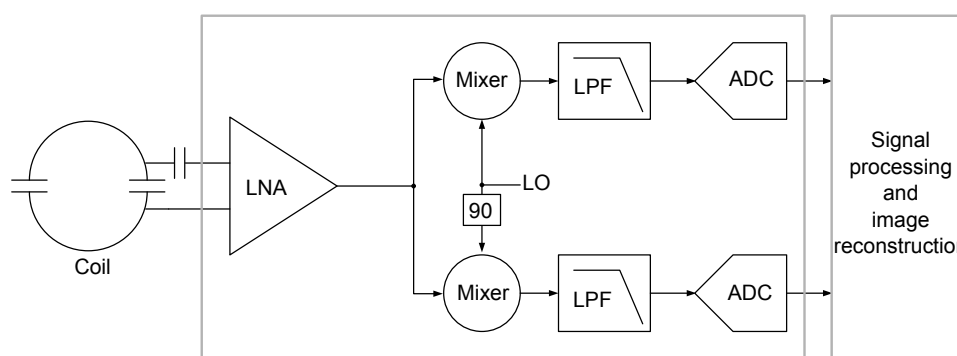


Figure 6.1.: The block diagram of the proposed MRI receiver architecture. It consists of low-noise amplification, quadrature demodulation, and analog-to-digital conversion.

to avoid signal attenuation as well as the bulky coaxial cables used to transfer the signals to the readout electronics. The output signal from the chip is digital, and therefore it is largely immune to noise. Moreover, having this signal in a digital form allows to apply time division multiplexing (TDM) in order to reduce the number of cables which can, in this case, be replaced by optical fibers.

Compared to the FDM architecture proposed in chapter 3, the new receiver's main addition is the ADC stage. Amongst the broad variety of ADCs [64, 71], the Sigma-Delta ($\Sigma\Delta$) ADC, which will be briefly introduced in section 6.2, is employed in this new receiver architecture. The reasons for choosing this particular ADC can be summarized as follows:

- It allows the use of a single bit quantizer, which is required to decrease the number of channels, while still preserving high resolution conversion.

- The resolution of the ADC, effective number of bits (ENOB), can be increased by simply increasing the sampling frequency. This offers a new degree of freedom to determine the number of channels that can be multiplexed.

6.2. Sigma-Delta ADC

The ADCs are divided mainly into two categories, namely the *Nyquist-rate* and the *oversampling* converters. In the former type, and as the name suggests, the ADC is operated at or slightly above the Nyquist rate, and each sample of the input signal is assigned a digital value irregardless of the previous and subsequent samples. Unlike these converters, the oversampling ADCs, where the $\Sigma\Delta$ ADC is a good example, operate at a sampling frequency f_s that is many-fold of the Nyquist rate. The ratio between the sampling frequency and the Nyquist rate is usually referred to as the oversampling ratio (OSR)

$$OSR = \frac{f_s}{2f_B} \quad (6.1)$$

where f_B is the bandwidth of the input signal. Also unlike the Nyquist-rate ADCs, the digital output of the $\Sigma\Delta$ ADC that corresponds to a single sample of the input signal depends on several previous samples. Compared to the Nyquist-rate ADCs which exhibit limited ENOB [8], the $\Sigma\Delta$ ADCs generally offer higher ENOB with reasonable conversion speed.

6.2.1. Working Principle

Before proceeding with the work principle of the $\Sigma\Delta$ modulators, a measure of the efficiency of the ADC has first to be defined.

A typical measure that is usually used is the signal to quantization noise ratio (SQNR) of the ADC for a sinusoidal input. This SQNR can be calculated in terms of the ENOB, for an ideal Nyquist-rate ADC, using the following equation [93]

$$SQNR (dB) = 6.02 (dB) \cdot ENOB + 1.76 (dB) \quad (6.2)$$

This equation demonstrates that each extra bit of the ADC's quantizer (doubling the number of quantization levels) enhances the SQNR by approximately 6 dB. The block diagram of a typical $\Sigma\Delta$ ADC is depicted in figure 6.2

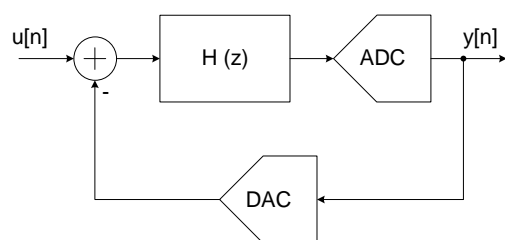


Figure 6.2.: The block diagram of a typical $\Sigma\Delta$ ADC.

from which it can be seen that the $\Sigma\Delta$ ADC is a feedback system that consists of a loop filter $H_L(z)$ (typically an integrator) and a low resolution (1-6 bits) ADC in the forward path, while it comprises a low resolution digital-to-analog converter (DAC) in the feedback path. Therefore, for each sample of the input signal, an error signal, that results from subtracting (hence the term Delta) $y[n - 1]$ from $u[n]$, is fed to the loop filter $H_L(z)$ which integrates (hence the term Sigma) it and then introduce it to the low-resolution ADC. For a better understanding of the working principle of the $\Sigma\Delta$ ADC, let's consider the case of a single bit quantizer as illustrated in figure 6.3. In this figure the output at any sample is a single bit (for example 1 or -1), and therefore can be directly fed back to the input. The total output of the ADC, in this case, will be a *pulse density modulated* version of the input signal as shown in figure 6.4. The $\Sigma\Delta$ ADC

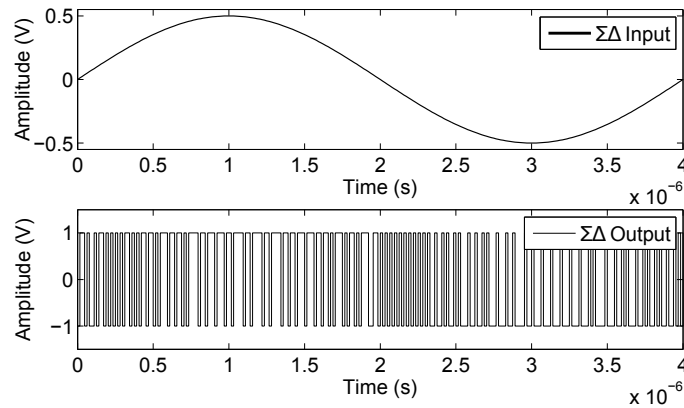


Figure 6.4: Input and output signals of a typical $\Sigma\Delta$ modulator.

in figure 6.3 is a nonlinear system due the nonlinear nature of the quantizer. This makes the mathematical analysis of the system complicated. However, a linearized model of the ADC can be obtained by replacing the quantizer with a gain element K_q and a quantization noise source $e[n]$ as displayed in figure 6.5. Assuming $K_q = 1$ for simplicity and applying

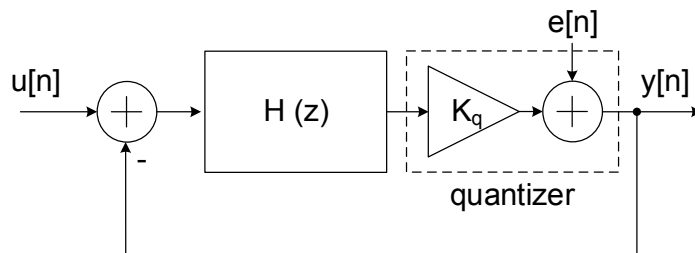


Figure 6.5: Linearized model of a $\Sigma\Delta$ ADC with single bit quantizer.

the superposition principle to this linearized model, a mathematical expression of $y[n]$ can be obtained as follows

$$Y(z) = \frac{H(z)}{1 + H(z)} \cdot U(z) + \frac{1}{1 + H(z)} \cdot E(z) \quad (6.3)$$

$$= STF \cdot U(z) + NTF \cdot E(z) \quad (6.4)$$

where STF is the *signal transfer function*, while NTF is the *noise transfer function*. They are calculated, in terms of the loop filter $H(z)$ as follows

$$STF = \frac{H(z)}{1 + H(z)} \quad (6.5)$$

$$NTF = \frac{1}{1 + H(z)} \quad (6.6)$$

These equations imply that if the loop filter $H(z)$ is designed such that it has sufficiently large magnitude at the desired frequency band of the input signal, then the magnitude of the STF will be approximately 1, while the quantization noise at the $\Sigma\Delta$ ADC's output will be significantly attenuated, since the magnitude of the NTF in this case is extremely small. This is the so called *noise shaping* [93], where the quantization noise is shaped by the NTF, so that it has low values in the signal band and higher values out of this band.

6.2.2. First-order $\Sigma\Delta$ ADC

The $\Sigma\Delta$ ADC can be divided into different categories according to different aspects. For example, they can be either analog or digital. Moreover, they can be divided into baseband and bandpass modulators according to the frequency of the input signal. The $\Sigma\Delta$ ADCs can also be categorized according to their order which is essentially determined by the order of the loop filter $H(z)$. Throughout the rest of this chapter, only baseband $\Sigma\Delta$ ADCs will be considered. Figure 6.6 exhibits a linearized model of first-order $\Sigma\Delta$ ADCs with a single-bit

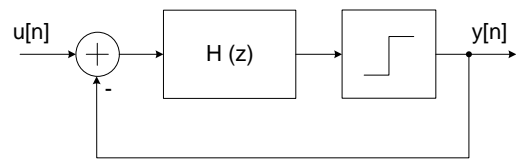


Figure 6.3.: $\Sigma\Delta$ ADC with a single bit quantizer.

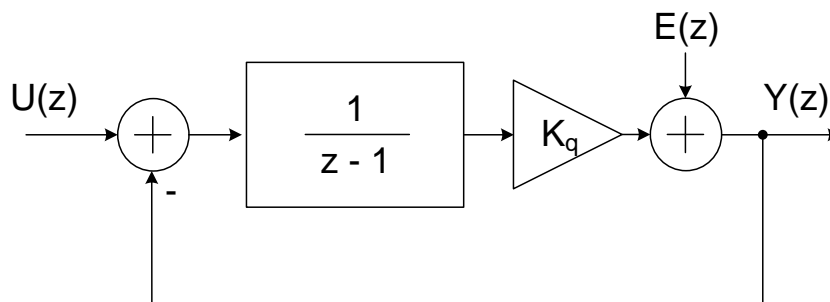


Figure 6.6.: Linearized model of a first-order $\Sigma\Delta$ ADC with a single-bit quantizer.

quantizer. In this figure the loop filter is nothing but an integrator with $H(z) = (z - 1)^{-1}$. Applying the superposition principle to the circuit and solving for $Y(z)$ result in

$$Y(z) = z^{-1} \cdot U(z) + (1 - z^{-1}) \cdot E(z) \quad (6.7)$$

$$STF = z^{-1} \quad (6.8)$$

$$NTF = 1 - z^{-1} \quad (6.9)$$

The magnitude of the frequency response for both the STF and the NTF is plotted in figure 6.7. The x-axis in this figure is the frequency normalized with the sampling frequency f_s . It is obvious from this figure that the signal level at the output of the ADC is constant,

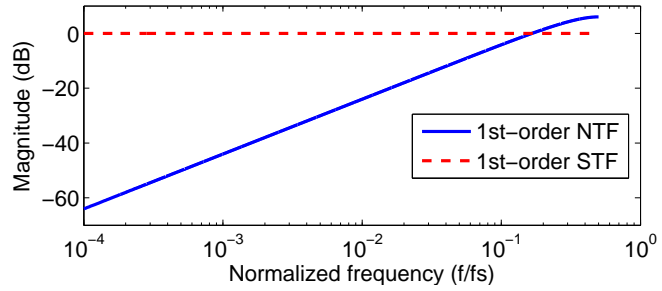


Figure 6.7: Magnitude of the frequency response for the STF and the NTF over normalized frequency.

while the quantization noise level is low for small frequencies (high OSR) and becomes higher as the frequency increases (lower OSR). Therefore for a specific sampling frequency f_s , the lower the signal frequency the lower the quantization noise and thus the higher the SQNR. With the NTF and the power spectral density (PSD) of the quantizer's noise, the in-band noise of the $\Sigma\Delta$ ADC can be calculated by integrating the PSD of the output noise over the desired band ($0 - f_B$) in this case. Thereby, the mean square of the in-band quantization noise at the output of the $\Sigma\Delta$ ADC is found to be [93]:

$$\bar{q}^2 = \frac{\pi^2 \bar{e}^2}{3(OSR)^3} \quad (6.10)$$

where $\bar{e}^2 = \Delta^2/12$ is the mean square of the quantization noise, and Δ is the step size of the quantizer. Just as it was demonstrated in figure 6.7, equation 6.10 shows that the in-band noise decreases with increasing the OSR, though this decrease is quite small. For example, doubling the OSR results in a 9 dB ($10 \cdot \log(1/2^3)$) decrease in the in-band noise which means approximately 1.5 bits more resolution.

6.2.3. Higher-order $\Sigma\Delta$ ADCs

The noise term ($NTF \cdot E(z)$) in equation 6.4 implies two strategies to decrease the in-band noise and thus enhancing the overall resolution of the ADC. Specifically, these strategies are:

1. Reducing the input quantization noise $E(z)$.
2. Redesigning $H(z)$ such that the NTF achieves more attenuation of the quantization noise in the desired frequency band.

Concerning the first item, the reduction of $E(z)$ requires necessarily minimizing Δ which, in turn, means employing quantizers with more bits. This method seems attractive, especially because it can significantly increase the SQNR of the $\Sigma\Delta$ ADC even with low OSR (each extra bit adds 6 dB to the SQNR). However, the need to multi-bit DACs in the feedback path makes the problem of inherent nonlinearity a major issue.

The other way to decrease the in-band noise is to exploit a higher order loop filter $H(z)$ such that the NTF provides more attenuation of the quantization noise within the desired band. Figure 6.8 displays the block diagram of a second order $\Sigma\Delta$ ADC. The output of this

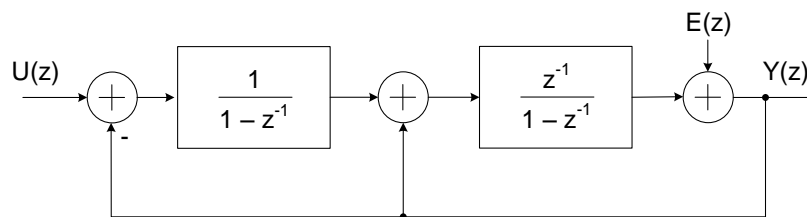


Figure 6.8.: Block diagram of a second-order $\Sigma\Delta$ ADC.

$\Sigma\Delta$ ADC is calculated as:

$$Y(z) = z^{-1} \cdot U(z) + (1 - z^{-1})^2 \cdot E(z) \quad (6.11)$$

$$STF = z^{-1} \quad (6.12)$$

$$NTF = (1 - z^{-1})^2 \quad (6.13)$$

Apparently, the STF is the same for both the first-order and the second-order $\Sigma\Delta$ ADC. However, the NTF of the second-order ADC is equal to the square of that of the first-order ADC, which means more attenuation of the quantization noise. This is demonstrated in figure 6.9 where the magnitude of the frequency response of the NTF for both the first-order and the second-order is plotted. It can be seen clearly from this figure that the

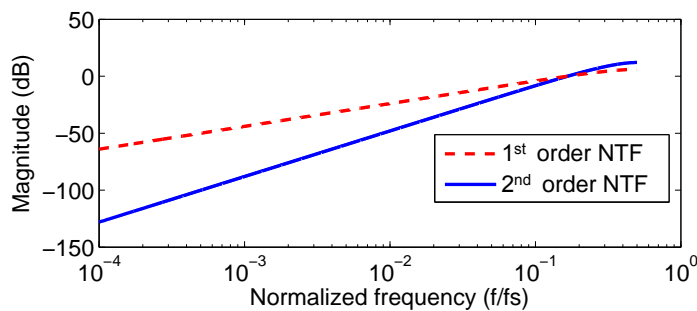


Figure 6.9: The magnitude of the frequency response of the NTF for the first-order and the second-order $\Sigma\Delta$ ADC.

second-order $\Sigma\Delta$ ADC features steeper attenuation (40 dB/decade) of the quantization

noise compared to the first-order which showed 20 dB/decade attenuation. Following the same procedure of deriving the in-band noise of the first-order modulator, the mean square of the in-band noise of the second-order modulator can be determined by the following equation [93]:

$$\bar{q}^2 = \frac{\pi^4 e^2}{5(OSR)^5} \quad (6.14)$$

which evidently shows that the second-order modulator exhibits less in-band noise than the first-order modulator for the same OSR. Moreover, equation 6.14 demonstrates that effect of OSR is more significant in the case of second-order $\Sigma\Delta$ ADCs. Thus doubling the OSR in this case improves the overall SQNR by approximately 15 dB which means 2.5 bits more ENOB. In general, for an L-th order $\Sigma\Delta$ ADC with a noise transfer function

$$NTF = (1 - z^{-1})^L \quad (6.15)$$

the mean square of the in-band quantization noise can be calculated as [93]:

$$\bar{q}^2 = \frac{\pi^{2 \cdot L} e^2}{(2L + 1)(OSR)^{2L+1}} \quad (6.16)$$

which imposes that the resolution of the $\Sigma\Delta$ ADC can be straightforwardly enhanced by increasing the order of the modulator. However, increasing the order of the $\Sigma\Delta$ modulator makes the problem of instability more pronounced. Nevertheless, the stability issues can be remedied by tolerating smaller input dynamic range.

6.3. System-Level Verification of the Proposed MRI Receiver

In order to verify the concept and functionality of the MR receiver architecture proposed in figure 6.1, a system-level platform was established. The Matlab graphical interface "Image_Reconstruct_DSM", displayed in figure 6.10, was created to control the system level simulation and image acquisition. This GUI is designed to emulate the acquisition and processing of the MR signals from the RF detection coil to the MR reconstructed image. Therefore, the simulation starts with uploading the MR coil signals which, as it was demonstrated in chapter 4, can be obtained for a certain MR image using the Matlab program in figure 4.2. After that, the user can set the gain and the noise figure of the LNA as well as the frequency mixer which, in this case, performs a direct frequency conversion on the MR signals by shifting them to near-DC band. Then these signals are introduced to a lowpass filter that rejects the undesired sidebands and limits the bandwidth of the signals in order to prevent aliasing.

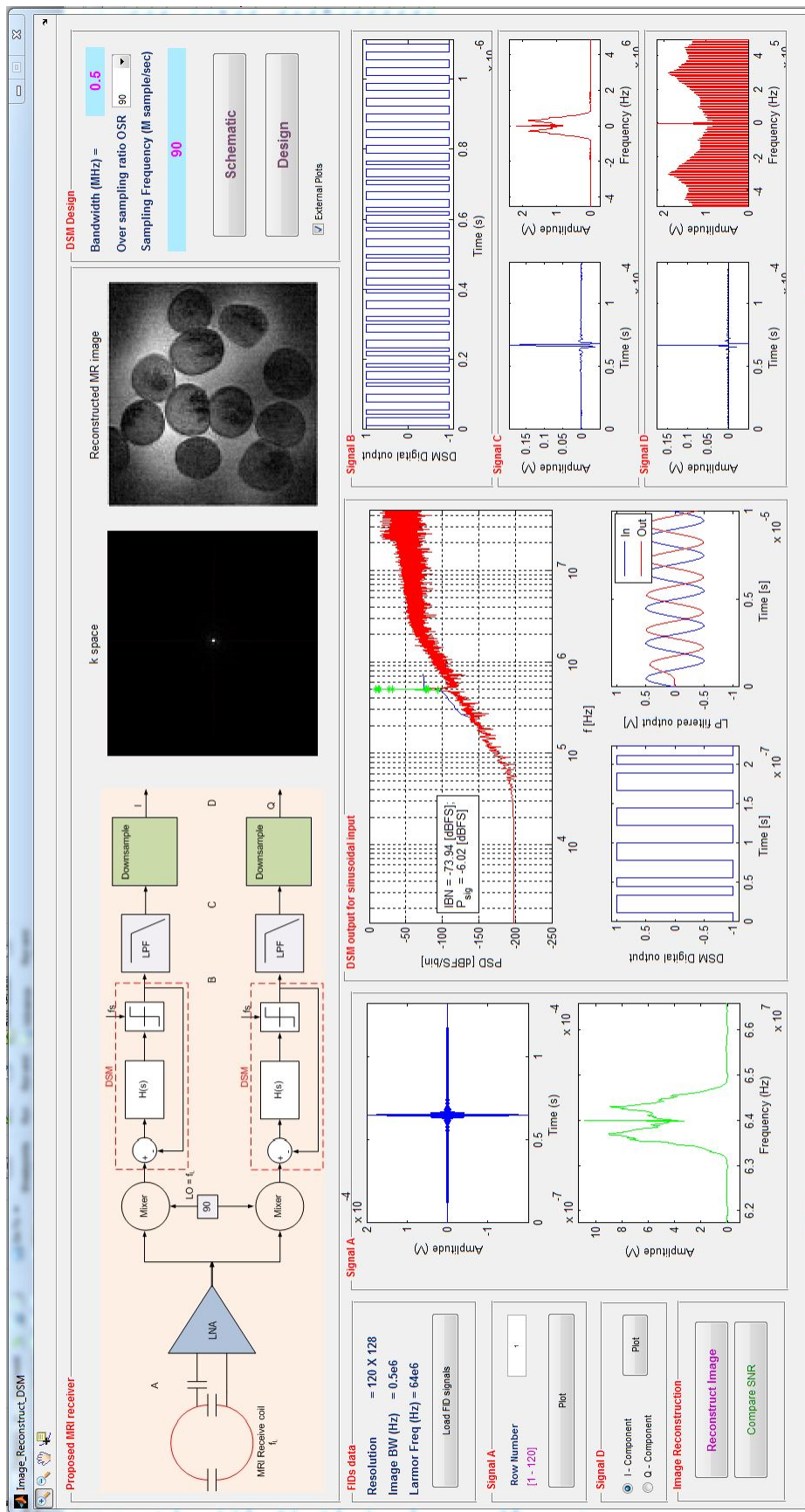


Figure 6.10.: Matlab GUI to perform a system-level simulation of the new MR receiver architecture described in figure 6.1.

6.3.1. Sigma-Delta ADC

After the MR signals have been directly demodulated and filtered, they are now ready for the analog-to-digital conversion through the $\Sigma\Delta$ ADC. The program in figure 6.10 assumes a 1 MHz fixed bandwidth for the MR signals, and accordingly enables the user to set the OSR. Having the OSR and the order of the loop filter (3-rd order filter was employed in this simulation), the Matlab program utilizes the "Delta-Sigma Toolbox" [93] to calculate the desired NTF, from which the loop filter $H(z)$ can be afterwards directly calculated. Then the Matlab GUI passes the coefficients of the loop filter $H(z)$ as well as the MR signals to a Simulink model of the $\Sigma\Delta$ ADC such as the one illustrated in figure 6.11, and then starts a transient simulation. The simulation outputs are thereafter transferred back to

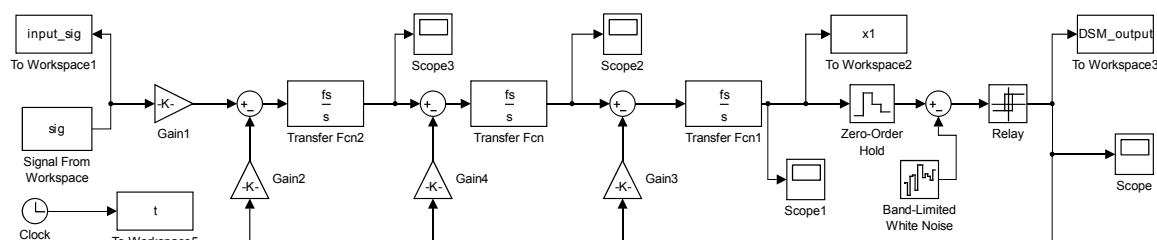


Figure 6.11.: Simulink model of a third-order $\Sigma\Delta$ ADC with a single bit quantizer.

the Matlab program in figure 6.10 where they are lowpass filtered and down-sampled to fill the k-space map. This process is repeated for each row of the k-space and once it is completely filled, a two-dimensional Fourier transform is applied in order to obtain the MR image. Figure 6.12 summarizes the results of the third-order $\Sigma\Delta$ ADC displayed in figure 6.11 for a sinusoidal input with an OSR = 120 (sampling frequency = 64 MSPS). In figure 6.12a the digital output stream of the ADC is plotted. This signal represents the pulse density modulated output of the input sinusoid. Figure 6.12b shows the input (blue) of the ADC and the decimated output (red) of it. The power spectral density of the ADC's digital output is plotted in figure 6.12c. The in-band quantization noise (IBN) in this case is approximately -77 dB relative to the full scale.

6.3.2. Simulation Results

The new MR receiver in figure 6.10 was tested by conducting a simulation of an imaging experiment. The fish oocytes MR image in figure 4.12a was employed to provide the simulation inputs through the Matlab program in figure 4.2, and the bandwidth of the

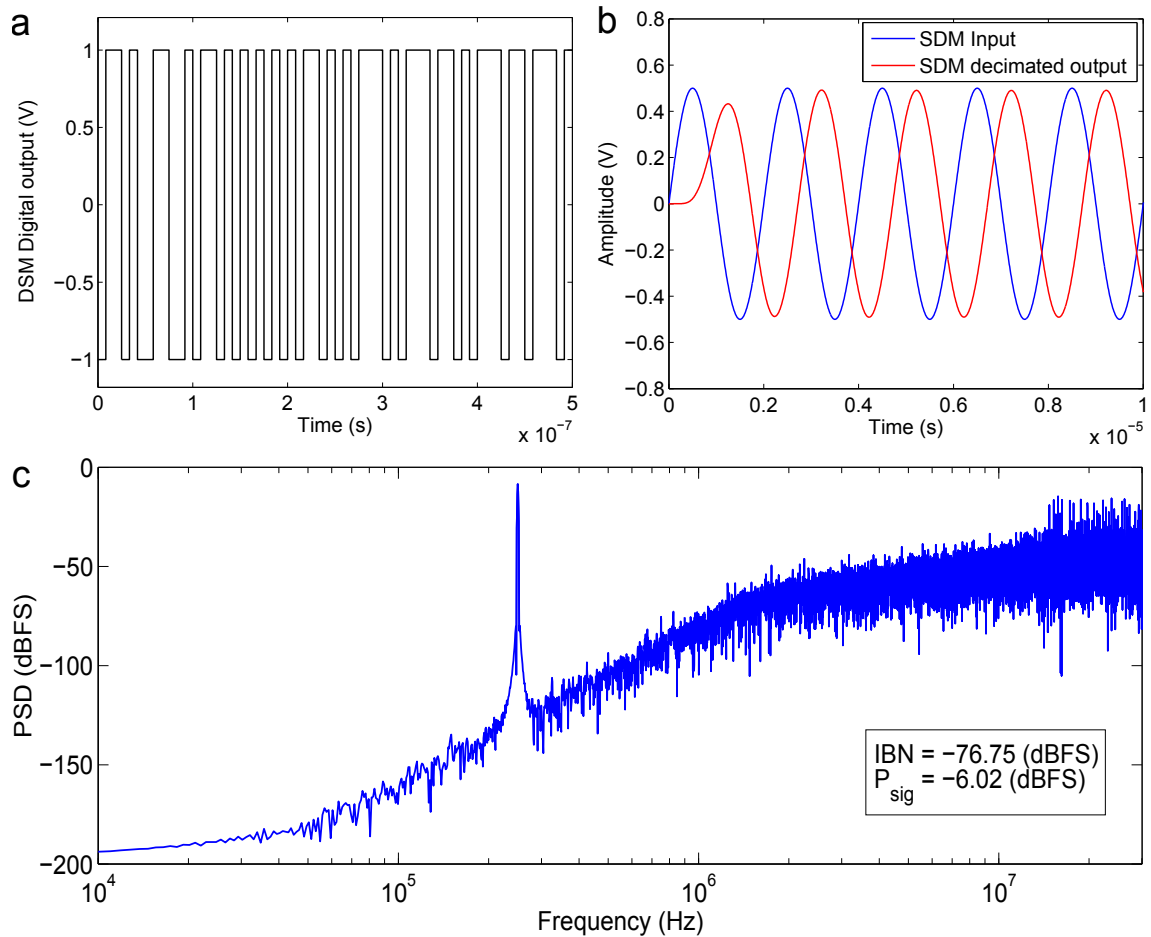


Figure 6.12.: Simulation results of the third-order $\Sigma\Delta$ ADC plotted in figure 6.11 for OSR = 120. (a) The digital output stream of the ADC. (b) The input sinusoid (blue) of the ADC and the decimated output (red). (c) The power spectral density (PSD) of the ADC's output. The in-band noise in this case is approximately -77 dBFS.

MR image, f_B , was set to 250 kHz. The noise contribution of the LNA and the frequency mixers was neglected by assuming them as ideal elements in order to allow characterizing the performance of the $\Sigma\Delta$ ADC in terms of image quality. Therefore, the simulation was repeated a number of time with the OSR being changed each time. Figure 6.13 illustrates the effect of changing the OSR on the resolution of the MR image. On the top left of the figure, the original MR image [36], which drove the simulation, is plotted. It exhibits an SNR of 14.4 dB. The other images within this figure show the reconstructed images for OSR values of 40 to 100 with a step of 10. This figure demonstrates evidently how the

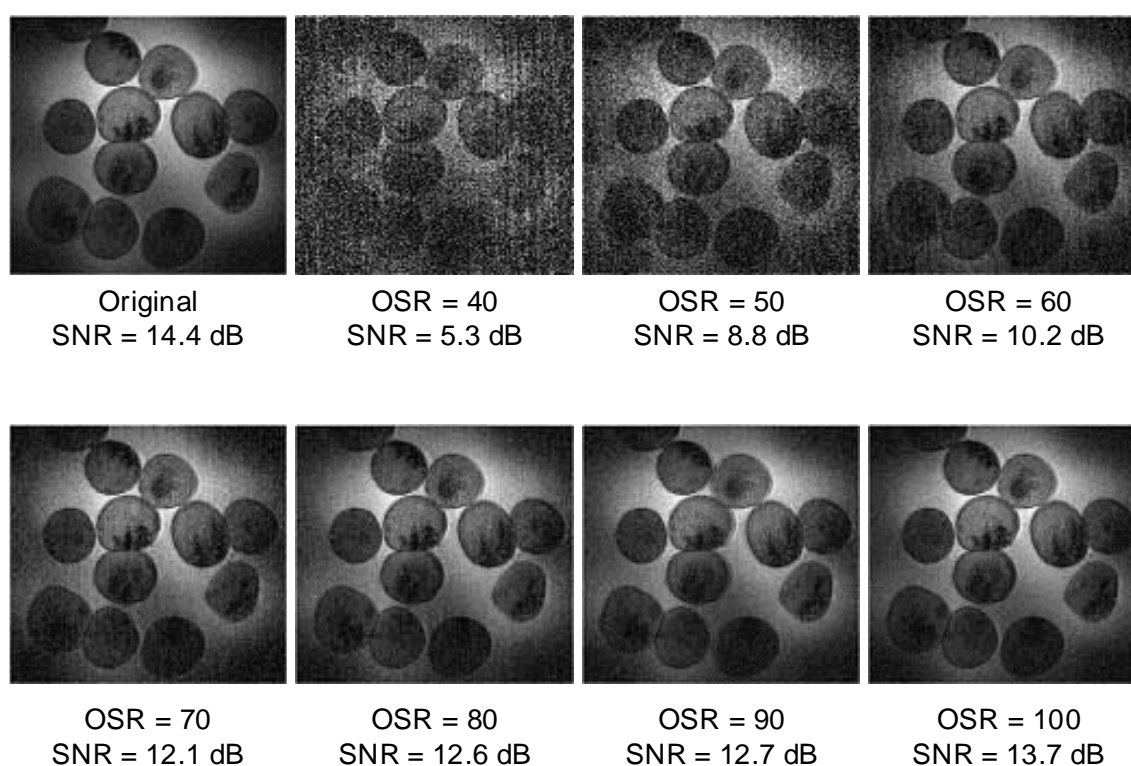


Figure 6.13.: Effect of increasing the oversampling ratio (OSR) of the $\Sigma\Delta$ ADC in the MR receiver in figure 6.10.

SNR of the images increases with increasing the OSR. However, the increase in the SNR decreases if the OSR is further increased. This is because the SNR in MR images depends on all rows of the k-space which, as explained in chapter 2, have relatively large differences in amplitudes. Nevertheless, an OSR of 100 seems to achieve a sufficiently high-resolution reconstruction of the image.

6.4. Circuit-Level Implementation of the Proposed MRI Receiver

Figure 6.14 displays the circuit implementation of the new MR receiver architecture shown in figure 6.1. In this implementation, the circuits of the LNA and the frequency mixer are exactly the same as the ones presented in chapter 3. The frequency conversion scheme exploited in this design is the direct demodulation. Therefore the local oscillator signal should ideally have the Larmor frequency f_0 . However, in this receiver the LO frequency was set 10 kHz below the f_0 in order to avoid the flicker noise of the mixer which is relatively high and can therefore ruin the whole image reconstruction process. After the demodulation the signals are lowpass filtered and introduced to a third-order baseband $\Sigma\Delta$ modulator that is realized with a distributed feedback topology [55]. The $\Sigma\Delta$ modulator utilizes the same topology of the op-amp presented in chapter 3 as an integrator to build its loop filter $H(s)$. Moreover, this op-amp, coupled with a D flip-flop, is used as a single-bit quantizer. Finally, a single-bit DAC that translates the digital output of the $\Sigma\Delta$ modulator to $\pm V_{ref}$, which is afterwards fed back to the modulator, is employed. Table 6.1 summarizes the key parameters of the $\Sigma\Delta$ modulator which were synthesized for the loop filter $H(z)$ that was calculated from the STF and NTF obtained from the "Delta-Sigma toolbox" [93] for a third order $\Sigma\Delta$ modulator. The PSD of the output of the CMOS $\Sigma\Delta$ modulator depicted

Table 6.1.: $\Sigma\Delta$ modulator parameters

Parameter	Value	Unit	Parameter	Value	Unit
C	1	pF	R6	10.131	k Ω
R1,2	338.88	k Ω	Clk	64	MSPS
R3,5	15.625	k Ω	V_{ref}	200	mV
R4	338.88	k Ω	Vdd	3.3	V

in figure 6.14 is plotted in figure 6.15. The input in this case is a sinusoid with a frequency of 250 kHz. The sampling frequency of the $\Sigma\Delta$ f_s is 64 MSPS, while the bandwidth over which the PSD of the signal is calculated is 250 kHz resulting in an OSR of 128. The peak amplitude of the input signal is 100 mV, while the feedback reference voltage V_{ref} is 200 mV. The in-band noise according to figure 6.15 was found to be approximately -62 dBFS, and the power of the signal was found to be 12.6 dBFS resulting in an SQNR of 74.6 dB that corresponds to an ENOB of approximately 12.433 bits. In figure 6.16, the simulated SNR of the $\Sigma\Delta$ ADC is plotted versus the input voltage normalized to the reference voltage V_{ref} . According to the figure, the SNR increases linearly with V_{in} until

6. New Fully Integrated Receiver Architecture

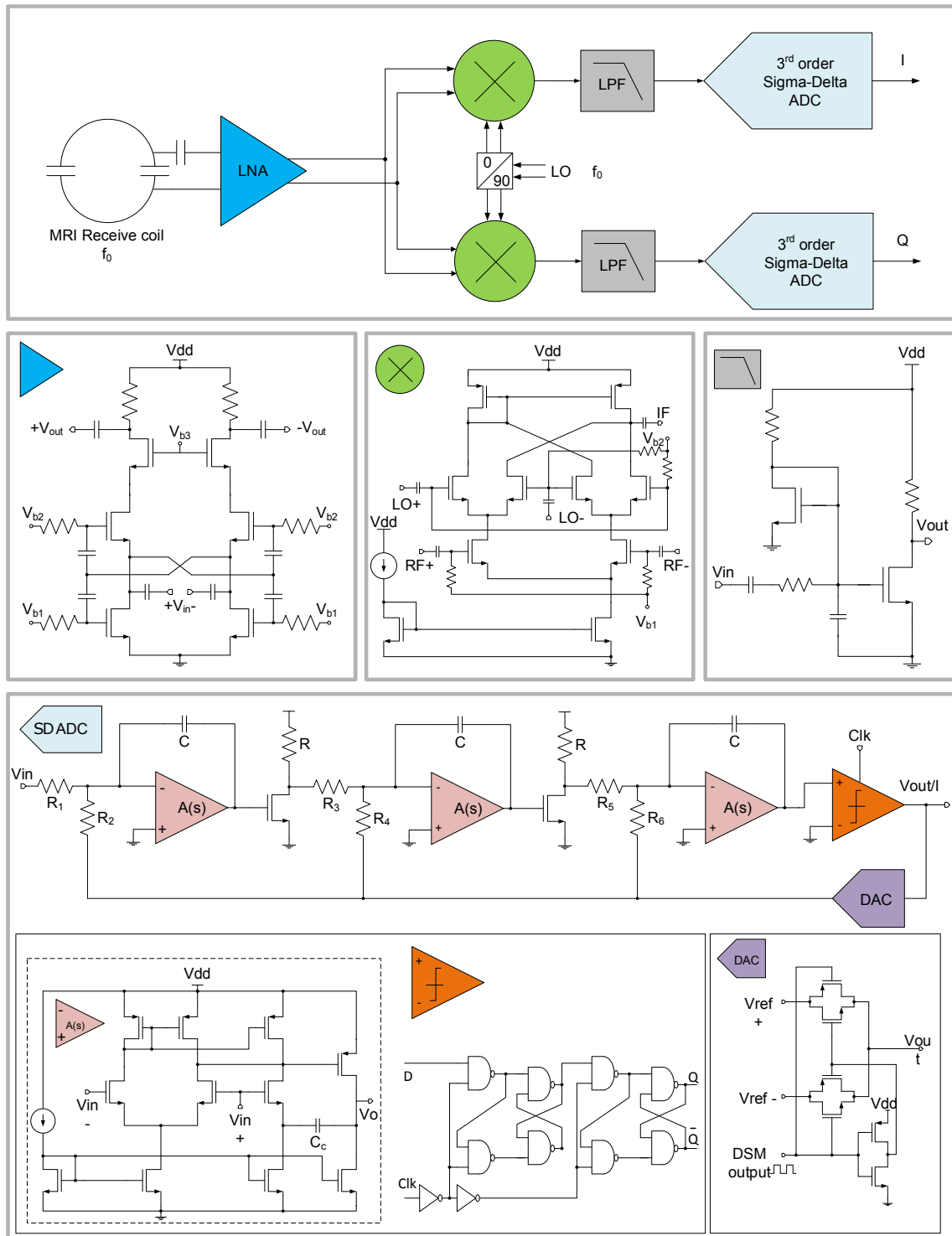


Figure 6.14.: Circuit implementation of the new MR receiver architecture sketched in figure 6.1.

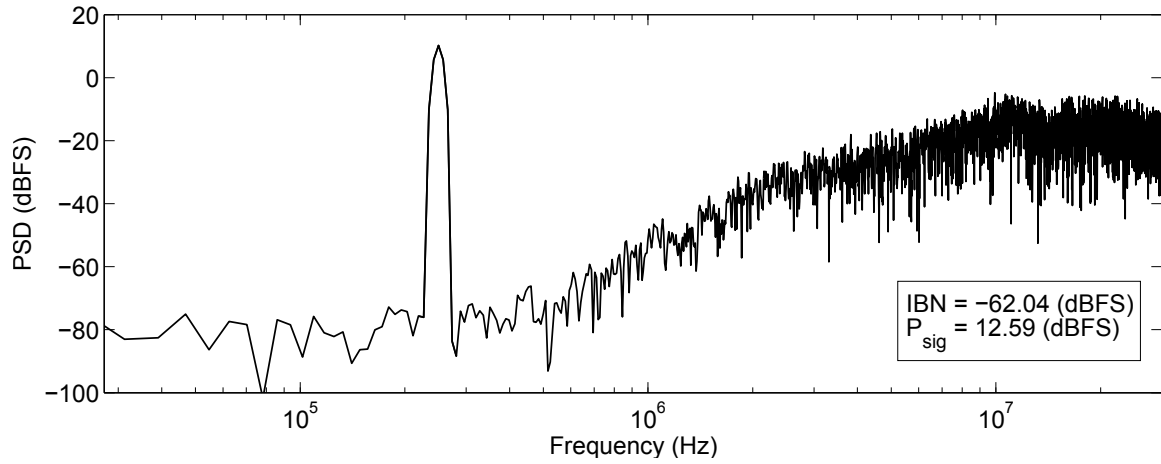


Figure 6.15.: Power spectral density of the output of the third-order $\Sigma\Delta$ modulator depicted in figure 6.14. The signal has a bandwidth of 250 kHz, while the OSR is 128.

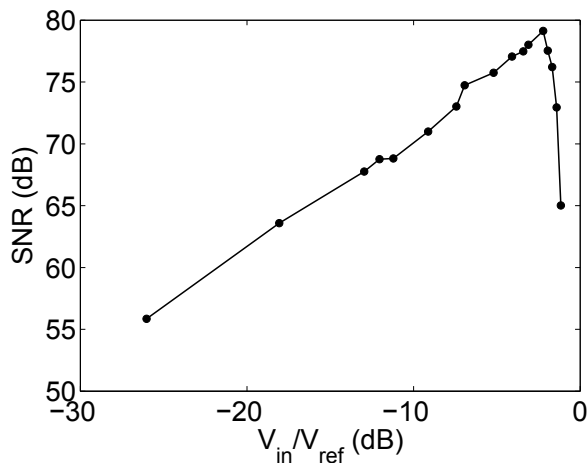


Figure 6.16: SNR of the $\Sigma\Delta$ modulator versus the normalized input voltage.

it reaches a maximum of approximately 80 dB (~ 13.3 bits) corresponding to normalized input of -2.2 dB ($V_{in} = 155$ mV), and after which the SNR decreases.

6.4.1. Simulation Results

In order to get a comprehensive insight into the performance of the entire circuit of the receiver, a simulation platform similar to the one in figure 4.1 was created. In this simulation flow, the Matlab program in figure 4.2 is employed to obtain the detection coil's signals of an original or emulated MR image. After this program is done, an "Ocean" script (see appendix A) is called to automatically feed the coil's signals to the circuit's simulator (Spectre), run the simulation, and save the results. For signal processing and image reconstruction, a new Matlab program "Image_Reconstruct_from_homodyne_receiver_with_DSM" with the user interface displayed in figure 6.17 was written. It starts by loading the simulation outputs. Then each signal will be filtered and down-sampled so as to fill the corresponding line of the k-space map. This process is repeated for all the lines of the k-space, and at the end the k-space in addition to the MR image are obtained. Thereafter, the performance of the circuit can be evaluated by conducting a comparison between the original and the reconstructed images by virtue of the program in figure 4.6.

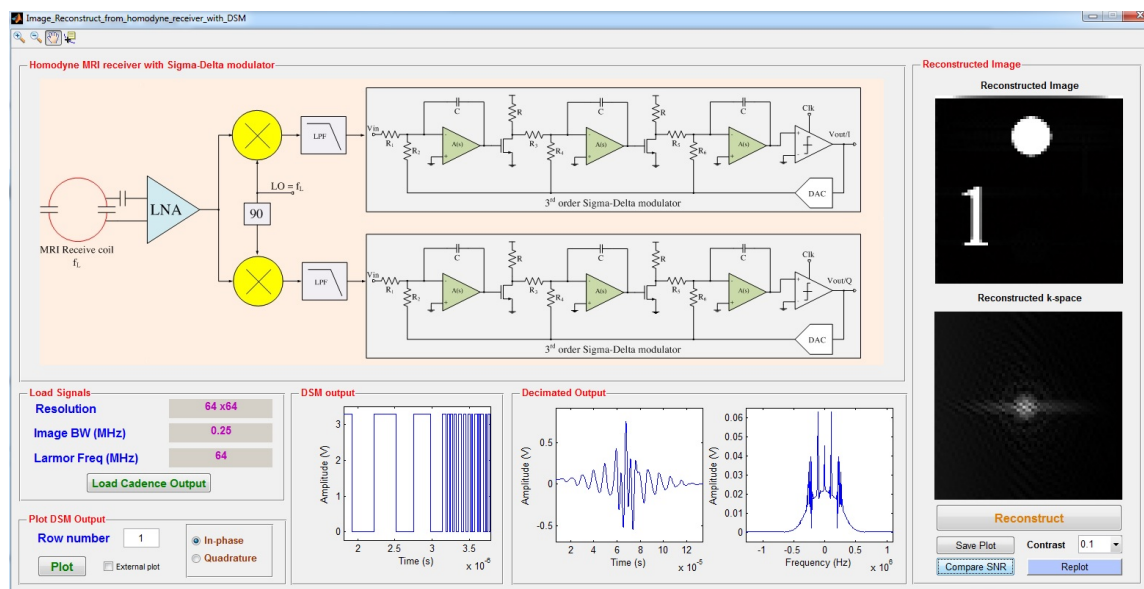


Figure 6.17.: A Matlab program to process the simulation outputs of the circuit in figure 6.14, and reconstructs the MR image.

Figure 6.18 shows the original fish oocytes image and the its reconstructed version after going through the MR receiver circuit in figure 6.14. The bandwidth of the image was set

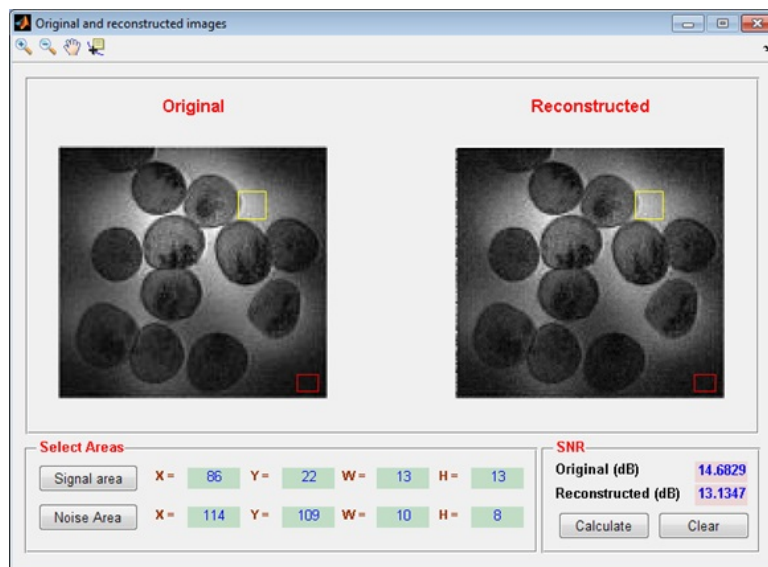


Figure 6.18: Original and reconstructed image resulting from the circuit-level simulation of the MR receiver in figure 6.14.

to 250 kHz. The input signals amplitude was adjusted to have a maximum of $100 \mu\text{V}$, while a 64 MSPS was chosen as a sampling frequency of the $\Sigma\Delta$ modulator. Hence, a 128 OSR was achieved. The simulation was run over approximately 2 weeks, and the size of the simulation outputs was 29.3 GB which took an i7-3.4 GHz computer around 15 minutes to process the data and reconstruct the image. The last figure patently shows that the MR image was successfully retrieved with no artifacts or distortion. However, a 1.55 dB reduction in the SNR can be observed. This SNR degradation is nothing but the noise contribution of the entire MR receiver.

6.5. Summary

In this chapter, a new fully integrated receiver architecture for MRI as well as MRS systems has been reported. The scheme, whose fundamental idea is to integrate the major part of the receiver's electronics including the ADC on a single chip, was tested at both the system-level and the transistor-level. While the system-level simulations are relatively good to get a general feeling about the system's performance and to prove its concept, the transistor-level simulations are based on highly accurate device models that consider noise, linearity, transition frequency f_T , parasitics, process variations and tolerances, etc. Therefore, they can account for almost all the circuit's non-idealities and consequently return greatly reliable results. Table 6.2 lists the Matlab programs that were presented in this chapter. It also gives a brief summary of what these programs specifically do.

Unlike the conventional MR receiver, the size-efficient (chip area is approximately 0.9 mm^2 for a single channel) receiver proposed in this chapter allows to directly digitize

Table 6.2.: Summary of the Matlab programs introduced in this chapter.

Image_Reconstruct_DSM

- Performs a system-level simulation of a homodyne MR receiver with a sigma-delta ADC.
 - Allows the user to vary the OSR of the $\Sigma\Delta$ ADC in order to characterize its effect on the image quality.
-

Image_Reconstruct_from_homodyne_receiver_with_DSM

- Processes the transient simulation outputs of a transistor-level CMOS MR Homodyne receiver with a $\Sigma\Delta$ ADC.
 - Reconstructs the MR image from the simulation outputs and compares it with the original image.
-

the MR signals within the coil, which facilitates handling, transferring, and processing these signals. Once the MR signals are converted to digital bit streams, it will be possible to apply the state-of-art high data rates solutions to multiplex numerous MR channels. For example, the multiplexer reported in [73] and realized in a 210 GHz f_T SiGe-bipolar technology, is capable of producing output bit rates up to 132 Gbps. This renders the multiplexing of 128 channels a straightforward task. In such a multiplexer, only a single LO will be used for all channels front ends which is a major advantage compared to the FDM.

7. Conclusion and Outlook

In this work several novel approaches for the development of the MR receiver's hardware have been introduced. These approaches targeted mainly the development of the RF receivers that interface the MR phased arrays. They focused on developing RF receivers that allow MR phased arrays with many coils, thus achieving higher resolution, larger FoV, and less scan time, with no penalty of increased size, cost, or complexity of the entire system. The new approaches introduced can be summarized as follows:

7.1. CMOS Frequency Division Multiplexer

A CMOS frequency multiplexer that is capable of merging up to eight channels was introduced as a efficient solution to the size and complexity issues associated with MR phased arrays. The multiplexer has eight channels, each of which consists mainly of an LNA, a frequency mixer, and a BPF. A detailed description of the design and simulation of the individual blocks of the multiplexer have been given. Furthermore, the measurements results of the multiplexer, fabricated in 0.35 μm technology from XFab, showed successful operation inside and outside high (up to 11.7 T) magnetic fields. Besides, the results of conducting spectroscopy and imaging experiments in 11.7 T and 9.4 T scanners respectively exhibited results that are in very good match with the counterpart results obtained from the scanners. The multiplexed output of the FDM can be processed by employing one of the following methods:

1. Using a high-resolution (14-bits or higher) large-bandwidth (at least 50 MHz) ADC to digitize the signal, and then performing quadrature demodulation and lowpass filtering in the digital domain. This is basically the approach employed in the UHFLI. The main advantage of this approach is the need for only one ADC which means a reduction in the complexity of the receiver and the number of cables as well. On the other hand, using a single ADC limits the number of channels the multiplex can combine, since adding more channels necessitates larger bandwidth of the ADC which is inversely proportional to the number of bits [48]. Moreover, the number of channels is limited by the input dynamic range of the ADC, since adding more channels increases the peak amplitude of the multiplexed signal and thus, after a

certain limit, saturates the ADC's input. Therefore, utilizing a single ADC seems to be a limiting factor that chains the extensibility and scalability of frequency multiplexing approach.

2. The other method is to perform the demultiplexing and the quadrature demodulation in the analog domain by means of a discrete-components solution or even by means of a CMOS integrated solution and then employ a number of ADC's twice the number of channels to digitize the MR signals. This approach seems to put fewer constraints on the number of channels that can be multiplexed. However, it still suffers from the receiver complexity.

Apart from the processing method, the CMOS FDM still confirms its significance in reducing the number of cables and the complexity of the MR reception array. Moreover, it shows full readiness to replace the commercial systems.

One last worth-mentioning issue regarding the CMOS FDM is the generation of the local oscillators. So far, the desired LOs were generated externally. However, for a final commercialized solution a monolithic system is a must. The LO frequencies required for the FDM are 390, 385, 380, 375, 370, 365, 360, and 355 MHz which are impossible to obtain from a single synthesized frequency by a simple integer N frequency divider. The easiest way, therefore, to generate such frequencies is to integrate eight voltage-controlled oscillators (VCOs) with eight phase-locked loops (PLLs) that locks the output frequencies to a single reference clock. However, this solution results in large increase in power consumption and chip area. In a future outlook, extensive study should be given to this part of the circuit so as to decrease the number of frequency synthesizers used. This includes, for example, choosing the LOs in a way such that each two or three can be generated from one frequency (e.g the 390 MHz and the 360 MHz can be obtained from a 4.68 GHz frequency). Apart from that, the CMOS FDM has the full susceptibility to future optimization in all aspects including power consumption, chip size, noise, gain, linearity, and number of channels to provide, at the end, a perfect alternative to the commercial systems.

7.2. New Simulation Method for MR Circuits Characterization

The second approach that was presented in this thesis is the development of a new simulation method that enables the MR circuit designer to characterize the circuit's performance via a virtual MRI experiment. The main idea of this simulation method is to reconstruct the MR FID signals of the reception coils from an MR image, and then using these signals

to drive a transient simulation of transistor-level or extracted-layout level of a custom MR circuit. After that, the simulation outputs are processed to reconstruct the original MR image. Finally, by comparing the original and the reconstructed MR images, many circuit parameters such as the gain, noise figure, linearity, etc. can be investigated. A transistor-level (with extracted layout for the frequency mixers) simulation of the CMOS FDM proposed in chapter 3 carried out to validate this new simulation method. The results of this simulation, especially the noise and the linearity, showed good resemblance to their counterparts obtained in chapter 3 by means of the conventional circuit simulations. Although the new simulation method is not expected to replace the conventional circuit simulation, it conceived to have a particular significance in the design of the MR circuits especially the integrated solutions which are expensive to fabricate. It will give the circuits designers more confident to take the decisions for fabrication.

Furthermore, the new simulation methodology offers a large room for further developments and enhancements by, for example, including space-time resolved simulations for the coil detectors, which currently would add additional complexity leading to even longer simulation times. However, it seems to be the most logical next-step in the way of developing the simulation method.

Because the implementation of the simulation methodology was limited to simple spin-echo sequences, which are not fundamental, nevertheless, generalization to more imaging sequences will require additional software or integration into an MRI simulation environment (such as Virtual MRI [37], jemris [100], SIMRI [14], Simplified MRI, or MRI Lab). The same is true for reconstruction operations that depend on the hardware topology.

7.3. New Fully Integrated MR Receiver

The third approach presented in the thesis is the design of a fully integrated MR receiver. What is special about this receiver is that it integrates most of the signal processing blocks, especially the analog to digital converter, on a single chip that is to be mounted just near the RF reception coil. In this case the MR signals are transferred from the inside of the MR magnet in a digital form, thus they are immune to noise, and furthermore they can be transferred over optical fibers which have much higher data rates than coaxial cables. The ADC employed in this approach is a third-order continuous time $\Sigma\Delta$ modulator which exhibits high resolution conversion (up to 12 bits) while using a single-bit quantizer, and thus allows to decrease the number of transmission media. The new approach was verified at both the system-level and the transistor-level, and the simulation results

showed successful reconstruction of the MR images with negligible degradation in the SNR.

The number of channels can be extended simply by integrating replicas of the proposed receiver on the same chip, and integrating high speed time multiplexers to combine the digitized MR signals from all channels thus maintaining the size efficiency of the system. The new approach is, therefore, expected to be superior to the FDM especially in the ability to multiplex more channels since it does not suffer from the limitations, such as the LO generation, BPF design, ADC bandwidth, and ADC dynamic range, that limit the number of channels in the FDM. However, the new approach entails more modifications and changes to the commercial MR system. Such modifications include using time domain demultiplexers, decimation filters, and optical detectors, in case optical fibers were used to carry the MR signals.

A. Appendix

A.1. Ocean Script Example

```
1 simulator( 'spectre )
2 design(  "/tmp/mj1014/Sim/16_channels_new1/spectre/schematic/netlist/
   netlist")
3 resultsDir(  "/tmp/mj1014/Sim/16_channels_new1/spectre/schematic" )
4 modelFile(
5     '("/usr/local/DesignKits/XFab/IC6/spectre/xh035/mos/param.scs" "3s")
6     '("/usr/local/DesignKits/XFab/IC6/spectre/xh035/mos/bip.scs" "tm")
7     '("/usr/local/DesignKits/XFab/IC6/spectre/xh035/mos/bsim3v3.scs" "tm
   ")
8     '("/usr/local/DesignKits/XFab/IC6/spectre/xh035/mos/cap.scs" "tm")
9     '("/usr/local/DesignKits/XFab/IC6/spectre/xh035/mos/dio.scs" "tm")
10    '("/usr/local/DesignKits/XFab/IC6/spectre/xh035/mos/ind.scs" "tm")
11    '("/usr/local/DesignKits/XFab/IC6/spectre/xh035/mos/res.scs" "tm")
12    )
13
14 analysis('tran ?stop "130u" ?tranNoise "Transient Noise" ?noiseymax "1
   G"
15 ?noisexmin "1" ?noiseseed "1" ?noisescale "1.5" ?noisetmin ""
16 ?noiseupdate "" ?noiseonoff "" ?noiseinst "" )
17 desVar(  "flo1" 390M )
18 desVar(  "flo2" 385M )
19 desVar(  "flo3" 380M )
20 desVar(  "flo4" 375M )
21 desVar(  "flo5" 370M )
22 desVar(  "flo6" 365M )
23 desVar(  "flo7" 360M )
24 desVar(  "flo8" 355M )
25 desVar(      "frf" 400M      )
26 envOption(      'analysisOrder  list("tran")      )
27
28 option( ?categ 'turboOpts
29     'numThreads  "4"
30     'mtOption  "Manual"
```

A. Appendix

```
31     'errorLevel  "Conservative"
32     'uniMode    "APS"
33     )
34
35 saveOption( ?elementInfo nil )
36 saveOption( ?modelParamInfo nil )
37 saveOption( 'save "" )
38 temp( 27 )
39
40 for( i 1 256
41
42     sprintf( x1 "path_1=/home/mj1014/Desktop/MRI/test/16_channels_new1/
43             rows_in/image1_row%d" i)
44     setShellEnvVar(x1)
45
46     sprintf( x2 "path_2=/home/mj1014/Desktop/MRI/test/16_channels_new1/
47             rows_in/image2_row%d" i)
48     setShellEnvVar(x2)
49
50     sprintf( x3 "path_3=/home/mj1014/Desktop/MRI/test/16_channels_new1/
51             rows_in/image3_row%d" i)
52     setShellEnvVar(x3)
53
54     sprintf( x4 "path_4=/home/mj1014/Desktop/MRI/test/16_channels_new1/
55             rows_in/image4_row%d" i)
56     setShellEnvVar(x4)
57
58     sprintf( x5 "path_5=/home/mj1014/Desktop/MRI/test/16_channels_new1/
59             rows_in/image5_row%d" i)
60     setShellEnvVar(x5)
61
62     sprintf( x6 "path_6=/home/mj1014/Desktop/MRI/test/16_channels_new1/
63             rows_in/image6_row%d" i)
64     setShellEnvVar(x6)
65
66     sprintf( x7 "path_7=/home/mj1014/Desktop/MRI/test/16_channels_new1/
67             rows_in/image7_row%d" i)
68     setShellEnvVar(x7)
69
70     sprintf( x8 "path_8=/home/mj1014/Desktop/MRI/test/16_channels_new1/
71             rows_in/image8_row%d" i)
72     setShellEnvVar(x8)
73
74     sprintf( x9 "path_9=/home/mj1014/Desktop/MRI/test/16_channels_new1/
75             rows_in/image9_row%d" i)
```

```
67  setShellEnvVar(x9)
68
69  sprintf( x10 "path_10=/home/mj1014/Desktop/MRI/test/16_channels_new1/
    rows_in/image10_row%d" i)
70  setShellEnvVar(x10)
71
72  sprintf( x11 "path_11=/home/mj1014/Desktop/MRI/test/16_channels_new1/
    rows_in/image11_row%d" i)
73  setShellEnvVar(x11)
74
75  sprintf( x12 "path_12=/home/mj1014/Desktop/MRI/test/16_channels_new1/
    rows_in/image12_row%d" i)
76  setShellEnvVar(x12)
77
78  sprintf( x13 "path_13=/home/mj1014/Desktop/MRI/test/16_channels_new1/
    rows_in/image13_row%d" i)
79  setShellEnvVar(x13)
80
81  sprintf( x14 "path_14=/home/mj1014/Desktop/MRI/test/16_channels_new1/
    rows_in/image14_row%d" i)
82  setShellEnvVar(x14)
83
84  sprintf( x15 "path_15=/home/mj1014/Desktop/MRI/test/16_channels_new1/
    rows_in/image15_row%d" i)
85  setShellEnvVar(x15)
86
87  sprintf( x16 "path_16=/home/mj1014/Desktop/MRI/test/16_channels_new1/
    rows_in/image16_row%d" i)
88  setShellEnvVar(x16)
89
90  run()
91  x = VT("/vout")
92  plot( x ?expr '( "x" ) )
93
94  sprintf( yy "/home/mj1014/Desktop/MRI/test/16_channels_new1/rows_out
    /16_channels_out%d.txt" i)
95  ocnPrint((VT "/vout") ?output yy ?numberNotation 'none ?precision 15 ?
    width 20)
96
97  )
```


B. Appendix

B.1. UHFLI Run Script

```
1 function data = run_UHFLI_script(port, api_level)
2     % Matlab script to run the UHFLI for an imaging experiment
3
4     ziAddPath;                                % add the path
5     % of the UHFLI toolbox
6     clear ziDAQ;                              % disconnect
7     % any devices
8     ziDAQ('connect', '127.0.0.1', 8004, 5);  % connect the
9     % UHFLI
10
11    % Check ziDAQ's ziAutoConnect (in the Utils/ subfolder) is in the
12    % path
13    if exist('ziAutoConnect','file') ~= 2
14        fprintf('Please configure your path using the ziDAQ function
15        ziAddPath().\n');
16        fprintf('This can be found in the API subfolder of your LabOne
17        installation.\n');
18        fprintf('On Windows this is typically:\n');
19        fprintf('C:\\Program Files\\Zurich Instruments\\LabOne\\API\\
20        MATLAB2012\\\n');
21        return
22    end
23
24    % open a connection to a Zurich Instruments server
25    if exist('port','var') && exist('api_level','var')
26        ziAutoConnect(port, api_level);
27    elseif exist('port','var')
28        ziAutoConnect(port);
29    else
30        ziAutoConnect();
31    end
32
33    % define some record module-related parameters
```

```
27 trigger_delay = 0;
28 trigger_duration = 10e-3;
29 trigger_count = 256;
30 trigger_level = 0.0200000;
31 trigger_holdOff_time = 0.1;
32 trigger_holdOff_count = 0;
33
34 % define some device configuration parameters
35 time_constant = 0.000001623 ;
36 sample_rate = 320000.000000000;
37 LO_freq = 380e6;
38 LO_amp = 800e-3;
39 IF_freq = 20e6;
40
41 % Presetting of the UHFLLI registers
42 device = ziAutoDetect();
43 devtype = ziDAQ('getBytes', ['/' device '/features/devtype']);
44 options = ziDAQ('getBytes', ['/' device '/features/options']);
45 ziDAQ('setInt', ['/' device '/system/extclk'], 1.000000000);
46 ziDAQ('setDouble', ['/' device '/demods/*/rate'], 0.0);
47 ziDAQ('setInt', ['/' device '/demods/*/trigger'], 0);
48 ziDAQ('setInt', ['/' device '/sigouts/*/enables/*'], 0);
49 ziDAQ('setInt', ['/' device '/demods/*/enable'], 0);
50
51 % Setting the LO
52 ziDAQ('setDouble', ['/' device '/oscs/0/freq'], LO_freq);
53 ziDAQ('setDouble', ['/' device '/sigouts/0/amplitudes/0'], LO_amp);
54 ziDAQ('setInt', ['/' device '/sigouts/0/imp50'], 1.000000000);
55 ziDAQ('setInt', ['/' device '/sigouts/0/on'], 1.000000000);
56 ziDAQ('setInt', ['/' device '/sigouts/0/enables/0'], 1.000000000);
57
58 % Setting the demodulator parameters
59 ziDAQ('setDouble', ['/' device '/oscs/1/freq'], IF_freq);
60 ziDAQ('setInt', ['/' device '/demods/1/oscselct'], 1.000000000);
61 ziDAQ('setInt', ['/' device '/demods/1/adcselct'], 0.000000000);
62 ziDAQ('setDouble', ['/' device '/demods/1/timeconstant'],
time_constant);
63 ziDAQ('setInt', ['/' device '/demods/1/enable'], 1.000000000);
64 ziDAQ('setDouble', ['/' device '/demods/1/rate'], sample_rate);
65
66 % Clearing and setting the buffers
67 ziDAQ('unsubscribe', '*');
68 pause(10*time_constant);
69 buffer_size = max(0.1, trigger_duration*1.1);
70 h = ziDAQ('record', buffer_size , 1);
```

```

71
72 % Adjusting the trigger signal
73 %     type:
74 %     NO_TRIGGER = 0
75 %     EDGE_TRIGGER = 1
76 %     DIGITAL_TRIGGER = 2
77 %     PULSE_TRIGGER = 3
78 %     TRACKING_TRIGGER = 4
79 ziDAQ('set', h, 'trigger/0/type', 3);
80 ziDAQ('set', h, 'trigger/0/source', 6);
81 ziDAQ('set', h, 'trigger/0/path', ['/' device '/demods/1/sample'])
82 ziDAQ('set', h, 'trigger/0/edge', 1)
83 ziDAQ('set', h, 'trigger/0/level', trigger_level);
84 ziDAQ('set', h, 'trigger/0/hysteresis', 0.0000000);
85 ziDAQ('set', h, 'trigger/0/count', trigger_count);
86 ziDAQ('set', h, 'trigger/0/holdoff/time', trigger_holdOff_time)
87 ziDAQ('set', h, 'trigger/0/holdoff/count', trigger_holdOff_count)
88 ziDAQ('set', h, 'trigger/0/delay', trigger_delay);
89 ziDAQ('set', h, 'trigger/0/duration', trigger_duration);
90
91
92 % Initializing the buffer and streaming start
93 ziDAQ('subscribe', h, ['/' device '/demods/1/sample']);
94 ziDAQ('execute', h);
95 pause(10)
96 data = ziDAQ('read', h);
97 ziDAQ('unsubscribe', h, ['/' device '/demods/1/sample']);
98 ziDAQ('clear', h);
99 end

```

B.2. Image Reconstruction Script

```

1 %% read lock-in amplifier's files and reconstruct the images
2 clear all
3 close all
4 clc
5
6 addpath(genpath('D:\Users\jw1498\Documents\MATLAB\My_Matlab_work'))
7 [f_name, f_path, a]=uigetfile();
8 f_path=f_path(1:end-2);
9 tot_image=zeros(256,256);
10 for ind_j=1:4

```

B. Appendix

```
11 load(strcat(f_path,num2str(ind_j-1),'\\',f_name));
12 ksize=[256,256];
13 ks=zeros(ksize(1),ksize(2));
14 history_s=size(history);
15 ind1=history_s(2)-ksize(1)+1;
16 ind2=history_s(2);
17
18 for ind_i=ind1:ind2
19     t=dev2024.demods.sample{1,ind_i}.timestamp;
20     t=double(t);
21     t=t-t(1);
22     t=t*(1/1.8e9);
23     x=dev2024.demods.sample{1,ind_i}.x;
24     y=dev2024.demods.sample{1,ind_i}.y;
25     a=x(1:8:end);
26     a=a(1:ksize(2));
27     b=y(1:8:end);
28     b=b(1:ksize(2));
29     ks(ind_i-(ind1-1),:)=a+1i*b;
30 end
31 ks=ks_flip(ks);
32 ks=ks_flip(ks');
33 ksf=(fft2(ks));
34 ksf=imrotate(mat2gray(abs(ksf)),-90);
35 ksf=circshift(ksf,[-20,-35]);
36 figure(ind_j), imshow(ksf)
37 imwrite(ksf,strcat('scan',num2str(ind_j),'.jpg'),'jpg');
38 tot_image=tot_image+ksf;
39 end
40 %%
41 tot_image1=mat2gray(tot_image);
42 figure, imshow(tot_image1)
43 imwrite(tot_image1,'tot_image.jpg','jpg');
44 %% SNR of the original and reconstructed images
45 global k_space_PShr f_path f_name_modified;
46 k_space_PShr=ifft2(tot_image1);
47 f_path='path to original image';
48 f_name_modified='original_image.jpg';
49 plot_original_and_reconstructed;
```

Bibliography

- [1] Medical X-ray Imaging. <http://www.fda.gov/radiation-emittingproducts/radiationemittingproductsandprocedures/medicalimaging/medicalx-rays/default.htm>.
- [2] XFab XH035 process data sheet. http://www.xfab.com/fileadmin/x-fab/download_center/technology/cmos/xh035_cmos__rf-cmos_data_sheet.pdf.
- [3] Asad Abidi et al. On the operation of cascode gain stages. *Solid-State Circuits, IEEE Journal of*, 23(6):1434–1437, 1988.
- [4] Phillip E Allen and Douglas R Holberg. *CMOS analog circuit design*. Taylor & Francis US, 2002.
- [5] Ahmed Amer, Emad Hegazi, and Hani Ragai. A low-power wideband CMOS LNA for WiMAX. *Circuits and Systems II: Express Briefs, IEEE Transactions on*, 54(1):4–8, 2007.
- [6] Jens Anders, Giuseppe Chiaramonte, Paul SanGiorgio, and Giovanni Boero. A single-chip array of NMR receivers. *Journal of Magnetic Resonance*, 201(2):239–249, 2009.
- [7] Jens Anders, Paul SanGiorgio, and Giovanni Boero. A fully integrated IQ-receiver for NMR microscopy. *Journal of Magnetic Resonance*, 209(1):1–7, 2011.
- [8] Pervez M Aziz, Henrik V Sorensen, et al. An overview of sigma-delta converters. *Signal Processing Magazine, IEEE*, 13(1):61–84, 1996.
- [9] Vlad Badilita, Kai Kratt, Nicoleta Baxan, Mohammad Mohmmadzadeh, Tobias Burger, Hans Weber, Dominik v Elverfeldt, Jürgen Hennig, Jan G Korvink, and Ulrike Wallrabe. On-chip three dimensional microcoils for MRI at the microscale. *Lab on a Chip*, 10(11):1387–1390, 2010.
- [10] AL Baert, Stefan O Schönberg, Olaf Dietrich, and Maximilian F Reiser. *Parallel imaging in clinical MR applications*. Springer Science & Business Media, 2007.

- [11] R Jacob Baker. *CMOS: circuit design, layout, and simulation*, volume 18. John Wiley & Sons, 2011.
- [12] Timothy J Barnes. SKILL: A CAD system extension language. In *Proceedings of the 27th ACM/IEEE Design Automation Conference*, pages 266–271. ACM, 1991.
- [13] Farbod Behbahani, Yoji Kishigami, John Leete, Asad Abidi, et al. CMOS mixers and polyphase filters for large image rejection. *Solid-State Circuits, IEEE Journal of*, 36(6):873–887, 2001.
- [14] H Benoit-Cattin, G Collewet, B Belaroussi, H Saint-Jalmes, and C Odet. The SIMRI project: a versatile and interactive MRI simulator. *Journal of Magnetic Resonance*, 173(1):97–115, 2005.
- [15] Stefan Berger and Siegmur Braun. *200 and more NMR experiments: a practical course*. Wiley-Vch Weinheim, 2004.
- [16] Matt A Bernstein, Kevin F King, and Xiaohong Joe Zhou. *Handbook of MRI pulse sequences*. Elsevier, 2004.
- [17] G Boero, J Frounchi, B Furrer, P-A Besse, and RS Popovic. Fully integrated probe for proton nuclear magnetic resonance magnetometry. *Review of Scientific Instruments*, 72(6):2764–2768, 2001.
- [18] Bruker. Micro Imaging Manual for AV3 Systems. *Bruker user manual*, 2010.
- [19] Mikaël Cimino, Hervé Lapuyade, Yann Deval, Thierry Taris, and Jean-Baptiste Bégueret. Design of a 0.9 V 2.45 GHz self-testable and reliability-enhanced CMOS LNA. *Solid-State Circuits, IEEE Journal of*, 43(5):1187–1194, 2008.
- [20] Sarah L Codd and Joseph D Seymour. *Magnetic resonance microscopy*. John Wiley & Sons, 2008.
- [21] Chris D Constantinides, Charles R Westgate, Walter G O’Dell, Elias A Zerhouni, and Elliot R McVeigh. A phased array coil for human cardiac imaging. *Magnetic resonance in medicine: official journal of the Society of Magnetic Resonance in Medicine/Society of Magnetic Resonance in Medicine*, 34(1):92, 1995.
- [22] Jan Crols and Michel SJ Steyaert. A single-chip 900 MHz CMOS receiver front-end with a high performance low-IF topology. *Solid-State Circuits, IEEE Journal of*, 30(12):1483–1492, 1995.

-
- [23] Hooman Darabi, Asad Abidi, et al. A 4.5-mW 900-MHz CMOS receiver for wireless paging. *Solid-State Circuits, IEEE Journal of*, 35(8):1085–1096, 2000.
- [24] Anagha Deshmane, Vikas Gulani, Mark A Griswold, and Nicole Seiberlich. Parallel MR imaging. *Journal of Magnetic Resonance Imaging*, 36(1):55–72, 2012.
- [25] Olaf Dietrich, José G Raya, Scott B Reeder, Maximilian F Reiser, and Stefan O Schoenberg. Measurement of signal-to-noise ratios in MR images: Influence of multichannel coils, parallel imaging, and reconstruction filters. *Journal of Magnetic Resonance Imaging*, 26(2):375–385, 2007.
- [26] F David Doty, George Entzminger, Cory D Hauck, and John P Staab. Practical aspects of birdcage coils. *Journal of Magnetic Resonance*, 138(1):144–154, 1999.
- [27] Richard R Ernst, Geoffrey Bodenhausen, Alexander Wokaun, et al. *Principles of nuclear magnetic resonance in one and two dimensions*, volume 14. Clarendon Press Oxford, 1987.
- [28] Thomas KF Foo, James R Macfall, H Dirk Sostman, and Cecil E Hayes. Single-breath-hold venous or arterial flow-suppressed pulmonary vascular MR imaging with phased-array coils. *Journal of Magnetic Resonance Imaging*, 3(4):611–616, 1993.
- [29] Horst Friebolin and Jack K Beconsall. *Basic one-and two-dimensional NMR spectroscopy*. VCH Weinheim, 1993.
- [30] Harald T Friis. Noise figures of radio receivers. *Proceedings of the IRE*, 32(7):419–422, 1944.
- [31] Andrew G Webb. Radiofrequency microcoils in magnetic resonance. *Progress in Nuclear Magnetic Resonance Spectroscopy*, 31(1):1–42, 1997.
- [32] Barrie Gilbert. A precise four-quadrant multiplier with sub-nanosecond response. *Solid-State Circuits, IEEE Journal of*, 3(4):365–373, 1968.
- [33] Jung-Suk Goo, Chang-Hoon Choi, Antonio Abramo, Jae-Gyung Ahn, Zhiping Yu, Thomas H Lee, and Robert W Dutton. Physical origin of the excess thermal noise in short channel MOSFETs. *Electron Device Letters, Ieee*, 22(2):101–103, 2001.
- [34] Vinu Govind, Sidharth Dalmia, and Madhavan Swaminathan. Design of integrated low noise amplifiers (LNA) using embedded passives in organic substrates. *Advanced Packaging, IEEE Transactions on*, 27(1):79–89, 2004.

- [35] Mark A Griswold, Peter M Jakob, Robin M Heidemann, Mathias Nittka, Vladimir Jellus, Jianmin Wang, Berthold Kiefer, and Axel Haase. Generalized auto-calibrating partially parallel acquisitions (GRAPPA). *Magnetic resonance in medicine*, 47(6):1202–1210, 2002.
- [36] Oliver G Gruschke, Nicoleta Baxan, Lars Clad, Kai Kratt, Dominik von Elverfeldt, Andreas Peter, Jürgen Hennig, Vlad Badilita, Ulrike Wallrabe, and Jan G Korvink. Lab on a chip phased-array MR multi-platform analysis system. *Lab on a Chip*, 12(3):495–502, 2012.
- [37] Thomas Hackländer and Heinrich Mertens. Virtual MRI: A PC-based simulation of a clinical MR scanner. *Academic radiology*, 12(1):85–96, 2005.
- [38] Christopher J Hardy, Paul A Bottomley, Ken W Rohling, and Peter B Roemer. An NMR phased array for human cardiac ^{31}P spectroscopy. *Magnetic resonance in medicine*, 28(1):54–64, 1992.
- [39] Christopher J Hardy, Robert D Darrow, Manojkumar Saranathan, Randy O Giaquinto, Yudong Zhu, Charles L Dumoulin, and Paul A Bottomley. Large field-of-view real-time MRI with a 32-channel system. *Magnetic resonance in medicine*, 52(4):878–884, 2004.
- [40] Christopher J Hardy, Randy O Giaquinto, Joseph E Piel, AAS Rohling, W Kenneth, Luca Marinelli, Daniel J Blezek, Eric W Fiveland, Robert D Darrow, and Thomas KF Foo. 128-channel body MRI with a flexible high-density receiver-coil array. *Journal of Magnetic Resonance Imaging*, 28(5):1219–1225, 2008.
- [41] Ray Hashman Hashemi, William G Bradley, and Christopher J Lisanti. *MRI: the basics*. Lippincott Williams & Wilkins, 2012.
- [42] Arjang Hassibi, Aydin Babakhani, and Ali Hajimiri. A spectral-scanning nuclear magnetic resonance imaging (MRI) transceiver. *Solid-State Circuits, IEEE Journal of*, 44(6):1805–1813, 2009.
- [43] Cecil E Hayes, Mark J Dietz, Bernard F King, and Richard L Ehman. Pelvic imaging with phased-array coils: Quantitative assessment of signal-to-noise ratio improvement. *Journal of magnetic resonance imaging*, 2(3):321–326, 1992.
- [44] Cecil E Hayes, Neil Hattes, and Peter B Roemer. Volume imaging with MR phased arrays. *Magnetic resonance in medicine*, 18(2):309–319, 1991.

-
- [45] Cecil E Hayes, C Mark Mathis, and Chun Yuan. Surface coil phased arrays for high-resolution imaging of the carotid arteries. *Journal of Magnetic Resonance Imaging*, 6(1):109–112, 1996.
- [46] Wang He, Xu Qin, Ren Jiejing, and Li Gengying. Four-channel magnetic resonance imaging receiver using frequency domain multiplexing. *Review of scientific instruments*, 78(1):015102, 2007.
- [47] Jens Höfflin, Christian Sander, Pascal Gieschke, Andreas Greiner, and Jan G Korvink. Subthreshold CMOS transistors are largely immune to magnetic field effects when operated above 11 T. *Concepts in Magnetic Resonance Part B: Magnetic Resonance Engineering*, 45(2):97–105, 2015.
- [48] David I Hoult. Receiver Design for MR. *eMagRes*, pages 1–21, 2011.
- [49] David I Hoult and RE Richards. The signal-to-noise ratio of the nuclear magnetic resonance experiment. *Journal of Magnetic Resonance (1969)*, 24(1):71–85, 1976.
- [50] DI Hoult, D Foreman, G Kolansky, and D Kripiakevich. Overcoming high-field RF problems with non-magnetic Cartesian feedback transceivers. *Magnetic Resonance Materials in Physics, Biology and Medicine*, 21(1-2):15–29, 2008.
- [51] DI Hoult, G Kolansky, and D Kripiakevich. A 'Hi-Fi' Cartesian feedback spectrometer for precise quantitation and superior performance. *Journal of Magnetic Resonance*, 171(1):57–63, 2004.
- [52] James S Hyde, A Jesmanowicz, W Froncisz, J Bruce Kneeland, Thomas M Grist, and Nicholas F Campagna. Parallel image acquisition from noninteracting local coils. *Journal of Magnetic Resonance (1969)*, 70(3):512–517, 1986.
- [53] Renuka P Jindal. Compact noise models for MOSFETs. *Electron Devices, IEEE Transactions on*, 53(9):2051–2061, 2006.
- [54] John Bertrand Johnson. Thermal agitation of electricity in conductors. *Physical review*, 32(1):97, 1928.
- [55] M José and Rocío del Río. *CMOS sigma-delta converters: Practical design guide*. John Wiley & Sons, 2013.
- [56] M Jouda, OG Gruschke, E Fischer, J Leupold, D Elverfeldt, J Hennig, and JG Korvink. CMOS frequency division multiplexer enables multi-channel magnetic resonance imaging with a single channel spectrometer. *MikroSystemTechnik 2015*, 2015.

- [57] Mazin Jouada, Oliver G Gruschke, and Jan G Korvink. A new fully integrated multichannel receiver design for magnetic resonance imaging. *Concepts in Magnetic Resonance Part B: Magnetic Resonance Engineering (submitted)*.
- [58] Mazin Jouada, Oliver G Gruschke, and Jan G Korvink. Implementation of an in-field CMOS frequency division multiplexer for 9.4 T magnetic resonance applications. *International Journal of Circuit Theory and Applications*, 2014.
- [59] Mazin Jouada, Oliver G Gruschke, and Jan G Korvink. Circuit level simulation of MRI receive chain using excitation derived from images. *Concepts in Magnetic Resonance Part B: Magnetic Resonance Engineering*, 44(4):102–113, 2015.
- [60] Lewis E Kay, Mitsuhiko Ikura, Rolf Tschudin, and Ad Bax. Three-dimensional triple-resonance NMR spectroscopy of isotopically enriched proteins. *Journal of Magnetic Resonance (1969)*, 89(3):496–514, 1990.
- [61] James Keeler. *Understanding NMR spectroscopy*. John Wiley & Sons, 2011.
- [62] Boris Keil, James N Blau, Stephan Biber, Philipp Hoecht, Veneta Tountcheva, Kawin Setsompop, Christina Triantafyllou, and Lawrence L Wald. A 64-channel 3 T array coil for accelerated brain MRI. *Magnetic Resonance in Medicine*, 70(1):248–258, 2013.
- [63] Boris Keil and Lawrence L Wald. Massively parallel MRI detector arrays. *Journal of Magnetic Resonance*, 229:75–89, 2013.
- [64] Walter Allan Kester. *Data conversion handbook*. Newnes, 2005.
- [65] K Kratt, V Badilita, T Burger, JG Korvink, and U Wallrabe. A fully MEMS-compatible process for 3D high aspect ratio micro coils obtained with an automatic wire bonder. *Journal of Micromechanics and Microengineering*, 20(1):015021, 2010.
- [66] Mieke Kriege, Cecile TM Brekelmans, Carla Boetes, Peter E Besnard, Harmine M Zonderland, Inge Marie Obdeijn, Radu A Manoliu, Theo Kok, Hans Peterse, Madeleine MA Tilanus-Linthorst, et al. Efficacy of MRI and mammography for breast-cancer screening in women with a familial or genetic predisposition. *New England Journal of Medicine*, 351(5):427–437, 2004.
- [67] Paul C Lauterbur et al. Image formation by induced local interactions: examples employing nuclear magnetic resonance. *Nature*, 242(5394):190–191, 1973.
- [68] Thomas H Lee. *The design of CMOS radio-frequency integrated circuits*. Cambridge university press, 2004.

- [69] Paul Leroux, Johan Janssens, and Michiel Steyaert. A 0.8-dB NF ESD-Protected 9-mW CMOS LNA operating at 1.23 GHz [for GPS receiver]. *Solid-State Circuits, IEEE Journal of*, 37(6):760–765, 2002.
- [70] Malcolm H Levitt. *Spin dynamics: basics of nuclear magnetic resonance*. John Wiley & Sons, 2001.
- [71] Franco Maloberti. *Data converters*. Springer Science & Business Media, 2007.
- [72] C Massin, F Vincent, A Homsy, K Ehrmann, G Boero, P-A Besse, A Daridon, E Verpoorte, NF De Rooij, and RS Popovic. Planar microcoil-based microfluidic NMR probes. *Journal of Magnetic Resonance*, 164(2):242–255, 2003.
- [73] Mounir Meghelli. 132-Gb/s 4: 1 multiplexer in 0.13- μm SiGe-bipolar technology. *Solid-State Circuits, IEEE Journal of*, 39(12):2403–2407, 2004.
- [74] Joël Mispelter, Mihaela Lupu, and André Briguet. *NMR probeheads for biophysical and biomedical experiments: theoretical principles & practical guidelines*. Imperial College Press, 2006.
- [75] Bradford A Moffat, Thomas L Chenevert, Theodore S Lawrence, Charles R Meyer, Timothy D Johnson, Qian Dong, Christina Tsien, Suresh Mukherji, Douglas J Quint, Stephen S Gebarski, et al. Functional diffusion map: a noninvasive MRI biomarker for early stratification of clinical brain tumor response. *Proceedings of the National Academy of Sciences of the United States of America*, 102(15):5524–5529, 2005.
- [76] PV Ananda Mohan. *VLSI Analog Filters: Active RC, OTA-C, and SC*. Springer Science & Business Media, 2012.
- [77] LA NacEachern and Tajinder Manku. A charge-injection method for Gilbert cell biasing. In *Electrical and Computer Engineering, 1998. IEEE Canadian Conference on*, volume 1, pages 365–368. IEEE, 1998.
- [78] Harry Nyquist. Thermal agitation of electric charge in conductors. *Physical review*, 32(1):110, 1928.
- [79] Erik Odeblad. Micro-NMR in high permanent magnetic fields. Theoretical and experimental investigations with an application to the secretions from single glandular units in the human uterine cervix. *Acta obstetricia et gynecologica Scandinavica*, 45:Suppl-2, 1965.

- [80] Timothy L Peck, Richard L Magin, and Paul C Lauterbur. Design and analysis of microcoils for NMR microscopy. *Journal of Magnetic Resonance, Series B*, 108(2):114–124, 1995.
- [81] Timothy L Peck, Richard L Magin, and Paul C Lauterbur. Design and analysis of microcoils for NMR microscopy. *Journal of Magnetic Resonance, Series B*, 108(2):114–124, 1995.
- [82] Jay R Porter, Steven M Wright, and Nader Famili. A four-channel time domain multiplexer: A cost-effective alternative to multiple receivers. *Magnetic resonance in medicine*, 32(4):499–504, 1994.
- [83] John G Proakis. *Digital signal processing: principles, algorithms, and application-3/E*. 1996.
- [84] Klaas P Pruessmann, Markus Weiger, Markus B Scheidegger, Peter Boesiger, et al. SENSE: sensitivity encoding for fast MRI. *Magnetic resonance in medicine*, 42(5):952–962, 1999.
- [85] II Rabi, JR Zacharias, S Millman, and P Kusch. A New Method of Measuring Nuclear Magnetic Moment. *Physical review*, 53(4):318–327, 1938.
- [86] Behzad Razavi. Design considerations for direct-conversion receivers. *Circuits and Systems II: Analog and Digital Signal Processing, IEEE Transactions on*, 44(6):428–435, 1997.
- [87] Behzad Razavi. *RF microelectronics*, volume 1. Prentice Hall New Jersey, 1998.
- [88] Behzad Razavi. *RF microelectronics*, volume 1. Prentice Hall New Jersey, 1998.
- [89] Peter B Roemer, William A Edelstein, Cecil E Hayes, Steven P Souza, and OM Mueller. The NMR phased array. *Magnetic resonance in medicine*, 16(2):192–225, 1990.
- [90] Cotter W Sayre. *Complete wireless design*. McGraw-Hill Professional, 2001.
- [91] Rolf Schaumann et al. *Design of analog filters*. Oxford University Press, 2001.
- [92] Melanie Schmitt, Andreas Potthast, David E Sosnovik, Jonathan R Polimeni, Graham C Wiggins, Christina Triantafyllou, and Lawrence L Wald. A 128-channel receive-only cardiac coil for highly accelerated cardiac MRI at 3 Tesla. *Magnetic resonance in Medicine*, 59(6):1431–1439, 2008.

-
- [93] Richard Schreier and Gabor C Temes. *Understanding delta-sigma data converters*, volume 74. IEEE press Piscataway, NJ, 2005.
- [94] Derek K Shaeffer and Thomas H Lee. A 1.5-V, 1.5-GHz CMOS low noise amplifier. *Solid-State Circuits, IEEE Journal of*, 32(5):745–759, 1997.
- [95] R.G. Shulman and D.L. Rothman. *Metabolism by In Vivo NMR*. Wiley, 2005.
- [96] Aaron Sodickson, Pieter F Baeyens, Katherine P Andriole, Luciano M Prevedello, Richard D Nawfel, Richard Hanson, and Ramin Khorasani. Recurrent CT, Cumulative Radiation Exposure, and Associated Radiation-induced Cancer Risks from CT of Adults. *Radiology*, 251(1):175–184, 2009.
- [97] Daniel K Sodickson and Warren J Manning. Simultaneous acquisition of spatial harmonics (SMASH): fast imaging with radiofrequency coil arrays. *Magnetic Resonance in Medicine*, 38(4):591–603, 1997.
- [98] Hyejeong Song, Huijung Kim, Kichon Han, Jinsung Choi, Changjoon Park, and Bumman Kim. A sub-2 db nf dual-band CMOS LNA for CDMA/WCDMA applications. *Microwave and Wireless Components Letters, IEEE*, 18(3):212–214, 2008.
- [99] C. Stagg and D.L. Rothman. *Magnetic Resonance Spectroscopy: Tools for Neuroscience Research and Emerging Clinical Applications*. Elsevier Science, 2013.
- [100] Tony Stöcker, Kaveh Vahedipour, Daniel Pflugfelder, and N Jon Shah. High-performance computing MRI simulations. *Magnetic Resonance in Medicine*, 64(1):186–193, 2010.
- [101] PJ Sullivan, BA Xavier, and WH Ku. Low voltage performance of a microwave CMOS Gilbert cell mixer. *Solid-State Circuits, IEEE Journal of*, 32(7):1151–1155, 1997.
- [102] Nan Sun, Yong Liu, Hakho Lee, Ralph Weissleder, and Donhee Ham. CMOS RF biosensor utilizing nuclear magnetic resonance. *Solid-State Circuits, IEEE Journal of*, 44(5):1629–1643, 2009.
- [103] J Thomas Vaughan and John R Griffiths. *RF coils for MRI*. John Wiley & Sons, 2012.
- [104] Lawrence L Wald, Susan E Moyher, Mark R Day, Sarah J Nelson, and Daniel B Vigneron. Proton spectroscopic imaging of the human brain using phased array detectors. *Magnetic resonance in medicine*, 34(3):440–445, 1995.
- [105] Neil HE Weste and Kamran Eshraghian. Principles of CMOS VLSI design: a systems perspective. *NASA STI/Recon Technical Report A*, 85:47028, 1985.

- [106] GC Wiggins, A Potthast, C Triantafyllou, FH Lin, T Benner, CJ Wiggins, and LL Wald. A 96-channel MRI system with 23-and 90-channel phase array head coils at 1.5 Tesla. In *Proceedings of the 13th Annual Meeting of ISMRM, Miami Beach, FL, USA*, page 671, 2005.
- [107] GC Wiggins, C Triantafyllou, A Potthast, A Reykowski, M Nittka, and LL Wald. 32-channel 3 tesla receive-only phased-array head coil with soccer-ball element geometry. *Magnetic resonance in medicine*, 56(1):216–223, 2006.
- [108] Graham C Wiggins, Jonathan R Polimeni, Andreas Potthast, Melanie Schmitt, Vijay Alagappan, and Lawrence L Wald. 96-Channel receive-only head coil for 3 Tesla: Design optimization and evaluation. *Magnetic Resonance in Medicine*, 62(3):754–762, 2009.
- [109] W Zhuo, Xia Li, S Shekhar, SHK Embabi, De Gyvez, J Pineda, DJ Allstot, and E Sanchez-Sinencio. A capacitor cross-coupled common-gate low-noise amplifier. *Circuits and Systems II: Express Briefs, IEEE Transactions on*, 52(12):875–879, 2005.
- [110] Wei Zhuo, Sherif Embabi, De Gyvez, José Pineda, and Edgar Sánchez-Sinencio. Using capacitive cross-coupling technique in RF low noise amplifiers and down-conversion mixer design. In *Solid-State Circuits Conference, 2000. ESSCIRC'00. Proceedings of the 26rd European*, pages 77–80. IEEE, 2000.

List of Figures

1.1.	Description of the main target of the thesis which is to find a remedy to the cost, size, and complexity issues associated with MR phased arrays. (left) 96-coils array with preamplifiers for head imaging [106]. The RF receivers are not shown in the image. (Right) Figurative plot of the imagined solution intended to replace the array in the left image.	2
2.1.	Dependence of the sign of the gyromagnetic ratio γ on the alignment of $\hat{\mu}$ with respect to \hat{S}	8
2.2.	Precessing of spin polarization axis around \mathbf{B}_0 . The direction of the precessing depends on the sign of γ	8
2.3.	Effect of applying an external magnetic field B_0 on the magnetic moments of an ensemble of nuclei. (a) No field is applied. The randomly distributed magnetic moments cancel each other and hence the net magnetization (longitudinal and transverse) is zero. (b) A magnetic field B_0 is applied in the z-direction. A net longitudinal magnetization M_0 is formed due to the difference between the parallel and antiparallel magnetic moments. The transverse magnetization M_{xy} is zero.	9
2.4.	Effect of applying an RF excitation pulse on the magnetization of a sample. (a) No RF pulse is applied. In this case $M_z = M_0$ and $M_{xy} = 0$. (b) Applying an RF pulse with duration τ_1 results in a tilt of the magnetization by a flip angle α_1 . In this case $M_z = M_0 \cos \alpha$ and $M_{xy} = M_0 \sin \alpha$. (c) A 90° pulse is utilized resulting in $M_z = 0$ and $M_{xy} = M_0$	10
2.5.	Behavior of the magnetization after being excited with 90° pulse. (a) After turning off the RF pulse, M_0 starts tilting towards B_0 while precessing with the Larmor frequency ω_0 . (b) Recovery of M_z and decay of M_{xy} over time. (c) The precessing magnetic moments induce an electrical current in a coil that is close enough to the sample. The signal generated in the coil is the MR FID which is basically a decaying sinusoid with frequency ω_0	11
2.6.	Block diagram of a typical magnetic resonance imaging scanner.	12
2.7.	Controlling the RF pulse duration τ and inherently the flip angle α by a gating signal.	13

2.8.	Block diagram of a typical receive chain in the magnetic resonance scanner.	14
2.9.	Different types of MR coils. (a) Example of an MR surface coil [72]. (b) MR volume coil example [65].	14
2.10.	Tuning and matching the MR coil to 50Ω at 400 MHz. (a) Circuit schematic showing the coil in parallel with the tuning capacitor C_t and in series with the matching capacitor C_m . (b) Real and imaginary part of the circuit impedance Z_{s1} with only C_t . (c) Real and imaginary parts of Z_s when both C_t and C_m are connected. (d) The input reflection coefficient S_{11} of the circuit.	16
2.11.	The total noise figure of a receiver chain consisting of a LNA followed by different signal processing blocks.	18
2.12.	Demonstration of the frequency mixing operation. (a) The RF signal in the time domain. (b) Fourier transform of the signal in (a). The RF signal is centered at f_0 . (c) The LO signal in the time domain. (d) Fourier transform of LO. (e) The IF signal (IF = RF x LO) in time domain. (f) Fourier transform of IF where the RF signal now is shifted to $(f_{LO} - f_0)$ and $(f_{LO} + f_0)$	20
2.13.	The effect of applying the gradient fields on the magnetic moments within the sample. (a) Due to B_0 a net magnetic moment, that aligns parallel to it, will be generated in each voxel of the sample. (b) An SSG is applied simultaneously with an RF pulse. In this case the magnetic moments within a single slice of the sample will respond to the RF pulse and will accordingly tilt by a certain angle. (c) The application of the PEG results in a change in the phase of the precessing magnetic moments that is proportional to their position on the axis of the gradient. (d) During the FEG gradient the magnetic moments will exhibit different frequencies beside the different phases due to PEG. The MR signal can therefore be recorded during the FEG.	24
2.14.	The timing diagram of a typical spin-echo imaging sequence.	25
2.15.	The timing diagram of a typical gradient-echo imaging sequence.	26
2.16.	Sampling the MR signal (echo) and filling the k-space matrix. Obtaining the MR image from the k-space matrix via two dimensional Fourier transform.	27
2.17.	Reducing the coupling and mutual inductances between the coils via geometrical overlapping and low input-impedance preamplifiers.	28
2.18.	Phased array of several hexagonally wire bonded micro coils [36]. The phased array of micro coils with tuning and matching electronics is mounted on a PCB. Seven low-noise preamplifiers are connected to the phased array.	30

2.19.	96-coil array for brain imaging implemented by Graham C. Wiggins and colleagues in 2009 [108]. The picture shows the RF coils placed on a helmet form and their respective preamplifiers. What is not illustrated in the figure are the bulky bundles of coaxial cables used to carry the MR signals to the 96 receivers.	31
2.20.	Demonstration of the principle of time division multiplexing.	33
2.21.	Block diagram of a four-channel time division multiplexer (TDM) introduced in [82].	33
2.22.	Demonstration of the principle of the frequency division multiplexing.	34
2.23.	Block diagram of a four-channel frequency division multiplexer designed for a 0.3 T MR scanner [46].	34
2.24.	Effects of increasing the number of receive coils of an MRI array. (a) The coil area decreases inherently as the number of coils increases, while the number of cables and RF receivers scales linearly. (b) Calculation of the enhancement of the SNR in the head areas close to the coils for different acceleration factors.	36
2.25.	Effect of increasing the number of coils in an MRI array on the overall power consumption, size, and complexity of the system. Discrete-components multiplexers can reduce the demands of power, size, and complexity. However, they fail to be an optimum solution, especially for massive number of coils. Therefore, CMOS integrated solutions are very promising in this case.	36
3.1.	Block diagram of the magnetic resonance system employing the CMOS frequency multiplexer as a novel solution for MR phased arrays. (a) Eight-coils MRI phased array. (b) Block diagram of the CMOS FDM consisting of eight channels, where each comprises a low-noise amplifier (LNA), a frequency mixer, and a bandpass filter. (c) Analog-to-digital converter to digitize the multiplexed signal and a signal processing unit to reconstruct the MR images.	39
3.2.	Proposed gain distribution of the different blocks of the CMOS FDM.	41
3.3.	Schematic of a typical common-source (CS) LNA.	43
3.4.	Simulation results of the CS-LNA. (a) Voltage gain and noise figure. (b) Input power reflection for 50 Ω source impedance. (c) 1-dB gain compression.	44
3.5.	Schematic of the differential common-gate common-source (CG-CS) low-noise amplifier (LNA) employed in the frequency division multiplexer.	45

3.6.	(a) The trade-off between the noise performance and the power consumption of the CG-LNA when the channel widths of M3 and M4 change. The simulation involved in this figure is periodic-steady state (pss) and a periodic s-parameters (psp) with a parametric sweep of the channel width. (b) Simplified noise model of the common-gate common-source low noise amplifier. This model shows the noise sources associated with one half of the amplifier circuit.	47
3.7.	Effect of the source impedance on the noise figure of the LNA.	48
3.8.	Voltage gain simulation of the CG-CS-LNA. (a) Gain over frequency. (b) 80-runs MonteCarlo simulation of the maxim gain of the LNA.	48
3.9.	Characteristics of the common-gate common-source LNA. (a) S11. (b) 1-dB gain compression.	49
3.10.	Plot of the Stern stability factor of the CG-CS-LNA. (a) K-factor. (b) Δ . . .	50
3.11.	Block diagram of the LNA-mixer interface. The local oscillator (LO) is generated using an external digital synthesizer (DDS). Commercially available DDS's (for example the LMK03806 from Texas Instruments) can provide sufficiently high precision and low jitter noise requirements as needed for the successful reception of the MR signals	51
3.12.	CMOS 0.35 μm double-balanced Gilbert mixer used in the MR FDM. . . .	51
3.13.	Transient simulation of the double-balanced Gilbert mixer in figure 3.12 for a sinusoidal input. RF = 400 MHz while LO = 390 MHz. (a) Time domain. (b) Frequency domain.	53
3.14.	Plot of the S-parameters of the double-balanced Gilbert mixer.	54
3.15.	Characteristics of the double-balanced Gilbert mixer. (a) Noise figure. (b) Conversion gain of the mixer versus the power of the local oscillator. . .	54
3.16.	A 4-th order Butterworth passive bandpass filter. (a) Schematic. (b) Frequency response.	56
3.17.	Schematic of a second-order bandpass filter realized using a multi-feedback RC active topology.	56
3.18.	(a) Frequency response of the bandpass filter depicted in figure 3.17. The lines marked with small circles and squares show the response of two second-order filters while the line marked with small triangles shows the response of a fourth-order filter realized by cascading the two second-order filters. (b) Result of 100 Monte-Carlo simulation runs for the extracted layout of a 10 MHz fourth-order BPF.	57

3.19. Frequency response of the extracted layouts of eight fourth-order bandpass filters employed in the MR FDM. The filters have center frequencies $f_{c,j}, j \in \{10, 15, 20, 25, 30, 35, 40, 45\}$ MHz.	58
3.20. High speed two-stage operational amplifier with indirect compensation.	58
3.21. Open-loop frequency response of the operational amplifier.	60
3.22. (a) The input-referred noise of the operational amplifier. (b) The opamp's output for a transient simulation of the opamp with a pulse excitation.	60
3.23. Closed-loop operation of the operational amplifier. (a) Circuit topology of adder. The output voltage is an amplified sum of the input voltages $V_{in1}, V_{in2}, V_{in3}, \dots$ (b) The frequency response of the circuit in (a) showing a maximum achievable gain of 20 dB over a wide frequency range up to 200 MHz.	61
3.24. (a) A differential buffer stage between the LNA and the mixer. (b) Single-ended buffer used after the mixer.	62
3.25. Biasing circuit.	63
3.26. The layout of the RF transistors employed in the design of the CMOS FDM. (a) NMOS. (b) PMOS.	64
3.27. Examples of common-centroid configurations that were employed in the design of the layout.	65
3.28. Chip layout.	66
4.1. Virtual MRI circuit simulator block diagram.	68
4.2. GUI of Matlab program to reconstruct MR coil echo signals from MR image.	69
4.3. Steps to reconstruct the MR echo for a single k-space image row. (a), (b) Samples of the In-phase and quadrature demodulated components of the MR signal. t_s is determined by the bandwidth of the signal. Zero padding is employed to avoid the effects caused by the transient response of the circuit. (c),(d) Defining the interpolation time step $t_{s_a} < t_s$ and applying high order interpolation for the in-phase and quadrature signals respectively. (e) Combining the I and Q components and shifting the signal to the desired Larmor frequency (64 MHz in this case). (f) FFT of the MR echo.	71
4.4. GUI of a Matlab script that reconstructs the MR image from the coil signals generated by the program in figure 4.2.	72
4.5. Spanned GUI from the program in figure 4.4 that allows the user to set the gain and noise figure of the different elements of the MR receiver.	72

4.6.	GUI of a Matlab program used to compare the original and the reconstructed MR image. It also determines the SNR of identical user-selectable regions of interest in both images, indicated here by yellow (signal region) and red (noise region) rectangles via equation 4.2.	73
4.7.	Effect of resolution of the ADC on the quality of the reconstructed image. (a) The original image. (b,c,d,e,f) The reconstructed images using an 8, 10, 12, 14, and 16-bit ADC respectively.	74
4.8.	GUI of a Matlab program that processes the outputs of the circuit simulation and reconstructs the MR images from these outputs. The program can process the simulation results from the 8-channel MR FDM in figure 3.1 as well as the 16-channel MR FDTD multiplexer depicted in figure 4.14. . .	76
4.9.	A block diagram that describes the signal flow in the Matlab program in figure 4.8 when it is used to process the output of the 8-channels FDM. .	76
4.10.	The output of the 8-channel MR FDM for a single row data from eight decoupled images. (a) The time domain output. (b) The FFT.	77
4.11.	Simulation of the 8-channel frequency division multiplexer presented in chapter 3. (a) Original images that were created using a bitmap editor so as to provide the simulation input as detailed in the text. (b) The eight reconstructed images from the multiplexed output.	78
4.12.	Simulation of an MR image of fish-oocytes using a single channel of the MR FDM in chapter 3. (a) The original image. (b) Reconstructed image from the CMOS circuit including the circuit's noise. (c) Reconstructed image from the circuit with additionally added 80 ppm jitter noise to the local oscillator.	79
4.13.	Simulation of a chest MR image to test the effect of the multiplexer's linearity on the MR image. (a) Original image. (b) Reconstructed image when the maximum peak amplitude of the coils signals is set to 100 μ V. SNR degradation in this case is 2 dB. (c) Reconstructed image when the maximum peak amplitude of the coils signals is 20 mV. SNR degradation in this case is 3 dB.	80
4.14.	Compact and integrated multi-channel MRI system. (a) MRI phased array of micro coils [36]. (b) Block diagram of the proposed 16-channel frequency-division and time-division multiplexer.	81
4.15.	A block diagram that describes the signal flow in the Matlab program in figure 4.8 when it is used to process the output of the 16-channels FDTD multiplexer.	82

4.16. Output of the multiplexer for a single k-space row from 16 different "channel" images. (a) Time domain signal. (b) FFT of (a).	83
4.17. Simulation of a 16-channel MRI experiment using the two CMOS multiplexers. The specially prepared channel images I_j were used to create the simulation input, as detailed in the text. (a) Reconstructed channel images R_j . (b) Corresponding k-space plots. (c) Corresponding difference images $E_j = (I_j - R_j)/I_j$ for each channel j.	84
5.1. Chip micro-photograph.	89
5.2. Measurements PCB.	90
5.3. Measurements of the low noise amplifier. (a) Voltage gain. (b) First-order input-referred intercept point IIP1.	91
5.4. Measurements of the frequency mixer. (a) The voltage gain. (b) The IIP1.	91
5.5. Normalized S_{21} of the BPF of channel 3 with center frequency $f_0 = 20$ MHz.	92
5.6. Measured output of the eight channels for an AC input excitation. The RF inputs have 400 MHz frequency and 1 mV amplitude, while the amplitude of the LO is 800 mV.	92
5.7. Measured gain of channel 3. (a) Gain versus LO frequency for a fixed LO power. (b) Gain versus LO power when the LO frequency is fixed.	93
5.8. Measured phase of each of the eight channels over a 4 MHz band centered at the IF frequency corresponding to the respective channel.	94
5.9. Heat distribution in the CMOS chip and the holding package due to approximately 1.07 W power consumption.	95
5.10. PCB to test the chip inside the MR scanner. The direction of the current in all the transistors in this case is parallel to the direction of \mathbf{B}_0	96
5.11. Characterizing the chip's performance inside and outside the 11.7 T magnetic field. (a) Channel's gain. (b) Channel's linearity.	96
5.12. Experiment setup in an 11.7 T spectrometer.	99
5.13. Acquired FID of the water sample without the CMOS chip. (a) Time. (b) FFT.	100
5.14. Acquired FID of the water sample through the CMOS chip. (a) Time. (b) FFT.	100
5.15. Spectroscopy of a 5 mL water sample with 100 mmol sugar in 11.7 T NMR scanner. The blue curve is from the scanner, while the red is from the chip.	101
5.16. Experiment setup in a 9.4 T scanner.	102
5.17. Employing an external decoupling signal to trigger the MR signal acquisition. (Yellow) decoupling signal used as a triggering signal. (Green) FID.	103
5.18. FID of a water sample in a 9.4 T scanner when the chip is mounted outside the magnet. The flip angle α is 30° . (a) Time domain. (b) FFT.	104

5.19. FID of the water sample when the chip is placed inside the magnet. The flip angle α in this case is 10° . (a) Time domain. (b) FFT which shows multiple peaks due the B_0 field inhomogeneities caused by the PCB.	105
5.20. FID of the water sample when the chip is placed inside the magnet. (a) Time domain. (b) FFT which shows a single peak after applying manual shimming.	105
5.21. (a) Layout of the reception coil. (b) Measured S11 of the coil.	106
5.22. The center echo acquired from a complete slice when no phase encoding gradient is applied. (a) Time domain. (b) FFT.	107
5.23. Reconstructed images from different scans from a single channel of the CMOS FDM.	108
5.24. Reconstructed images from different scans when the scanner's reference clock signal is exploited as external reference to UHFLI.	108
5.25. SNR comparison between the original image obtained by the Bruker system and the image reconstructed through the CMOS chip.	109
5.26. SNR comparison between the original image obtained from the Bruker system and the image reconstructed from the simulation method described in chapter 4.	110
5.27. MRI receive array of two surface coils. The distance between the coils is three times the coil diameter in order to minimize coupling. The sample for each coil is Gadolinium-doped water of 1.5 mL volume.	111
5.28. Results of the MRI experiment using two-coil array. (a) Image reconstructed from coil 1. (b) Image reconstructed from coil 2. (c) Image obtained from a sum of squares of (a) and (b).	111
6.1. The block diagram of the proposed MRI receiver architecture. It consists of low-noise amplification, quadrature demodulation, and analog-to-digital conversion.	114
6.2. The block diagram of a typical $\Sigma\Delta$ ADC.	115
6.4. Input and output signals of a typical $\Sigma\Delta$ modulator.	116
6.5. Linearized model of a $\Sigma\Delta$ ADC with single bit quantizer.	116
6.3. $\Sigma\Delta$ ADC with a single bit quantizer.	117
6.6. Linearized moder of a first-order $\Sigma\Delta$ ADC with a single-bit quantizer. . .	117
6.7. Magnitude of the frequency response for the STF and the NTF over normalized frequency.	118
6.8. Block diagram of a second-order $\Sigma\Delta$ ADC.	119
6.9. The magnitude of the frequency response of the NTF for the first-order and the second-order $\Sigma\Delta$ ADC.	119

6.10. Matlab GUI to perform a system-level simulation of the new MR receiver architecture described in figure 6.1.	121
6.11. Simulink model of a third-order $\Sigma\Delta$ ADC with a single bit quantizer. . .	122
6.12. Simulation results of the third-order $\Sigma\Delta$ ADC plotted in figure 6.11 for OSR = 120. (a) The digital output stream of the ADC. (b) The input sinusoid (blue) of the ADC and the decimated output (red). (c) The power spectral density (PSD) of the ADC's output. The in-band noise in this case is approximately -77 dBFS.	123
6.13. Effect of increasing the oversampling ratio (OSR) of the $\Sigma\Delta$ ADC in the MR receiver in figure 6.10.	124
6.14. Circuit implementation of the new MR receiver architecture sketched in figure 6.1.	126
6.15. Power spectral density of the output of the third-order $\Sigma\Delta$ modulator depicted in figure 6.14. The signal has a bandwidth of 250 kHz, while the OSR is 128.	127
6.16. SNR of the $\Sigma\Delta$ modulator versus the normalized input voltage.	127
6.17. A Matlab program to process the simulation outputs of the circuit in figure 6.14, and reconstructs the MR image.	128
6.18. Original and reconstructed image resulting from the circuit-level simulation of the MR receiver in figure 6.14.	129

List of Tables

3.1.	Parameters used to calculate the maximum amplitude of the MR signal.	41
3.2.	Summary of the common-source LNA simulation parameters.	45
3.3.	Summary of the common-gate common-source LNA simulation parameters.	50
3.4.	Summary of the frequency mixer's simulation parameters.	55
3.5.	Summary of the operational amplifier parameters.	61
3.6.	Post-layout simulation results of the CMOS FDM channels.	66
4.1.	Computed performance of the 16-channel multiplexer.	85
4.2.	Summary of the Matlab programs that were presented in this chapter.	87
5.1.	Comparison between this work and other works.	97
5.2.	The main parameters of the imaging experiment in a 9.4 T MR scanner employing the CMOS FDM.	107
5.3.	The main parameters of the imaging experiment using a two-channel MRI array.	111
6.1.	$\Sigma\Delta$ modulator parameters	125
6.2.	Summary of the Matlab programs introduced in this chapter.	130

Acknowledgments

First and foremost, I would like to express my sincere and deepest thanks and gratitude to my supervisor Prof. Dr. Jan G. Korvink for giving me the chance to conduct my PhD research in his laboratory on magnetic resonance imaging. I am very grateful to him for his great support, guidance, and encouragement from the initial level to the final level of my work. The monthly meetings were extremely helpful and very inspiring. I enjoyed the discussions in these meetings very much, and they made me use my time in the most efficient way. I am very thankful to Prof. Dr. Jan G. Korvink for the very stimulating and exciting research environment he established.

I would also express my deep thanks and acknowledgments to my group leader Dr. Oliver G. Gruschke for his great support. I still remember his words in my first day in the laboratory "Yes! its doable". I am very thankful to him for giving me the time for a lot of fruitful discussions and for the long measurements days in the university hospital in Freiburg. Deep thanks to Oliver's group: Erwin, Robert, and Katharina for the nice monthly meetings.

I am very grateful to Prof. Dr. Jens Anders for agreeing to co-examine my thesis. I also would like to deeply thank him for hosting me in a visit to his lab.

It is a pleasure to acknowledge Prof. Dr.-Ing. Christoph Stiller for accepting to be the chairman of the exam session.

Many thanks should go to the entire group of Prof. Dr. Jan G. Korvink for the very nice work atmosphere. No one has ever hesitated to offer help and give advice. You guys were awesome. I would particularly thank Gaby Kieninger for helping me go through many administrative regulations. I also would thank Jens Höfflin for helping me to do the measurements on the 11.7 T Bruker scanner.

I would also thank very much Prof. Dr. Jürgen Hennig for allowing me to conduct experiments on the 9.4 T Bruker scanner in the university hospital. Besides, I would

B. Acknowledgments

express my acknowledgments to Dr. Elmar Fischer, Dr. Jochen Leupold, and Dr. Dominik von Elverfeldt for discussions and helping me to do some experiments on the 9.4 T scanner.

I would also gratefully acknowledge the partial funding from the Fritz-Hüttinger foundation, and subsequent project funding from the ERC under grant number 290586 - NMCEL.

I cannot find words to express my heartfelt gratitude and gratefulness to my lovely wife Rawan for her great patience and continuous support and encouragement. I am indebted to her for taking care of our lovely kids Saba and Omar, whom I would lovingly thank for their nice daily wishes.

Last but not the least, I would express my heartfelt thanks to my lovely parents Zakia and Mohammed, my wife's parents, and to all my family members and friends.

Thank you very much... !

List of Publications

Peer-reviewed Articles

1. **Jouda, M.**, Gruschke, O.G. and Korvink, J.G., 2014. *Implementation of an in-field CMOS frequency division multiplexer for 9.4 T magnetic resonance applications*. International Journal of Circuit Theory and Applications.
2. **Jouda, M.**, Gruschke, O.G. and Korvink, J.G., 2015. *Circuit level simulation of MRI receive chain using excitation derived from images*. Concepts in Magnetic Resonance Part B: Magnetic Resonance Engineering, 44(4), pp.102-113.
3. **Jouda, M.**, Gruschke, O.G. and Korvink, J.G., 2016. *A new fully integrated multi-channel receiver design for magnetic resonance imaging*. Concepts in Magnetic Resonance Part B: Magnetic Resonance Engineering. (under review).

Conference Contributions

1. **Jouda, M.**, Gruschke, O.G. and Korvink, J.G., 2013, June. *CMOS 8-channel frequency division multiplexer for 9.4 T magnetic resonance imaging*. In Ph. D. Research in Microelectronics and Electronics (PRIME), 2013 9th Conference on (pp. 25-28). IEEE.
2. **Jouda, M.**, Gruschke, O.G. and Korvink, J.G., 2014. *Design, Simulation, and Characterization of a CMOS Heterodyne Receiver Front-End using Real MRI Data*. Euromar conference 2014, Zürich, Switzerland (Poster).
3. **Jouda, M.**, Gruschke, O.G., Fischer, E., Leupold, J., Elverfeldt, D., Hennig, J. and Korvink, J.G., 2015. *Magnetic resonance spectroscopy and imaging using a CMOS frequency division multiplexer*. Euromar conference 2015, Prague, Czech Republic (Presentation).
4. **Jouda, M.**, Gruschke, O.G., Fischer, E., Leupold, J., Elverfeldt, D., Hennig, J. and Korvink, J.G., 2015. *CMOS frequency division multiplexer enables multi-channel magnetic resonance imaging with a single channel spectrometer*. MikroSystemTechnik 2015.

5. Zadeh, S.G., Kudryavtsev, M., **Jouda, M.**, Korvink, J.G. and Bechtold, T., 2015. *System Level Simulation of Compact Parametric Model of Magnetic Resonance Micro Sensor*. MikroSystemTechnik 2015.